



Universiteit  
Leiden  
The Netherlands

## **X-ray spectroscopy of interstellar dust: from the laboratory to the Galaxy**

Zeegers, S.T.

### **Citation**

Zeegers, S. T. (2018, November 1). *X-ray spectroscopy of interstellar dust: from the laboratory to the Galaxy*. Retrieved from <https://hdl.handle.net/1887/66668>

Version: Not Applicable (or Unknown)

License: [Licence agreement concerning inclusion of doctoral thesis in the Institutional Repository of the University of Leiden](#)

Downloaded from: <https://hdl.handle.net/1887/66668>

**Note:** To cite this publication please use the final published version (if applicable).

Cover Page



Universiteit Leiden



The handle <http://hdl.handle.net/1887/66668> holds various files of this Leiden University dissertation.

**Author:** Zeegers, S.T.

**Title:** X-ray spectroscopy of interstellar dust: from the laboratory to the Galaxy

**Issue Date:** 2018-11-01

# **X-ray spectroscopy of interstellar dust**

from the laboratory to the Galaxy



# **X-ray spectroscopy of interstellar dust**

from the laboratory to the Galaxy

## **Proefschrift**

ter verkrijging van  
de graad van Doctor aan de Universiteit Leiden,  
op gezag van Rector Magnificus prof. mr. C. J. J. M. Stolker,  
volgens besluit van het College voor Promoties  
te verdedigen op donderdag 1 november 2018  
klokke 12:30 uur

door

**Sascha Tamara Zeegers**  
geboren te Alkmaar  
in 1985

## Promotiecommissie

**Promotor:** Prof. dr. Alexander G.G.M. Tielens

**Co-promotor:** Dr. Elisa Costantini

**Overige leden:** Dr. C. Jäger (University of Jena, Germany)  
Prof. dr. J. Kaastra  
Dr. F. Kemper (Academia Sinica, Taiwan)  
Prof. dr. F. Paerels (Columbia University, NY)  
Prof. dr. H. J. A. Röttgering

Dedicated to my parents: Marianne and Siem

Dit proefschrift werd ondersteund door  
de Nederlandse Organisatie voor Wetenschappelijk Onderzoek (NWO) en  
het Leids Kerkhoven Bosscha fonds.

Cover design: The artwork on the front cover shows an artist's impression of the Galaxy. It was made combining various textile techniques, using wool, silk, fabrics, beads and yarn. The silver stars indicate the position of bright X-ray binaries near the center of the Galaxy and are surrounded by small olivine beads. This artwork was made and designed by Marianne Zeegers, who is a certified textile crafts artist. The back cover shows the X-ray spectrum of olivine around the silicon K-edge.

ISBN: 978-94-028-1234-3

© 2018 Sascha Zeegers

# Contents

<b>1</b>	<b>Introduction</b>	<b>1</b>
1.1	Detecting dust in space . . . . .	1
1.1.1	Discovering dust . . . . .	1
1.1.2	The life cycle of dust in the universe . . . . .	1
1.2	Observational constraints on dust properties . . . . .	5
1.2.1	Composition of interstellar dust . . . . .	5
1.2.2	Grain sizes and size distributions . . . . .	7
1.2.3	Open questions on interstellar dust . . . . .	9
1.3	Using the X-rays to study dust . . . . .	10
1.3.1	X-ray Absorption Fine Structures . . . . .	11
1.3.2	From X-ray laboratory studies of interstellar dust to extinction models . . . . .	13
1.3.3	Mapping the dust in the Galaxy . . . . .	16
1.3.4	X-ray scattering haloes . . . . .	17
1.4	Thesis outline . . . . .	17
1.5	Future dust studies in the X-rays . . . . .	19
<b>2</b>	<b>Absorption and scattering by interstellar dust in the silicon K-edge of GX 5-1</b>	<b>31</b>
2.1	Introduction . . . . .	32
2.2	X-ray absorption edges . . . . .	34
2.3	Laboratory data analysis . . . . .	35
2.3.1	The samples . . . . .	35
2.3.2	Analysis of laboratory data . . . . .	36
2.4	Extinction cross-sections . . . . .	40
2.4.1	Optical constants . . . . .	40
2.4.2	Mie scattering calculations . . . . .	41
2.5	GX 5-1 . . . . .	43
2.6	Data analysis of GX 5-1 . . . . .	44
2.6.1	Continuum and neutral absorption . . . . .	45
2.6.2	Fit to Chandra ACIS HETG data of the silicon edge . . . . .	47
2.6.3	Hot ionized gas on the line of sight in the Si K-edge region? . . . . .	49
2.7	Discussion . . . . .	50
2.7.1	Abundances towards GX 5-1 . . . . .	50
2.7.2	Comparison to iron-poor, amorphous, and crystalline dust . . . . .	53
2.7.3	Comparison with dust compositions along other sight lines . . . . .	54
2.7.4	Limiting factors in the analysis of the Si K-edge . . . . .	55
2.7.5	Scattering and particle size distributions . . . . .	56

2.8	Summary . . . . .	58
2.A	Correction for saturation . . . . .	59
2.B	Si K-edge models . . . . .	60
<b>3</b>	<b>Dust absorption and scattering in the silicon K-edge</b>	<b>71</b>
3.1	Introduction . . . . .	72
3.2	X-ray absorption edges . . . . .	74
3.2.1	The samples . . . . .	74
3.2.2	Analysis of laboratory data . . . . .	75
3.2.3	X-ray Absorption Fine Structures . . . . .	76
3.3	Extinction cross sections . . . . .	78
3.4	Data analysis of the LMXB . . . . .	79
3.4.1	Source selection . . . . .	79
3.4.2	Modeling procedure . . . . .	79
3.4.3	Silicon abundances and depletion . . . . .	85
3.5	Discussion . . . . .	86
3.5.1	Dust composition toward the Galactic Center . . . . .	86
3.5.2	Silicon abundances and depletion . . . . .	88
3.6	Summary and Conclusion . . . . .	91
3.A	Data tables LMXBs . . . . .	92
3.B	Si K-edge models . . . . .	94
<b>4</b>	<b>X-ray extinction from interstellar dust</b>	<b>113</b>
4.1	Introduction . . . . .	114
4.1.1	The elements in this study . . . . .	116
4.2	Extinction profiles . . . . .	118
4.2.1	Laboratory data for aluminum . . . . .	119
4.3	Simulations . . . . .	119
4.4	Discussion . . . . .	121
4.4.1	Carbon . . . . .	121
4.4.2	Aluminum and calcium . . . . .	121
4.4.3	Sulfur . . . . .	123
4.4.4	Titanium and nickel . . . . .	124
4.5	Conclusion . . . . .	124
4.A	Extinction profiles . . . . .	128
<b>5</b>	<b>Interstellar dust scattering of X-rays: the case of AU Microscopii</b>	<b>139</b>
5.1	Introduction . . . . .	140
5.2	X-ray dust models for debris disk: the halo model . . . . .	142
5.2.1	Particle size distribution . . . . .	143
5.2.2	Scattering efficiency versus energy and particle size . . . . .	146
5.2.3	Dust mixtures in debris disks . . . . .	147
5.3	X-ray scattering by dust in the AU Mic debris disk . . . . .	148
5.4	The halo modeling . . . . .	150
5.5	Discussion . . . . .	152

---

5.6 Conclusion . . . . .	154
Nederlandstalige samenvatting	161
Westfriese samenvatting	171
English summary	179
Curriculum Vitae	187
Acknowledgments	189
List of acronyms	191



# 1 | Introduction

## 1.1 Detecting dust in space

### 1.1.1 Discovering dust

The space between stars, also called the interstellar medium (ISM), is not a perfect vacuum. Between the stars, we can observe clouds of dust and gas of varying shapes, densities and sizes. These clouds can be observed, for instance, as dark patches in our own Galaxy contrasting with the light from the stars, as can be seen in Figure 1.1, panel a. In the 18th century the interest in these dark parts increased, due to the developments in the quality of telescopes, which made it possible to observe them in more detail. Caroline Herschel wrote to her nephew John Herschel encouraging him to observe a certain part of the sky, of which she said John's father, William Herschel, described it as a hole in the sky. However, in the early 20th century, these 'holes' were eventually discovered to be foreground clouds obscuring the stars behind them. In the 1890s Barnard started to photograph these clouds (eventually published in a catalogue, Barnard (1919)), which revealed many details of these clouds, invisible to the naked eye. Agnes Clerke described them in her book 'Problems in Astrophysics' as obscuring bodies (Clerke, 1903). Even in the case where no clouds are observed towards a star, it was found that extinction of light still takes place (Struve, 1847). It took until  $\sim 1930$  to prove that the extinction, shown by the reddening of stars, is indeed caused by interstellar dust particles (independently described by Schalén (1929) and Trumpler (1930)). Since its discovery, the way dust has been perceived slowly changed. At first it was completely ignored, then it was considered to be a hindrance when trying to observe the stars and galaxies, but since the 1960s, dust has been more and more seen as an important component that drives many processes in the universe (Greenberg, 1963).

### 1.1.2 The life cycle of dust in the universe

The important role of dust in the universe is best shown by its role in every stage of the life cycle of stars. Of the normal matter in our Galaxy, about  $5 - 10 \times 10^9 M_{\odot}$  (solar masses) resides in the ISM in the form of gas and dust, which is about 5-10% of the total mass of all the stars in the Galaxy (e.g., Tielens, 2010; McMillan, 2017). Only 1% of the mass of the ISM is in the form of dust (Boulanger et al., 2000). Although, looking at the big picture, dust may seem to contribute little to the total content of the universe, it is nevertheless a very important component, since it plays a defining role in every stage of the life cycle of stars.

The life cycle of stars is shown in its five different stages in Figure 1.2.

1. Sources of interstellar dust: Our starting point in this figure, is actually the last phase in

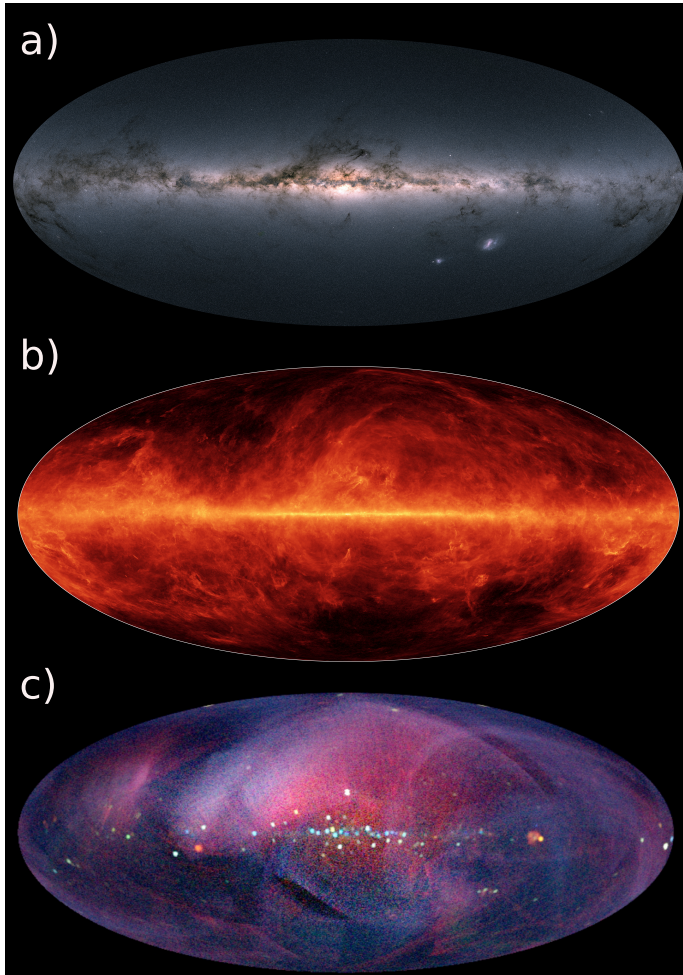


**Figure 1.1:** The Galaxy at three different wavelengths: a) The visible-near infrared: GAIA 330-1050 nm, image credit: ESA/Gaia/DPAC - b) infrared: Planck cold dust (20 K) map, image credits: ESA/NASA/JPL-Caltech - c) The X-rays: 0.5-16 keV MAXI all-sky survey, image credits: JAXA/RIKEN/MAXI team.

the life of a star. Stars enrich the universe with elements, produced during the nucleosynthesis process and in this way, provide the building blocks for the interstellar dust particles. Dust is thought to form as condensates in the atmospheres of evolved stars (mainly stars in the Asymptotic Giant Branch (AGB) phase) and consequently ejected in the ISM. Other potential sources of interstellar dust are supernovae (type Ia and type II), young stellar objects, red super giants and Wolf Rayet stars (Tielens, 2001). It is uncertain how much each of these sources contribute to the total dust budget. Especially the contribution of supernovae type II, is much debated (Cherchneff, 2013). Although

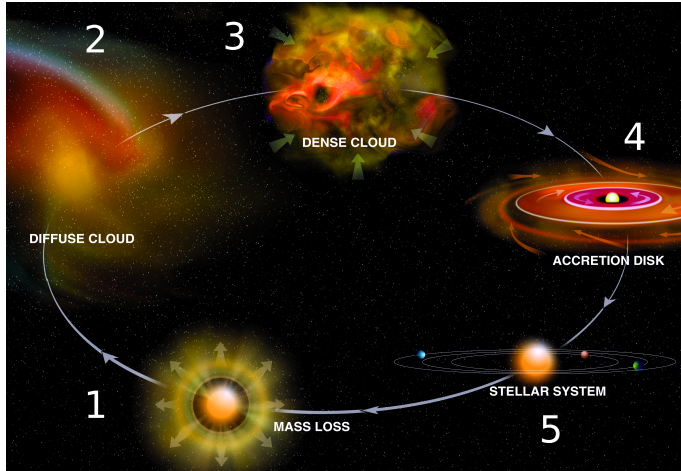


**Figure 1.2:** The life cycle of stars and interstellar dust in five stages: 1) evolved star, 2) diffuse cloud, 3) dense cloud, 4) protostellar disk phase and 5) evolved planetary system. At each stage in this cycle dust plays a crucial role. Image credit: Bill Saxton, NRAO/AUI/NSF.

recent observations by ALMA (Atacama Large Millimeter/submillimeter Array) show that more than  $0.2 M_{\odot}$  of dust is produced in the central part of SN 1987a, the reverse shock, which arises after the shock wave of the supernova rams into the ISM, may (partly) destroy these dust particles again (Indebetouw et al., 2014).

2. Diffuse clouds: The next stage shows a diffuse cloud. The ISM is not a homogeneous medium, but is rather patchy, i.e., the gas and dust in the ISM can be found in clouds of various densities. Most of the volume of the ISM is filled with a low density intercloud medium ( $n_{\text{H}} \approx 0.004 - 30 \text{ cm}^{-3}$ , where  $n_{\text{H}}$  is the density of hydrogen). Diffuse clouds have slightly higher densities of  $\sim n_{\text{H}} = 10^2 \text{ cm}^{-3}$  and extinction of  $A_V < 1$ <sup>1</sup>. Once ejected in the ISM, dust is rapidly mixed with other dust and gas and will cycle many times between the cloud and intercloud phase on a very fast timescale ( $\approx 3 \times 10^7 \text{ yr}$ ) (Tielens et al., 2005). Dust particles in diffuse clouds and in the intercloud medium find themselves in a violent environment. Collisions with cosmic rays may destroy the internal crystalline structure of the grains. Dust can be destroyed by supernovae shocks through sputtering and shattering (e.g., Guillet et al., 2007, 2009; Jones and Nuth, 2011). This destruction process is in fact predicted to be so successful, that it is still not clear why not all of the dust has been destroyed, since the formation timescale of the

<sup>1</sup>Extinction due to dust ( $A_{\lambda}$ ) varies with wavelength  $\lambda$  and depends on the composition and size distribution of ID particles. It can be connected to reddening of starlight by the extinction factor  $R_V = A_V / (A_B - A_V) \equiv A_V / (E(B - V))$ , where  $A_B$  and  $A_V$  are the extinctions measured at the  $B$  (4405 Å) and the  $V$  (5470 Å) photometric bands. Their difference is equal to the color excess or “reddening”  $E(B - V)$ , i.e., the difference between the observed color of the star and the color it would have when unaffected by extinction. In the Galaxy  $R_V = 3.1$  in the diffuse ISM. Since gas and dust are well mixed in the ISM,  $A_V$ , commonly used to indicate the extinction along the line of sight, is a measure for the column density of hydrogen  $N_{\text{H}}$ :  $N_{\text{H}}/A_V = 1.9 \times 10^{21} \text{ cm}^{-2} \text{ magn}^{-1}$ , for  $R_V = 3.1$  (Bohlin et al., 1978).

dust ( $\sim 2000$  Myr) is assumed to be much longer than the destruction timescale ( $\sim 500$  Myr) (Jones et al., 1994, 1996; Jones and Nuth, 2011). A solution to the problem of the formation of grains may be found in (re-)forming dust in the ISM itself (Dwek, 1998; Zhukovska et al., 2008; Draine, 2009; Zhukovska et al., 2018). In diffuse environments, dust is also exposed to stellar radiation (UV photons and X-rays) and cosmic rays. The grains absorb UV radiation and re-emit in the infrared. When observing the galaxy in the mid infrared, most of the observed radiation is emitted by dust particles, as can be seen in Figure 1.1 (panel b). Due to the grain heating by UV radiation, dust in diffuse clouds plays an important role in  $\text{H}_2$  formation on the surface of grains (Gould and Salpeter, 1963; Cazaux and Tielens, 2004; Wakelam et al., 2017). The same supernovae shocks that may destroy the dust particles, as well as stellar winds, collisions between clouds and turbulence, can also cause a disturbance in the diffuse cloud which may lead to compression of the cloud into a denser, translucent, cloud. Translucent clouds can be found within diffuse clouds, with  $1 < A_V < 2.5$  and densities of  $n_{\text{H}} \approx 10^3 \text{ cm}^{-3}$ . At this stage, the cloud becomes dense enough for dust grains to shield the interior of the cloud from optical and UV radiation, allowing molecules to form (Ciolek, 1995; van Dishoeck, 2014). Dust may act as a coolant for the gas in the case where the surrounding gas has a higher temperature than the dust grains, causing the cloud to cool down further and compress (Falgarone and Puget, 1985; Galli et al., 2002; Li et al., 2003).

3. Dense clouds: From the diffuse and translucent clouds, we now go to the next stage, namely a dense cloud. Dense clouds are defined as clouds with  $A_V > 3$  and densities of  $n_{\text{H}} = 10^3 - 10^6 \text{ cm}^{-3}$ . Most of the gas is now in the form of molecules. In these dense clouds, dust grains can catalyze chemical reactions on their surfaces by bringing atoms and molecules together (van Dishoeck, 2014, and references therein). They may grow in size due to coagulation (Ossenkopf, 1993) and layers of ice can form around the dust particles, of which water ice is observed to be the main constituent (Whittet et al., 1997; Pontoppidan, 2004). A dust particle may go through multiple cycles in and out of the dense cloud into the diffuse ISM and back. However, when the cloud becomes so massive that the gas pressure no longer support it, the cloud can become gravitationally unstable and will eventually collapse (Shu et al., 1993).
4. Consequently, a star forms at the center of the cloud. The nebula has now flattened into a disk. Again, dust plays an important role as the building blocks in the formation of planets inside the disk. When the gas has been dissipated from the disk, a dusty debris disk remains (Wyatt, 2008). The star will start to blow the smallest dust particles out of the disk, depending on strength of the solar wind and the radiation pressure of the star.
5. When the star has cleared its surroundings, a planetary system emerges. As the star ages, it will start to return matter into the ISM and the whole process can start again.

Cosmic dust can be observed virtually everywhere: in our solar system, around young stars, in giant clouds, the Galaxy, but also in distant galaxies (Hughes et al., 1998) and it is already present in the earliest eras of the universe (Watson et al., 2015). Interestingly these galaxies are the dustiest of them all, suggesting that dust is rapidly and effectively formed in the early universe. Hence, studying dust can help us to understand how the universe evolved. Besides

the arguments in favor of dust studies already given, there is of course another important reason to study dust, because we and everything around us all consists of cosmic dust. Therefore, if we want to understand the origin of life, it is necessary to understand the origin, formation and composition of cosmic dust.

## 1.2 Observational constraints on dust properties

After establishing that dust was actually present in the universe, it became necessary to model the interstellar dust. In the first place to take the extinction into account, in order to obtain accurate distance estimates of stars. However, since dust plays a role in many processes in the universe, it has become an essential component in many astronomical models. In order to develop accurate interstellar dust models, is important to understand the properties of dust: what interstellar dust exactly consists of, how it interacts with radiation, what the grain size distribution is, what shape and internal structure of the grains is and whether these properties change in different environments. Most of the properties of dust that are derived so far, have been obtained from observations of dust in the Galaxy. We list the main properties and findings in this paragraph.

### 1.2.1 Composition of interstellar dust

To understand interstellar dust (ID), a key parameter in this research field is to determine its composition. An important constraint on the composition of dust is given by the abundance of elements. We assume that the abundance is similar to the solar environment. Since the solar system abundances (in this thesis we will use the abundance set of Lodders and Palme (2009)) are well known, it is possible to predict the abundances in the ISM. In the upper panel of Figure 1.3 the abundance of elements versus the ionization energy of the corresponding atom can be seen. However, not all elements are abundant in the gas phase of the ISM. Some of the most abundant elements are missing in the gas phase (also referred to as depleted from the gas phase) and are thought to be instead included in dust particles. The depletion of elements from O to Zn is given in the middle panel Figure 1.3 (Jenkins, 2009).

The combination of abundance and depletion, indicates that dust should mainly consist of C, O, Mg, Si, Fe and possibly S. Besides these elements, less abundant, but highly depleted elements, such as Ti, Ca, Ni and Al can also be present in dust. The abundant elements He (not shown in Figure 1.3) and Ne are chemically inert and therefore do not contribute to the composition of dust. N is not a large constituent of dust either, but this is explained by its inclusion in the highly stable gas form of  $N_2$  (Gail and Sedlmayr, 1986).

Besides depletion studies, the composition of interstellar dust can be identified using more direct methods, such as identification through IR spectroscopy of circumstellar or interstellar dust and through studies of pre-solar interstellar dust grains recovered from meteorites or interplanetary dust particles. An overview of detected dust species is given in Table 1.1 (Tielens et al., 2005). There is a wide variety of dust species, reflecting the wide range of stellar sources of interstellar dust with different physical conditions (temperature, pressure, elemental abundances).

The way dust is produced is also an important factor in the composition of dust. However,

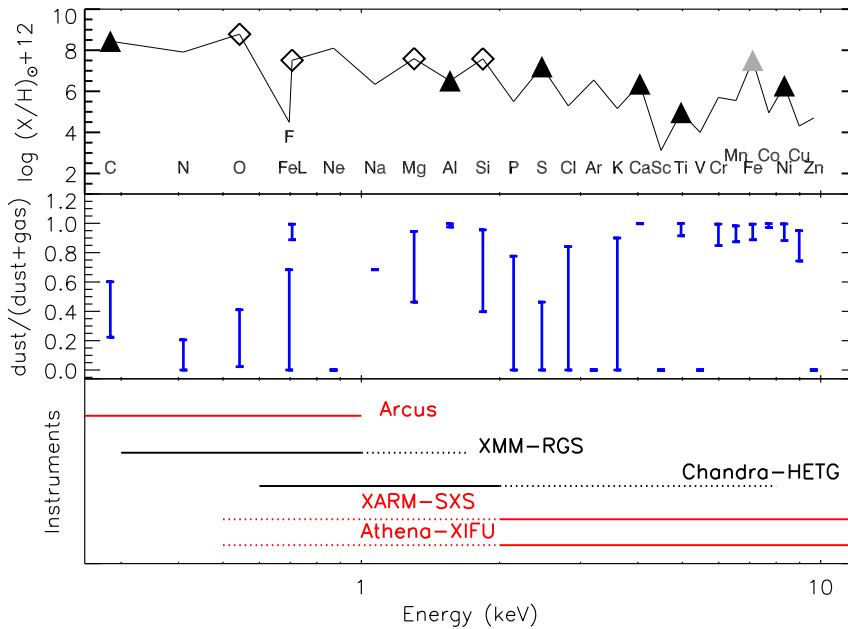


**Figure 1.3:** Figure taken from Chapter 4. Upper panel: abundance pattern as a function of energy for the absorbing elements in the X-ray band. Abundances of elements versus their K- or L-shell ionization energies. Abundances follow Lodders and Palme (2009) and they are expressed in terms of  $\log(X/H)+12$ . In this framework, the abundance of hydrogen is 12. The open diamonds mark the elements that are accessible by current X-ray instruments. The triangles are the relevant elements that will be accessible by future instruments to study dust. Middle panel: range of depletions. Lower panel: energy range covered by present (black) and future (red) missions. The solid line highlights the energy range where the capabilities of the instruments are optimal for observing absorption by dust.

there is much uncertainty in how much each of the dust producing sources contribute to the total dust budget. The most studied and understood dust producing sources in the Galaxy are AGB stars. AGB stars are either oxygen rich or carbon rich. One of the first molecules to form in the atmospheres of these stars is CO. Depending on the surplus of either carbon or oxygen, AGB stars are thought to produce carbonaceous or silicate dust grains (Andersen, 2007).

Combining abundance and depletion studies, theory and observations, dust in the ISM can be roughly divided into two main groups, namely silicates (e.g., pyroxene and olivine types) and carbonaceous dust, with the addition of oxides (e.g., MgO, SiO, SiO<sub>2</sub>), carbides (mainly SiC) and metallic iron (Draine, 2011).

Since the main building blocks of silicates, the elements Si, O, Mg and Fe, are found to be depleted in dust, interstellar silicates are assumed to be a major constituent of dust. This is indeed supported by observations. Silicates are detected in the ISM in infrared spectra by their characteristic 10  $\mu\text{m}$  (stretching of the Si-O bond) and 20  $\mu\text{m}$  (bending of the O-Si-O structure) features (e.g., Knacke and Thomson, 1973). These features indeed show that silicates are abundant in the interstellar medium and give the opportunity to investigate which species of silicates may be present. It is of great advantage that a wide variety of silicates are also

present on earth and can be characterized in laboratories through standard mineralogical and chemical techniques (Jaeger et al., 1994). The infrared spectra of interstellar silicate analogues offer the possibility for comparison with observations. The main contributions to the silicate infrared features are pyroxenes ( $\text{Mg}_x\text{Fe}_{(1-x)}\text{SiO}_3$ ) and olivines ( $\text{Mg}_{2x}\text{Fe}_{(2-2x)}\text{SiO}_4$ ) with  $0 < x < 1$ , although the ratio in which they occur in space is uncertain, as well as their Mg/Fe ratio (Kemper et al., 2004; Chiar and Tielens, 2006; Min et al., 2007). From the infrared features, it was also determined that  $<2\%$  of dust in the Galaxy is in crystalline grains (Kemper et al., 2004). Therefore, most of the dust, as observed in the infrared, is amorphous, meaning the crystalline structure in these grains is negligible.

Carbon is often mainly modelled by graphite (e.g., Mathis et al., 1977), but given that silicates are mostly amorphous, it is suspected that carbon dust particles also underwent amorphization and also exist in the ISM in the form of (hydrogenated) amorphous carbon (Compiègne et al., 2011). Furthermore, smaller amounts of carbon can be locked up in nano-diamond particles (Tielens et al., 1987; Lewis et al., 1987) and Polycyclic Aromatic Hydrocarbons (PAHs, e.g., Tielens, 2013). Figure 1.4 shows two grains, a) SiC and b) graphite, from interstellar origin, retrieved from the Murchison meteorite (Zinner, 2007). The grains show both a crystalline and amorphous structure, indicating the wide variation in the shape of dust grains.

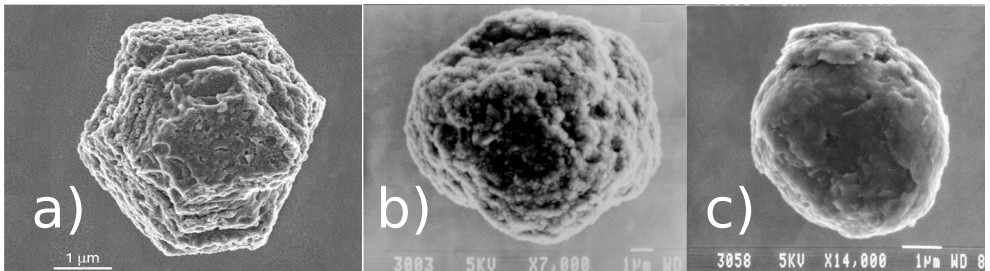


**Figure 1.4:** Presolar carbon grains from the Murchison meteorite: a) silicon carbide, b) and c) graphite adapted from Zinner (2007), image credit: Sachiko Amari and Scott Messenger.

## 1.2.2 Grain sizes and size distributions

The sizes of dust grains are an important modelling parameter, since they are connected with their origin and evolution. Grain size distributions are used many in interstellar dust models. There are many different size distribution models, with different input parameters for the grain composition and particle size range. All these size distributions seem to agree that most of the dust mass is in the large grains, while the surface area is dominated by the smaller grains. The extinction curve, which is shown in the right panel of Fig 1.5, can be used to determine the sizes of interstellar dust grains (Greenberg, 1968). Specifically, the extinction at a certain wavelength depends on a typical grains size, since the extinction cross section  $C_{\text{ext}} \propto \pi a^2$  and the grain size extinction is consequently dominated by particles of size  $a = \lambda/\pi^2$ , where  $\lambda$  is the wavelength. Small grains ( $\sim 0.01 \mu\text{m}$ ) dominate the extinction in the UV, while large grains

( $\sim 0.3 \mu\text{m}$ ) are responsible for the extinction in the near infrared. In this way, a size distribution can be tested by fitting them to the interstellar extinction curve. Mathis et al. (1977) developed a size distribution model (MRN, Mathis-Rumpl-Nordsieck) for average diffuse clouds that consists of two separate dust grain components, namely bare spherical silicate and graphite grains. Due to its simplicity, MRN can be easily implemented in numerical programs and is therefore still used in many interstellar dust models. The MRN distribution is given by:  $n(a)da = A \cdot a^{-3.5}da$ , where  $a$  is the particle size,  $n(a)$  is the number of grains, and  $A$  is the normalisation constant which depends on the type of dust (e.g., silicates or graphite). Particle sizes range between  $0.005 < a < 0.25 \mu\text{m}$ . The left panel of Figure 1.5 shows interstellar grain size distributions derived from the extinction curve (as shown in the right panel). The size distributions are plotted as mass fractions, where  $m(a)$  the differential mass, instead of the more commonly used number of grains  $n(a)$  (Kim et al., 1994). The mass distribution derived from the extinction curve is shown by the histogram with the contributions of graphite and silicate displaced by a factor of 10, for clarity. The MRN distribution is shown by the solid lines. This simple exponential function fits the extinction well, but at larger wavelengths the size distribution departs from an exponential. It also shows a sharp cut off at particles sizes beyond  $0.25 \mu\text{m}$ . The dashed line in Figure 1.5 (right panel) (Kim et al., 1994), for example, shows a size distribution with a smooth cut-off at large particle sizes. More elaborate size distributions may include more complex grain composition and non-spherical grains (e.g., Weingartner and Draine, 2001; Zubko et al., 2004; Draine and Li, 2007; Shen et al., 2008; Draine and Fraisse, 2009; Hoffman and Draine, 2016). In this thesis, we will mainly use MRN size distributions, but also discuss alternative distributions and their implications.

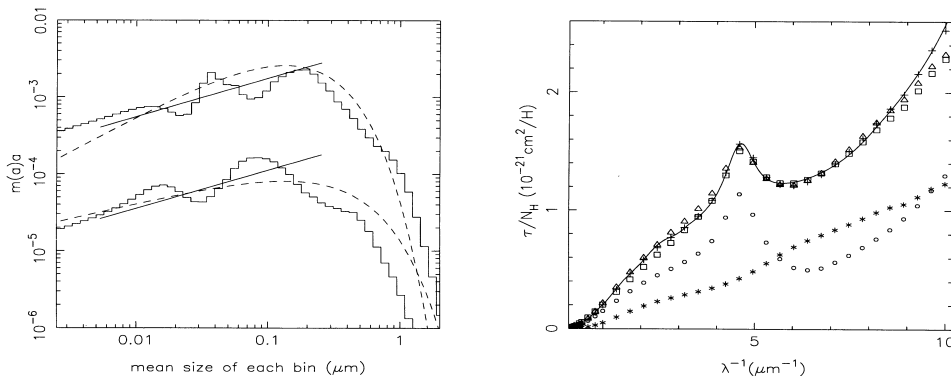


**Figure 1.5:** Left: interstellar grain size distributions - plotted as mass fractions - derived from the extinction curve (as shown in the right panel). The top histogram shows the mass fractions per particle size bin of silicates and the lower histogram shows graphite, displaced downward by a factor of 10. The solid line shows the MRN size distribution. The dashed curves are size distributions derived by Kim et al. (1994). Right: the corresponding extinction curve normalized to the hydrogen column density. The calculated extinction curve is compared to the observations in the right panel. The contributions due to graphite (o) and silicates (\*) are shown separately. Figure taken from Kim et al. (1994).

### 1.2.3 Open questions on interstellar dust

In the past decades, our understanding of ID has hugely improved. However, there are still significant gaps in our knowledge. Here we list the main open questions on ID that will be considered in this thesis.

- We do not yet completely understand the composition of dust. For instance, we do not know which types of silicates are most abundant in the ISM and consequently what the ratio is between olivine and pyroxene. Furthermore, there are large uncertainties about how Fe, S, O and C are incorporated into dust (e.g., Mathis, 1996; Dwek, 1997; Wakelam and Herbst, 2008; Wang et al., 2015; Dwek, 2016). Iron bearing silicates cannot account for all the iron locked up in dust. Sulfur is only found to be depleted along some lines of sight, but it has surprisingly been detected in grains of interstellar origin retrieved from meteorites and interplanetary dust particles (e.g., Bernatowicz, 1997; Zinner and Amari, 1999; Westphal et al., 2014). A possible solution to both of these problems can be found in the form of metallic iron and/or iron sulfate inclusions in silicates, also referred to as GEMS (glass with embedded metal and sulfides, Bradley, 1994; Floss et al., 2006; Keller and Messenger, 2013). The depletion of oxygen cannot be explained solely through silicates, leaving still an amount of oxygen unaccounted for. In the case of carbon, we encounter the opposite problem, since traditional ID models require twice as much carbon in dust than is actually observed from depletion studies.
- We do not yet understand how dust is produced and how it is processed in the ISM. For instance, there are uncertainties about the amorphization processes of dust. Since most of the silicate dust appears to be amorphous, this may suggest either strong amorphization in the ISM, perhaps due to cosmic rays, or grain growth in the ISM itself. However, considering that 5-15% of the stardust formed around oxygen rich stars is in the form of crystalline magnesium rich silicates (Kemper et al., 2001; Molster et al., 2002; Waters, 2004) and that crystalline interstellar grains have been retrieved from meteorites and interplanetary dust particles, the amount of crystalline grains observed in the ISM is surprisingly low.
- We do not precisely understand if the properties of dust change with different environments. The chemical composition of dust may change with environment since we observe an increase in abundances of elements toward the central part of the Galaxy (Pedicelli et al., 2009; Rolleston et al., 2000; Davies et al., 2009). Furthermore, the wide range in depletion of some elements like Mg, Si and S seems to suggest a difference in composition of dust along varying sight lines. However, we do not yet know how the composition of interstellar dust changes with the environment. In dense environments, dust grains may have the opportunity to grow and therefore we might expect larger grains in denser environments. However, although this works well in modelling of dust grains, observations seem to indicate that dust in the Galaxy is well mixed.

In the remainder of the introduction we will discuss how the X-ray band can help to solve these issues.

### 1.3 Using the X-rays to study dust

Astronomy has always benefitted from observations at wavelengths that are beyond the range of sensitivity of our own eyes. The X-rays provide interesting advantages when studying interstellar dust with respect to other wavelengths:

- X-rays are sensitive to a wide range of column densities ( $N_{\text{H}} \sim 10^{(20-23)} \text{ cm}^{-2}$ ); this makes it possible to analyze the dust content in various regions of the Galaxy.
- Scattering and absorption of dust can be simultaneously studied.
- Absorption of both gas and dust can as well be measured simultaneously for elements with absorption features in the X-ray band. For these elements, depletion is easy to determine, because the dust abundance does not have to be inferred from a reference solar abundance.

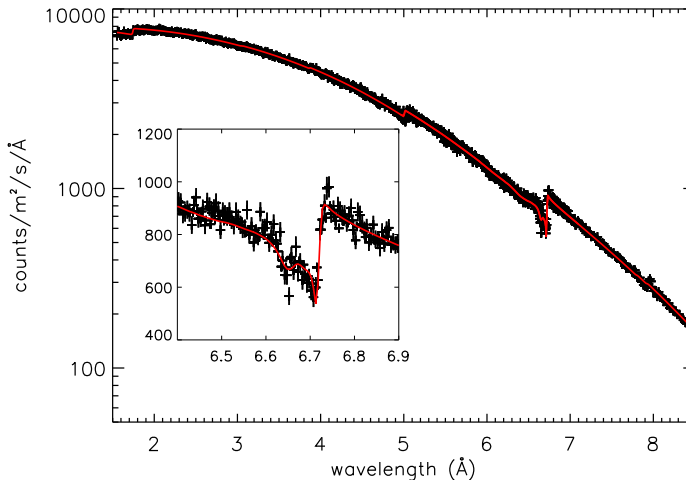


**Figure 1.6:** Spectrum of the low mass X-ray binary GX 5-1 with Si K-edge at 6.7Å. The source is observed by *Chandra* using the HETGS instrument. The red line shows a fit to the spectrum using our silicate dust extinctions models described in Chapter 2 and 3. The inset shows the details of the area around the Si K-edge, where the XAFS are visible.

The launch of the X-ray satellites *XMM-Newton* and *Chandra* marked the start of a new era in the study of interstellar dust using X-ray spectroscopy. These telescopes have a spectral resolution which is suitable to study the details in the spectra of X-ray sources which arise due to absorption and scattering by dust particles along the line of sight (LOS). The X-ray spectra of X-ray binaries can be used to study the intervening gas and dust along their lines of sight, simply using them as a lantern shining through the ISM. These sources consist of two components, a neutron star or a black hole which accretes material from a companion star, usually a normal star (*viz.*, a non-giant star). These systems are very bright in X-rays, because the accreted material from the companion star forms a disk around the accretor, which emits

in the X-rays due to the gravitational potential energy of the in-falling matter. X-ray binaries are divided in two groups, Low Mass X-ray binaries (LMXB) and high mass X-ray binaries, depending on the mass of the companion star (Lewin et al., 1997). The bright LMXBs are particularly useful in dust studies due to their high flux and simple spectra. Most LMXB do not show sharp intrinsic absorption features in the soft and intermediate X-rays (i.e., photon energies lower than 10 keV), but are rich with absorption from the ISM. Most of the X-ray binaries can be found in the plane of the Galaxy. The X-ray sky can be observed in Figure 1.1 panel c), where the many of the point sources are bright X-ray binaries. An example of a spectrum is given in Figure 1.6. Around  $6.74 \text{ \AA}$  we can observe a discontinuity in the spectrum, which is called an ‘edge’. An edge occurs at wavelength where the energy of the incoming X-ray photons equals the binding energy of a core electron. The X-ray photon can be effectively absorbed and ionizes the core electron, causing a steep increase in absorption. The edge is usually indicated by the element and the electron shell, for instance in the case of Figure 1.6 we observe the Si K-edge. Depending on the brightness of the source, the column density along the LOS, and the characteristics of the telescope, we can observe the edges of different elements. Figure 1.3 shows the ionization energies of the elements C to Zn. The extinction features of O, Mg, Si and Fe in the X-ray band, fall within the range of the range of XMM-Newton and Chandra. These elements are also the main building blocks of silicates, making the X-ray band especially suitable for the study of silicon based dust. As can be observed in Figure 1.6, the edge is not smooth, but contains features. These features, X-ray Absorption Fine Structures (XAFS), can be used as a fingerprint for the type dust we are observing, since each different dust composition results in a unique pattern (Rehr and Albers, 2000). The extinction models that can be derived from laboratory studies can be used to characterize ID (e.g., Martin, 1970; Martin and Sciama, 1970; Evans, 1986; Woo, 1995; Forrey et al., 1998; Draine, 2003; Lee and Ravel, 2005; Lee et al., 2009; Costantini et al., 2012).

### 1.3.1 X-ray Absorption Fine Structures

XAFS arise from the wavelike nature of electrons and the fact that an atom in a dust grain is surrounded by neighboring atoms (Meurant, 1983). When an incoming X-ray photon encounters a dust grain, it can be absorbed by an atom in the grain, as shown in Figure 1.7. Consequently, an electron in one of the inner shells of the atom is expelled to the continuum. The ejected photoelectron has a kinetic energy which is equal to the difference between the excitation energy of the atom and the energy of the incoming photon. The electron now behaves like a wave, also indicated as a photoelectron. This can be seen in the panel a) of Figure 1.7, where the photoelectron is depicted as a wave emanating from the site of the absorbing atom. If there are no neighboring atoms, we obtain an absorption feature as shown on the right in panel a). However, in panel b), the absorbing atom is surrounded by neighboring atoms, as is the case in dust grains, and the photoelectron is now scattered by these atoms. New waves emanate from the site of the neighboring atoms. These waves are superimposed on the initial wave and cause alternating constructive or destructive interference at the site of the absorbing atom, depending on the kinetic energy of the photoelectron. In this way, the probability of the photoelectric effect to occur is changed at the site of the absorbing atom. The XAFS pattern depends on the type of element and the position of the neighboring atoms. Each different dust composition will give a different and unique XAFS pattern. Even when

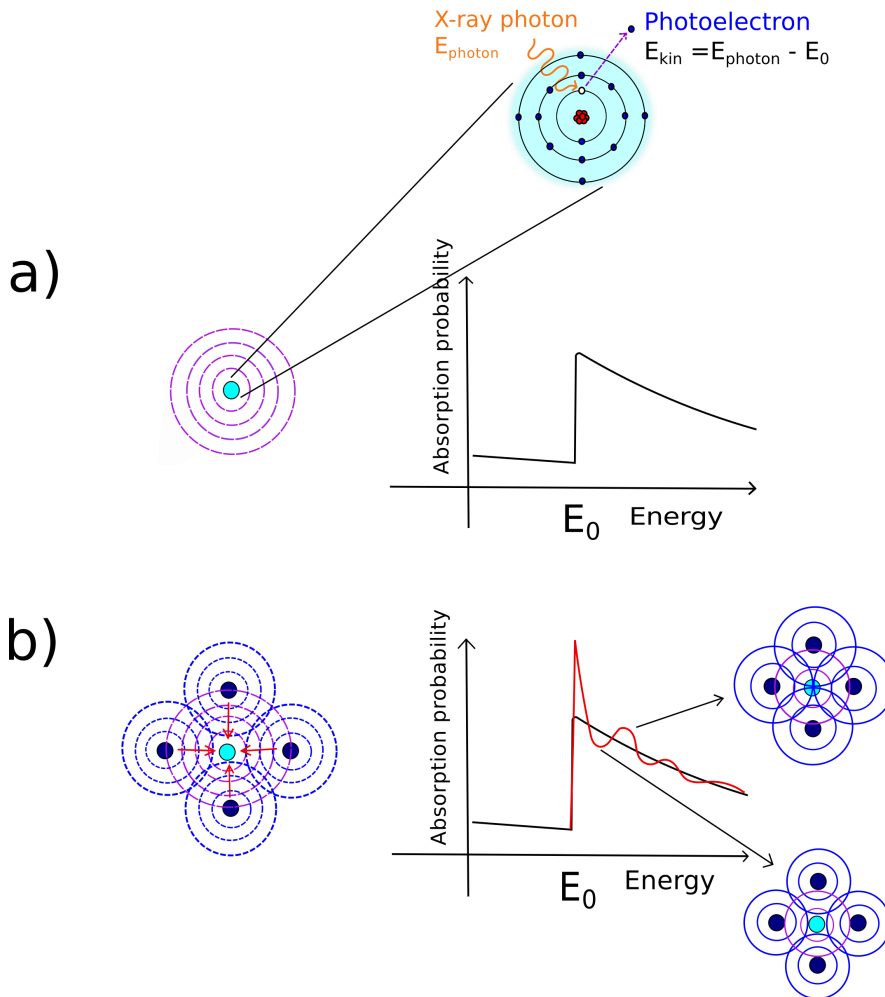


**Figure 1.7:** X-ray absorption fine structures (XAFS) are features observed in X-ray absorption spectra. Above panel a) we show the photoelectric effect. An X-ray photon is absorbed and a core-level electron is promoted out of the atom. The electron has a kinetic energy which is equal to the difference of the photon energy  $E_{\text{photon}}$  and the binding energy  $E_0$  of the electron. Panel a): The resulting photoelectron can be considered as a wave emanating from the site of the atom, indicated by the purple circles. On the right the resulting absorption probability versus the energy is shown. The probability increases at the energy of the binding energy and then gradually decays with increasing energy. Panel b): Here we show the same situation, but now the absorbing atom is surrounded by neighboring atoms. The initial wave is scattered by these atoms and new waves emanate from these sites, indicated by blue circles. On the right we show again the resulting absorption probability, where the black line indicates the situation of panel a) and the red line shows the modified absorption (i.e., XAFS) when the neighboring atoms are present. The scattered blue waves are superimposed on the initial purple wave and cause alternating constructive or destructive interference at the site of the absorbing atom, depending on the kinetic energy of the photoelectron. This process is shown by the two insets on the right.

the composition of the material is kept the same, differences will occur when the lattice structure in which the atoms find themselves changes, because the distance between the atoms changes. XAFS are therefore suitable to study the level of crystallinity. Figure 1.8 shows a set of six absorption measurements of silicates with different crystalline structures and different compositions (Zeegers et al., 2017). When a sample is amorphous (i.e., the regular crystalline lattice structure has been destroyed) it loses its clearly peaked crystalline structure, as can be observed by the difference between amorphous and crystalline pyroxene, indicated by sample 2 and 3. A difference can be observed between two types of silicates as demonstrated here by the difference between olivine ( $[\text{Mg}, \text{Fe}]_2\text{SiO}_4$ ) and pyroxene ( $[\text{Mg}, \text{Fe}]\text{SiO}_3$ ).

### 1.3.2 From X-ray laboratory studies of interstellar dust to extinction models

In order to derive the properties of ID from the X-ray spectra, it is necessary to have a set of detailed extinction cross section models to analyze the edges in the spectra. The composition of these models should reflect the dust present in the ISM. Since we know from observations that interstellar dust mainly consists of silicates and carbonaceous particles, we can measure the properties of similar types of dust in the laboratory. Many of these analogues have been developed, but their spectra are mostly measured at longer wavelength, with a focus on infrared studies. On the other hand, literature data of XAFS in edges interesting for astronomy, does not contain measurements tailored to use in the ID studies, since these edges are often measured for commercial and industrial purposes. When available in literature, these materials are mostly crystalline, while dust in the ISM appears to be mostly amorphous (Kemper et al., 2004). This lack of available models led to the start of laboratory measurement campaigns to create a database for of edges of interstellar dust analogues (Lee et al., 2009; Costantini and de Vries, 2013).

In 2010 we started a large campaign at SRON Utrecht in the Netherlands (Costantini and de Vries, 2013). The aim is to measure XAFS of all the available edges in the X-ray band for a wide range of dust analogues, in order to avoid uncertainties in the interpretation of the X-ray spectra and to provide extinction models over a broad wavelength range. Since the X-ray band, with the edges of O, Si, Fe and Mg that can be observed with the available telescopes, is currently particularly suitable for silicates, we focused on these dust species. Each wavelength or energy range has its own dedicated laboratory instrumentation to measure the XAFS. For edges in the soft X-rays ( $<1$  keV) scanning electron microscope, with a free electron laser, can be used to measure the edges of, for instance, O K and Fe L. At higher energies (1 - 10 keV) a dedicated beamline at a synchrotron facility can be used to measure the edges of e.g., Mg K-, Si K-, S K- and Fe K-edges. As an example, Figure 1.8 shows the resulting laboratory measurements of the Si K-edge.

From the resulting laboratory absorption measurements, the refractive index can be obtained. The complex refractive index is given by:  $m = n + ik$ , where the optical constants  $n$  and  $k$  are the respective real and imaginary part. The refractive index is an important property of materials, because when  $n$  and  $k$  are known, we can model how a material interacts with light. The two are related to each other through the Kramers-Kronig relations (see, Bohren, 2010, for an extensive review of the Kramers-Kronig relations). From the laboratory measurements,  $k$  can be obtained, and using the Kramers-Kronig equation  $n$  can be derived (described in detail in Chapter 2). The optical constants can consequently be used to derive extinction, which

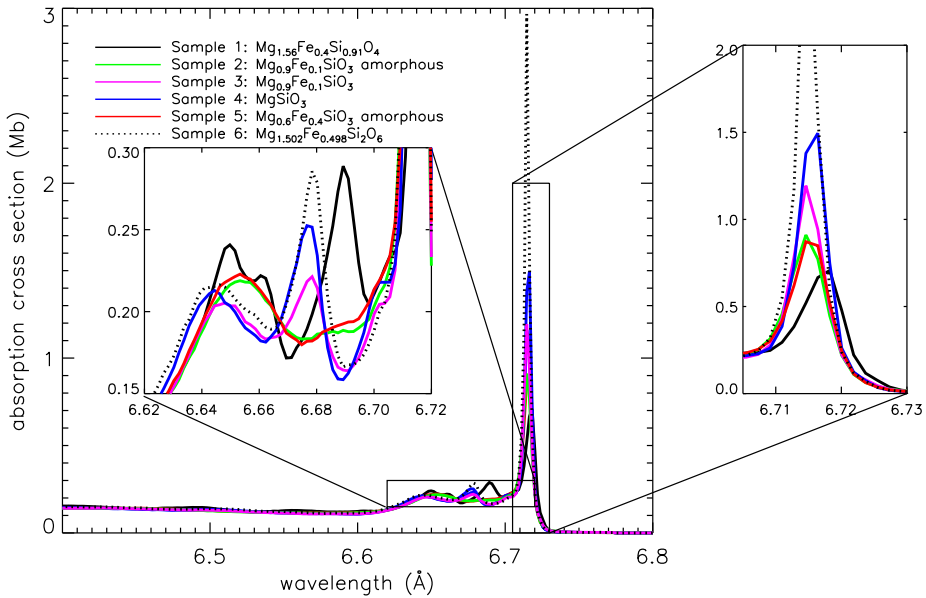


**Figure 1.8:** Figure taken from Chapter 2, showing the absorption cross sections of the Si K-edge of six silicate samples. The inset shows the XAFS, where the differences between the crystalline structures of olivines and pyroxenes can be observed by comparison of e.g., sample 1 and 4. The effect of amorphization can be observed by comparing e.g., sample 2 and 3, where some of the XAFS features are absent in the amorphous sample.

consists of absorption and scattering. There are several approximations to obtain the extinction efficiency ( $Q_{\text{ext}}$ ). They all require energy, the optical constants and a particle size as input parameters. Figure 1.9 lists the different approximation methods of extinction. The most used approximations in the X-rays are Rayleigh-Gans, Mie Theory (Mie, 1908), which can only be used for spherical grains, and Anomalous Diffraction Theory (ADT, van de Hulst, 1957). It depends on the parameter space of interest (i.e., particle size and energy) which of these methods is preferred. These methods return  $Q_{\text{ext}}$ , per wavelength or per energy unit, particle size and, if required, per scattering angle. To obtain the total cross sections per energy or wavelength unit ( $C_{\text{ext}} = \pi a^2 Q_{\text{ext}}$ ), we need to integrate over the particle size distribution. The size distribution has an important effect on the resulting extinction models, which is shown in Figure 1.10 and Chapter 2.

The extinction cross section models can be implemented in a spectral fitting code and the spectra of an X-ray source can consequently be fitted with the dust models (Figure 1.6). From these fits, we can obtain information on the composition, crystallinity and size distribution of the grains.

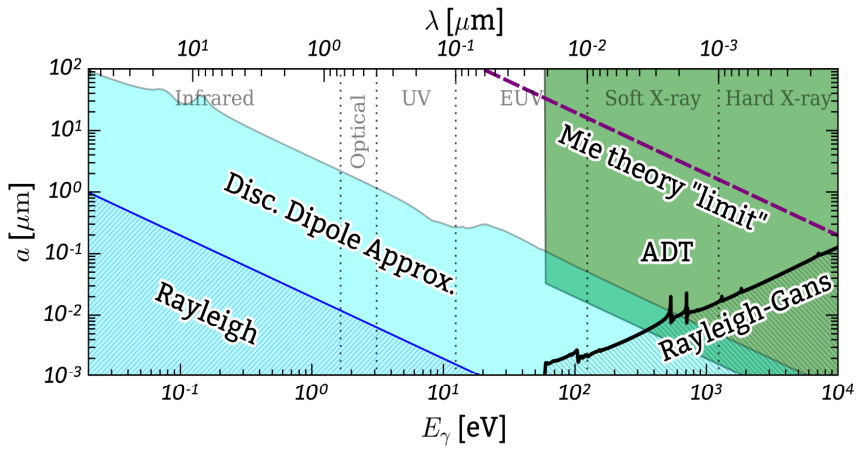


**Figure 1.9:** Validity regions for approximation schemes to calculate scattering and absorption by nonspherical dust grains. The Mie Theory is only valid for models with spherical grains. At X-ray energies Mie Theory, discrete dipole approximation (DDA), anomalous diffraction theory (ADT) and Rayleigh-Gans approximation can be used, depending on the energy range and the particle sizes involved. Adapted from Hoffman and Draine (2016).

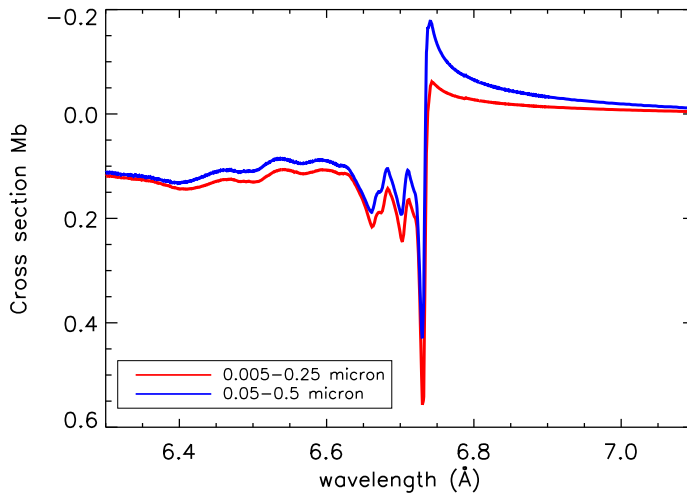


**Figure 1.10:** Two different size distributions that demonstrate the effects of scattering on the Si K-edge. The red line corresponds to an MRN size distribution. A size distribution with large particles is shown by the blue line. The difference can mainly be observed just before the edge, around  $6.75\text{\AA}$ , where the scattering feature near the edge is enhanced in the model that includes large particles, Chapter 2.

### 1.3.3 Mapping the dust in the Galaxy

For accurate modelling of interstellar dust, it is important to know whether the properties of dust change when the environment in which they are located changes. We can map the dust in different environments of the Galaxy by studying the extinction features of X-ray binaries along a variety of sight lines, since these sources are naturally distributed over the Galactic plane. The study profits from the large amount of archival data of these observatories, built up in the past 19 years. The spectra of many X-ray binaries have been observed and are currently publicly available in the corresponding databases, namely *Chandra* TGCat and the XMM-*Newton* Science archive. Not all the absorption edges can be accessed at the same time. When the column density increases, the soft energy X-rays will become more and more absorbed by the ISM. This allows to observe edges at higher energies for denser sightlines, provided that the source is bright enough at the wavelength of the edge and not all the X-rays are absorbed.

The diffuse sightlines have been studied using the O K-edge and Fe L-edge (Lee et al., 2009; Costantini et al., 2012; Pinto et al., 2013). A column density of  $2 \times 10^{21} \text{ cm}^{-2}$  along the line of sight is necessary to observe the edges and study these environments.

From these observations, it was found that in these diffuse environments, 15-20% of the oxygen and 65-90% of the iron is depleted in dust (Costantini et al., 2012; Pinto et al., 2013). Along the line of sight of LMXB 4U 1820-30 Costantini et al. (2012) found that Mg-rich silicates and metallic iron fitted the edges of O K and Fe L, respectively. Therefore, they suggest that the dust may consist of iron-poor silicates with metallic iron inclusion, supporting the presence of GEMS in the ISM. After analyzing the spectra of 9 X-ray binaries, Pinto et al. (2013) find that the ISM appears chemically homogeneous on large scales, showing similar gas ionization ratios and dust mixtures. A limiting factor at that time was the sparse availability of models of the dust edges. Upcoming studies will be more elaborate on the dust content at these diffuse lines of sight (Psaradaki et al., in prep.). The X-rays also provide the opportunity to measure abundances of the elements of observable edges. For many elements, a gradient in the abundance can be observed, indicating that the abundance gradually increases toward the Galactic center (e.g., Rolleston et al., 2000; Pedicelli et al., 2009; Davies et al., 2009; Pinto et al., 2013). This gradient depends on the stellar elemental yields. In the X-rays, this increase in abundances is observed in the diffuse ISM for the elements O, Ne, Fe and Mg. However, most of these abundance gradients are not well defined in the central Galactic environment.

In this thesis, we study the most central part of the Galaxy, with high column-density sight lines. The dense ISM can be explored using the edges of Mg K (Rogantini et al., in prep.), Si K (Chapter 2 and 3), S K (Chapter 4) and Fe K (Rogantini et al., 2018). The Si K-edge is currently particularly suitable for this study, since it lies in the optimal point of the *Chandra* HETGS grating's effective area and resolution. In order to observe this edge, we need a line of sight column density of  $1 - 10 \times 10^{22} \text{ cm}^{-2}$ . Along these sight lines the X-rays will pass many dense areas, namely several spiral arms and the Galactic Bulge, depending on the distance of the source, as can be seen in Figure 1.11. This is ideal to study the dense areas of the Galaxy and investigate whether this environment is significantly different from the diffuse environments.

### 1.3.4 X-ray scattering haloes

X-rays are efficiently scattered at small angles by interstellar dust grains, producing a halo of diffuse emission around the source. This was first predicted by Overbeck (1965) and detected for the first time by Rolf (1983). The haloes are very narrow, usually of arcminute scale angular size, because X-rays are strongly forward scattered. The halo is very faint in comparison to the source, since it contains at most 20% of the brightness of the source (Predehl and Schmitt, 1995). In order to observe the halo, it is necessary to use sensitive instruments with sub arcminute angular resolution, which is provided by *XMM-Newton* and (especially) *Chandra*. The intensity and shape of the halo depend on the source flux from which the scattered X-rays originate, but also the particle size distribution, the chemical composition of the dust and the location of the dust grain along the line of sight (e.g., Mauche and Gorenstein, 1986; Predehl and Schmitt, 1995; Predehl and Klose, 1996; Costantini et al., 2005). The scattering haloes can therefore be used to constrain and test dust models (e.g., Smith et al., 2006). In order to derive the properties of the dust from the observations, the halo can be modelled. However, in the modelling, the position of the dust along the line of sight is degenerate with the dust size distribution and this degeneracy can only be broken in some special cases. For example, observations of expanding X-ray dust scattering rings around variable X-ray sources provide an opportunity to investigate the location of dust clouds along the line of sight (Tiengo et al., 2010). In Chapter 5 of this thesis, we explore the possibilities of observing a scattering halo produced by a debris disk. In this special case, the degeneracy is broken as well, since the position of the dust along the line of sight is known.

## 1.4 Thesis outline

High resolution X-ray spectroscopy is an important tool in interstellar dust studies. By studying dust features in X-ray spectra and scattering haloes around X-ray sources, we may be able to answer fundamental questions about interstellar dust, such as the composition of interstellar dust, the processing of dust in the ISM and the possible differences of the dust properties in different environments of the Galaxy. In this thesis, we mainly use the Si K-edge to study the properties of silicate dust, one of the main constituents of ID. The study profits from new laboratory data of interstellar dust analogues. Observing the Si K-edge requires high column densities and we therefore observe sources whose radiation passes through the dense environment of the central Galactic region.

## Chapter 2

In this chapter, we present a pilot study of the Si K-edge in the observations of the X-ray binary GX 5-1. This bright X-ray binary is located near the Galactic center and the spectrum contains a prominent Si K-edge feature, as can be seen in Figure 1.11. We present laboratory measurements of silicate compounds that we took in 2012 at the Soleil synchrotron facility in Paris using the Lucia beamline. The sample set consisted of pyroxenes with varying Fe/Mg ratios and an olivine. Among the pyroxene silicates there were two amorphous samples present. Using the extinction models obtained from the laboratory data, we derived the properties of the interstellar silicate dust along the line of sight by fitting the Si K-edge seen in absorption

in the spectrum of GX 5-1. The impact of the presence of large particles along the line of sight is studied by modelling the edge with two different particle size distributions.

### Chapter 3

In this chapter we used high-quality grating spectra of nine LMXBs to study the ISM in the central part of the Galaxy. The location of the sources can be observed in Figure 1.11. The sources are located in or near the Galactic Bulge. This is an old and probably well mixed environment of the Galaxy, which may be reflected by the composition of the dust we observe. The previous set of 6 samples present in Chapter 2 has been expanded to 15, including, i.a., amorphous olivine, and quartz samples. We use the Si K-edge in the high-quality spectra of the X-ray binaries provided by the *Chandra* observatory to study the properties of the dust along different sightlines. Moreover, we are able to study the abundance and depletion of silicon in detail in an area where it is otherwise difficult to obtain constraints on these parameters.

### Chapter 4

In Chapter 4 we present an outlook for edge studies with future telescopes, as listed in Figure 1.3. We focus on the K-edges of C, S, Al, Ni, Ti and Ca. We make use of literature data for all the edges, with the exception of the Al K-edge, which was measured by us at Soleil with the Lucia beamline. We model the edges of these elements using the techniques developed in Chapter 2 and apply them to simulations of spectra produced by future X-ray telescopes taking into account the expected performance of the detectors concerning resolution and sensitivity. In the case of carbon and sulfur, the characterization of the chemistry of the absorbing dust can be determined. Observations of the sulfur edge may give more insight in the presence of sulfur in dust and in GEMS in particular. Since iron sulfates are thought to be an important constituent of GEMS, we use these compounds in our modelling. This characterization of the chemistry, will be more difficult for the other elements. The cosmic abundance of both Ni and Ti does not allow a detailed study of the features in the edge. Despite the high abundance, the modest changes in the shape of the edges of Al and Ca may not be significant do not show much variation. However, the observation of these edges will provide the opportunity to directly measure the depletions of these elements.

### Chapter 5

In Chapter 5 we explore the theory of X-ray scattering for a new parameter space, where the small angle approach is no longer valid and where the size distribution of the dust includes large ( $> 1 \mu\text{m}$ ) particles. We apply this theory, for the first time, to the environment of stellar debris disks where such conditions apply. We use as a best test case the debris disk around the star AU Microscopii. This star is a flaring M star, which is bright in the X-rays. A debris disk is a circumstellar belt of dust and debris. The sizes of the particles in the disk range from small dust particles up to large unobservable planetesimals (e.g., Lagrange et al., 2000; Wyatt and Dent, 2002). The system is well studied and we can make use of the known geometry of the disk. Since we know where the dust is located, we can model the predicted scattering halo using different dust composition. We find that models with a steeper slope, moderately strong

stellar wind model and a composition of silicates and graphite are the ones that would enhance a theoretical halo. After comparing the models with observations of the system, we find that the models do not produce a significant scattering halo, using the current spatial resolution. Future X-ray mission may enable us to observe the X-ray halo of debris disks. Such a X-ray telescope would require a PSF which has a FWHM  $< 0.5$  arcsec, i.e., smaller than the FWHM of Chandra.

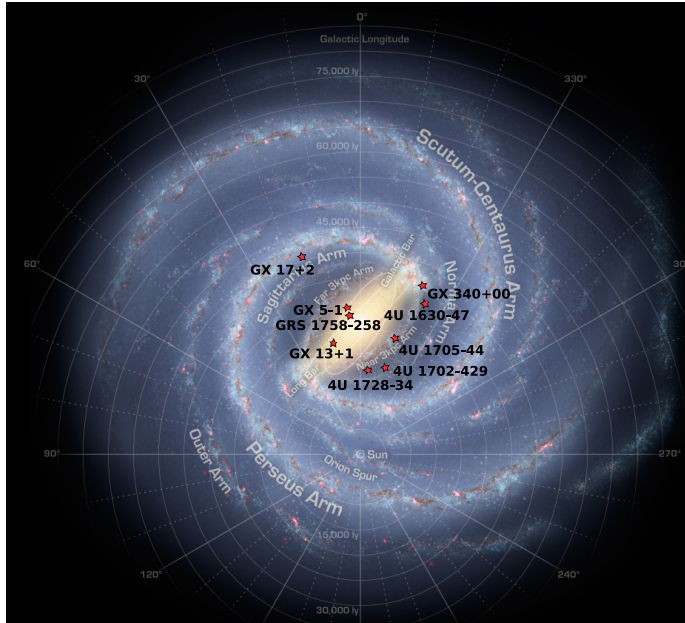


Figure 1.11: Artist's conception of a top-down view of the Milky Way, based on infrared images from NASA's Spitzer Space Telescope. The red stars indicate the position of the LMXBs studied in this thesis. Image credit: NASA/JPL-Caltech/R. Hurt

## 1.5 Future dust studies in the X-rays

There is a bright future for X-rays and interstellar dust. There are currently three upcoming X-ray observatories suitable for dust studies, which are currently at different stages of development. In chronological order this will be: XARM (expected to launch in 2021), Arcus (final selection in 2019, expected launch in 2023) and *Athena* (expected to launch in the early 2030s). These observatories will explore different parts of the energy spectrum, as is shown in Figure 1.3, allowing to study previously unavailable edges in detail. In the near future, there will be the XARM observatory, that will allow us to study the S and Fe K-edge. XARM is the successor of the lost Hitomi observatory and will have the same calorimeter detector characteristics on board (Mitsuda et al., 2014). The C K-edge will become available with the Arcus observatory around 2023 (Smith et al., 2017), if the mission is selected for the next phase in

2019. Around 2030, the *Athena* observatory containing the calorimeter X-IFU will provide us with unprecedented spectral resolution (Barret et al., 2016). It will be suitable to study the Fe K-edge in detail. Both the chemistry and the size distribution of the grains can be studied in detail (Rogantini et al., 2018). Using *Athena* and XARM, we will be able to discriminate between different dust species in the case of both Fe and S. Together these edges will be useful in the possible detection of GEMS in the ISM. Furthermore, *Athena* will allow to investigate the contribution of dust from less abundant elements, such as Al, Ni, and Ca. X-ray halo studies will profit from improvements in the spatial resolution. LYNX (also known as the X-ray Surveyor) and/or AXIS, may provide a spatial resolution that makes it possible to better constrain the dust size distribution and composition of the dust in for instance a debris disk system such as AU Mic.

Besides these new upcoming observatories, *Chandra* and *XMM-Newton* will still be available. Initially, these observatories would have a mission duration for 5 and 10 years respectively, but the missions have been extended several times. In 2016, following a very positive outcome from engineering studies, the *Chandra* team announced that it is planning and looking forward at least ten more years of operations. This will make it possible to observe more X-ray binaries and to re-observe other X-ray binaries in order to refine the quality of the observations.

Other advances will be obtained from laboratory studies. The aim for X-ray dust studies is to combine the measured edges of interstellar dust analogues in global extinction models over a broad wavelength range. Our campaign to measure all the relevant edges is currently ongoing, but by the time these new observatories will be put into operation, we will be ready to observe the extinction features of dust in detail.

Table 1.1: An inventory of circumstellar dust

material	AGB	Post-AGB	PN	Nova	T Tauri	Herbig AeBe	RSG	Wolf Rayet	LBV	SN Type II	Massive YSO
amorphous silicates	1, 2	1	1	1	1	1	1	1	1	1	1
crystalline forsterite	1, 2	1	1	1	1	1	1	1	1		
crystalline enstatite	1, 2	1	1	1	1	1	1	1	1		
aluminum oxide	1 (?), 2									2	
spinel	1 (?), 2									2	
TiO <sub>2</sub>	2										
hibonite	2										
MgO	1										
Fe	1 (?)									1	
PAHs	1, 2	1	1	1	1	1	1	(1)	1		
Amorphous carbon	2	1	1	1	1			1			
Graphite	2			2						2	
Diamond		1				1				2	
SiC	1, 2		1	2						2	
other carbides	2	1 (?)								2	
Si <sub>3</sub> N <sub>4</sub>										2	
MgS	1	1	1						1		
carbonate			1 (?)		1 (?)	1 (?)					
ice	1	1	1		1	1	1				1

1 - Astronomical data; 2 - Meteoritic data; AGB: Low mass ( $< 8 M_{\odot}$ ) stars on the Asymptotic Giant Branch. Post-AGB: Low mass ( $< 8 M_{\odot}$ ) stars in transition from the AGB phase to the planetary nebula phase. PN: The white dwarf remaining after the phase of prodigious mass loss on the AGB ionizes the ejecta forming a glowing nebula called a planetary nebula. Nova: The cataclysmic nuclear explosion caused by the accretion of hydrogen onto the surface of a white dwarf star. T Tauri: A low mass ( $\sim 1 M_{\odot}$ ) protostar. Herbig AeBe: Intermediate-mass ( $1.5 < M < 10 M_{\odot}$ ) pre main-sequence stars with spectral types A or B. RSG (Red supergiant): Late and cool ( $T \sim 3000 K$ ) stage in the evolution of massive stars ( $M > 8 M_{\odot}$ ). Wolf Rayet: Hot stars characterized by massive stellar winds; some condense carbon dust in their ejecta. LBV (Luminous blue variable): The most massive, brightest and bluest stars are variable and may experience periods of eruptive mass loss. SN type II: The explosion of a massive ( $M > 8 M_{\odot}$ ) star at the end of its lifetime. Massive YSO: Luminous and massive protostar characterized by vast amounts of cold dust and gas. Astronomical identifications which are particularly ambiguous are labelled with (?) in this table. Table taken from Tielens et al. (2005).



## References

- Andersen, A. C. (2007). Dust from AGB Stars. In Kerschbaum, F., Charbonnel, C., and Wing, R. F., editors, *Why Galaxies Care About AGB Stars: Their Importance as Actors and Probes*, volume 378 of *Astronomical Society of the Pacific Conference Series*, page 170.
- Barnard, E. E. (1919). On the dark markings of the sky, with a catalogue of 182 such objects. *ApJ*, 49.
- Barret, D., Lam Trong, T., den Herder, J.-W., Piro, L., and et al. (2016). The Athena X-ray Integral Field Unit (X-IFU). In *Space Telescopes and Instrumentation 2016: Ultraviolet to Gamma Ray*, volume 9905 of *Proc. SPIE*, page 99052F.
- Bernatowicz, T. J. (1997). Presolar Grains From Meteorites. In Pendleton, Y. J., editor, *From Stardust to Planetesimals*, volume 122 of *Astronomical Society of the Pacific Conference Series*, page 227.
- Bohlin, R. C., Savage, B. D., and Drake, J. F. (1978). A survey of interstellar H I from L-alpha absorption measurements. II. *ApJ*, 224:132–142.
- Bohren, C. F. (2010). What did kramers and kronig do and how did they do it? *European Journal of Physics*, 31(3):573.
- Boulanger, F., Cox, P., and Jones, A. P. (2000). Course 7: Dust in the Interstellar Medium. In Casoli, F., Lequeux, J., and David, F., editors, *Infrared Space Astronomy, Today and Tomorrow*, page 251.
- Bradley, J. P. (1994). Chemically Anomalous, Preaccretionally Irradiated Grains in Interplanetary Dust From Comets. *Science*, 265:925–929.
- Cazaux, S. and Tielens, A. G. G. M. (2004). H<sub>2</sub> Formation on Grain Surfaces. *ApJ*, 604:222–237.
- Cherchneff, I. (2013). Dust production in Supernovae. In *Proceedings of The Life Cycle of Dust in the Universe*, page 18.
- Chiar, J. E. and Tielens, A. G. G. M. (2006). Pixie Dust: The Silicate Features in the Diffuse Interstellar Medium. *ApJ*, 637:774–785.
- Ciolek, G. E. (1995). Ambipolar Diffusion, Interstellar Dust, and the Formation of Protoplanetary Cores. In Ferrara, A., McKee, C. F., Heiles, C., and Shapiro, P. R., editors, *The Physics of the Interstellar Medium and Intergalactic Medium*, volume 80 of *Astronomical Society of the Pacific Conference Series*, page 174.

- Clerke, A. M. (1903). *Problems in Astrophysics*. Bull. Amer. Math. Soc.
- Compiègne, M., Verstraete, L., Jones, A., Bernard, J.-P., Boulanger, F., Flagey, N., Le Bourlot, J., Paradis, D., and Ysard, N. (2011). The global dust SED: tracing the nature and evolution of dust with DustEM. *A&A*, 525:A103.
- Costantini, E. and de Vries, C. P. (2013). Characterizing the chemistry of interstellar dust: the X-ray view. *Mem. Soc. Astron. Italiana*, 84:592.
- Costantini, E., Freyberg, M. J., and Predehl, P. (2005). Absorption and scattering by interstellar dust: an XMM-Newton observation of Cyg X-2. *A&A*, 444:187–200.
- Costantini, E., Pinto, C., Kaastra, J. S., in't Zand, J. J. M., Freyberg, M. J., Kuiper, L., Méndez, M., de Vries, C. P., and Waters, L. B. F. M. (2012). XMM-Newton observation of 4U 1820-30. Broad band spectrum and the contribution of the cold interstellar medium. *A&A*, 539:A32.
- Davies, B., Origlia, L., Kudritzki, R.-P., Figer, D. F., Rich, R. M., Najarro, F., Negueruela, I., and Clark, J. S. (2009). Chemical Abundance Patterns in the Inner Galaxy: The Scutum Red Supergiant Clusters. *ApJ*, 696:2014–2025.
- Draine, B. T. (2003). Scattering by Interstellar Dust Grains. II. X-Rays. *ApJ*, 598:1026–1037.
- Draine, B. T. (2009). Interstellar Dust Models and Evolutionary Implications. In Henning, T., Grün, E., and Steinacker, J., editors, *Cosmic Dust - Near and Far*, volume 414 of *Astronomical Society of the Pacific Conference Series*, page 453.
- Draine, B. T. (2011). *Physics of the Interstellar and Intergalactic Medium*. Princeton University Press.
- Draine, B. T. and Fraise, A. A. (2009). Polarized Far-Infrared and Submillimeter Emission from Interstellar Dust. *ApJ*, 696:1–11.
- Draine, B. T. and Li, A. (2007). Infrared Emission from Interstellar Dust. IV. The Silicate-Graphite-PAH Model in the Post-Spitzer Era. *ApJ*, 657:810–837.
- Dwek, E. (1997). Can Composite Fluffy Dust Particles Solve the Interstellar Carbon Crisis? *ApJ*, 484:779–784.
- Dwek, E. (1998). The Evolution of the Elemental Abundances in the Gas and Dust Phases of the Galaxy. *ApJ*, 501:643.
- Dwek, E. (2016). Iron: A Key Element for Understanding the Origin and Evolution of Interstellar Dust. *ApJ*, 825:136.
- Evans, A. (1986). EXAFS studies of interstellar dust. *MNRAS*, 223:219–224.
- Falgarone, E. and Puget, J. L. (1985). A model of clumped molecular clouds. I - Hydrostatic structure of dense cores. *A&A*, 142:157–170.

- Floss, C., Stadermann, F. J., Bradley, J. P., Dai, Z. R., Bajt, S., Graham, G., and Lea, A. S. (2006). Identification of isotopically primitive interplanetary dust particles: A NanoSIMS isotopic imaging study. *Geochim. Cosmochim. Acta*, 70:2371–2399.
- Forrey, R. C., Woo, J. W., and Cho, K. (1998). Model for Astrophysical X-Ray Absorption Fine Structure. *ApJ*, 505:236–243.
- Gail, H.-P. and Sedlmayr, E. (1986). The primary condensation process for dust around late M-type stars. *A&A*, 166:225–236.
- Galli, D., Walmsley, M., and Gonçalves, J. (2002). The structure and stability of molecular cloud cores in external radiation fields. *A&A*, 394:275–284.
- Gould, R. J. and Salpeter, E. E. (1963). The Interstellar Abundance of the Hydrogen Molecule. I. Basic Processes. *ApJ*, 138:393.
- Greenberg, J. M. (1963). Interstellar Grains. *ARA&A*, 1:267.
- Greenberg, J. M. (1968). *Interstellar Grains*, page 221. the University of Chicago Press.
- Guillet, V., Jones, A. P., and Pineau Des Forêts, G. (2009). Shocks in dense clouds. II. Dust destruction and SiO formation in J shocks. *A&A*, 497:145–153.
- Guillet, V., Pineau Des Forêts, G., and Jones, A. P. (2007). Shocks in dense clouds. I. Dust dynamics. *A&A*, 476:263–277.
- Hoffman, J. and Draine, B. T. (2016). Accurate Modeling of X-ray Extinction by Interstellar Grains. *ApJ*, 817:139.
- Hughes, D. H., Serjeant, S., Dunlop, J., Rowan-Robinson, M., Blain, A., Mann, R. G., Ivison, R., Peacock, J., Efsthathiou, A., Gear, W., Oliver, S., Lawrence, A., Longair, M., Goldschmidt, P., and Jenness, T. (1998). High-redshift star formation in the Hubble Deep Field revealed by a submillimetre-wavelength survey. *Nature*, 394:241–247.
- Indebetouw, R., Matsuura, M., Dwek, E., Zanardo, G., Barlow, M. J., Baes, M., Bouchet, P., Burrows, D. N., Chevalier, R., Clayton, G. C., Fransson, C., Gaensler, B., Kirshner, R., Lakićević, M., Long, K. S., Lundqvist, P., Martí-Vidal, I., Marcaide, J., McCray, R., Meixner, M., Ng, C.-Y., Park, S., Sonneborn, G., Staveley-Smith, L., Vlahakis, C., and van Loon, J. (2014). Dust Production and Particle Acceleration in Supernova 1987A Revealed with ALMA. *ApJ*, 782:L2.
- Jaeger, C., Mutschke, H., Begemann, B., Dorschner, J., and Henning, T. (1994). Steps toward interstellar silicate mineralogy. 1: Laboratory results of a silicate glass of mean cosmic composition. *A&A*, 292:641–655.
- Jenkins, E. B. (2009). A Unified Representation of Gas-Phase Element Depletions in the Interstellar Medium. *ApJ*, 700:1299–1348.
- Jones, A. P. and Nuth, J. A. (2011). Dust destruction in the ISM: a re-evaluation of dust lifetimes. *A&A*, 530:A44.

- Jones, A. P., Tielens, A. G. G. M., and Hollenbach, D. J. (1996). Grain Shattering in Shocks: The Interstellar Grain Size Distribution. *ApJ*, 469:740.
- Jones, A. P., Tielens, A. G. G. M., Hollenbach, D. J., and McKee, C. F. (1994). Grain destruction in shocks in the interstellar medium. *ApJ*, 433:797–810.
- Keller, L. P. and Messenger, S. (2013). On the origins of GEMS grains: A reply. *Geochim. Cosmochim. Acta*, 107:341–344.
- Kemper, F., Vriend, W. J., and Tielens, A. G. G. M. (2004). The Absence of Crystalline Silicates in the Diffuse Interstellar Medium. *ApJ*, 609:826–837.
- Kemper, F., Waters, L. B. F. M., de Koter, A., and Tielens, A. G. G. M. (2001). Crystallinity versus mass-loss rate in asymptotic giant branch stars. *A&A*, 369:132–141.
- Kim, S.-H., Martin, P. G., and Hendry, P. D. (1994). The size distribution of interstellar dust particles as determined from extinction. *ApJ*, 422:164–175.
- Knacke, R. F. and Thomson, R. K. (1973). Infrared Extinction Cross Sections of Silicate Grains. *PASP*, 85:341.
- Lagrange, A.-M., Backman, D. E., and Artymowicz, P. (2000). Planetary Material around Main-Sequence Stars. *Protostars and Planets IV*, page 639.
- Lee, J. C. and Ravel, B. (2005). Determining the Grain Composition of the Interstellar Medium with High-Resolution X-Ray Spectroscopy. *ApJ*, 622:970–976.
- Lee, J. C., Xiang, J., Ravel, B., Kortright, J., and Flanagan, K. (2009). Condensed Matter Astrophysics: A Prescription for Determining the Species-specific Composition and Quantity of Interstellar Dust Using X-rays. *ApJ*, 702:970–979.
- Lewin, W. H. G., van Paradijs, J., and van den Heuvel, E. P. J. (1997). *X-ray Binaries*.
- Lewis, R. S., Ming, T., Wacker, J. F., Anders, E., and Steel, E. (1987). Interstellar diamonds in meteorites. *Nature*, 326:160–162.
- Li, D., Goldsmith, P. F., and Menten, K. (2003). Massive Quiescent Cores in Orion. I. Temperature Structure. *ApJ*, 587:262–277.
- Lodders, K. and Palme, H. (2009). Solar System Elemental Abundances in 2009. *Meteoritics and Planetary Science Supplement*, 72:5154.
- Martin, P. G. (1970). On the interaction of cosmic X-rays with interstellar grains. *MNRAS*, 149:221.
- Martin, P. G. and Sciama, D. W. (1970). A Proposal for an X-ray Analysis of Interstellar Grains. *Astrophys. Lett.*, 5:193.
- Mathis, J. S. (1996). Dust Models with Tight Abundance Constraints. *ApJ*, 472:643.

- Mathis, J. S., Rumpl, W., and Nordsieck, K. H. (1977). The size distribution of interstellar grains. *ApJ*, 217:425–433.
- Mauche, C. W. and Gorenstein, P. (1986). Measurements of X-ray scattering from interstellar grains. *ApJ*, 302:371–387.
- McMillan, P. J. (2017). The mass distribution and gravitational potential of the Milky Way. *MNRAS*, 465:76–94.
- Meurant, G. (1983). *Solid State Physics*. Number v. 37 in Solid State Physics. Elsevier Science.
- Mie, G. (1908). Beiträge zur Optik trüber Medien, speziell kolloidaler Metallösungen. *Annalen der Physik*, 330:377–445.
- Min, M., Waters, L. B. F. M., de Koter, A., Hovenier, J. W., Keller, L. P., and Markwick-Kemper, F. (2007). The shape and composition of interstellar silicate grains. *A&A*, 462:667–676.
- Mitsuda, K., Kelley, R. L., Akamatsu, H., Bialas, T., Boyce, K. R., and et al. (2014). Soft x-ray spectrometer (SXS): the high-resolution cryogenic spectrometer onboard ASTRO-H. In *Space Telescopes and Instrumentation 2014: Ultraviolet to Gamma Ray*, volume 9144 of *Proc. SPIE*, page 91442A.
- Molster, F. J., Waters, L. B. F. M., Tielens, A. G. G. M., Koike, C., and Chihara, H. (2002). Crystalline silicate dust around evolved stars. III. A correlations study of crystalline silicate features. *A&A*, 382:241–255.
- Ossenkopf, V. (1993). Dust coagulation in dense molecular clouds: The formation of fluffy aggregates. *A&A*, 280:617–646.
- Overbeck, J. W. (1965). Small-Angle Scattering of Celestial X-Rays by Interstellar Grains. *ApJ*, 141:864.
- Pedicelli, S., Bono, G., Lemasle, B., François, P., Groenewegen, M., Lub, J., Pel, J. W., Laney, D., Piersimoni, A., Romaniello, M., Buonanno, R., Caputo, F., Cassisi, S., Castelli, F., Leurini, S., Pietrinferni, A., Primas, F., and Pritchard, J. (2009). On the metallicity gradient of the Galactic disk. *A&A*, 504:81–86.
- Pinto, C., Kaastra, J. S., Costantini, E., and de Vries, C. (2013). Interstellar medium composition through X-ray spectroscopy of low-mass X-ray binaries. *A&A*, 551:A25.
- Pontoppidan, K. M. (2004). *Fire and ice. Infrared spectroscopy as a probe of ice and gas in star-forming regions*. PhD thesis, Leiden University, P.O. Box 9504, 2300 RA Leiden, The Netherlands.
- Predehl, P. and Klose, S. (1996). Dust scattered X-ray haloes as diagnostic tools: potential and current limitations. *A&A*, 306:283.
- Predehl, P. and Schmitt, J. H. M. M. (1995). X-raying the interstellar medium: ROSAT observations of dust scattering halos. *A&A*, 293:889–905.

- Rehr, J. J. and Albers, R. C. (2000). Theoretical approaches to x-ray absorption fine structure. *Reviews of Modern Physics*, 72:621–654.
- Rogantini, D., Costantini, E., Zeegers, S. T., de Vries, C. P., Bras, W., de Groot, F., Mutschke, H., and Waters, L. B. F. M. (2018). Investigating the interstellar dust through the Fe K-edge. *A&A*, 609:A22.
- Rolf, D. P. (1983). Evidence for the detection of X-ray scattering from interstellar dust grains. *Nature*, 302:46–48.
- Rolleston, W. R. J., Smartt, S. J., Dufton, P. L., and Ryans, R. S. I. (2000). The Galactic metallicity gradient. *A&A*, 363:537–554.
- Schalén, C. (1929). Zur Frage einer allgemeinen Absorption des Lichtes im Weltraum. *Astronomische Nachrichten*, 236:249.
- Shen, Y., Draine, B. T., and Johnson, E. T. (2008). Modeling Porous Dust Grains with Ballistic Aggregates. I. Geometry and Optical Properties. *ApJ*, 689:260–275.
- Shu, F., Najita, J., Galli, D., Ostriker, E., and Lizano, S. (1993). The collapse of clouds and the formation and evolution of stars and disks. In Levy, E. H. and Lunine, J. I., editors, *Protostars and Planets III*, pages 3–45.
- Smith, R. K., Abraham, M., Allured, R., Bautz, M., Bookbinder, J., and et al (2017). Arcus: exploring the formation and evolution of clusters, galaxies, and stars. In *Society of Photo-Optical Instrumentation Engineers (SPIE) Conference Series*, volume 10397, page 103970Q.
- Smith, R. K., Dame, T. M., Costantini, E., and Predehl, P. (2006). The X-Ray Halo of GX 5-1. *ApJ*, 648:452–460.
- Struve, W. (1847). *Etudes d'astronomie stellaire*.
- Tielens, A. G. G. M. (2001). The Composition of Circumstellar and Interstellar Dust. In Woodward, C. E., Bica, M. D., and Shull, J. M., editors, *Tetons 4: Galactic Structure, Stars and the Interstellar Medium*, volume 231 of *Astronomical Society of the Pacific Conference Series*, page 92.
- Tielens, A. G. G. M. (2010). *The Physics and Chemistry of the Interstellar Medium*.
- Tielens, A. G. G. M. (2013). The molecular universe. *Reviews of Modern Physics*, 85:1021–1081.
- Tielens, A. G. G. M., Seab, C. G., Hollenbach, D. J., and McKee, C. F. (1987). Shock processing of interstellar dust - Diamonds in the sky. *ApJ*, 319:L109–L113.
- Tielens, A. G. G. M., Waters, L. B. F. M., and Bernatowicz, T. J. (2005). Origin and Evolution of Dust in Circumstellar and Interstellar Environments. In Krot, A. N., Scott, E. R. D., and Reipurth, B., editors, *Chondrites and the Protoplanetary Disk*, volume 341 of *Astronomical Society of the Pacific Conference Series*, page 605.

- Tiengo, A., Vianello, G., Esposito, P., Mereghetti, S., Giuliani, A., Costantini, E., Israel, G. L., Stella, L., Turolla, R., Zane, S., Rea, N., Götz, D., Bernardini, F., Moretti, A., Romano, P., Ehle, M., and Gehrels, N. (2010). The Dust-scattering X-ray Rings of the Anomalous X-ray Pulsar 1E 1547.0-5408. *ApJ*, 710:227–235.
- Trumpler, R. J. (1930). Absorption of Light in the Galactic System. *PASP*, 42:214.
- van de Hulst, H. C. (1957). *Light Scattering by Small Particles*.
- van Dishoeck, E. F. (2014). Astrochemistry of dust, ice and gas: introduction and overview. *Faraday Discussions*, 168:9.
- Wakelam, V., Bron, E., Cazaux, S., Dulieu, F., Gry, C., Guillard, P., Habart, E., Hornekar, L., Morisset, S., Nyman, G., Pirronello, V., Price, S. D., Valdivia, V., Vidali, G., and Watanabe, N. (2017). H<sub>2</sub> formation on interstellar dust grains: The viewpoints of theory, experiments, models and observations. *Molecular Astrophysics*, 9:1–36.
- Wakelam, V. and Herbst, E. (2008). Polycyclic Aromatic Hydrocarbons in Dense Cloud Chemistry. *ApJ*, 680:371–383.
- Wang, S., Li, A., and Jiang, B. W. (2015). The interstellar oxygen crisis, or where have all the oxygen atoms gone? *MNRAS*, 454:569–575.
- Waters, L. B. F. M. (2004). Dust in evolved stars. In Witt, A. N., Clayton, G. C., and Draine, B. T., editors, *Astrophysics of Dust*, volume 309 of *Astronomical Society of the Pacific Conference Series*, page 229.
- Watson, D., Christensen, L., Knudsen, K. K., Richard, J., Gallazzi, A., and Michałowski, M. J. (2015). A dusty, normal galaxy in the epoch of reionization. *Nature*, 519:327–330.
- Weingartner, J. C. and Draine, B. T. (2001). Dust Grain-Size Distributions and Extinction in the Milky Way, Large Magellanic Cloud, and Small Magellanic Cloud. *ApJ*, 548:296–309.
- Westphal, A. J., Stroud, R. M., Bechtel, H. A., Brenker, F. E., and et al. (2014). Evidence for interstellar origin of seven dust particles collected by the Stardust spacecraft. *Science*, 345:786–791.
- Whittet, D. C. B., Boogert, A. C. A., Gerakines, P. A., Schutte, W., Tielens, A. G. G. M., de Graauw, T., Prusti, T., van Dishoeck, E. F., Wesselius, P. R., and Wright, C. M. (1997). Infrared Spectroscopy of Dust in the Diffuse Interstellar Medium toward Cygnus OB2 No. 12. *ApJ*, 490:729–734.
- Woo, J. W. (1995). EXAFS and XANES: New Astrophysical Tools to Study the Solid State Structure of Interstellar Grains. *ApJ*, 447:L129.
- Wyatt, M. C. (2008). Evolution of Debris Disks. *ARA&A*, 46:339–383.
- Wyatt, M. C. and Dent, W. R. F. (2002). Collisional processes in extrasolar planetesimal discs - dust clumps in Fomalhaut’s debris disc. *MNRAS*, 334:589–607.

- Zeegers, S. T., Costantini, E., de Vries, C. P., Tielens, A. G. G. M., Chihara, H., de Groot, F., Mutschke, H., Waters, L. B. F. M., and Zeidler, S. (2017). Absorption and scattering by interstellar dust in the silicon K-edge of GX 5-1. *A&A*, 599:A117.
- Zhukovska, S., Gail, H.-P., and Trieloff, M. (2008). Evolution of interstellar dust and stardust in the solar neighbourhood. *A&A*, 479:453–480.
- Zhukovska, S., Henning, T., and Dobbs, C. (2018). Iron and Silicate Dust Growth in the Galactic Interstellar Medium: Clues from Element Depletions. *ApJ*, 857:94.
- Zinner, E. (2007). 1 . 02 presolar grains.
- Zinner, E. and Amari, S. (1999). Presolar grains from meteorites: AGB star matter in the laboratory. In Le Bertre, T., Lebre, A., and Waelkens, C., editors, *Asymptotic Giant Branch Stars*, volume 191 of *IAU Symposium*, page 59.
- Zubko, V., Dwek, E., and Arendt, R. G. (2004). Interstellar Dust Models Consistent with Extinction, Emission, and Abundance Constraints. *ApJS*, 152:211–249.

# 2 | Absorption and scattering by interstellar dust in the silicon K-edge of GX 5-1

## Abstract

*Context* We study the absorption and scattering of X-ray radiation by interstellar dust particles, which allows us to access the physical and chemical properties of dust. The interstellar dust composition is not well understood, especially on the densest sight lines of the Galactic Plane. X-rays provide a powerful tool in this study.

*Aims* We present newly acquired laboratory measurements of silicate compounds taken at the Soleil synchrotron facility in Paris using the Lucia beamline. The dust absorption profiles resulting from this campaign were used in this pilot study to model the absorption by interstellar dust along the line of sight of the low-mass X-ray binary (LMXB) GX 5-1.

*Methods* The measured laboratory cross-sections were adapted for astrophysical data analysis and the resulting extinction profiles of the Si K-edge were implemented in the SPEX spectral fitting program. We derive the properties of the interstellar dust along the line of sight by fitting the Si K-edge seen in absorption in the spectrum of GX 5-1.

*Results* We measured the hydrogen column density towards GX 5-1 to be  $3.40 \pm 0.1 \times 10^{22} \text{ cm}^{-2}$ . The best fit of the silicon edge in the spectrum of GX 5-1 is obtained by a mixture of olivine and pyroxene. In this study, our modeling is limited to Si absorption by silicates with different Mg:Fe ratios. We obtained an abundance of silicon in dust of  $4.0 \pm 0.3 \times 10^{-5}$  per H atom and a lower limit for total abundance, considering both gas and dust, of  $> 4.4 \times 10^{-5}$  per H atom, which leads to a gas to dust ratio of  $> 0.22$ . Furthermore, an enhanced scattering feature in the Si K-edge may suggest the presence of large particles along the line of sight.

## 2.1 Introduction

Cosmic silicates form an important component of the dust present in the interstellar medium (ISM). These silicate dust particles are thought to be mainly produced in oxygen-rich asymptotic giant branch (AGB) stars (e.g., Gail et al., 2009). Besides AGB stars, other sources such as novae, supernovae type II (Wooden et al., 1993; Rho et al., 2008, 2009), young stellar objects (Dwek and Scalo, 1980), and red giant stars (Nittler et al., 1997) can produce silicate dust. Even dust formation in the ISM may occur in interstellar clouds (Jones and Nuth, 2011). Although the amounts of dust contributed by these sources is still debated (Meikle et al., 2007; Jones and Nuth, 2011), silicate dust is abundant in the ISM and can be found in many different stages of the life cycle of stars (Henning, 2010). The physical and chemical composition of silicate dust has traditionally been studied at various wavelengths ranging from the radio to the UV and at different sight lines across the Galaxy (Draine and Li, 2001; Dwek et al., 2004). However, there are still many open questions about, for instance, the chemical composition of silicates (Li and Draine, 2001; Gail, 2010), the production and destruction rate of dust (Jones et al., 1994, 1996), the amount of crystalline dust in the interstellar medium, (Kemper et al., 2004) and the particle size distribution and the shape of dust grains (e.g., Min et al., 2006, 2008; Voshchinnikov et al., 2006; Mutschke et al., 2009). Furthermore, it is not precisely known how the dust composition and the dust particle size distribution change in different regions throughout the Galaxy (Chiar and Tielens, 2006; Min et al., 2007).

Elements such as C, O, Fe, Si, and Mg appear to be under-abundant in the cold phase of the ISM (Jenkins, 2009; Savage and Sembach, 1996). The abundances of these elements relative to hydrogen were found to be less than in the Sun, the Solar system, or in nearby stars (Draine, 2003). The atoms that appear to be missing, are thought to be locked up in dust. This is referred to as depletion from the gas phase, which is defined here as the ratio of the dust abundance to the total amount of a given element. A large fraction of C, O, Fe, Si, and Mg is therefore thought to be depleted and locked up in dust (Henning, 2010; Savage and Sembach, 1996; Jenkins, 2009). Aside from carbon, which is mostly present in dust in graphite and polycyclic aromatic carbon (e.g., Zubko et al., 2004; Draine and Li, 2007; Tielens, 2008), these elements form the main constituents of cosmic silicates (Mathis, 1998). Silicon in dust is mainly present in the ISM in the form of silicates, although it may also exist, in relatively small percentages, in the form of SiC: 0.1%, (Kemper et al., 2004), 9-12% (Min et al., 2007). Mg and Fe oxides are observed in stellar spectra (Posch et al., 2002; Henning et al., 1995), but there is no observational evidence for them in the diffuse ISM (Whittet et al., 1997; Chiar and Tielens, 2006). However, these compounds have been isolated as stardust in Solar system meteorites (Anders and Zinner, 1993).

An important property of interstellar dust is crystallinity. From observations of the  $10\ \mu\text{m}$  and  $18\ \mu\text{m}$  features, Kemper et al. (2004) concluded that along sight lines towards the Galactic center only 1.1% (with a firm upper limit of 2.2%) of the total amount of silicate dust has a crystalline structure. On the other hand, some of the interstellar dust grains captured by the Stardust Interstellar Dust Collector (Westphal et al., 2014) showed a large fraction of crystalline material. The cores of these particles contained crystalline forsteritic olivine. Westphal et al. (2014) conclude that crystalline materials are probably preserved in the interiors of larger ( $> 1\ \mu\text{m}$ ) particles. Interestingly, dust is found to be in crystalline form at the start and at the end of the life cycle of stars, whereas very little crystalline dust appears to survive

the harsh environment of the ISM. There are indications that the amount of crystalline dust depends on the environment. For instance, silicate dust in starburst galaxies appears in large fractions in crystalline form (Spoon et al., 2006; Kemper et al., 2011), probably reflecting freshly produced dust. Indeed, silicates in the ISM can be amorphous either because during the formation process the silicates condense as amorphous grains (Kemper et al., 2004; Jones et al., 2012) or the crystal structure is destroyed in the ISM by cosmic ray bombardments, UV/X-ray radiation, and supernova shock waves (Bringa et al., 2007). In the first case the silicates will have a non-stoichiometric composition and in the second case they will have the stoichiometry of the former crystal (Kemper et al., 2004). The dust features of amorphous dust are smoother than those of crystalline dust, which makes the determination of the structure and composition of the interstellar dust from spectral studies more difficult.

From X-ray observations of sight lines towards the Galactic plane and infrared observations towards the Galactic center, silicates were found to be Mg-rich rather than Fe-rich (Costantini et al., 2005, 2012; Lee et al., 2009; Min et al., 2007). However, Fe is heavily depleted (70 – 99%) and probably mostly locked up in dust grains (Wilms et al., 2000; Whittet, 2003). It is not certain in which exact form Fe is incorporated into dust (Whittet et al., 1997; Chiar and Tielens, 2006). Since the composition of certain silicates allows iron rich compounds, it is possible that some of the iron is locked up in these silicate grains. Another and possibly complementary scenario to preserve Fe in dust prescribes that Fe could be locked up in Glass with Embedded Metal and Sulfides (GEMS) of interstellar origin (e.g., Bradley, 1994; Floss et al., 2006; Keller and Messenger, 2013).

The abundances of most of the important metals decrease with distance from the Galactic Plane, which can be described by a gradient with an average slope of  $0.06 \text{ dex kpc}^{-1}$  (Chen et al., 2003, and references therein). Although the ISM shows this general gradient, the ISM is also very patchy. The measurements of abundances show a large scatter as function of the Galactic radius, due to local influences of, for instance, supernova ejecta and infalling metal-poor gas onto the disk (Nittler, 2005). The  $10 \mu\text{m}$  feature provides information about the Si abundance in the Galaxy, which in turn can provide restrictions on the dust composition and possibly on the dust size distribution (Tielens et al., 1996). It is not precisely known how the dust distribution and the dust composition change relative to the environment. Simple dust size distributions, such as the Mathis-Rumpl-Nordsieck (MRN, Mathis et al. (1977)) distribution, consisting of solid spherical dust particles, may not be sufficient to explain the observations towards dense regions of the Galaxy. Dust particles may be non-spherical and porous due to the formation processes of dust (Min et al., 2006; Chiar and Tielens, 2006; Min et al., 2007). Furthermore, Hoffman and Draine (2016) show the importance of incorporating non-spherical dust particles into X-ray scattering analyses.

X-ray observations provide a hitherto relatively unexplored but powerful probe of interstellar dust (Draine, 2003; Lee et al., 2009; Costantini et al., 2012). The extinction features near the X-ray edges of O, Mg, Si, and Fe can be analyzed depending on the column density on the line of sight towards the source and the sensitivity of the detector. The X-ray Absorption Fine Structures (XAFS, Meurant, 1983) near the atomic absorption edges of elements provide a unique fingerprint of the dust. These XAFS have been observed in the X-ray spectra of astrophysical objects in data from *XMM* and *Chandra* (Lee et al., 2001; Ueda et al., 2005; Kaastra et al., 2009; de Vries and Costantini, 2009; Pinto et al., 2010, 2013; Costantini et al., 2012; Valencic and Smith, 2013). The X-rays provide important advantages compared

to longer wavelengths and, in that way, provide an independent method to study silicate dust. The two most important advantages are that it is possible to measure the quantity of absorbing gas and dust simultaneously and to directly determine the composition of the dust. In particular, it is, in principle, possible to address the abundance, composition, stoichiometry, crystallinity, and size of interstellar silicates.

Bright X-ray binaries, distributed along the Galactic Plane, can be used as background sources to probe the intervening dust and gas in ISM along the line of sight. In this way, a large range of column densities can be investigated and it is possible to analyze dust in various regions in the Galaxy. Dust in diffuse regions along the Galactic plane has been studied in the X-rays by Lee et al. (2009), Pinto et al. (2010), Costantini et al. (2012), and Pinto et al. (2013) for several sight lines. The dense ISM has been less extensively studied in the X-rays. These dense environments (hydrogen column density  $> 1 \times 10^{22} \text{ cm}^{-2}$ ) can be studied in the X-rays by observing the Mg and Si K-edge. In this chapter, we will focus in the Si K-edge.

The information on silicon in silicates of astronomical interest is very limited and sparse. The Si K-edge of some silicates has been measured by, for example, Li et al. (1995); Poe et al. (1997), but most of these silicates cannot be used in astronomical studies because they also contain elements which are not abundant in the ISM. In this first study of the Si K-edge in astronomical data with a physically motivated model, we present a new set of laboratory measurements of Si K-edges of six silicate dust samples. The samples contain both crystalline and amorphous silicates. Further details about these samples are given in Section 2.3.1. The measurements are part of a large laboratory measurement campaign aimed at the characterization of interstellar dust analogs (Costantini and de Vries, 2013).

We analyze the interstellar matter along the line of sight of X-ray binary GX 5-1 using models based on new laboratory measurements and discuss the properties and composition of the dust. The chapter is structured in the following way: in Section 2.2, we explain the usage of XAFS to study interstellar dust. In Section 2.3, the data analysis of the laboratory samples is described. Section 2.4 shows the calculation of the extinction cross-section (absorption and scattering) of the samples. Section 2.5 describes the source GX 5-1. In Section 2.6, we fit the models to the spectrum of GX 5-1 and determine the best fit to the data using the samples from Section 2.3. We discuss our results in Section 2.7 and conclude in Section 2.8.

## 2.2 X-ray absorption edges

XAFS are best understood in terms of the wave behavior of the photoelectron. These structures arise when an X-ray photon excites a core electron. The outwardly propagating photoelectron wave will be scattered by the neighboring atoms. From these atoms new waves will emanate and will be superimposed on the wave function of the photoelectron. The wave function of the scattered photoelectron is therefore modified due to constructive and destructive interference. In this way, the absorption probability is modified in a unique manner, because it depends on the configuration of the neighboring atoms. These modulations can be used to determine the structure of the silicate dust in the ISM, because the modulations show unique features for different types of dust.

## 2.3 Laboratory data analysis

### 2.3.1 The samples

We analyzed six samples of silicates. The compounds are presented in Table 2.1. Three of the samples were natural crystals, that is, two orthopyroxenes, one of them magnesium-rich (sample 4: enstatite, origin Kiloza, Tanzania), one with a higher iron content (sample 6: hypersthene, origin: Paul Island, Labrador), and one is an iron-rich olivine (sample 1: olivine, origin: Sri Lanka). See also Jaeger et al. (1998) and Olofsson et al. (2012) for infrared data of the enstatite and the olivine crystals.

The three other samples, that is, sample 2, sample 3 (which is the crystalline counterpart of sample 2), and sample 5, were synthesized for this analysis in laboratories at AIU Jena and Osaka University. The amorphous  $\text{Mg}_{0.9}\text{Fe}_{0.1}\text{SiO}_3$  sample has been synthesized by quenching of a melt according to the procedure described by Dorschner et al. (1995). The crystalline counterpart was obtained by slow cooling of silicate material produced under Ar atmosphere in an electric arc, similarly to that described for Mg/Fe oxides in Henning et al. (1995).

We were motivated in the choice of the sample by the almost absolute absence of XAFS measurements for silicates of astronomical interest. In order to produce laboratory analogs of interstellar dust silicates, four main criteria were considered:

- The samples (or a mixture of these samples) should reflect the interstellar dust silicates of “mean” cosmic composition.
- The samples have an olivine or pyroxene stoichiometry.
- The samples contain differences in the Mg:Fe ratio.
- The sample set contains both amorphous and crystalline silicates.

The composition of the samples present in our study is chosen in such a way that mixtures of these samples can reflect the cosmic silicate mixture as described by Draine and Lee (1984). According to observations of 10 and 20  $\mu\text{m}$  feature in the infrared, the silicate dust mixture consists of an olivine and pyroxene stoichiometry (Kemper et al., 2004; Min et al., 2007). The dominating component seems to be silicates of an olivine stoichiometry (Kemper et al., 2004). Min et al. (2007) show that the stoichiometry lies in between that of olivine and pyroxene, which suggests a mixture of these two silicate types. Therefore, our sample set contains both pyroxenes and an olivine silicate. The samples show variations in the Mg:Fe ratio. These variations reflect the results from previous studies of interstellar dust. Kemper et al. (2004) infer from the observed stellar extinction that  $\text{Mg}/(\text{Mg} + \text{Fe}) \sim 0.5$ , whereas Min et al. (2007) conclude that  $\text{Mg}/(\text{Mg} + \text{Fe}) \sim 0.9$ . Silicates with a high magnesium fraction of  $\text{Mg}/(\text{Mg} + \text{Fe}) \sim 0.8$  have been found in environments that show silicates with a crystalline structure, for example around evolved stars (Molster et al., 2002a,b,c; de Vries et al., 2010), in comets, (Wooden et al., 1999; Messenger et al., 2005) and in disks around T Tauri stars (Olofsson et al., 2009). Therefore, our samples have ratios of  $\text{Mg}/(\text{Mg} + \text{Fe})$  that vary between 0.5 and 0.9. The sample set also contains both amorphous and crystalline silicates.

Besides the two amorphous pyroxene samples present in this set, another highly suitable candidate would be an amorphous olivine, which is not present in this analysis. In general,

amorphous olivine is difficult to synthesize, because this particular silicate crystallizes extremely quickly. A rapid-quenching technique is necessary to prevent the crystallization process. For compounds with a higher iron content, this technique may not be fast enough to prevent both phase separation and crystallization. Even at moderately high Fe contents, the silicates would show variations of the Mg:Fe ratio throughout the sample. These variations are problematic in the comparison with their crystalline counterpart. In the initial phase of this campaign, we indeed also analyzed the amorphous olivine, originally used in Dorschner et al. (1995). The inspection with the electron microscope revealed this particular sample to be both partially inhomogeneous in composition and contaminated by tungsten. This element has significant M-edges around the Si K-edge (i.e., the M1-M5 edges of tungsten fall in a range between 1809 and 2819 eV, where the Si K-edge is at 1839 eV). For these reasons, the amorphous olivine from Dorschner et al. (1995) was discarded at a very early stage of this campaign, as it was unsuitable for fluorescence measurements in the X-rays.

### 2.3.2 Analysis of laboratory data

Ideally one would like to measure the absorption of the samples directly in transmission through the sample, because this would resemble the situation in the ISM more closely. However, to measure the dust samples in transmission around the energy of the Si K-edge, we need optically thin samples, which implies a sample thickness of 1.0 - 0.5  $\mu\text{m}$ . This is impossible to obtain for practical reasons. In our analysis of the silicon K-edge we make use of optically thick samples (i.e., the sample is much thicker than the penetration depth) and therefore it is necessary to use a different technique with which the absorption can be derived. There are two processes that can be used in this case, which occur after the core electron is excited by an X-ray photon. The excited photoelectron leaves a core hole. This can be filled by an electron from a higher shell that falls into the vacancy. The excess energy can either be released as a fluorescent photon or another electron gets ejected. The latter is called the Auger effect (Meitner, 1922). Depending on the attenuation of the signal, both effects can be used to derive the amount of absorption around the edge. Since the fluorescent signal of our measurements was strong enough, we used the fluorescent measurements of the Si  $K_\alpha$  line in our analysis of the Si K-edge.

The absorption (given here by the absorption coefficient  $\alpha(E)$ ) can be derived from the fluorescent spectrum by dividing the fluorescent intensity ( $I_f$ ) by the beam intensity ( $I_0$ ).

$$\alpha(E) \propto I_f/I_0 \quad (2.1)$$

The samples were analyzed at the Soleil synchrotron facility in Paris using the Lucia beamline. They were placed in the X-ray beam and the reflecting fluorescent signal was measured by four silicon drift diode detectors. The beam has an energy range of 0.8 - 8 keV. The energy source of the X-ray beam is an undulator, which creates a collimated beam. The beam is first focused by a spherical mirror and then passes two sets of planar mirrors that act as a lower pass filter. This procedure reduces the high-order contamination from the undulator and the thermal load received by the monochromator crystals. The monochromator crystals then rotate the beam and keep the exit beam at a constant height. There are five different crystals available. During our measurements, we made use of the KTP monochromatic crystals. In the energy range of 1280 to 2140 eV, the KTP monochromatic system has an energy resolution between

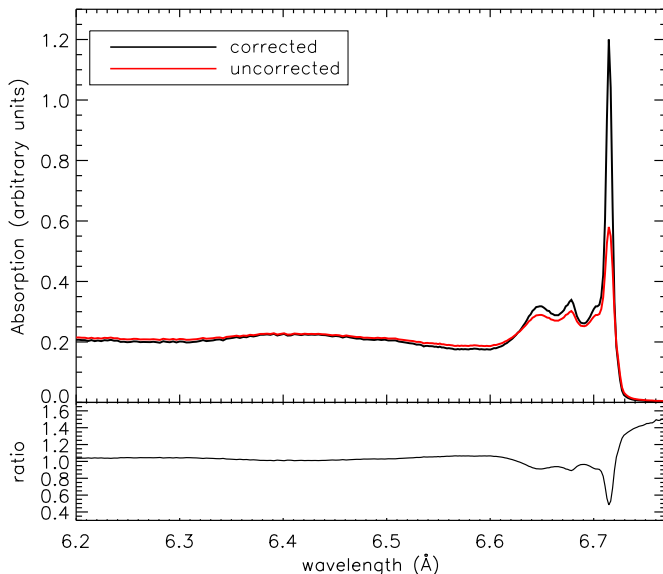


**Figure 2.1:** Example of the difference between the sample corrected for saturation and the uncorrected measurement. Shown is sample 3, crystalline pyroxene. The lower panel shows the ratio of the corrected and uncorrected measurement.

0.25 and 0.31 eV (Flank et al., 2006). The beam energy can be increased gradually (stepped by the resolution of the monochromator) in order to measure the absorption at the pre-edge (1800 - 1839 eV), the edge itself (at 1839 eV), and the post-edge (1839 - 2400 eV). The measurements were made with 0.5 eV energy spacing between measurements close to the edge. The added signal of the four silicon drift diode detectors yields the total fluorescent spectrum from the sample, from which the absorption coefficient  $\alpha(E)$  can be derived using the beam intensity  $I_0$  as indicated in Equation 2.1.

All six samples were stuck on two identical copper sample plates. The silicates were ground to a powder and pressed into a layer of indium foil, which made it possible for the samples to stick to the copper plates. Each sample was measured twice and therefore four measurements of each compound were obtained. This was done to avoid any dependence in the measurement on the position of the sample on the copper plate. The average of the four measurements is used in this analysis. The dispersion among the measurements is small; 3%.

The measurements of the samples were corrected for pile-up and saturation. Pile-up is caused by the detection of two photons instead of one at the same time on the detector. This can be seen on the detector as an extra fluorescent line at twice the energy of the expected fluorescent  $K_{\alpha}$  line. This means that some of the intensity of the original line would be lost. To correct for this effect, we isolated both the silicon fluorescent line and the associated pile-up line from the fluorescent spectrum. The contribution of the pile-up line is then weighed and

added to the original line. A comparison between the corrected and uncorrected data shows that the influence of pile-up in the sample is minimal ( $< 1\%$ ).

As indicated by Equation 2.1, the intensity of fluorescence is proportional to the absorption probability, but this is a slight oversimplification. The fluorescent light has to travel through the sample before it can be detected. On the way through the sample, the photons can be absorbed by the sample itself and the fluorescence intensity is attenuated. This effect is called saturation. This means that the measured fluorescent signal  $I_f$  is no longer proportional to the absorption coefficient. In our measurements, the samples were all placed at an angle  $\theta = 45^\circ$ ; therefore, the angular dependence can be neglected. Another advantage of positioning the sample in this way is, that the beam and the detector are now at a  $90^\circ$  angle. Due to the polarisation of the radiation from the incident beam, the beam is greatly suppressed at this angle and almost no radiation from the beam can reach the detector directly. The measured fluorescence intensity divided by the intensity of the beam can now be expressed as:

$$\frac{I_f}{I_0} = \epsilon_f \frac{\Omega}{4\pi} \frac{\alpha_e(E)}{\alpha_{\text{tot}}(E) + \alpha_{\text{tot}}(E_f)} [1 - e^{-[\alpha_{\text{tot}}(E) + \alpha_{\text{tot}}(E_f)]x_n / \sin(\theta)}] \quad (2.2)$$

In this equation,  $\epsilon_f$  is the fluorescence efficiency,  $x_n / \sin(\theta)$  is the effective optical path (where  $x_n$  is the penetration depth into the sample and  $\theta$  is the angle between the sample surface and the beam),  $\Omega$  is the solid angle of the detector,  $E_f$  is the energy of the fluorescent X-ray photons,  $\alpha_e(E)$  is the absorption from the element of interest and  $\alpha_{\text{tot}}$  is the total absorption defined as:  $\alpha_{\text{tot}} = \alpha_e(E) + \alpha_b(E)$ .  $\alpha_b(E)$  denotes the absorption from all other atoms and other edges of interest. For concentrated samples,  $\alpha_b(E)$  can become dominant and the XAFS will be damped by this saturation effect. In the ISM, the dust is very diluted, so saturation will not occur in real observations, but has to be corrected for in bulk matter.

In the case of a thick sample, the exponential term in Equation 2.2 becomes small and can be ignored:

$$\frac{I_f}{I_0} = \epsilon_f \frac{\Omega}{4\pi} \frac{\alpha_e(E)}{\alpha_{\text{tot}}(E) + \alpha_{\text{tot}}(E_f)} \quad (2.3)$$

The correction has been done using the FLUO software developed by Daniel Haskel. FLUO is part of the UWXAFS software (Stern et al., 1995). A detailed explanation of this correction can be found in Appendix 2.A.<sup>1</sup> This routine uses tabulated absorption cross-sections to correct most of the distortion in order to recover the actual absorption coefficient. In comparison to the correction for pile-up, the correction of the absorption spectra for saturation is considerable as can be seen in Figure 2.1.

Figure 2.2 shows the amount of absorption, indicated by the cross-section (in arbitrary units), corrected for saturation and pile-up as a function of the energy of the silicon K-edge for all the samples. This figure shows the differences in the XAFS for different compounds. The structure of olivine (sample 1), for example, shows a peak at  $6.69 \text{ \AA}$  that is not observed in the pyroxene samples. There is also a clear difference between amorphous and crystalline samples. Indeed, the structures that are present between  $6.70$  and  $6.66 \text{ \AA}$  in sample 3, for example, are washed out in the amorphous counterpart: sample 2.

<sup>1</sup><http://www.aps.anl.gov/~haskel/fluio.html>

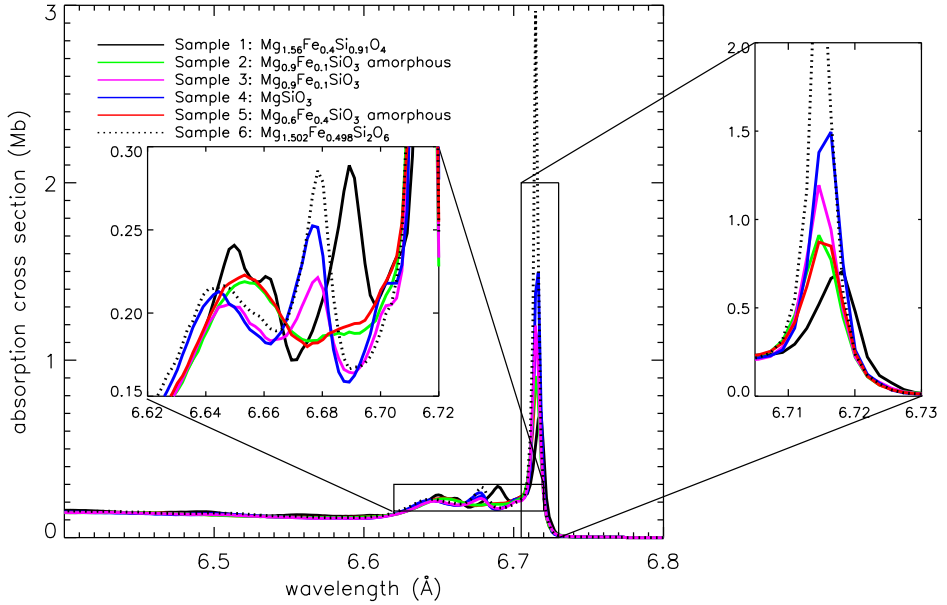


Figure 2.2: The Si K-edge of the six samples. The x-axis shows the energy in Å and the y-axis shows the amount of absorption indicated by the cross-section (in Mb per Si atom).

Table 2.1: Samples

No. sample	Name	Chemical formula	Structure
1	Olivine	$Mg_{1.56}Fe_{0.4}Si_{0.91}O_4$	crystal
2	Pyroxene	$Mg_{0.9}Fe_{0.1}SiO_3$	amorphous
3	Pyroxene	$Mg_{0.9}Fe_{0.1}SiO_3$	crystal
4	Enstatite	$MgSiO_3$	crystal*
5	Pyroxene	$Mg_{0.6}Fe_{0.4}SiO_3$	amorphous
6	Hypersthene	$Mg_{1.502}Fe_{0.498}Si_2O_6$	crystal

\*Sample 4 contains a very small amount iron, which is not significant in our analysis. The Fe:Mg ratio is  $4 \times 10^{-2}$ .

## 2.4 Extinction cross-sections

We derived the amount of absorption of each sample in arbitrary units from the laboratory data. These measurements need to be converted to extinction cross-sections (in units Mb) in order to implement them into the AMOL model of the fitting routine SPEX (Kaastra et al., 1996) for further analysis. The total extinction cross-section can be calculated by using the Mie theory (Mie, 1908). In order to do so, we first need to derive the optical constants of the samples. In this section, we explain the methods used to obtain the extinction cross-section of each sample.

### 2.4.1 Optical constants

When light travels through a material, it can be transmitted, absorbed, or scattered. The transmittance  $T$  is defined as the ratio of transmitted  $I$  and incident light  $I_0$ . The amount of light that is absorbed or transmitted depends on the distance the light travels through the material and on the properties of the material. The transmittance is described by the Beer-Lambert law (Equation 2.4):

$$T = \frac{I}{I_0} = e^{-\alpha x} = e^{-x/l} \quad (2.4)$$

In this equation,  $x$  is the depth of the radiation in the material and  $\alpha$  is the extinction coefficient. The transmittance is also equivalent to  $e^{-x/l}$ , where  $x$  is again the depth of the radiation into the material and  $l$  is the mean free path (e.g., the average distance travelled by a photon before it is absorbed). The extinction coefficient depends on the properties of the material and is independent of the distance  $x$  traveled through medium. However,  $\alpha$  does depend on the wavelength of the incident light. It can be expressed as  $\alpha = \rho\kappa_\lambda$ , where  $\rho$  is the specific density of the material and  $\kappa_\lambda$  is the cross-section per unit mass. The Beer Lambert law is an approximation, assuming that the reflections at the surfaces of the material are negligible. In the X-rays, the contribution of reflection becomes very small.

In order to determine  $\alpha$  from our measurements, we transform the absorption in arbitrary units obtained from the laboratory fluorescent measurements in Section 2.3, to a transmission spectrum. In order to do this, we use the tabulated values of the mean free path  $l$  provided by the Center for X-ray Optics at Lawrence Berkeley National laboratory<sup>2</sup>. These values of  $l$  are calculated at certain energies over a range from 10 to 30000 eV. For each compound, the value of  $l$  can be determined over this range, taking the influence of all the possible absorption edges of the compound into account. Subsequently, Equation 2.4 can be used to calculate the transmission  $T$ . We assume that  $x$  mimics an optically thin layer of dust to resemble the conditions in the ISM. Because  $\alpha$  is independent of the depth the light travels into the material, we only need to make sure that we choose an optically thin value of  $x$ . Around 1839 eV, which is the position of the Si K-edge,  $l$  has a value of  $3 - 5 \mu\text{m}$  (depending on the pre- or post edge side). This means that if we select a thickness of  $0.5 \mu\text{m}$  (a value far below the penetration depth), the sample becomes optically thin and in that way we can mimic the conditions in the diffuse ISM. We now transform our absorption in arbitrary units from the

<sup>2</sup><http://www.cxro.lbl.gov/>

laboratory data of Section 2.3 to transmission in arbitrary units. This laboratory transmission spectrum can be fitted to the transmission spectrum obtained from tabulated data. In this way, we can determine  $\alpha$  as a function of energy (or wavelength) in detail around the edge, since  $\alpha = \frac{-\ln T}{x}$ .

In order to eventually determine the absolute extinction cross-section of the silicate we need to calculate its refractive index. The complex refractive index  $m$  is given by:

$$m = n + ik, \quad (2.5)$$

where  $n$  and  $k$  are the real and imaginary part of  $m$  (also referred to as optical constants).

The imaginary part of the refractive index depends on the attenuation coefficient  $\alpha$ :

$$\alpha = \frac{4\pi k}{\lambda}. \quad (2.6)$$

Since we already obtained  $\alpha$  from the laboratory data in combination with the tabulated values, the imaginary part of the refractive index can be derived:

$$k = \frac{\alpha\lambda}{4\pi}. \quad (2.7)$$

The real and imaginary part of the refractive index are not independent. They are related to each other by the Kramers-Kronig relations (Bohren, 2010), in particular by:

$$n(\omega) = 1 + \frac{2}{\pi} P \int_0^{\infty} \frac{\omega' k(\omega')}{\omega'^2 - \omega^2} d\omega', \quad (2.8)$$

where  $\omega$  is the frequency at which the real refractive index is evaluated and  $P$  indicates that the Cauchy principle value is to be taken. The real part of the refractive index can be calculated using a numerical solution of the Kramers Kronig transforms. In this chapter, we use a numerical method using the fast Fourier transform routines (FFT) as described in Bruzzoni et al. (2002). An example of the real and the imaginary part of the refractive index of sample 1 (olivine) is shown in Figure 2.3.

## 2.4.2 Mie scattering calculations

When the optical constants  $n$  and  $k$  are calculated, we proceed with deriving the extinction cross-section for comparison with observational data. We use Mie theory to calculate the extinction efficiency ( $Q_{\text{ext}}(\lambda, a, \theta)$ ), calculated at each wavelength ( $\lambda$ ) and particle size ( $a$ ). The application of the Mie theory makes it possible to consider the contribution of both scattering and absorption to the cross-section. We assume a smooth dust distribution along the line of sight.

We use the grain-size distribution of Mathis et al. (1977) (MRN) with a grain size interval of ( $a_-, a_+$ ) is (0.005, 0.25 $\mu\text{m}$ ). The MRN size distribution depends on the physical and chemical state of the dust grains. It is described by the following equation (in the case of silicate particles):

$$n(a)da = A_{\text{IH}} a^{-3.5} da \quad (2.9)$$

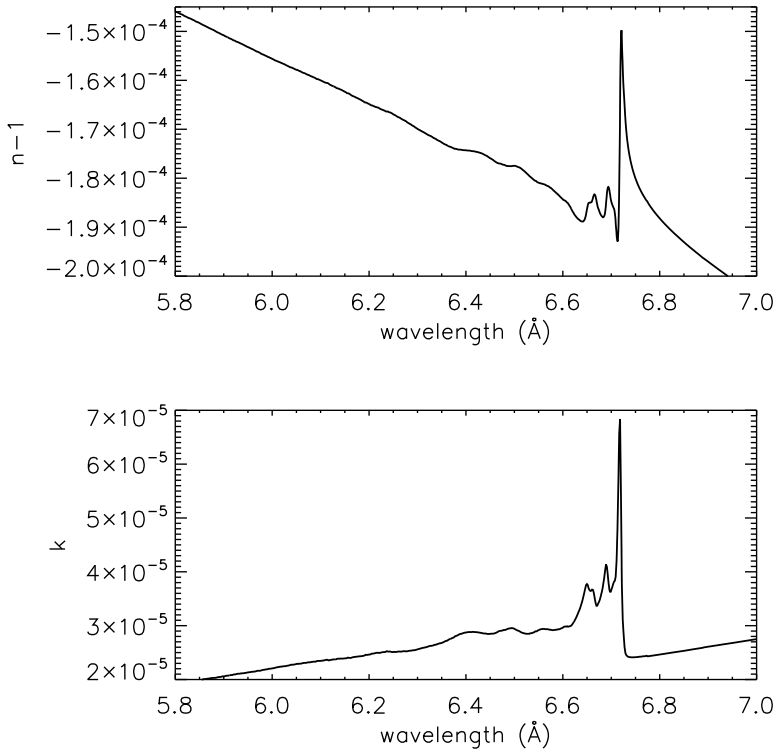


Figure 2.3: The refractive index of sample 1 (olivine). The upper panel shows the real of the refractive index ( $n$ ) and the lower panel shows the imaginary part of the refractive index indicated by  $n$  and  $k$  respectively.

In this equation,  $a$  is the particle size.  $A$  is the normalization constant, which depends on the type of dust. In the case of silicate (relevant in this chapter):

$A_{\text{sil}} = 7.8 \times 10^{-26} \text{ cm}^{2.5} (\text{H atom})^{-1}$  (Draine and Lee, 1984).  $n(a)$  is the number of grains and  $n_{\text{H}}$  is the number density of H nuclei (in both atoms and molecules).

One of the main advantages of using a MRN distribution is the simplicity of the model, which prevents the introduction of many free parameters. We can now calculate the extinction cross-section  $C_{\text{ext}}$  by applying the Mie theory (Mie 1908). We use the MIEV0 code (Wiscombe, 1980), which needs  $m$  and  $X$ , where  $X = \frac{2\pi a}{\lambda}$ , as input and returns the extinction cross-section  $C_{\text{ext}}$ .

To obtain the total scattering cross-section per wavelength unit ( $\sigma_{\text{ext}}(\lambda)$ ), we need to integrate over the particle size distribution.

$$\sigma_{\text{ext}}(\lambda) = \int_{a_-}^{a_+} C_{\text{ext}}(a, \lambda) n(a) da \quad (2.10)$$

To make the extinction cross-sections of the compounds compatible with the Verner cross-sections used by SPEX, we need to subtract the underlying continuum of the Henke tables (Henke et al., 1993). We remove the slope of the pre and post-edge by subtracting a smooth continuum in an energy range of 1.7-2.4 keV, which does not contain the edge. The result for sample 1 (olivine) is shown in Figure 2.4. The continua have been calculated in the same way as the edges, but in this case the atomic edge jump was taken out of the cross-section. We then calculate the extinction cross-section in the same way as is described above, to obtain the continuum without the edge. To remove the continuum of the extinction profile, we subtract the continua without edges. This subtraction, which was done over the full energy range, puts cross-section of the pre-edge at zero and therefore the scattering feature before the edge obtains a negative value. We then implement the models in SPEX. During the fitting, the continuum is naturally given by the X-ray continuum emission of the source.

A side note has to be made that SPEX fits the edges to the Verner tables instead of Henke. This means that there is a small discrepancy between the two parametrizations of approximately 2-5 percent, around the silicon edge (J. Wilms, private communications). This is well within the limit of precision that we can achieve from observations.

## 2.5 GX 5-1

As a first test of these new samples, we apply the new models to the source GX 5-1, which serves as a background source to observe the intervening gas and dust along the line of sight. GX 5-1 is a bright low-mass X-ray binary at  $(l, b) = (5.077, -1.019)$ . Christian and Swank (1997) estimated distance to GX 5-1 to be 9 kpc. However, this distance may be regarded as an upper limit and the actual distance could be up to 30% (or 2.7 kpc) less, because the luminosity derived from the disk model used in their analysis exceeds the Eddington limit for accretion of either hydrogen or helium. GX 5-1 has been observed multiple times, for instance by *Einstein* (Christian and Swank, 1997; Giacconi et al., 1979), as well as ROSAT using the Position Sensitive Proportional Counter (Predehl and Schmitt, 1995), and there are several observations by *Chandra*. In this work we use observations of the high-resolution spectrum of GX 5-1 collected by the HETG instrument on board *Chandra*. The Galactic coordinates

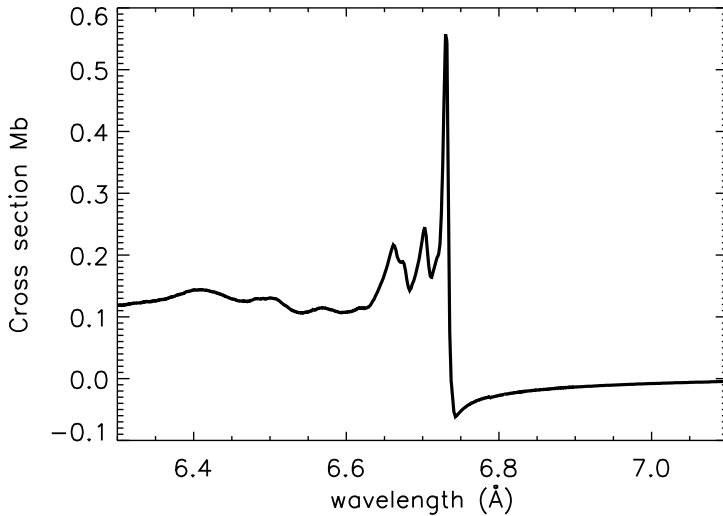


Figure 2.4: Model of the Si K-edge of olivine (sample 1) as implemented in SPEX, without the continuum of the extinction profile. The cross-section in Mb is given per Si-atom.

combined with the distance indicate that GX5-1 is located near the Galactic center (assuming a distance towards the Galactic center of 8.5 kpc). Due to the uncertainty in the distance of GX 5-1, the source may either be in front, behind or embedded in the Galactic center region (Smith et al., 2006). The proximity to this region enables us to probe the dust and gas along one of the densest sight lines of the Galaxy. From CO emission observations towards the line of sight of GX 5-1 (observed by Dame et al. (2001)), Smith et al. (2006) concluded that there are three dense regions along the line of sight, namely the 3 kpc spiral arm, the Giant Molecular Ring and the Galactic center. The three regions are at distances of 5.1, 4.7, and 8.5 kpc respectively, (Smith et al., 2006). The Giant Molecular Ring is assumed to be a region with a high molecular cloud density, which can be found approximately half way between the Sun and the Galactic center. All these regions may provide a contribution to the observed dust along the line of sight. The observation in the analysis of this chapter therefore consists of a mixture of dust and gas in these regions.

## 2.6 Data analysis of GX 5-1

The spectrum of GX 5-1 has been measured by the HETG instrument of the Chandra space telescope. This instrument contains two gratings: HEG and MEG with a resolution of 0.012 Å and 0.023 Å (full width at half maximum), respectively (Canizares et al., 2005). The energy resolution of our models is therefore well within the resolution of the Chandra Space Telescope HETG detector. There are multiple observations of GX 5-1 available in

the Chandra Transmission Gratings Catalog and Archive <sup>3</sup>, but only the observations in TE mode could be used to observe the Si K-edge (OBSID 716). This edge is not readily visible in the CC-mode, where it is filled up by the bright scattering halo radiation of the source. The edge has a slight smear as well as different optical depth. This effect is particularly evident in the CC mode, where the two arms of the grating are now compressed into one dimension, together with the scattering halo image (N. Schulz, private comm.)<sup>4</sup>.

GX 5-1 is the second brightest persistent X-ray source after the Crab Nebula (Smith et al., 2006). Due to the brightness of the source (with a flux of  $F_{0.5-2\text{keV}} = 4.7 \pm 0.8 \times 10^{-10} \text{ erg cm}^{-2} \text{ s}^{-1}$  and  $F_{2-10\text{keV}} = 2.1 \pm 0.6 \times 10^{-8} \text{ erg cm}^{-2} \text{ s}^{-1}$  2.2), the Chandra observation suffers from pile-up. This effect is dramatic in the MEG data, but also has an effect on the HEG grating. We, therefore, cannot use the MEG grating and need to ignore the HEG data below 4.0 Å. However, in this observation, GX 5-1 was also observed using both a short exposure of 0.2385 ks and a long exposure of 8.9123 ks. This is not a standard mode, but was especially constructed to evaluate the pile-up in the long exposure. The spectrum with an exposure time of 0.2385 ks does not suffer from pile-up due to the short exposure time per frame in the TE mode and can therefore be used to determine both the continuum and the hydrogen column density of the source.

Figure 2.5 shows the broad band spectrum of GX 5-1. The spectrum shows the presence of a strong Si K-edge at 6.7 Å superimposed on a strongly rising continuum towards shorter wavelength. The Si K-edge shows a strong transition with clear absorption structure at shorter wavelength, which is the tell-tale signature of solid-state absorption and an anomalous dispersion peak at the long wavelength, which reveals the presence of large grains (Van de Hulst, 1958).

### 2.6.1 Continuum and neutral absorption

Before we can calculate the mixture of dust that best fits the data of GX 5-1, we need to determine the column density of hydrogen ( $N_{\text{H}}$ ) towards GX 5-1 and the underlying continuum of the source. Earlier research of Predehl and Schmitt (1995) using data from the ROSAT satellite shows that the value of the column density ranges between  $2.78$  and  $3.48 \times 10^{22} \text{ cm}^{-2}$  depending on the continuum model. The disadvantage of the ROSAT data is that it only covers the lower-energy side (with 2 keV as the highest energy available (Trümper, 1982)) of the spectrum and therefore prevents the fitting of the hard X-ray energy side. This made it hard to predict which model would fit the spectrum the best and in that way influenced the value of  $N_{\text{H}}$ . Other more recent measurements of the value of the column density were taken by Ueda et al. (2005);  $2.8 \times 10^{22} \text{ cm}^{-2}$ , based on fits on the same Chandra HETG data used in this analysis and Asai et al. (2000);  $3.07 \pm 0.04 \times 10^{22} \text{ cm}^{-2}$  (using ASCA archival data).

The short Chandra HETG exposure does not suffer from pile-up and contains both the soft and the hard X-ray tail of the spectrum, therefore it can be used to derive the continuum and the  $N_{\text{H}}$  for this analysis. The spectrum is best modelled by two black body curves using the bb model in SPEX. The spectrum is absorbed by a cold absorbing neutral gas model, simulated by the HOT model in SPEX. The temperature of this gas is frozen to a value of  $kT = 5 \times 10^{-4} \text{ keV}$ , in order to mimic a neutral cold gas. HEG and MEG spectra of the

<sup>3</sup> <http://tgcat.mit.edu/>

<sup>4</sup> [http://exc.harvard.edu/cal/Acis/Cal\\_prods/ccmode/ccmode\\_final\\_doc03.pdf](http://exc.harvard.edu/cal/Acis/Cal_prods/ccmode/ccmode_final_doc03.pdf)

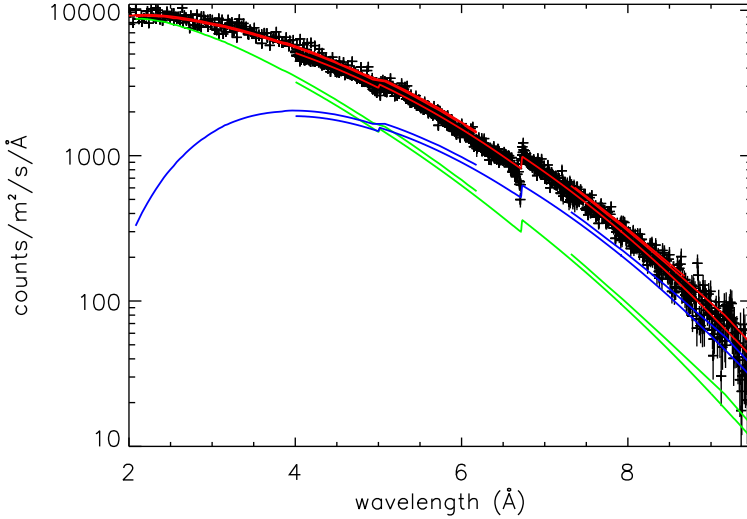


Figure 2.5: The continuum of GX 5-1. Data from the HEG short exposure, MEG short exposure and HEG long exposure (OBSID 716) were used to fit the continuum. The resulting fit to each of the three data sets is shown by a red line. The model consists of two absorbed black bodies. The two black bodies in the model are shown in figure by the green and blue lines. For clarity, only the black body models of the HEG grating (both long and short exposure) are shown and the MEG data has been omitted in the figure, therefore each black body model shows two curves.

short exposure are fitted simultaneously with this model. The best fit for the continuum and the  $N_{\text{H}}$  is shown in Figure 2.5 and Table 2.2. It is necessary to constrain the  $N_{\text{H}}$  well on the small wavelength ranges that are used in the following part of the analysis. In this way, the continuum is frozen and cannot affect the results of the dust measurements (see Section 2.6.2). Therefore, we use the HEG data of the long exposure to further constrain the column density. In the short exposure, we ignore the data close to the edge (6.2 - 7.2 Å), because the long exposure provides a much more accurate measurement of this part of the spectrum. In this way, the fit will not be biased by the lower signal-to-noise in the short exposure in this region. When we fit the model to the data, we obtain a good fit to the data with  $C^2/\nu = 1.16$ . For now, we only take cold gas into account to fit the continuum spectrum. This resulted in a column density of  $3.40 \pm 0.1 \times 10^{22} \text{ cm}^{-2}$  (see Figure 2.5 and Table 2.2). All the fits in this chapter generated by SPEX are using C-statistics (Cash, 1979) as an alternative to  $\chi^2$ -statistics. C-statistics may be used regardless of the number of counts per bin, so in this way we can use bins with a low count rate in the spectral fitting.<sup>5</sup> Errors given on parameters are 1  $\sigma$  errors.

<sup>5</sup> See for an overview about C-statistics the SPEX manual: <https://www.sron.nl/files/HEA/SPEX/manuals/manual.pdf> and <http://heasarc.gsfc.nasa.gov/lheasoft/xanadu/xspec/manual/XSappendixStatistics.html>

Table 2.2: Broad band modeling of the source using HEG and MEG data from Chandra HETG

$N_{\text{H}}$	$3.4 \pm 0.1 \times 10^{22}$	$\text{cm}^{-2}$
$T_{bb1}$	$0.59 \pm 0.02$	keV
$T_{bb2}$	$1.44 \pm 0.05$	keV
$F_{0.5-2\text{keV}}$	$4.7 \pm 0.8 \times 10^{-10}$	$\text{erg cm}^{-2} \text{s}^{-1}$
$F_{2-10\text{keV}}$	$2.1 \pm 0.6 \times 10^{-8}$	$\text{erg cm}^{-2} \text{s}^{-1}$
$C^2/\nu$	1169/1005	

Table 2.3: Depletion ranges used in the spectral fitting

Element	Depletion range
Silicon	0.8 – 0.97
Iron	0.7 – 0.97
Magnesium	0.9 – 0.97
Oxygen	0.2 – 0.4

Depletion ranges in this table are based on depletion values from Wilms et al. (2000), Costantini et al. (2012) and Jenkins (2009).

## 2.6.2 Fit to Chandra ACIS HETG data of the silicon edge

After obtaining the  $N_{\text{H}}$  value, we fit the dust models of the six dust samples to the Chandra HETG data. The shape of the continuum is fixed for now, to avoid any dependence of the fit on the continuum. The column density used for this fit is the  $N_{\text{H}}$  derived in Section 2.6.1 and can vary in a range of  $1\sigma$  from this value. To rule out any other dependence, we only use the data in a range around the edge: 6 – 9 Å. In this way we include the more extended XAFS features as well as part of the continuum in order to fit the pre and post edge to the data. The depletion values and ranges that were assumed for the cold gas component are listed in Table 2.3. Furthermore, SPEX uses protosolar abundances for the gas phase that are taken from Lodders and Palme (2009).

The SPEX routine AMOL can fit a dust mixture consisting of four different types of dust at the same time. Therefore, we test all possible configurations of the dust species and compare all the outcomes. We follow the same method as described in Costantini et al. (2012), where the total number of fits  $n$  is given by  $n = n_{\text{edge}}!/(4!(n_{\text{edge}} - 4)!)$  and  $n_{\text{edge}}$  is the number of available edge profiles.

In Figure 2.6 we show the results of a fit of the SPEX model to the observed spectrum of GX 5-1. The best fit is shown by the red line. The mixture that fits the data best consists mainly of crystalline olivine (sample 1, green line) and a smaller contribution of amorphous pyroxene (sample 5, purple line) and neutral gas (blue line).

The reduced  $C^2$  value of the best fit is 1.05. We find that most dust mixtures that contain olivine fit the edge well and when pyroxene, with a high concentration of iron, is added to the fit, we obtain even better fits. When olivine is left out of the fit, the reduced  $C^2$  values increase from 1.05 to values of approximately 2. From our fitting procedure, we conclude that the dust mixture consists of  $86 \pm 7\%$  olivine dust and  $14 \pm 2\%$  pyroxene dust.

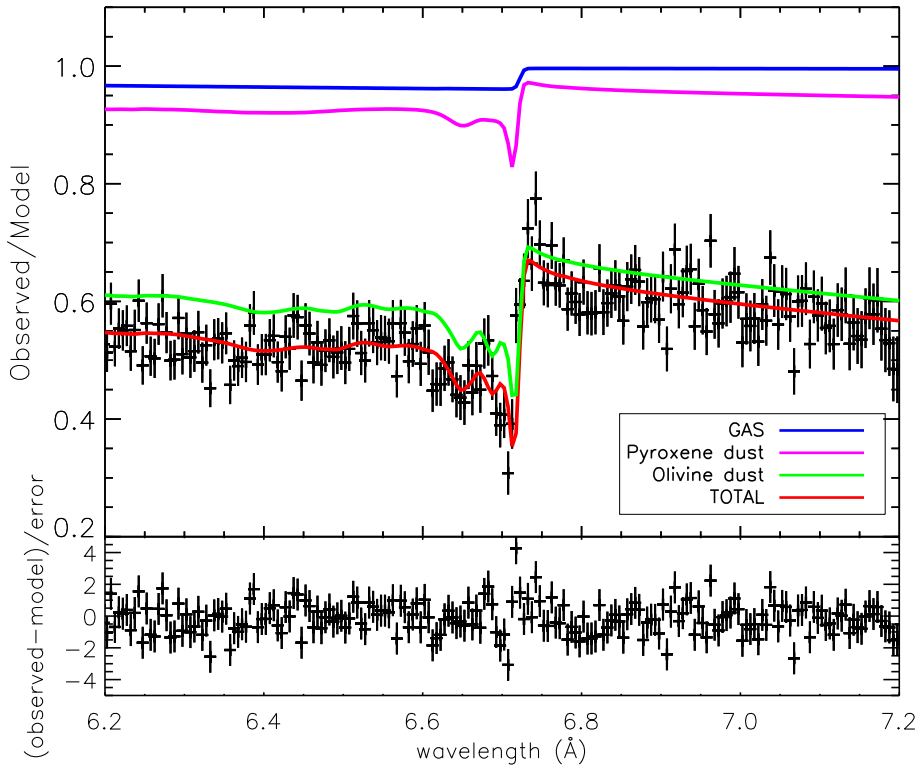


**Figure 2.6:** The fit to the spectrum of GX 5-1 is shown in red. The contribution of the continuum is divided out. The other lines show the contribution of the absorbing components to the transmission. The purple line shows the contribution of pyroxene (sample 5), the green line the contribution of olivine (sample 1) and the blue line the contribution of gas. The lower panel shows the model residuals of the fit in terms of the standard deviation  $\sigma$ .

Table 2.4: Abundances and depletions

Element	$N^{\text{tot}}$	depletion	$A_Z$ ( $10^{-5}$ H atom $^{-1}$ )	$A_Z^{\text{dust}}$ ( $10^{-5}$ H atom $^{-1}$ )	$A_Z/A_{\odot}$
Silicon	> 1.4	< 0.87	> 4.4	$4.0 \pm 0.3$	> 1.14
Iron	> 0.7	< 0.76	> 2.5	$1.7 \pm 0.1$	> 0.79
Magnesium	> 2.1	< 0.97	> 6.2	$6.1 \pm 0.3$	> 1.6
Oxygen	> 23	< 0.23	> 64	$17 \pm 1$	> 1.06

Abundances are indicated by  $A_Z$ . Solar abundances are taken from Lodders and Palme (2009). Total column densities (gas and dust)  $N^{\text{tot}}$  are in units of  $10^{18}\text{cm}^{-2}$ .

We calculated the dust abundances of silicon, oxygen, magnesium and iron to be respectively  $4.0 \pm 0.3 \times 10^{-5}$  per H atom,  $17 \pm 1 \times 10^{-5}$  per H atom,  $6.1 \pm 0.3 \times 10^{-5}$  per H atom, and  $1.7 \pm 0.1 \times 10^{-5}$  per H atom. Unfortunately, the depletion hits the higher limit of the ranges set in Table 2.3. These ranges were set in order to keep the fit within reasonable depletion values. For this reason, we can only give upper limits to the depletion values we found, which are for O: < 0.23, for Mg: < 0.97, for Si: < 0.87 and for Fe: < 0.76. Table 2.4 lists the total column density, the depletion values, dust abundances, total abundances (including both gas and dust), and solar abundances for all the elements mentioned above. The total abundances can only be given as lower limits, since we can only put a lower limit on the gas abundance due to the upper limits on the depletion values. From our best fitting dust mixture, the total abundance of silicon along the line of sight towards GX 5-1 can be calculated using the column density of the best fit and the total amount of silicon atoms in both gas and solid phase. The resulting abundance is:  $> 4.4 \times 10^{-5}$  per H atom. The gas to dust ratio of silicon is 0.22.

### 2.6.3 Hot ionized gas on the line of sight in the Si K-edge region?

Hot ionized gas along the line of sight might influence the silicon edge. In the energy range of the edge, we may observe absorption lines of this hot gas that may influence the shape of the silicon absorption edge. It may also be possible that this hot gas is intrinsic to the source. To be certain that this is not the case, we fitted the edge again as described above, but this time we add a slab of hot gas along the line of sight to our model. The lower and upper limits of the gas temperature are based upon the ionization fractions of neon by Yao and Wang (2005) and Yao et al. (2006). They observed hot gas in the ISM and compare the observed lines to ionization fractions for O, Ne, and Fe to determine the temperature of the gas. In this chapter, we use the Ne IX line to set the lower and upper limit of the hot gas (0.08 - 2.7 keV). At these temperatures of the hot gas, helium-like transitions of Si can occur at 6.69 and 6.65 Å. These lines can create additional features in the Si K-edge, so we fit the edge again with SPEX including an extra HOT model to model the hot gas. We do not detect any ionized gas along the line of sight towards GX 5-1. The gas temperature of the hot model hits the set limit of 0.08 keV, which is too cold to form any absorption lines near the silicon K-edge. Any ionized gas is therefore not likely to contaminate the Si K-edge in this data set.

## 2.7 Discussion

### 2.7.1 Abundances towards GX 5-1

#### 2.7.1.1 Si abundance

In Section 2.6.2 we find that the abundance of silicon in dust is  $4.0 \pm 0.3 \times 10^{-5}$  per H atom. We can compare this result to observations at infrared wavelengths in the solar neighborhood and towards the Galactic center. The 10 and 20  $\mu\text{m}$  lines of the Si-O bending and stretching modes were observed in order to measure the silicon abundances. We derived these abundances using the results from Aitken and Roche (1984), Roche and Aitken (1985), and Tielens et al. (1996). The silicon abundance was derived in two different regions of the Galaxy, namely the local solar neighborhood and a region close to the Galactic center. In the local solar neighborhood towards sight lines of bright nearby Wolf-Rayet stars the abundance of silicon in dust can be derived, resulting in a value of  $5.2 \pm 1.8 \times 10^{-5}$  per H atom (Roche and Aitken, 1984; Tielens et al., 1996). Measuring the Si abundance towards the Galactic center from the 10  $\mu\text{m}$  absorption may be challenging. The abundances depend on an estimate of the visual extinction ( $A_V$ ) derived from the  $N_H/A_V$  ratio for the local Solar neighborhood from UV studies of the atomic and molecular hydrogen column densities (Bohlin et al., 1978), and this procedure may be more uncertain towards the Galactic center (Tielens et al., 1996). The silicon abundance may therefore suffer from additional uncertainty. The same analysis has also been carried out for sight lines towards the Galactic center (Tielens et al., 1996; Aitken and Roche, 1984). Towards the sight line of a cluster of compact infrared sources 2 pc away from the Galactic center (Roche and Aitken, 1985), the silicon abundance in dust was derived, resulting in a value of  $3.0 \pm 1.8 \times 10^{-5}$  per H atom. This is almost half of the value of the dust abundance measured in the local solar neighborhood. This discrepancy is not well understood. An explanation could be that the difference in abundance is caused by presence of large particles (grain sizes  $> 3 \mu\text{m}$ ) near the Galactic center, which, however, is difficult to observe in the infrared (Tielens et al., 1996).

The abundance of silicon in dust found in Section 2.6.2, falls in between the two results for the local ISM and the Galactic center obtained in the infrared. When we consider the total abundance (including the contribution from gas), this increases the total abundance to  $> 4.4 \times 10^{-5}$  per H atom, which would correspond more with values found in the local solar neighborhood than those of the Galactic center. When we compare the total abundance of silicon to the protosolar abundance from Lodders and Palme (2009), we find only a small deviation from the solar abundance, namely:  $A_Z/A_\odot > 1.14$ . Furthermore, since we probe the inner regions of the Galaxy, it is not unrealistic to encounter a total abundance of silicon larger than solar along the line of sight.

Another comparison can be made using the observations towards the low-mass X-ray binaries 4U 1820-30 (Costantini et al., 2012) and X Per (Valencic and Smith, 2013). In contrast to GX 5-1, these lines of sight probe the diffuse ISM. Towards 4U 1820-30 the abundance is  $4.8_{-0.5}^{+0.8} \times 10^{-5}$  per H atom and towards X Per is  $3.6 \pm 0.5 \times 10^{-5}$  per H atom. The lower limit of the Si abundance found in our analysis does, therefore, agree with the results of the diffuse ISM. The actual value of the Si abundance might indeed be higher than the average Si abundance in the diffuse ISM, but we need upper limits to the abundances to confirm this

Table 2.5: Unconstrained silicon: abundances and depletions

Element	$N^{\text{tot}}$	Depletion	$A_Z$ ( $10^{-5}$ H atom $^{-1}$ )	$A_Z^{\text{dust}}$ ( $10^{-5}$ H atom $^{-1}$ )	$A_Z/A_{\odot}$
Silicon	$1.8 \pm 0.3$	$0.68 \pm 0.12$	$5.0 \pm 0.5$	$3.8 \pm 0.5$	$1.30 \pm 0.12$
Iron	$> 0.7$	$< 0.75$	$> 2.5$	$1.7 \pm 0.2$	$> 0.76$
Magnesium	$> 2.1$	$< 0.97$	$> 6.1$	$6.3 \pm 0.5$	$> 1.6$
Oxygen	$> 23$	$< 0.22$	$> 0.63$	$16 \pm 2$	$> 1.03$

Same as Table 2.4, but depletion of silicon is left as a free parameter without boundary values. Abundances are indicated by  $A_Z$ . Solar abundances are taken from Lodders and Palme (2009). Total column densities (gas and dust)  $N^{\text{tot}}$  are in units of  $10^{18}$  cm $^{-2}$ .

by obtaining better estimates on the depletion values. This may be obtained by releasing the range on the silicon depletion, which is discussed in Section 2.7.1.2.

### 2.7.1.2 Depletion of silicon

Since the depletion value of silicon reached the lower limit, we also show the results of a fit without restrictions on the silicon depletion values. These results are shown in Table 2.5 and Figure 2.7. By releasing the range on the silicon depletion, we get a better impression of the total abundance of silicon.

Since we are currently analyzing the K-edge of silicon, we are able to directly measure the abundance of depletion in both gas and dust of this element only. The abundances of other elements are derived indirectly from the model and their depletion values should thus be kept in a limited range. We performed the fit again, leaving the depletion of Si free to vary without predefined boundaries. In this case, we obtain a depletion value of  $0.68 \pm 0.12$ . This value is within the 1 sigma error consistent with the value in Table 2.4. The best fit in Figure 2.7 shows the same samples as the best fit in Section 2.6.2 (namely sample 1 olivine and sample 5 pyroxene), but there is a relatively larger contribution of gas, at the expense of the amorphous pyroxene contribution. As a consequence, the dust abundance value is reduced. Both  $A_Z$  and  $A_Z/A_{\odot}$  are now constrained.  $A_Z/A_{\odot}$  seems to show a clearer overabundance of Si. This is expected in environments close to the Galactic center. The value of the total silicon abundance,  $A_Z = 5.0 \pm 0.5 \times 10^{-5}$  per H atom, is comparable with values found in the local solar neighborhood. The differences between  $N^{\text{tot}}$ , the depletion,  $A_Z$ ,  $A_Z^{\text{dust}}$ , and  $A_Z/A_{\odot}$  in Table 2.4 and Table 2.5 are small in the case of the other elements: Fe, Mg, and O. This is expected, because the range on the depletion ranges of these elements were kept the same in both fits. The number of fit parameters did not change, nor did the quality of the fit. Therefore, the reduced  $C^2$  value of the fit remains at 1.05. However, since the depletion of silicon in dense environments is expected to be higher than  $0.68 \pm 0.12$ , as is shown in previous studies (Wilms et al., 2000; Jenkins, 2009; Costantini et al., 2012), we conservatively keep the silicon depletion constrained by the limits in Table 2.4 in further analysis of the edge.

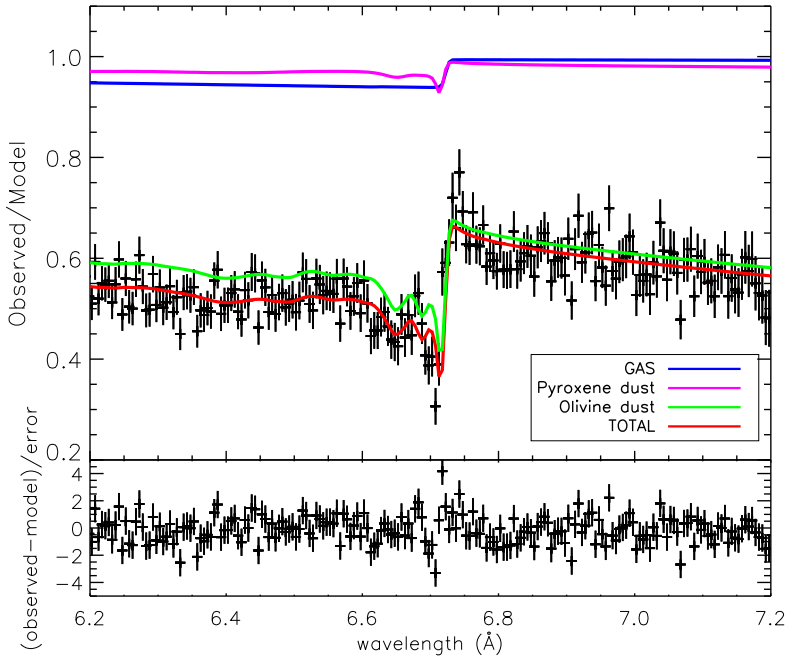


**Figure 2.7:** The upper panel shows a fit of the Si K-edge, where the depletion of silicon is left as a free parameter without boundary values. The best fitting mixture consist out of the same compounds as the fit in Section 2.6.2: sample 1 (crystalline olivine) and sample 5 (amorphous pyroxene). The lower panel shows the model residuals of the fit in terms of the standard deviation  $\sigma$ .

### 2.7.1.3 Other abundances: oxygen, magnesium and iron

The abundances of the other elements are listed in Table 2.4. Silicon and oxygen show abundances comparable to the solar values of Lodders and Palme (2009). Magnesium and iron show a deviation from protosolar abundances. The abundances in the Galaxy follow a gradient of increasing abundance towards the plane of the Galaxy. In the inner regions of the Galaxy, the abundances of the elements are expected to be supersolar (see Section 2.1). Most of the lower limits on the abundances correspond to values found in studies of the diffuse ISM (Pinto et al., 2010; Costantini et al., 2012; Valencic and Smith, 2013). Since we can only show lower limits, we expect the true abundance to be higher, which would correspond with the expected increase of abundances toward the region around the Galactic center. The abundance of magnesium is supersolar, whereas the iron abundance in our result is subsolar. The missing iron can be present in other forms of dust. A possibility could be that iron is included in metallic form in GEMS (Bradley, 1994).

### 2.7.2 Comparison to iron-poor, amorphous, and crystalline dust

An insightful way to compare the best fitting mixture to all the other possible mixtures is by comparing the best fitting mixtures with the two distinct variations in the samples: iron-rich/iron-poor and crystalline/amorphous. We select three different types of mixtures that we compare to the best fitting mixture, namely an iron-poor mixture (since the best-fitting mixture is iron-rich), a mixture of amorphous compounds and a mixture of crystalline compounds. The results are shown in Figure 2.8.

The fit that resembles the best fit the most, is the fit containing only crystalline compounds. This fit consists only of olivine, which is the compound that is dominating the best fit of Section 2.6.2. The fit improves when amorphous pyroxene is added. The different compounds show a strong variation in the absorption at wavelengths of less than  $6.6 \text{ \AA}$  relative to the K-edge at  $6.7 \text{ \AA}$ , see Fig 2.11. This difference causes the poor fits for amorphous or iron samples (Fig 2.8). The resulting fits in Figure 2.8 strongly depend on the amount of silicon atoms available in the solid state, which is restricted by the column density  $N_{\text{H}}$ . As can be observed in Fig 2.11 not every edge of the samples is equally deep. Models that produce deep absorption features around the edge, demand the presence of a certain amount of silicon in dust present along the line of sight. The amount of silicon present constrains the best fitting model in this way. The result of fitting a sample to the edge that requires a larger amount of silicon along the line of sight can be observed in the iron-poor and amorphous windows of Fig 2.8. Here the edge of the models is too deep and the post edge (which is here the part below  $6.6 \text{ \AA}$ ) never recovers to fit the data in this part of the plot. The amount of Si along the line of sight can be enhanced if the  $N_{\text{H}}$  increases. When we enhance  $N_{\text{H}}$  to values  $> 5 \times 10^{22} \text{ cm}^{-2}$  the iron-poor and amorphous models start to fit the edge, but such a  $N_{\text{H}}$  is too high for GX 5-1. A well-determined column density of hydrogen is, for this reason, of great importance.

The best fit in Section 2.6.2 shows that we detect  $86 \pm 7\%$  of crystalline olivine dust and only  $14 \pm 2\%$  of amorphous pyroxene dust. This result gives us a relatively high crystallinity, that is,  $79 - 93\%$  of the total amount of dust has a crystalline structure. This somewhat surprising result may be in line with recent results from the Stardust mission (Westphal et al., 2014) and detection of dust in external galaxies (Spoon et al., 2006; Kemper et al., 2011), which

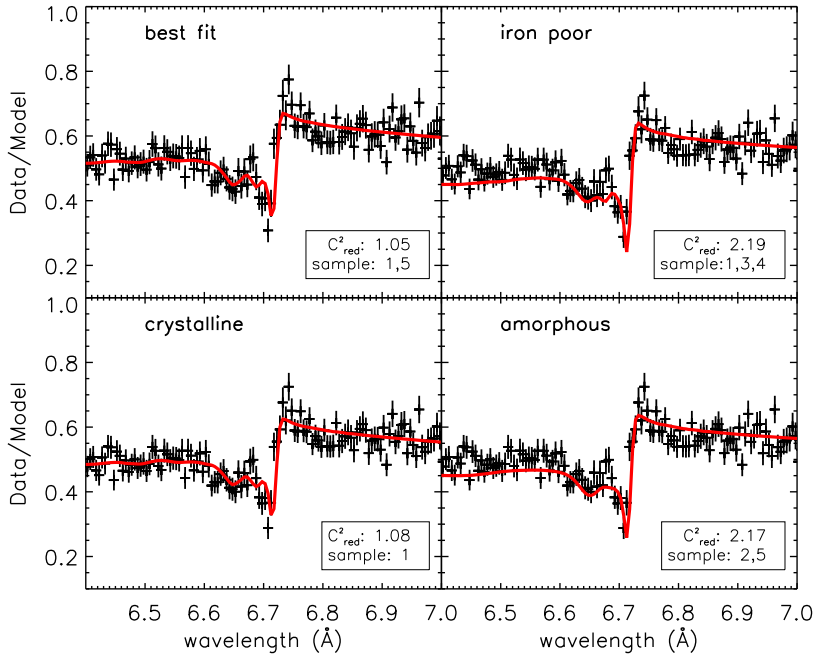


Figure 2.8: Comparison of the best fit (upper left window) with iron-poor dust mixtures, strictly crystalline mixtures and amorphous mixtures.

suggests that crystalline dust may be more abundant than expected (Kemper et al., 2004); see Section 2.1. Limitations on this result are addressed in Section 2.7.4.

### 2.7.3 Comparison with dust compositions along other sight lines

We can compare the best fitting dust mixture to results from studies of dust in the infrared and X-ray studies of dust in the diffuse ISM. The bending and stretching modes of silicon in the infrared are often attributed to a mixture of enstatite and olivine (Kemper et al., 2004; Chiar and Tielens, 2006). More detailed studies on the dust composition can be acquired from X-ray studies. Studies of the diffuse ISM show variation of the composition of the ISM along different lines of sight (Lee et al., 2009; Pinto et al., 2010; Costantini et al., 2012; Valencic and Smith, 2013). From studies of the Fe L and O K-edge, Pinto et al. (2010) concluded that the dust composition of interstellar dust is probably chemically inhomogeneous, since they found indications for iron rich silicates toward X-ray binary GS 1826-238. Lee et al. (2009), on the contrary, find that Fe oxides provide a better fit to the data of Cyg X-1. Costantini et al. (2012) concluded from an analysis of the oxygen K-edge and the iron L-edge of the source 4U 1820-30, that GEMS could possibly be present along this line of sight. Their best fitting

mixture, is a mixture of enstatite and metallic iron, which suggests that the dust in this region mostly consists of enstatite with metallic inclusions.

Along the line of sight toward X Per a dust mixture of  $\text{MgSiO}_3$  and iron-bearing silicates such as  $\text{Mg}_{1.6}\text{Fe}_{0.4}\text{SiO}_4$  provide a good fit to the observed spectrum (Valencic and Smith, 2013). They conclude that although  $\text{MgSiO}_3$  is the dominating compound, the fit improves when iron-bearing silicates are included. The best fitting dust mixture in this study consists of the compounds that contain the largest amount of iron available in our set of compounds. Compared to the amount of magnesium present in these samples however, we can still consider this dust mixture as relatively iron-poor. This is also reflected in the abundances of iron and magnesium of the best fit.

#### 2.7.4 Limiting factors in the analysis of the Si K-edge

The modeling of a photoelectric edge such as the Si K-edge involves many components, which may influence the resulting shape of the edge. This requires a careful analysis of the resulting best-fit. This paragraph provides more insight into the quality of the fits and the limitations that arise in the analysis.

The quality of the fit depends in the first place on the resolution of the instrument. The observations used in this analysis were observed with the HEG grating of the *Chandra* X-ray telescope. This grating provides us with the best resolution currently available close to the Si K-edge. The bright source provides us with a high flux near the Si K-edge and the edge falls well within the range of the grating, where the effective area of the instrument is large. The minimum S/N per bin near the Si K-edge is 20, which is sufficient for the study.

Additionally, the accuracy of the results depends on the degrees of freedom of the fit and, of course, on the completeness of the dust models. SPEX allows a maximum input of four different dust components in the same fit. If we examine the output of the fits for all the possible dust mixtures, most of the resulting fits contain two dust components with negligible contribution from the other two possible components. In almost all the fits, one of the dust components dominates. The contribution of the second component is, in most cases, no more than 20% and in two cases there is a contribution of a third component, which is never more than 1–2%. When we analyze the fits that are within 3 sigma of the best-fit values presented in Section 2.6.2, the dominating component in these fits is crystalline olivine. Interestingly, all the dust mixtures where olivine is not included do not fall within 3 sigma of our best fit and can be ruled out.

Our set of models is sufficient for a pilot study of the Si K-edge, but should be expanded for further analysis. The main limiting factor in this analysis is the absence of an amorphous olivine model as a counterpart to the crystalline olivine model (see Section 2.3.1). We note that the crystalline counterpart cannot be taken as a proxy for the amorphous one. As an example, see the profiles of pyroxenes in amorphous and crystalline form in Figure 2.2. The sharp features of the XAFS in the observation of GX 5-1 are indicative of a crystalline structure (Figure 2.2). However, if the shape of the amorphous olivine would follow that of a crystalline counterpart albeit less sharp, the fit may allow the presence of more amorphous olivine. At the moment we are unable to test this (see the discussion in Section 2.3.1). Therefore, we conclude that the interesting possibility of a high fraction of crystalline dust along this line of sight must be further verified.

Another limitation in our analysis could be the Mg:Fe ratio in our samples. The resulting abundances and depletion values in our analysis depend strongly on the best-fitting dust mixture. The silicates in our sample are mainly olivines and pyroxenes with different Mg:Fe ratios. All the samples are relatively iron-poor with a maximum Fe contribution of  $Mg/(Mg+Fe)$  of 0.6 and although there are indications that interstellar and circumstellar may indeed be iron-poor (Molster et al., 2002a,b,c; Chiar and Tielens, 2006; Blommaert et al., 2014), it would be beneficial to include silicates with a higher iron content.

In order to better constrain the depletion values, it is necessary to expand the fit to a broader wavelength range and incorporate multiple edges in the analysis depending on the observed  $N_H$ . In the case of GX 5-1 iron cannot be directly observed. The  $N_H$  is not high enough to imprint a significant Fe K-edge. On the lower energy side, interstellar absorption suppresses the Fe L-edges at  $\sim 0.7$  keV and the O K-edge at 0.543 keV. The iron abundance in silicates can therefore only be inferred from the best fitting dust mixture. Finally, the Mg K-edge in GX 5-1 suffers from a lower signal to noise ratio with respect to the Si K-edge, mainly because of the relatively high column density value. However, the Mg K-edge can in principle help significantly in breaking model degeneracies.

### 2.7.5 Scattering and particle size distributions

We use a MRN distribution to describe the particle size distribution. The distribution with particles sizes ranging between  $0.005 \mu\text{m}$  and  $0.25 \mu\text{m}$  implies that most of the mass is in the large particles, while most of the surface area is in the small particles. MRN offers a simple parameterization, useful in this study. It is beyond the scope of this work to test more sophisticated models such as Weingartner and Draine (2001) and Zubko et al. (2004). We note, however, that these size distributions have a maximum size cutoff around  $0.25 \mu\text{m}$  and the silicate-type distributions do not differ dramatically from one another.

In Figure 2.6, it can be observed that there is a feature between  $6.8 \text{ \AA}$  and the edge at  $6.7 \text{ \AA}$ . The MRN distribution predicts a large amount of small particles in our models. These particles do not add significantly to the scattering features of the extinction profiles. The model does not fit the data in the area around  $6.7 \text{ \AA}$ , well, which may indicate the presence of larger particles along the line of sight than present in our model (Van de Hulst, 1958). This section therefore contains an investigation of the effect of the particle size distribution and focuses, in particular, on the presence of particles larger than  $0.25 \mu\text{m}$ . In order to model the enhancement of the scattering peak around  $6.7 \text{ \AA}$  we introduce a range of particle sizes:  $0.05 - 0.5 \mu\text{m}$ . The effect of a change in the size distribution is shown in Figure 2.9. The olivine Si K-edge with a MRN distribution with particle sizes of  $0.005 - 0.25 \mu\text{m}$  is shown in red and in blue the same edge is shown but now with a MRN size distribution that has a particle range of  $0.05 - 0.5 \mu\text{m}$ .

The edge is fitted again with models of the same compounds, that contain the new particle distribution. We use the same parameters as in the first fit in Section 2.6.2. The results are shown in Figure 2.10. The reduced  $C^2$  value of the best fit is: 1.08. There is a small contribution (of less than 2% of the total amount of dust) of hypersthene (sample 6) in this fit in addition to amorphous pyroxene (sample 5) and crystalline olivine (sample 1). The contribution is so small that it does not significantly change any of the results derived above. The silicon abundance remains at  $4.0 \pm 0.4 \times 10^{-5}$  per H atom. The scattering feature before the edge is better fitted using a model with larger particles, which leads to the possibility of the presence of particles

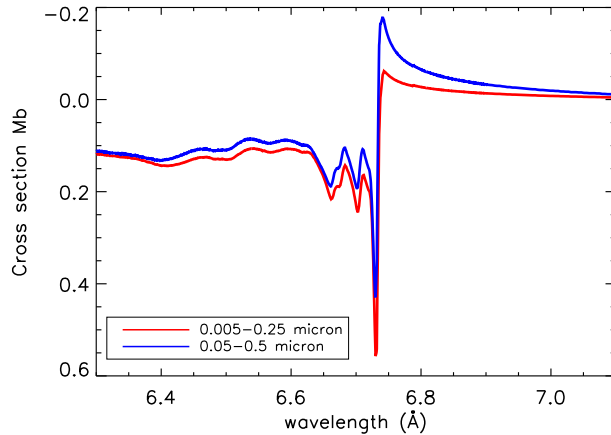


Figure 2.9: The effect of a change in the size distribution on the extinction. The olivine Si K-edge with an MRN distribution with particle sizes of 0.005 – 0.25  $\mu\text{m}$  micron is shown in red. The blue line shows the same edge, but now the particle sizes range between 0.05 – 0.5  $\mu\text{m}$ .

larger than 0.25  $\mu\text{m}$ . It is possible that in environments such as the Galactic center region we observe a substantial amount of particles larger than 0.25  $\mu\text{m}$  (Ossenkopf et al., 1992; Ormel et al., 2009, 2011). In our analysis, we assume that the dust particles are solid spheres, while it is more likely that large particles in dense environments are grown by coagulation of dust particles (Jura, 1980). Porous dust particles show an enhanced extinction profile when compared to solid particles of the same mass due to their larger surface area. Solid particles are too massive to be abundant enough to cause the enhanced scattering. Another indicator that dust particles are non-spherical is the observation of polarized starlight. Spheroidal grain models are able to reproduce these observations (Kim and Martin, 1995; Draine, 2009) and allow for larger particles in the size distribution (Draine, 2009). The effects of large porous grains in X-rays have also been studied by Hoffman and Draine (2016). They conclude that grains with a significant porosity produce narrower forward scattering peaks than equal-mass non-porous grains. Chiar and Tielens (2006) analyzed the possibility of the presence of solid and porous spherical dust particles along sight lines toward four Wolf Rayet stars. They conclude that a mixture of solid and porous silicates fits the 9.7  $\mu\text{m}$  and 18  $\mu\text{m}$  absorption features. The presence of large porous dust particles along the line of sight toward GX 5-1 could be an explanation for the observed prominent scattering features in the Si K-edge. The presence of larger grains is also derived from studies of the mid-infrared extinction law. The extinction curve in the diffuse ISM is represented by  $R_V = 3.1$ , while higher values of  $R_V$  (i.e., 4-6) are observed for dense clouds, which may indicate the presence of larger grains (Weingartner and Draine, 2001). Xue et al. (2016) calculate the intrinsic mid-infrared color excess from the stellar effective temperatures in order to determine the mid-infrared extinction. They find that the extinction curve is consistent with the  $R_V = 5.5$  model curve and agrees well with the WD01 (Weingartner and Draine, 2001) interstellar dust model. The sight line toward GX 5-1 traverses the molecular ring and likely probes a mixture of diffuse and dense medium.

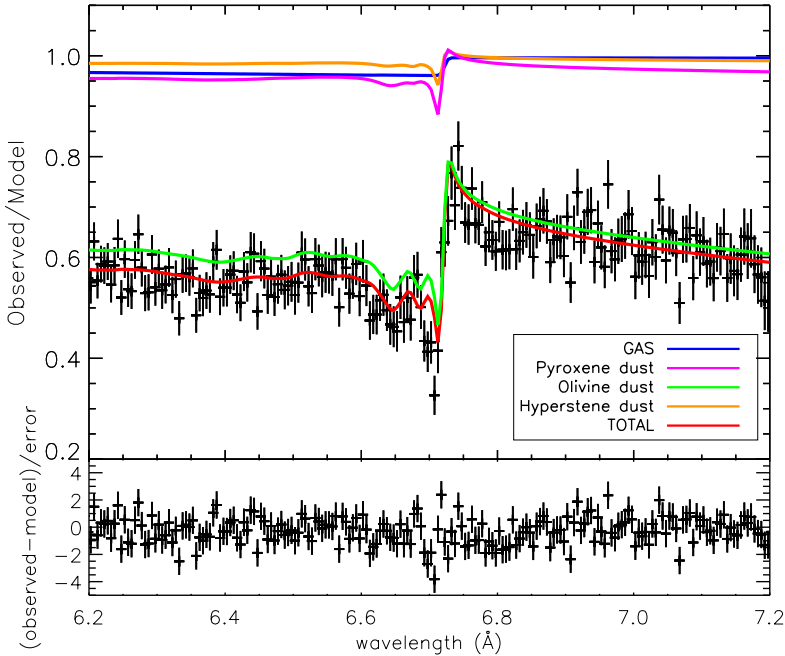


Figure 2.10: The upper panel shows a fit of the Si K-edge with particles of sizes in a range of  $0.1 - 0.5 \mu\text{m}$ . The best fitting mixture consist out of the same compounds as the fit in Section 2.6.2: sample 1 (crystalline olivine) and sample 5 (amorphous pyroxene) with a small addition of sample 6 (hypersthene). The lower panel shows the models residuals of the fit in terms of the standard deviation  $\sigma$ .

The dense region may be associated with the molecular ring, characterized by larger grains (Ormel et al., 2009, 2011).

## 2.8 Summary

In this chapter, we analyzed the X-ray spectrum of the low-mass X-ray binary GX 5-1, where we focused, in particular, on the modeling of the Si K-edge. The Si K-edges of six silicate dust samples were measured at the Soleil synchrotron facility in Paris. Using these new measurements, we calculated the extinction profiles of these samples in order to make them suitable for the analysis of the ISM toward GX 5-1. The extinction profiles of the Si K-edge were added to the AMOL model of the spectral fitting program SPEX. We obtained a best fit to the Chandra HETG data of GX 5-1 and arrive at the following results:

1. We established conservative lower limits on the abundances of Si, O, Mg, and Fe:  $A_{\text{Si}}/A_{\odot} > 1.14$ ,  $A_{\text{O}}/A_{\odot} > 1.06$ ,  $A_{\text{Mg}}/A_{\odot} > 1.6$ ,  $A_{\text{Fe}}/A_{\odot} > 0.79$ . Except for iron, all the lower limits on the abundances show abundances similar to, or above, protosolar

values. We obtained upper limits on the depletion:  $< 0.87$  for silicon,  $< 0.23$  for oxygen,  $< 0.97$  for magnesium and  $< 0.76$  for iron.

2. There may be indications for large dust particles along the line of sight due to enhanced scattering features in the Si K-edge. The scattering feature longward of the Si K-edge is better fitted using a model with larger particles, which indicates the presence of particles larger than  $0.25 \mu\text{m}$  up to  $0.5 \mu\text{m}$ .
3. The sharp absorption features observed in the Si K-edge suggest a possibly significant amount of crystalline dust with respect to the total amount of dust. However, more laboratory measurements are required to draw any conclusion on this subject.

## Acknowledgments

Dust studies at SRON and Leiden Observatory are supported through the Spinoza Premie of the Dutch science agency, NWO. We would like to thank Jörn Wilms and the anonymous referee for providing us with helpful comments and suggestions. This research made use of the Chandra Transmission Grating Catalog and archive (<http://tgcat.mit.edu>). Furthermore, we made use of the FLUO correction code provided by Daniel Haskel. H.M. and S.Z. are grateful for support of the Deutsche Forschungsgemeinschaft under Mu 1164/7-2 and Mu 1164/8-1. We acknowledge SOLEIL for provision of synchrotron radiation facilities and we would like to thank Delphine Vantelon for assistance in using beamline LUCIA. E.C. acknowledges support from NWO-Vidi grant 639.042.525.

## 2.A Correction for saturation

In Section 2.3, we describe the effect of saturation. In order to correct for saturation, we used the FLUO correction code by Daniel Haskel, which is part of the UWXAFS software package (Stern et al., 1995). In this appendix, we give a brief summary of the correction method, which can also be found in the documentation of the FLUO code. Equation 2.3 corresponds to pre-edge subtracted data, that is, for energies lower than the edge  $I_f/I_0$ , which is zero. The signal can be normalized by performing an edge-step normalization. The normalized signal  $N$  is given by:

$$N = \frac{I_f(E)}{I_0} = \left[ \frac{\epsilon_f(E)\alpha_e(E)}{\epsilon_f(E_0^+)\alpha_e(E_0^+)} \right] \left[ \frac{\alpha_{\text{tot}}(E_f) + \alpha_b(E_0^+) + \alpha_e(E_0^+)}{\alpha_{\text{tot}}(E_f) + \alpha_b(E) + \alpha_e(E)} \right], \quad (2.11)$$

where  $\alpha_{\text{tot}} = \alpha_b + \alpha_e$ ,  $\alpha_e$  is the absorption from the element of interest,  $\alpha_b$  denotes the absorption from all other atoms and other edges of interest and  $E_0^+$  indicates the energy above the main absorption edge. Dividing the denominator by  $\alpha_e(E_0^+)$  gives:

$$N = \frac{\alpha_e(E)}{\alpha_e(E_0^+)} \frac{\epsilon_f(E)}{\epsilon_f(E_0^+)} \left[ \frac{\frac{\alpha_{\text{tot}}(E_f)}{\alpha_e(E_0^+)} + \frac{\alpha_b(E_0^+)}{\alpha_e(E_0^+)} + \frac{\alpha_e(E_0^+)}{\alpha_e(E_0^+)}}{\frac{\alpha_{\text{tot}}(E_f)}{\alpha_e(E_0^+)} + \frac{\alpha_b(E)}{\alpha_e(E_0^+)} + \frac{\alpha_e(E)}{\alpha_e(E_0^+)}} \right]. \quad (2.12)$$

Defining  $\beta = \frac{\alpha_{\text{tot}}(E_f)}{\alpha_e(E_0^+)}$ ,  $\gamma = \frac{\alpha_b(E)}{\alpha_e(E_0^+)}$ , and  $\gamma' = \frac{\alpha_b(E_0^+)}{\alpha_e(E_0^+)}$  and solving for  $\frac{\alpha_e(E)}{\alpha_e E_0^+}$  gives:

$$\frac{\alpha_e(E)}{\alpha_e(E_0^+)} = \frac{N(\beta + \gamma)}{(\beta + \gamma' + 1) - N}. \quad (2.13)$$

Since we are only concerned with a small energy range at the interval of the XAFS region, the following approximation was made:  $\frac{\epsilon_f(E)}{\epsilon_f(E_0^+)} \approx 1$  in Equation 2.13. Furthermore,  $\alpha_b(E) \approx \alpha_b(E_0^+)$  which leads to:  $\gamma \approx \gamma'$ . FLUO uses tabulated cross-section from the McMaster tables to calculate  $\beta$  and  $\gamma$ . It will also perform an edge-step normalization in order to obtain  $N$ . In this way  $\frac{\alpha_e(E)}{\alpha_e(E_0^+)}$  can be derived.

## 2.B Si K-edge models

Here we show the extinction profiles around the Si K-edge for the compounds used in this analysis. These profiles are implemented in the AMOL model of the fitting code SPEX. The numbers of the samples correspond to the numbers given in Table 2.1 in which the chemical formulas and the structure (crystalline or amorphous) are given. The absolute cross-sections of the models used in this analysis are available in tabular form on the following website: [www.sron.nl/~elisa/VIDI/](http://www.sron.nl/~elisa/VIDI/).

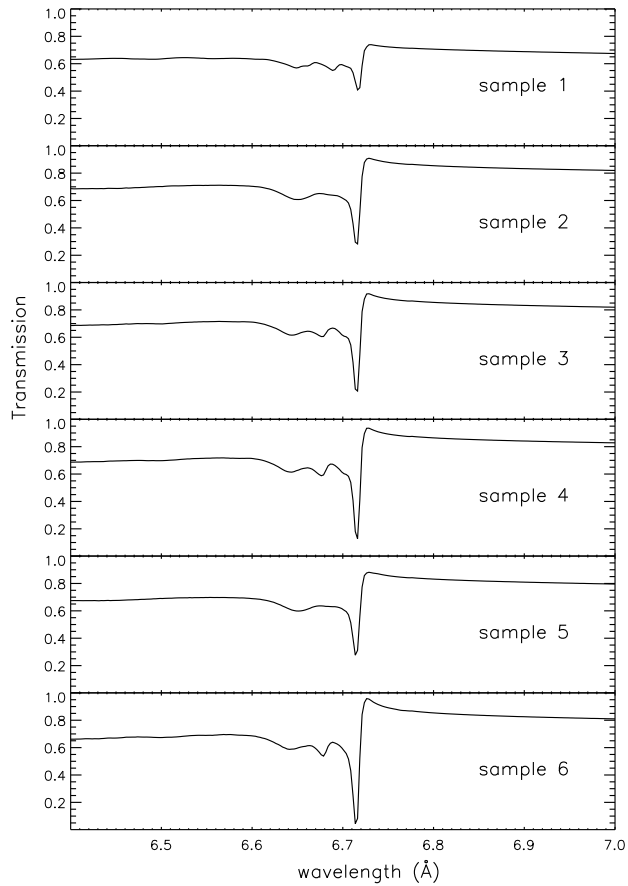


**Figure 2.11:** Transmission of the six dust extinction models (absorption and scattering) from the analysis of the Si K-edge. The silicon column density has been set here to  $10^{18} \text{ cm}^{-2}$  for all the dust models. Each model is indicated by a number corresponding to the numbers in Table 2.1. The table also gives the chemical formula and the structure (crystalline or amorphous) of the dust compound.



## References

- Aitken, D. K. and Roche, P. F. (1984). A study of the unidentified dust emission features near 10 microns. *MNRAS*, 208:751–761.
- Anders, E. and Zinner, E. (1993). Interstellar grains in primitive meteorites - Diamond, silicon carbide, and graphite. *Meteoritics*, 28:490–514.
- Asai, K., Dotani, T., Nagase, F., and Mitsuda, K. (2000). Iron K Emission Lines in the Energy Spectra of Low-Mass X-Ray Binaries Observed with ASCA. *ApJS*, 131:571–591.
- Blommaert, J. A. D. L., de Vries, B. L., Waters, L. B. F. M., Waelkens, C., Min, M., Van Winckel, H., Molster, F., Decin, L., Groenewegen, M. A. T., Barlow, M., García-Lario, P., Kerschbaum, F., Posch, T., Royer, P., Ueta, T., Vandenbussche, B., Van de Steene, G., and van Hoof, P. (2014). Herschel/PACS observations of the 69  $\mu\text{m}$  band of crystalline olivine around evolved stars. *A&A*, 565:A109.
- Bohlin, R. C., Savage, B. D., and Drake, J. F. (1978). A survey of interstellar H I from L-alpha absorption measurements. II. *ApJ*, 224:132–142.
- Bohren, C. F. (2010). What did kramers and kronig do and how did they do it? *European Journal of Physics*, 31(3):573.
- Bradley, J. P. (1994). Chemically Anomalous, Preaccretionally Irradiated Grains in Interplanetary Dust From Comets. *Science*, 265:925–929.
- Bringa, E. M., Kucheyev, S. O., Loeffler, M. J., Baragiola, R. A., Tielens, A. G. G. M., Dai, Z. R., Graham, G., Bajt, S., Bradley, J. P., Dukes, C. A., Felter, T. E., Torres, D. F., and van Breugel, W. (2007). Energetic Processing of Interstellar Silicate Grains by Cosmic Rays. *ApJ*, 662:372–378.
- Bruzzone, P., Carranza, R., Lacoste, J. C., and Crespo, E. (2002). Kramers'kronig transforms calculation with a fast convolution algorithm. *Electrochimica Acta*, 48(4):341 – 347.
- Canizares, C. R., Davis, J. E., Dewey, D., Flanagan, K. A., Galton, E. B., Huenemoerder, D. P., Ishibashi, K., Markert, T. H., Marshall, H. L., McGuirk, M., Schattner, M. L., Schulz, N. S., Smith, H. I., and Wise, M. (2005). The Chandra High-Energy Transmission Grating: Design, Fabrication, Ground Calibration, and 5 Years in Flight. *PASP*, 117:1144–1171.
- Cash, W. (1979). Parameter estimation in astronomy through application of the likelihood ratio. *ApJ*, 228:939–947.

- Chen, L., Hou, J. L., and Wang, J. J. (2003). On the Galactic Disk Metallicity Distribution from Open Clusters. I. New Catalogs and Abundance Gradient. *AJ*, 125:1397–1406.
- Chiar, J. E. and Tielens, A. G. G. M. (2006). Pixie Dust: The Silicate Features in the Diffuse Interstellar Medium. *ApJ*, 637:774–785.
- Christian, D. J. and Swank, J. H. (1997). The Survey of Low-Mass X-Ray Binaries with the Einstein Observatory Solid-State Spectrometer and Monitor Proportional Counter. *ApJS*, 109:177–224.
- Costantini, E. and de Vries, C. (2013). Characterizing the chemistry of interstellar dust: the X-ray view. *Mem. Soc. Astron. Italiana*, 84:592.
- Costantini, E., Freyberg, M. J., and Predehl, P. (2005). Absorption and scattering by interstellar dust: an XMM-Newton observation of <ASTROBJ>Cyg X-2</ASTROBJ>. *A&A*, 444:187–200.
- Costantini, E., Pinto, C., Kaastra, J. S., in't Zand, J. J. M., Freyberg, M. J., Kuiper, L., Méndez, M., de Vries, C. P., and Waters, L. B. F. M. (2012). XMM-Newton observation of 4U 1820-30. Broad band spectrum and the contribution of the cold interstellar medium. *A&A*, 539:A32.
- Dame, T. M., Hartmann, D., and Thaddeus, P. (2001). The Milky Way in Molecular Clouds: A New Complete CO Survey. *ApJ*, 547:792–813.
- de Vries, B. L., Min, M., Waters, L. B. F. M., Blommaert, J. A. D. L., and Kemper, F. (2010). Determining the forsterite abundance of the dust around asymptotic giant branch stars. *A&A*, 516:A86.
- de Vries, C. P. and Costantini, E. (2009). Physical properties of amorphous solid interstellar material from X-ray absorption spectroscopy of <ASTROBJ>Scorpius X-1</ASTROBJ>. *A&A*, 497:393–398.
- Dorschner, J., Begemann, B., Henning, T., Jaeger, C., and Mutschke, H. (1995). Steps toward interstellar silicate mineralogy. II. Study of Mg-Fe-silicate glasses of variable composition. *A&A*, 300:503.
- Draine, B. T. (2003). Scattering by Interstellar Dust Grains. II. X-Rays. *ApJ*, 598:1026–1037.
- Draine, B. T. (2009). Interstellar Dust Models and Evolutionary Implications. In Henning, T., Grün, E., and Steinacker, J., editors, *Cosmic Dust – Near and Far*, volume 414 of *Astronomical Society of the Pacific Conference Series*, page 453.
- Draine, B. T. and Lee, H. M. (1984). Optical properties of interstellar graphite and silicate grains. *ApJ*, 285:89–108.
- Draine, B. T. and Li, A. (2001). Infrared Emission from Interstellar Dust. I. Stochastic Heating of Small Grains. *ApJ*, 551:807–824.

- Draine, B. T. and Li, A. (2007). Infrared Emission from Interstellar Dust. IV. The Silicate-Graphite-PAH Model in the Post-Spitzer Era. *ApJ*, 657:810–837.
- Dwek, E. and Scalo, J. M. (1980). The evolution of refractory interstellar grains in the solar neighborhood. *ApJ*, 239:193–211.
- Dwek, E., Zubko, V., Arendt, R. G., and Smith, R. K. (2004). Probing Interstellar Dust Models Through SAXS (Small Angle X-Ray Scattering). In Witt, A. N., Clayton, G. C., and Draine, B. T., editors, *Astrophysics of Dust*, volume 309 of *Astronomical Society of the Pacific Conference Series*, page 499.
- Flank, A.-M., Cauchon, G., Lagarde, P., Bac, S., Janousch, M., Wetter, R., Dubuisson, J.-M., Idir, M., Langlois, F., Moreno, T., and Vantelon, D. (2006). Lucia, a microfocus soft {XAS} beamline. *Nuclear Instruments and Methods in Physics Research Section B: Beam Interactions with Materials and Atoms*, 246(1):269 – 274. Synchrotron Radiation and Materials Science Proceedings of the E-MRS 2005 Symposium O on Synchrotron Radiation and Materials Science E-MRS 2005 Symposium O.
- Floss, C., Stadermann, F. J., Bradley, J. P., Dai, Z. R., Bajt, S., Graham, G., and Lea, A. S. (2006). Identification of isotopically primitive interplanetary dust particles: A NanoSIMS isotopic imaging study. *Geochim. Cosmochim. Acta*, 70:2371–2399.
- Gail, H.-P. (2010). Formation and Evolution of Minerals in Accretion Disks and Stellar Outflows. In Henning, T., editor, *Lecture Notes in Physics, Berlin Springer Verlag*, volume 815 of *Lecture Notes in Physics, Berlin Springer Verlag*, pages 61–141.
- Gail, H.-P., Zhukovska, S. V., Hoppe, P., and Trieloff, M. (2009). Stardust from Asymptotic Giant Branch Stars. *ApJ*, 698:1136–1154.
- Giacconi, R., Branduardi, G., Briel, U., Epstein, A., Fabricant, D., Feigelson, E., Forman, W., Gorenstein, P., Grindlay, J., Gursky, H., Harnden, F. R., Henry, J. P., Jones, C., Kellogg, E., Koch, D., Murray, S., Schreier, E., Seward, F., Tananbaum, H., Topka, K., Van Speybroeck, L., Holt, S. S., Becker, R. H., Boldt, E. A., Serlemitsos, P. J., Clark, G., Canizares, C., Markert, T., Novick, R., Helfand, D., and Long, K. (1979). The Einstein /HEAO 2/ X-ray Observatory. *ApJ*, 230:540–550.
- Henke, B., Gullikson, E., and Davis, J. (1993). X-ray interactions: Photoabsorption, scattering, transmission, and reflection at  $e = 50\text{--}30,000$  eV,  $z = 1\text{--}92$ . *Atomic Data and Nuclear Data Tables*, 54(2):181–342.
- Henning, T. (2010). Cosmic Silicates. *ARA&A*, 48:21–46.
- Henning, T., Begemann, B., Mutschke, H., and Dorschner, J. (1995). Optical properties of oxide dust grains. *A&AS*, 112:143.
- Hoffman, J. and Draine, B. T. (2016). Accurate Modeling of X-ray Extinction by Interstellar Grains. *ApJ*, 817:139.

- Jaeger, C., Molster, F. J., Dorschner, J., Henning, T., Mutschke, H., and Waters, L. B. F. M. (1998). Steps toward interstellar silicate mineralogy. IV. The crystalline revolution. *A&A*, 339:904–916.
- Jenkins, E. B. (2009). A Unified Representation of Gas-Phase Element Depletions in the Interstellar Medium. *ApJ*, 700:1299–1348.
- Jones, A. P. and Nuth, J. A. (2011). Dust destruction in the ISM: a re-evaluation of dust lifetimes. *A&A*, 530:A44.
- Jones, A. P., Tielens, A. G. G. M., and Hollenbach, D. J. (1996). Grain Shattering in Shocks: The Interstellar Grain Size Distribution. *ApJ*, 469:740.
- Jones, A. P., Tielens, A. G. G. M., Hollenbach, D. J., and McKee, C. F. (1994). Grain destruction in shocks in the interstellar medium. *ApJ*, 433:797–810.
- Jones, O. C., Kemper, F., Sargent, B. A., McDonald, I., Gielen, C., Woods, P. M., Sloan, G. C., Boyer, M. L., Zijlstra, A. A., Clayton, G. C., Kraemer, K. E., Srinivasan, S., and Ruffle, P. M. E. (2012). On the metallicity dependence of crystalline silicates in oxygen-rich asymptotic giant branch stars and red supergiants. *MNRAS*, 427:3209–3229.
- Jura, M. (1980). Origin of large interstellar grains toward Rho Ophiuchi. *ApJ*, 235:63–65.
- Kaastra, J. S., de Vries, C. P., Costantini, E., and den Herder, J. W. A. (2009). Effective area calibration of the reflection grating spectrometers of XMM-Newton. I. X-ray spectroscopy of the Crab nebula. *A&A*, 497:291–310.
- Kaastra, J. S., Mewe, R., and Nieuwenhuijzen, H. (1996). SPEX: a new code for spectral analysis of X & UV spectra. In Yamashita, K. and Watanabe, T., editors, *UV and X-ray Spectroscopy of Astrophysical and Laboratory Plasmas*, pages 411–414.
- Keller, L. P. and Messenger, S. (2013). On the origins of GEMS grains: A reply. *Geochim. Cosmochim. Acta*, 107:341–344.
- Kemper, F., Markwick, A. J., and Woods, P. M. (2011). The crystalline fraction of interstellar silicates in starburst galaxies. *MNRAS*, 413:1192–1199.
- Kemper, F., Vriend, W. J., and Tielens, A. G. G. M. (2004). The Absence of Crystalline Silicates in the Diffuse Interstellar Medium. *ApJ*, 609:826–837.
- Kim, S.-H. and Martin, P. G. (1995). The size distribution of interstellar dust particles as determined from polarization: Spheroids. *ApJ*, 444:293–305.
- Lee, J. C., Ogle, P. M., Canizares, C. R., Marshall, H. L., Schulz, N. S., Morales, R., Fabian, A. C., and Iwasawa, K. (2001). Revealing the Dusty Warm Absorber in MCG -6-30-15 with the Chandra High-Energy Transmission Grating. *ApJ*, 554:L13–L17.
- Lee, J. C., Xiang, J., Ravel, B., Kortright, J., and Flanagan, K. (2009). Condensed Matter Astrophysics: A Prescription for Determining the Species-specific Composition and Quantity of Interstellar Dust Using X-rays. *ApJ*, 702:970–979.

- Li, A. and Draine, B. T. (2001). On Ultrasmall Silicate Grains in the Diffuse Interstellar Medium. *ApJ*, 550:L213–L217.
- Li, D., Bancroft, G. M., Fleet, M. E., and Feng, X. H. (1995). Silicon k-edge xanes spectra of silicate minerals. *Physics and Chemistry of Minerals*, 22(2):115–122.
- Lodders, K. and Palme, H. (2009). Solar System Elemental Abundances in 2009. *Meteoritics and Planetary Science Supplement*, 72:5154.
- Mathis, J. S. (1998). The Near-Infrared Interstellar Silicate Bands and Grain Theories. *ApJ*, 497:824–832.
- Mathis, J. S., Rumpl, W., and Nordsieck, K. H. (1977). The size distribution of interstellar grains. *ApJ*, 217:425–433.
- Meikle, W. P. S., Mattila, S., Pastorello, A., Gerardy, C. L., Kotak, R., Sollerman, J., Van Dyk, S. D., Farrah, D., Filippenko, A. V., Höflich, P., Lundqvist, P., Pozzo, M., and Wheeler, J. C. (2007). A Spitzer Space Telescope Study of SN 2003gd: Still No Direct Evidence that Core-Collapse Supernovae are Major Dust Factories. *ApJ*, 665:608–617.
- Meitner, L. (1922). Über die Entstehung der  $\beta$ -Strahl-Spektren radioaktiver Substanzen. *Zeitschrift für Physik*, 9:131–144.
- Messenger, S., Keller, L. P., and Lauretta, D. S. (2005). Supernova Olivine from Cometary Dust. *Science*, 309:737–741.
- Meurant, G. (1983). *Solid State Physics*. Number v. 37 in Solid State Physics. Elsevier Science.
- Mie, G. (1908). Beiträge zur Optik trüber Medien, speziell kolloidaler Metallösungen. *Annalen der Physik*, 330:377–445.
- Min, M., Dominik, C., Hovenier, J. W., de Koter, A., and Waters, L. B. F. M. (2006). The 10  $\mu\text{m}$  amorphous silicate feature of fractal aggregates and compact particles with complex shapes. *A&A*, 445:1005–1014.
- Min, M., Hovenier, J. W., Waters, L. B. F. M., and de Koter, A. (2008). The infrared emission spectra of compositionally inhomogeneous aggregates composed of irregularly shaped constituents. *A&A*, 489:135–141.
- Min, M., Waters, L. B. F. M., de Koter, A., Hovenier, J. W., Keller, L. P., and Markwick-Kemper, F. (2007). The shape and composition of interstellar silicate grains. *A&A*, 462:667–676.
- Molster, F. J., Waters, L. B. F. M., and Tielens, A. G. G. M. (2002a). Crystalline silicate dust around evolved stars. II. The crystalline silicate complexes. *A&A*, 382:222–240.
- Molster, F. J., Waters, L. B. F. M., Tielens, A. G. G. M., and Barlow, M. J. (2002b). Crystalline silicate dust around evolved stars. I. The sample stars. *A&A*, 382:184–221.

- Molster, F. J., Waters, L. B. F. M., Tielens, A. G. G. M., Koike, C., and Chihara, H. (2002c). Crystalline silicate dust around evolved stars. III. A correlations study of crystalline silicate features. *A&A*, 382:241–255.
- Mutschke, H., Min, M., and Tamanai, A. (2009). Laboratory-based grain-shape models for simulating dust infrared spectra. *A&A*, 504:875–882.
- Nittler, L., Alexander, C., Gao, X., Walker, R., and Zinner, E. (1997). Presolar  $\text{Al}_2\text{O}_3$  grains as probes of stellar nucleosynthesis and galactic chemical evolution. *Nuclear Physics A*, 621(1-2):113–116. Nuclei in the Cosmos.
- Nittler, L. R. (2005). Constraints on Heterogeneous Galactic Chemical Evolution from Meteoritic Stardust. *ApJ*, 618:281–296.
- Olofsson, J., Augereau, J.-C., van Dishoeck, E. F., Merín, B., Lahuis, F., Kessler-Silacci, J., Dullemond, C. P., Oliveira, I., Blake, G. A., Boogert, A. C. A., Brown, J. M., Evans, II, N. J., Geers, V., Knez, C., Monin, J.-L., and Pontoppidan, K. (2009). C2D Spitzer-IRS spectra of disks around T Tauri stars. IV. Crystalline silicates. *A&A*, 507:327–345.
- Olofsson, J., Juhász, A., Henning, T., Mutschke, H., Tamanai, A., Moór, A., and Ábrahám, P. (2012). Transient dust in warm debris disks. Detection of Fe-rich olivine grains. *A&A*, 542:A90.
- Ormel, C. W., Min, M., Tielens, A. G. G. M., Dominik, C., and Paszun, D. (2011). Dust coagulation and fragmentation in molecular clouds. II. The opacity of the dust aggregate size distribution. *A&A*, 532:A43.
- Ormel, C. W., Paszun, D., Dominik, C., and Tielens, A. G. G. M. (2009). Dust coagulation and fragmentation in molecular clouds. I. How collisions between dust aggregates alter the dust size distribution. *A&A*, 502:845–869.
- Ossenkopf, V., Henning, T., and Mathis, J. S. (1992). Constraints on cosmic silicates. *A&A*, 261:567–578.
- Pinto, C., Kaastra, J. S., Costantini, E., and de Vries, C. (2013). Interstellar medium composition through X-ray spectroscopy of low-mass X-ray binaries. *A&A*, 551:A25.
- Pinto, C., Kaastra, J. S., Costantini, E., and Verbunt, F. (2010). High-resolution X-ray spectroscopy of the interstellar medium. XMM-Newton observation of the LMXB GS 1826-238. *A&A*, 521:A79.
- Poe, B., Seifert, F., Sharp, T., and Wu, Z. (1997). ELNES spectroscopy of mixed Si coordination minerals. *Physics and Chemistry of Minerals*, 24(7):477–487.
- Posch, T., Kerschbaum, F., Mutschke, H., Dorschner, J., and Jäger, C. (2002). On the origin of the  $19.5 \mu\text{m}$  feature. Identifying circumstellar Mg-Fe-oxides. *A&A*, 393:L7–L10.
- Predehl, P. and Schmitt, J. H. M. M. (1995). X-raying the interstellar medium: ROSAT observations of dust scattering halos. *A&A*, 293:889–905.

- Rho, J., Kozasa, T., Reach, W. T., Smith, J. D., Rudnick, L., DeLaney, T., Ennis, J. A., Gomez, H., and Tappe, A. (2008). Freshly Formed Dust in the Cassiopeia A Supernova Remnant as Revealed by the Spitzer Space Telescope. *ApJ*, 673:271–282.
- Rho, J., Reach, W. T., Tappe, A., Hwang, U., Slavin, J. D., Kozasa, T., and Dunne, L. (2009). Spitzer Observations of the Young Core-Collapse Supernova Remnant 1E0102-72.3: Infrared Ejecta Emission and Dust Formation. *ApJ*, 700:579–596.
- Roche, P. F. and Aitken, D. K. (1984). An investigation of the interstellar extinction. I - Towards dusty WC Wolf-Rayet stars. *MNRAS*, 208:481–492.
- Roche, P. F. and Aitken, D. K. (1985). An investigation of the interstellar extinction. II - Towards the mid-infrared sources in the Galactic centre. *MNRAS*, 215:425–435.
- Savage, B. D. and Sembach, K. R. (1996). Interstellar Abundances from Absorption-Line Observations with the Hubble Space Telescope. *ARA&A*, 34:279–330.
- Smith, R. K., Dame, T. M., Costantini, E., and Predehl, P. (2006). The X-Ray Halo of GX 5-1. *ApJ*, 648:452–460.
- Spoon, H. W. W., Tielens, A. G. G. M., Armus, L., Sloan, G. C., Sargent, B., Cami, J., Charmandaris, V., Houck, J. R., and Soifer, B. T. (2006). The Detection of Crystalline Silicates in Ultraluminous Infrared Galaxies. *ApJ*, 638:759–765.
- Stern, E., Newville, M., Ravel, B., Yacoby, Y., and Haskel, D. (1995). The {UWXAFS} analysis package: philosophy and details. *Physica B: Condensed Matter*, 208-209:117–120. Proceedings of the 8th International Conference on X-ray Absorption Fine Structure.
- Tielens, A. G. G. M. (2008). Interstellar Polycyclic Aromatic Hydrocarbon Molecules. *ARA&A*, 46:289–337.
- Tielens, A. G. G. M., Wooden, D. H., Allamandola, L. J., Bregman, J., and Witteborn, F. C. (1996). The Infrared Spectrum of the Galactic Center and the Composition of Interstellar Dust. *ApJ*, 461:210.
- Trümper, J. (1982). The ROSAT mission. *Advances in Space Research*, 2:241–249.
- Ueda, Y., Mitsuda, K., Murakami, H., and Matsushita, K. (2005). Study of the Galactic Interstellar Medium from High-Resolution X-Ray Spectroscopy: X-Ray Absorption Fine Structure and Abundances of O, Mg, Si, S, and Fe. *ApJ*, 620:274–286.
- Valencic, L. A. and Smith, R. K. (2013). Interstellar Abundances toward X Per, Revisited. *ApJ*, 770:22.
- Van de Hulst, H. C. (1958). Buchbesprechungen über: Light scattering by small particles. (Ref. W. Franz). *ZAp*, 45:149.
- Voshchinnikov, N. V., Il'in, V. B., Henning, T., and Dubkova, D. N. (2006). Dust extinction and absorption: the challenge of porous grains. *A&A*, 445:167–177.

- Weingartner, J. C. and Draine, B. T. (2001). Dust Grain-Size Distributions and Extinction in the Milky Way, Large Magellanic Cloud, and Small Magellanic Cloud. *ApJ*, 548:296–309.
- Westphal, A. J., Stroud, R. M., Bechtel, H. A., Brenker, F. E., Butterworth, A. L., Flynn, G. J., Frank, D. R., Gainsforth, Z., Hillier, J. K., Postberg, F., Simionovici, A. S., Sterken, V. J., Nittler, L. R., Allen, C., Anderson, D., Ansari, A., Bajt, S., Bastien, R. K., Bassim, N., Bridges, J., Brownlee, D. E., Burchell, M., Burghammer, M., Changela, H., Cloetens, P., Davis, A. M., Doll, R., Floss, C., Grün, E., Heck, P. R., Hoppe, P., Hudson, B., Huth, J., Kearsley, A., King, A. J., Lai, B., Leitner, J., Lemelle, L., Leonard, A., Leroux, H., Lettieri, R., Marchant, W., Ogliore, R., Ong, W. J., Price, M. C., Sandford, S. A., Tresseras, J.-A. S., Schmitz, S., Schoonjans, T., Schreiber, K., Silversmit, G., Solé, V. A., Srama, R., Stadermann, F., Stephan, T., Stodolna, J., Sutton, S., Trieloff, M., Tsou, P., Tyliczszak, T., Vekemans, B., Vincze, L., Von Korff, J., Wordsworth, N., Zevin, D., Zolensky, M. E., and aff14 (2014). Evidence for interstellar origin of seven dust particles collected by the Stardust spacecraft. *Science*, 345:786–791.
- Whittet, D. C. B., editor (2003). *Dust in the galactic environment*.
- Whittet, D. C. B., Boogert, A. C. A., Gerakines, P. A., Schutte, W., Tielens, A. G. G. M., de Graauw, T., Prusti, T., van Dishoeck, E. F., Wesselius, P. R., and Wright, C. M. (1997). Infrared Spectroscopy of Dust in the Diffuse Interstellar Medium toward Cygnus OB2 No. 12. *ApJ*, 490:729–734.
- Wilms, J., Allen, A., and McCray, R. (2000). On the Absorption of X-Rays in the Interstellar Medium. *ApJ*, 542:914–924.
- Wiscombe, W. J. (1980). Improved Mie scattering algorithms. *Appl. Opt.*, 19:1505–1509.
- Wooden, D. H., Harker, D. E., Woodward, C. E., Butner, H. M., Koike, C., Witteborn, F. C., and McMurry, C. W. (1999). Silicate Mineralogy of the Dust in the Inner Coma of Comet C/1995 01 (Hale-Bopp) Pre- and Postperihelion. *ApJ*, 517:1034–1058.
- Wooden, D. H., Rank, D. M., Bregman, J. D., Witteborn, F. C., Tielens, A. G. G. M., Cohen, M., Pinto, P. A., and Axelrod, T. S. (1993). Airborne spectrophotometry of SN 1987A from 1.7 to 12.6 microns - Time history of the dust continuum and line emission. *ApJS*, 88:477–507.
- Xue, M., Jiang, B. W., Gao, J., Liu, J., Wang, S., and Li, A. (2016). A Precise Determination of the Mid-infrared Interstellar Extinction Law Based on the APOGEE Spectroscopic Survey. *ApJS*, 224:23.
- Yao, Y., Schulz, N., Wang, Q. D., and Nowak, M. (2006). Chandra Detection of Fe XVII in Absorption: Iron Abundance in the Hot Gaseous Interstellar Medium. *ApJ*, 653:L121–L124.
- Yao, Y. and Wang, Q. D. (2005). X-Ray Absorption Line Spectroscopy of the Galactic Hot Interstellar Medium. *ApJ*, 624:751–764.
- Zubko, V., Dwek, E., and Arendt, R. G. (2004). Interstellar Dust Models Consistent with Extinction, Emission, and Abundance Constraints. *ApJS*, 152:211–249.

# 3

## Dust absorption and scattering in the silicon K-edge

### Abstract

*Context* The composition and properties of interstellar silicate dust are not well understood. In the X-rays, interstellar dust can be studied in detail, by making use of the fine structure features in the Si K-edge. The features in the Si K-edge offer a range of possibilities to study silicon-bearing dust, such as investigating the crystallinity, abundance and the chemical composition along a given line of sight.

*Aims* We present newly acquired laboratory measurements of the silicon K-edge of several silicate-compounds which complement our measurements from our earlier pilot study. The resulting dust absorption profiles serve as templates for the interstellar absorption that we observe. The absorption profiles were used to model the interstellar dust in the dense environments of the Galaxy.

*Methods* The laboratory measurements, taken at the Soleil synchrotron facility in Paris, were adapted for astrophysical data analysis and implemented in the SPEX spectral fitting program. The models were used to fit the spectra of nine low-mass X-ray binaries located in the Galactic center neighborhood in order to determine the dust properties along those lines of sight.

*Results* Almost all lines of sight can be well fitted by amorphous olivine. We also established upper limits on the amount of crystalline material that the modeling allows. We find that iron-poor pyroxenes do not provide a good match to the data. We obtained values of the total silicon abundance, silicon dust abundance and depletion along each of the sightlines. We find a possible gradient of  $0.06 \pm 0.02$  dex/kpc for the total silicon abundance versus the Galactocentric distance. We do not find a relation between the depletion and the extinction along the line of sight.

### 3.1 Introduction

Silicates form an important and abundant component of the interstellar dust (Tielens, 2001). They are found at every evolutionary stage in the life cycle of stars, such as interstellar clouds, the circumstellar environment of oxygen rich Asymptotic Giant Branch (AGB) stars, protostellar disks, meteorites, comets, on Earth and on other planets (Henning, 2010). It is therefore crucial to understand the composition and properties of the silicate dust in order to make correct assumptions about each of the many processes in the universe in which the dust plays a role.

Observations of the gas abundances in interstellar environments have given an indication of the dust composition in the Galaxy. From observations of the Sun, nearby stars and the solar system it is known which elements are expected to be abundant in the ISM. However, certain elements are depleted from the cold gas phase and are assumed to be residing in dust particles (Draine, 2003). Here we define depletion as the ratio of the dust abundance to the total amount of a given element (i.e. both gas and dust). A large fraction of the abundant elements carbon, oxygen, silicon, iron and magnesium are thought to be depleted in dust (Jenkins, 2009; Savage and Sembach, 1996). These elements form the basic constituents of silicates, except for carbon which forms its own grain population of carbonaceous dust (Weingartner and Draine, 2001). However, the precise composition of interstellar silicates remains unknown. The bulk of the interstellar silicate dust is thought to consist of olivine and pyroxene types of dust, with iron and magnesium and smaller contributions of less abundant elements, such as calcium (Tielens, 2001). In addition there may be oxides (e.g. SiO, SiO<sub>2</sub>) present, since they are observed in stellar spectra (Posch et al., 2002; Henning et al., 1995), and silicon could also be present in small amount in the form of silicon carbide (SiC, Kemper et al., 2004; Min et al., 2007).

Much of our knowledge of interstellar silicates comes from the study of infrared absorption and emission features. In the infrared, silicates are mainly observed by using the Si-O bending and stretching modes at 10 and 20  $\mu\text{m}$ . Draine and Lee (1984) used synthetic optical functions in combination with the observational opacities of the 9.7  $\mu\text{m}$  feature to derive an average composition of the silicate dust (called astrosilicate), finding an olivine type with a composition of Mg<sub>1.1</sub>Fe<sub>0.9</sub>SiO<sub>4</sub> and in this way the silicate grains would incorporate 90%, 95%, 94% and 16% of the total Si, Mg, Fe and O, respectively. Nonetheless, interstellar silicates are expected to form a mixture of different silicate types, including olivine, but also, for example, pyroxene. Studies by Kemper et al. (2004), Chiar and Tielens (2006) and Min et al. (2007) compared laboratory spectra with observations and find that a combination of olivine and pyroxene dust models fit the 10  $\mu\text{m}$  feature, although they find varying contributions of olivine and pyroxene as well as for the iron to magnesium ratio.

An important property of the dust is the crystallinity, from which we can learn about the formation history of the dust. However, the formation process of crystalline dust is not well understood (Speck et al., 2011). We know, from observations of circumstellar dust, that evolved oxygen rich AGB stars produce silicate dust and that up to about 15% of this dust is in crystalline form. The dust is then subsequently injected in the ISM by stellar winds (Sylvester et al., 1999; Kemper et al., 2004). Crystalline dust is thought to be formed close to the star and is expected to be mostly magnesium rich. Further from the star the temperatures are lower and the silicates do not get the opportunity to crystallize (Molster et al., 2002). However,

this formation process of crystalline dust is not certain. Speck et al. (2015) found crystalline dust at the outer edge of the star HD 161796 and amorphous dust in the inner part of the dust shell. They propose that crystallization may happen when the dust encounters the ISM. Further away from dust forming stars, in the diffuse ISM, the smooth features of the  $\sim 10\ \mu\text{m}$  and  $\sim 20\ \mu\text{m}$  indicate that most of the interstellar dust appears amorphous. Only 1.1% of the dust along the lines of sight toward carbon-rich Wolf-Rayet stars near the center of the Galaxy appears to be crystalline (Kemper et al., 2004). From the mass budget of stellar dust sources the amount of crystalline dust in the ISM is expected from the to be  $\sim 5\%$  (Kemper et al., 2004), which suggests considerable re-processing of the dust in the ISM. Over time, the silicates may lose their crystalline structure in the violent environment of the ISM, where the dust is bombarded by radiation and cosmic rays on a timescale of  $\sim 70\ \text{Myr}$  (Bringa et al., 2007). These processes may be the cause of the amorphisation of crystalline dust in the ISM (Jäger et al., 2003, and references therein). Interestingly, silicates are again abundant in crystalline form in proto-planetary disks. The cores of some interstellar grains retrieved by the stardust mission, also show the presence of crystalline dust (Westphal et al., 2014), showing the possibility that at least some of the crystalline interstellar dust may survive in the ISM.

The soft X-ray part of the spectrum provides an alternative wavelength range for the study of interstellar dust (Draine, 2003; Lee et al., 2009; Costantini et al., 2012). X-ray binaries are used as a background source to observe the intervening gas and dust along the line of sight. In the spectra of these X-ray binaries, we can observe several absorption edges. Depending on the column density along the line of sight and the brightness of the source, it is possible to access the absorption edges of different elements. X-ray Absorption Fine Structures (XAFS) near the atomic absorption edges of elements can be used as a unique fingerprint of the dust along the line of sight toward the source. XAFS are observed in X-ray spectra of various astrophysical sources of *Chandra* and *XMM-Newton* (Lee et al., 2001; Ueda et al., 2005; Kaastra et al., 2009; de Vries and Costantini, 2009; Pinto et al., 2010, 2013; Costantini et al., 2012; Valencic and Smith, 2013; Zeegers et al., 2017, Chapter 2). These provide a powerful tool to study the composition, abundance, crystallinity, stoichiometry, and size of interstellar silicates (de Vries and Costantini, 2009, Chapter 2).

Interstellar dust may show slight variations in different environments. For example, from dense molecular clouds we know, that dust may incorporate a layer of ice around the grains, but also in less dense environments the dust may show variations in composition and properties. For instance, the abundances of several elements, show a decrease with distance from the Galactic center (Rolleston et al., 2000; Chen et al., 2003; Davies et al., 2009). The ISM is also known to be patchy and therefore may allow the observation of local differences in the chemistry along different lines of sight (Bohlin et al., 1978; Nittler, 2005). The X-rays provide the possibility to study dust in different environments. In this study, we focus on the silicon K-edge, which gives access to denser regions in the central part of the Galaxy.

In our pilot study, we showed the analysis of the silicon K-edge of GX 5-1 (Chapter 2). Here we expanded the number of sources we study to a total of nine. Furthermore, we expanded the set of silicate samples with respect to the previous study from six to fifteen. The sample set contains the interstellar dust analogues pyroxenes, olivines and silicon dioxide, that can be used to analyze interstellar silicate dust. These measurements are part of a larger laboratory measurement campaign (Costantini and de Vries, 2013).

The chapter is structured in the following way: In Section 3.2 we explain the analysis of

our laboratory data and the use of XAFS to investigate the composition of interstellar dust. In Section 3.3 we explain how we obtained the extinction cross-section and implemented them in the extinction profiles that can be used as interstellar dust models in an X-ray fitting code. In Section 3.4 we show the source selection, data and spectral analysis. In Section 3.5 we discuss the results and the chemistry of the dust toward the dense central area of the Galaxy. Lastly, in Section 3.6, we give a summary and our conclusion.

## 3.2 X-ray absorption edges

### 3.2.1 The samples

In this analysis, we make use of 14 different dust samples for which we measured the Si K-edges. The composition and structure of these dust samples are listed in Table 3.1, where the first five samples are the same as in Chapter 2. The additional samples, 6 to 14, were measured in January 2017 at the Soleil synchrotron facility in Paris.

There are several olivine- and pyroxene-type silicates among the samples, as well as different types of quartz. Although technically quartz types (samples 13-15) are oxides, we will refer to all the samples in the paper as silicates. Samples 2, 3, 5, 6, 7, 8, and 10 were synthesized for this analysis in laboratories at AIU Jena and Osaka University. In particular, the amorphous samples (2, 5, 7, 8 and 10) have been synthesized by quenching of a melt according to the procedure described by Dorschner et al. (1995). There are also synthesized crystalline samples in the sample set, such as fayalite (sample 9). The crystals of this sample have been grown by a method called the ‘scull method’ (Lingenberg, 1986). More details about samples 1-5 can be found in Zeegers et al. 2017 and more details about samples 6-15 can be found in Table 3.1.

The samples were all chosen because of their relevance as a possible component of the silicate dust in the ISM. We used the following criteria in the selection of this sample set:

- The sample set consists out of pyroxenes, olivines and oxides
- The silicate samples have different iron to magnesium ratios
- The samples contain both amorphous and crystalline silicates

The motivation of these selection criteria is based primarily on Draine and Lee (1984), who derived a general composition of ‘astronomical silicate’ based upon infrared emissivities inferred from observations of circumstellar and interstellar grains. The composition of this silicate is used as a starting point for the composition of the silicates in our sample set. The content of the sample set is then more refined by involving the results of detailed studies of the 9.7 and 18  $\mu\text{m}$  features in the infrared, which give an indication of the silicate dust composition. Since we expect amorphous silicates to be abundantly present (Kemper et al., 2004), the sample set contains seven amorphous samples of which six have a different composition, one olivine, two quartz types and four pyroxenes. From studies in the 8 – 13  $\mu\text{m}$  band it can be concluded that a mix of predominantly pyroxenes and olivines fit the observed spectra well (Kemper et al., 2004; Chiar and Tielens, 2006; Min et al., 2007). While Kemper et al. (2004) find that olivine dust dominates by mass in the ISM, Chiar and Tielens (2006) find that pyroxene dominates. Both pyroxenes and olivines are therefore well represented in

Table 3.1: Samples

No.	Name	Chemical formula	Structure
1	Olivine	$\text{Mg}_{1.56}\text{Fe}_{0.4}\text{Si}_{0.91}\text{O}_4$	crystal
2	Pyroxene	$\text{Mg}_{0.9}\text{Fe}_{0.1}\text{SiO}_3$	amorphous
3	Pyroxene	$\text{Mg}_{0.9}\text{Fe}_{0.1}\text{SiO}_3$	crystal
4	Enstatite	$\text{MgSiO}_3$	crystal*
5	Pyroxene	$\text{Mg}_{0.6}\text{Fe}_{0.4}\text{SiO}_3$	amorphous
6	Pyroxene	$\text{Mg}_{0.6}\text{Fe}_{0.4}\text{SiO}_3$	crystal
7	Olivine	$(\text{Mg}_{0.5}\text{Fe}_{0.5})_2\text{SiO}_4$	amorphous
8	Pyroxene	$\text{Mg}_{0.75}\text{Fe}_{0.25}\text{SiO}_3$	amorphous
9	Fayalite	$\text{Fe}_2\text{SiO}_4$	crystal
10	Enstatite	$\text{MgSiO}_3$	amorphous
11	Forsterite	$\text{Mg}_2\text{SiO}_4$	crystal
12	Quartz	$\text{SiO}_2$	crystal
13	Quartz	$\text{SiO}_2$	amorphous
14	Quartz	$\text{SiO}_2$	amorphous

\*Sample 4 contains a very small amount iron, which is not significant in our analysis. The Fe:Mg ratio is  $4 \times 10^{-2}$ . Sample 6 is a pyroxene and the crystalline counterpart of sample 5. Sample 7 is an amorphous olivine with equal contributions of iron and magnesium. Sample 8 is an amorphous pyroxene with an iron to magnesium ratio of 1:3. Sample 9, fayalite, was synthesized at the at the University of Frankfurt, Physical Institute (Fabian et al., 2001). Sample 10 is an amorphous enstatite, which was synthesized at AIU Jena. Sample 11, forsterite, is a commercial product from the company Alfa Aesar. Sample 12 is a natural rock crystal from Brazil (Zeidler et al., 2013). Sample 13, an amorphous silica, is a commercial product of company Qsil Ilmenau, Germany, named “ilmasil”. Sample 14, is a commercial amorphous silica powder supplied by the company Fisher Scientific. Sample 13 and 14 differ in degree of amorphisation as can be observed by the XAFS in the lower right panel of Figure 3.16 in Appendix 3.B.

our sample set. Furthermore, different values of the Mg/Fe ratio have been found in silicate dust in the ISM (Kemper et al., 2004; Min et al., 2007). In order to be able to investigate this ratio, we use dust samples with different iron to magnesium ratios. In the case of olivine type silicates we explore both extremes, namely fayalite and forsterite. Fayalite is the iron end-member of the olivine-group, whereas forsterite is the magnesium end-member. Our sample also contains an amorphous olivine with equal amounts of iron and magnesium.

### 3.2.2 Analysis of laboratory data

A self-evident method to measure the degree of absorption of a sample would be to measure the transmission of the radiation through the sample. This can be done by measuring the ratio of the intensity of the incoming beam to that of the transmitted beam. In order to appear optically thin at the energy around the Si K-edge, such a measurement would require a sample thickness of  $1.0 - 0.5 \mu\text{m}$ . It is impractical to perform measurements with such thin samples at X-ray energies. Therefore, the degree of absorption of the samples cannot be measured directly through transmission. Instead, the absorption is derived from the fluorescent measurements of the Si  $K\alpha$  line in our analysis of the Si K-edge. An overview of the theory behind this method can be found in Section 2.3.2 of Chapter 2.

The fluorescent measurements of the samples were performed at the SOLEIL synchrotron facility in Paris using the LUCIA beamline (Flank et al., 2006). The first run was completed and published in Chapter 2, the second run was completed in 2017 and presented in this chapter. All the samples were pulverised into a fine powder. This powder was then pressed into a layer of indium, which was stuck on a copper sample plate. The sample plate was placed in the X-ray beam in a vacuum environment. The reflecting fluorescent signal was measured by a silicon drift diode detector. Each sample was measured at two different positions on the sample plate and for each position the measurement was repeated once, resulting in a total of four measurements per sample. The change in position is necessary to avoid any dependence of the measurement on the position of the sample on the copper plate. We took the average of the resulting four measurements. In order to obtain the noise in the measurements, we determined the dispersion among the measurements. We found a small dispersion of 5% among the measurements. This is slightly higher than in our previous sample set of Chapter 2, but still considered negligible. After the measurements have been obtained they need to be corrected for two effects, namely pile-up and for saturation. Pile-up occurs when two photons hit the detector at once and are recorded as one event with double the energy. This effect can be seen in the spectrum as a spurious line appearing at twice the expected energy. This effect is, however, minimal ( $< 1\%$ ). Saturation occurs because the measured fluorescent signal is not directly proportional to the absorption. The effect of saturation becomes important when a sample is concentrated, which is the case here (de Groot, 2012). We use the program FLUO to correct for saturation when needed (Stern et al., 1995). More details can be found in Chapter 2, since here we follow the same correction procedure. We note that a crystalline pyroxene was omitted from our sample set, which is present in Chapter 2 and indicated there as sample 6. The correction is on average three times larger than in the other samples, which indicates that the sample could be overcorrected after the application of FLUO. The overcorrection may be the result of a mismatch between the given composition and the measured compound, although this may not necessarily be the case (Ravel and Newville, 2005). However, since the cause of the large correction could not be retrieved in this case, the sample was removed from sample set.

### 3.2.3 X-ray Absorption Fine Structures

XAFS are modulations that arise when an X-ray photon excites a core electron in an atom. These modulations are a fingerprint of the type of dust and can therefore be used to discriminate between different types of dust in the ISM. XAFS arise from the wave-like nature of the photoelectric state. When a core electron is excited by an incoming X-ray with the right energy, the ionized electron will then behave like a photoelectron. This can be interpreted as a wave emanating from the site of the absorbing atom. Depending on the available energy, the photoelectron can scatter around the neighboring atoms. Due to this interaction, the initial wave is scattered and new waves emanate from the neighboring atoms. These waves are superimposed on the original wave creating interference. This subsequently changes the probability of the photoelectric effect. We observe the constructive and destructive interference in the edge as a function of energy, i.e. the XAFS. Depending on the elements and the position of the neighboring atoms, the XAFS are modified in a unique way, reflecting the crystallinity and chemical composition of the material.

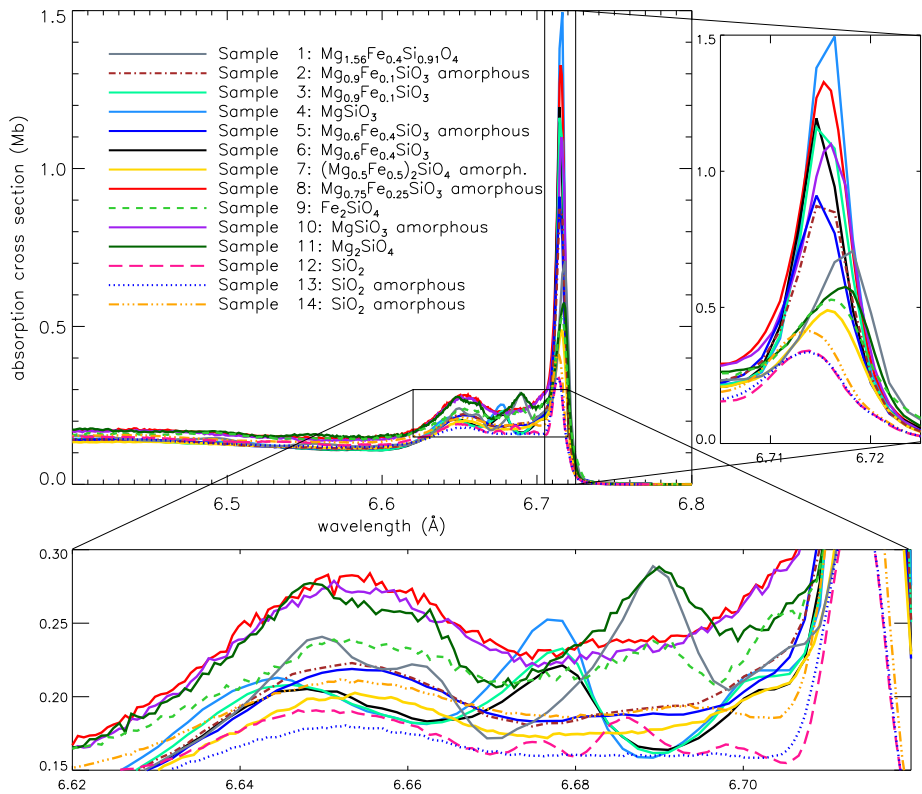


**Figure 3.1:** The Si K-edge of dust samples 1-14 (samples 1-5 are also shown in Chapter 2). The x-axis shows the energy in Å and the y-axis shows the amount of absorption indicated by the cross-section (in Mb per Si atom).

The resulting absorption cross-sections can be found in Figure 3.1. We highlight the XAFS in the left inset panel. Samples 2, 5, 7, 8, 10, 13 and 14 are amorphous. Since these amorphous samples do not have a regular crystalline structure, they lose the distinct signature which is present in their crystalline counterparts. This effect can be observed in Figure 3.1 between 6.67 and 6.70 Å. The XAFS of amorphous materials are very similar in shape, as can be observed by comparing sample 7, 8 and 10. It is therefore difficult to distinguish an amorphous pyroxene and an amorphous olivine. The differences between these edges will then also depend on slight shifts in the ionisation energy and the peak intensity at this energy. This is shown by the inset panel on the right of Figure 3.1. In the case of sample 12, 13 and 14 we can compare three samples of which the composition is the same, but the crystallinity varies. It can be observed that the resulting absorption cross-sections of quartz are very similar since the composition does not change between the samples, but that the crystalline sample shows features between 6.67 and 6.70 Å. Distinct differences can be observed in the case of the crystalline pyroxene of sample 7 and forsterite (sample 12) around 6.66 and 6.70 Å, illustrating the difference between crystalline pyroxene-type silicates and crystalline olivine-type silicates. The effect of the varying iron content of the samples is subtler and shows itself by shifts in the peak of the XAFS (e.g. samples 9 and 11). Furthermore, the samples can also be characterized by the peak strength of the edge between 6.71 and 6.72 Å and the energy position of this peak.

### 3.3 Extinction cross sections

The extinction cross-sections for each of the samples can be derived from the laboratory data. In this section, we will give a summary of the methods that are used to derive the cross-sections. For a full description about the calculation of the extinction cross-section we refer to Chapter 2. From the laboratory data, we obtain the attenuation coefficient ( $\alpha$ ). The Beer-Lambert law can be used to derive  $\alpha$ :

$$T = \frac{I}{I_0} = e^{-\alpha x} = e^{-x/l}. \quad (3.1)$$

Here  $T$  is the transmittance, which can be obtained by assuming an optically thin sample thickness  $x$  and by using tabulated values of the mean free path  $l$  (e.g., the average distance travelled by a photon before it is absorbed), provided by the Center for X-ray Optics (CXRO) at Lawrence Berkeley National laboratory. The laboratory absorption edges were transformed into transmission spectra and fitted to the transmittance  $T$  obtained from tabulated transmission data, as well provided by CXRO. Consequently, from  $\alpha$  the imaginary part of the refractive index  $k$  can be derived, since the attenuation coefficient can be described as:

$$\alpha = \frac{4\pi k}{\lambda}, \quad (3.2)$$

where  $\lambda$  is the wavelength. The real part of the refractive index is then calculated by using a numerical solution to the Kramers-Kronig relations (Bohren, 2010). The method used for this calculation is the same as in Chapter 2, namely the fast Fourier transform routines (FFT) as described in Bruzzoni et al. (2002). We use Mie theory (Mie, 1908) to calculate the extinction efficiency at each wavelength and grain size. The grain size distribution used in this analysis is

the MRN distribution, with a grain size range of  $0.005 - 0.25 \mu\text{m}$ . The grains are modelled as solid spheres. The MIEVO code (Wiscombe, 1980) was used to calculate the extinction efficiency, which needs the optical constants, wavelength and grain size as input parameters. From the obtained extinction efficiency we calculate the extinction cross-sections. These extinction cross-section are implemented in the AMOL model of the fitting code SPEX (Kaastra et al., 1996), where they are used for further analysis. Figure 3.15 shows the resulting extinction profiles of each of the dust models. The absolute cross-section are available in tabular form<sup>1</sup>.

## 3.4 Data analysis of the LMXB

### 3.4.1 Source selection

We selected nine low mass X-ray binary sources for our analysis from the *Chandra* Transmission Gratings Catalog and Archive<sup>2</sup>. The selection depends on the brightness of the source and the hydrogen column density  $N_{\text{H}}$  towards the source. In order to have the best view of the silicon K-edge, the column density of the source should be between  $10^{22}$  and  $10^{23} \text{cm}^{-2}$ . It is furthermore important that the source is bright in order to observe the edge with a high signal to noise. The flux level needs to be  $> 0.5 \times 10^{-12} \text{erg cm}^{-2}\text{s}^{-1}$  at energies between 0.5–2 keV. The source should preferably not strongly fluctuate in brightness, since this will affect the quality of the edge in the spectrum. We therefore inspected the light curves for strong dips in the brightness. We did not find this to be a problem in any of the selected sources. Sources with the desired column density lie preferentially around the Galactic Center (GC) area (Table 3.2).

Another more practical selection criterion is that the source has to be observed in TE mode. The ACIS detectors on-board *Chandra* can operate in different observing modes, namely continues clocking (CC) mode and timed exposure (TE) mode. The CC mode is not suitable for measurements of the Si K-edge since the edge is filled by the bright scattering halo radiation of the source. The edge has a different optical depth in comparison with the TE mode and seems slightly smeared. The effect of the scattering halo is particularly evident in the CC mode because the two arms of the mode are now compressed into one. An overview of the sources that are used in this study is given in Table 3.2. Here we also indicate the OBSIDs of the spectra of the sources, the distance and the Galactic coordinates.

### 3.4.2 Modeling procedure

After the selection of the sources as described in the previous section, we inspected the spectra for pile-up. Pile-up occurs when two or more photons are detected as one single event and therefore occurs often in the spectra of bright sources, such as the X-ray binaries used in this work. Both gratings (HEG and MEG) are affected, but the effect is especially evident in the MEG grating. The parts of the spectra of the MEG grating that were too affected by pile-up were ignored. This was done in the case of all the X-ray binaries, but the ignored range varies per source. This is described for each individual source in Appendix 3.A. Before we can

<sup>1</sup> [www.sron.nl/~elisa/VIDI/](http://www.sron.nl/~elisa/VIDI/)

<sup>2</sup> <http://tgcatalog.mit.edu/>

Table 3.2: Sources

Name	obsid(s)	distance	coordinates	
		kpc	$l$ (deg)	$b$ (deg)
GX 5-1	19449, 20119	$9.2^1$	5.08	-1.02
GX 13+1	11814, 11815, 11816, 11817	$7 \pm 1^2$	13.52	+0.11
GX 340+00	1921, 18085, 19450, 20099	$11 \pm 0.3^3$	339.59	-0.08
GX 17+2	11088	$12.6^4$	16.43	+1.28
4U 1705-44	5500, 18086, 19451, 20082	$7.6 \pm 0.3^5$	343.32	-2.34
4U 1630-47	13714, 13715, 13716, 13717	$10^6$	336.91	+0.25
4U 1728-34	2748	$5.2 \pm 0.5^7$	354.30	-0.15
4U 1702-429	11045	$7^8$	343.89	-1.32
GRS 1758-258	2429, 2750	$8.5^9$	4.51	-1.36

All observations were done in TE mode. Christian and Swank (1997)<sup>1</sup> Bandyopadhyay et al. (1999)<sup>2</sup> Christian and Swank (1997)<sup>3</sup> Lin et al. (2012)<sup>4</sup> Galloway et al. (2008)<sup>5</sup> Parmar et al. (1986); Augusteijn et al. (2001)<sup>6</sup> Galloway et al. (2008)<sup>7</sup> Oosterbroek et al. (1991)<sup>8</sup> Keck et al. (2001)<sup>9</sup>

study the interstellar dust, we first have to model the underlying continuum of each source and inspect the spectra for the presence of outflowing ionized gas and hot gas present along the line of sight, as described in Sections 3.4.2.1 and 3.4.2.2.

### 3.4.2.1 Continuum and neutral absorption

The underlying continuum of each source is fitted using the spectral analysis code SPEX. We tested several additive SPEX models in our analysis, namely blackbody, disk-blackbody, power law and Comptonisation models. The X-ray radiation from the source is then absorbed by a neutral absorber. This model is represented by the multiplicative HOT model in SPEX. In order to mimic a neutral cold gas, the temperature of this gas is frozen to a value of  $kT = 5 \times 10^{-4}$  keV. After obtaining a best fit for the continuum with absorption of neutral cold gas we are able to determine the column density of hydrogen toward the source.

We will use GX 5-1 as an example to explain our method of fitting the sources. The results of the best fits of the other X-rays binaries and the details of the fitting method used in each case can be found in Appendix 3.A. Two spectra were used in the fit of GX 5-1, with obsids 19449 and 20119. These observations have an excellent signal-to-noise ratio, in the case of obsid 19449 this is around the Si K-edge  $S/N \approx 100$  per bin and for obsid 20119  $S/N \approx 60$  per bin. The MEG grating shows signs of pile up in both data sets above an energy of 2.5 keV and the data was therefore ignored above this value of the energy. Since the Silicon K-edge starts around 1.84 keV the MEG data is included in the analysis of the edge. This is the case for every X-ray binary in our analysis. We used a Comptonisation model and a disk-blackbody model to describe the underlying continuum of GX 5-1. We found a column density of  $5.8 \pm 0.2 \times 10^{22} \text{cm}^{-2}$ . The broadband fit of GX 5-1 is shown in Figure 3.2. For clarity, the data displayed in this figure belongs to obsid 19449, since this dataset dominates the fitting of the spectrum due to its superior quality. The fit already includes the dust model of which the details are described in Section 3.4.2.3. The parameter values of the best fit of

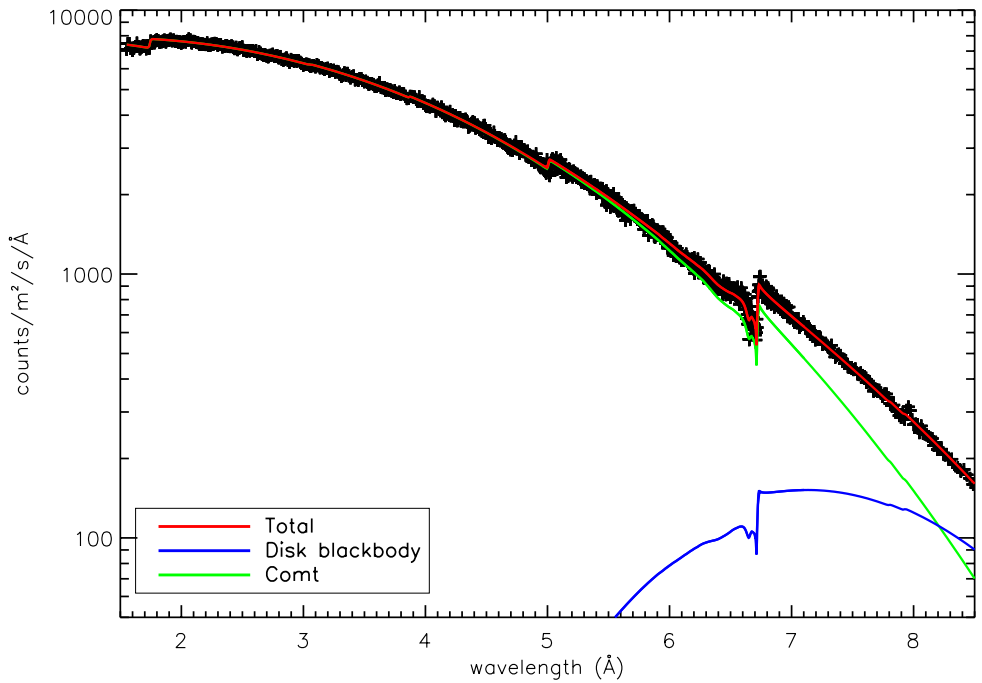


Figure 3.2: Broad band fit of GX 5-1 with the data of obsid 19449 with the disk blackbody model indicated by the blue line and the green line indicates the Comptonisation model. The red line shows the total fit. The AMOL dust models are included in the fit.

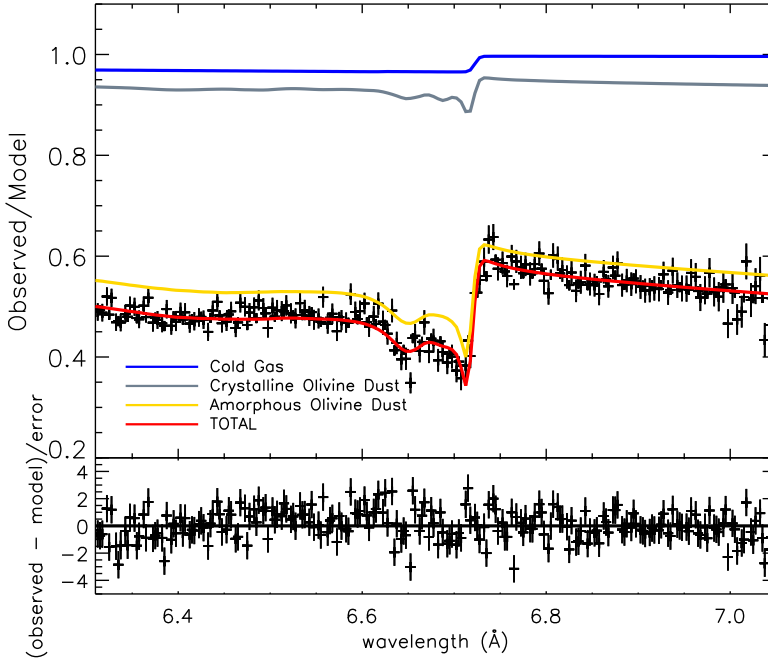


Figure 3.3: Fit of the Si K-edge of X-ray binary GX 5-1. The best fitting dust mixture is shown by the yellow line (amorphous olivine, sample 8) and the grey line (crystalline olivine dust, sample 1). The cold gas contribution is shown by the blue line and the total, cold gas and dust, by the red line.

GX 5-1 can be found in Table 3.5. Errors given on parameters are 1 sigma errors, which is the case for all errors shown in this analysis.

#### 3.4.2.2 Hot ionized gas on the line of sight in the Si K-edge region?

We tested whether there was hot gas along the line of sight towards the sources (fitted in the spectra using again the HOT model, which has a tuneable temperature), as well as outflowing ionized gas related to the source (fitted in the spectra using the XABS model of SPEX). If absorption lines of this gas appear near the edge, it is important to take these lines into account for accurate modeling.

We found outflowing gas from the source in two cases, namely for GX 13+1 and 4U 1630-47. These sources show strong absorption lines in their spectra. In the case of GX 13+1, a second, but non-outflowing, ionized gas component was also found (Table 3.7).

Collisionally ionized hot absorbing gas in the ISM is thought to have temperatures between  $\sim 10^6 - 10^7$  K (Yao and Wang, 2007; Wang, 2009; Wang et al., 2013). For GRS 1758-258, GX 17+2 and 4U 1705-44 a hot component was found with temperatures within

the range mentioned, namely  $1.5^{+0.6}_{-0.3} \times 10^7$  K,  $1.6 \pm 0.2 \times 10^6$  K and  $2.1^{+0.9}_{-0.6} \times 10^6$  K, respectively. The hydrogen column density of the gas is for all sources of the order of  $10^{20}$  cm<sup>-2</sup>, (Table 3.9), which is in correspondence with the typical expected hydrogen column densities of such a gas (Yao and Wang, 2005; Yao et al., 2006; Yao and Wang, 2007). We did not find evidence for outflowing ionized gas along the line of sight of GX 5-1 and neither did we find any contribution of hot gas. This is also the case for 4U 1702-429, 4U 1728-34 and GX 340+00. The values of the parameters of the HOT and the XABS model can be found in the tables with the best fits of the sources in Appendix 3.A.

### 3.4.2.3 Dust Mixtures and the SPEX AMOL model

After obtaining the underlying continuum and the column density of hydrogen towards the source, we proceed by adding the dust model to the fit. We also take into account the presence of hot and outflowing ionized gas along the line of sight as mentioned in Section 3.4.3. The AMOL routine in SPEX is used to fit the dust models to the data. AMOL can fit four dust models simultaneously. We want to test all possible unique combinations of the 14 dust models. To execute these fits, we follow the method of Costantini et al. (2012), namely the total number of fits ( $n$ ) is given by  $n = n_{\text{dust}}! / (4!(n_{\text{dust}} - 4)!)$  and where  $n_{\text{dust}}$  is the number of available dust models and 4 is the number of models that can be tested in the same run. This results in 1001 possible unique combinations to fit the 14 dust models.

From all these combinations, we can select the best fitting mixture. Of each possible dust mixture, we determined the reduced  $C^2$  values. All the fits in this chapter generated by SPEX are using C-statistics (Cash, 1979) as an alternative to  $\chi^2$ -statistics. C-statistics may be used regardless of the number of counts per bin, therefore we can use bins with a low count rate in the spectral fitting. The best fit is given by the lowest reduced  $C^2$  value (Kaastra, 2017). As an example, we show the resulting best fit of GX 5-1 in Figure 3.3. Here we show the contribution of cold gas, and the two best fitting dust samples in the mixture: sample 1 crystalline olivine contributing 11% and sample 7 amorphous olivine contributing 89% to the total column density of silicon in dust. The other two samples in the mix do not contribute significantly. The best fits of the sources in our sample are described in Section 3.5.

In Figure 3.4 the best fitting dust mixtures of all nine X-ray binaries considered here are indicated by the green bars. On the x-axis we show the numbers belonging to each dust sample, which can be retrieved from Table 3.1. The y-axis indicates the relative contribution of each of the dust sample in the fit with respect to the dust column density of silicon. The best fits represent one of the 1001 possible dust mixtures per source and it is useful to take the performance of the other dust mixtures into account before discussing the results. Therefore, an insightful way to study whether a certain dust mixture fits the edge well, is by showing how much a dust mixture deviates from the best fitting mixture. Each dust mixture is represented in Figure 3.4 by four colored filled circles, i.e. the number of dust samples per fit. The position of the filled circles on the y axis shows the contribution of the dust sample to the fit. For each of the 1001 dust mixtures a set of four filled circles is plotted. The colors of the filled circles correspond with the one, two and three sigma deviations from the best fit, as shown in the legend of Figure 3.4.

In the ideal case, the dust samples that correspond with the best fit, will also be represented in the results of similar dust mixtures. In the case of GX 5-1 for instance, the best fit consists

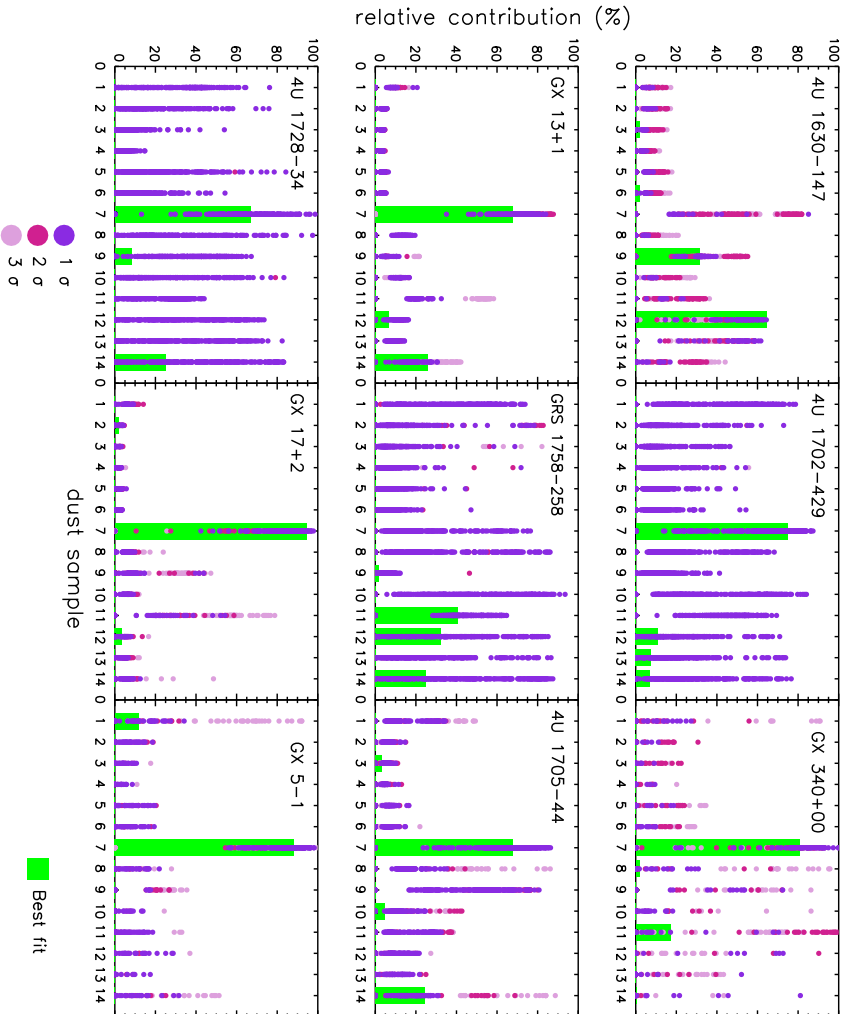


Figure 3.4: The figure shows best fitting dust mixtures in comparison with other possible dust mixtures. In green the relative contribution of each of the dust components in the best fit is shown. The other dust mixtures are represented by the colored dots. The colors indicate the 1, 2 and 3 sigma deviations from the best fitting dust mixture. Per fit 4 dust samples are fitted to the spectra of the X-ray binaries.

Table 3.3: Abundances and depletions of Silicon

Source	$N_{\text{Si}}^{\text{tot}}$ ( $10^{18} \text{ cm}^{-2}$ )	depletion	$A_{\text{Si}}$ ( $10^{-5} \text{ H atom}^{-1}$ )	$A_{\text{Si}}^{\text{dust}}$ ( $10^{-5} \text{ H atom}^{-1}$ )	$A_{\text{Si}}/A_{\odot}$
GX 5-1	$1.7 \pm 0.2$	$0.89 \pm 0.05$	$2.9 \pm 0.2$	$2.5 \pm 0.2$	$0.8^{+0.2}_{-0.1}$
GX 13+1	$1.4 \pm 0.2$	$0.94 \pm 0.02$	$4.6 \pm 0.7$	$4.4 \pm 0.7$	$1.2 \pm 0.2$
GX 340+00	$2.9 \pm 0.6$	$0.77 \pm 0.10$	$4.5 \pm 0.9$	$3.6 \pm 0.9$	$1.2^{+0.2}_{-0.3}$
GX 17+2	$1.1 \pm 0.2$	$0.95 \pm 0.03$	$5.2 \pm 0.4$	$5.1 \pm 0.4$	$1.3 \pm 0.1$
4U 1705-44	$0.9 \pm 0.2$	$0.91 \pm 0.05$	$4.3 \pm 1.1$	$4.0 \pm 1.1$	$1.1 \pm 0.3$
4U 1630-47	$4.8 \pm 1.3$	$0.76^{+0.23}_{-0.28}$	$4.9 \pm 1.3$	$4.5 \pm 1.3$	$1.3 \pm 0.4$
4U 1728-34	$1.4 \pm 0.4$	$0.95^{+0.02}_{-0.10}$	$4.1 \pm 1.4$	$3.9 \pm 1.4$	$1.1 \pm 0.4$
4U 1702-429	$0.7 \pm 0.3$	$0.93 \pm 0.15$	$3.2 \pm 1.5$	$3.0 \pm 1.5$	$0.8 \pm 0.4$
GRS 1758-258	$1.0 \pm 0.4$	$0.75 \pm 0.2$	$3.9 \pm 1.5$	$2.9 \pm 1.5$	$1.0 \pm 0.4$
average	$1.8 \pm 0.2$	$0.87 \pm 0.04$	$4.0 \pm 0.4$	$3.8 \pm 0.4$	$1.1 \pm 0.1$

Abundances are indicated by  $A_{\text{Si}}$ . Solar abundances are taken from Lodders and Palme (2009).  $N_{\text{Si}}^{\text{tot}}$  indicates the total column density of silicon (gas and dust).

of two dust samples, leaving two options open, which in the case of the best fit does not contribute significantly. This means that out of the 1001 possibilities, there are 91 similar mixtures as can be seen in Figure 3.4 by the dominant selection of samples 1 and 7. In the case that the best fit is unique we expect a clustering of the similar mixtures around the best fit. This effect can be observed in the frame of GX 13+1 in Figure 3.4 for sample 7 and in lesser degree in GX 5-1 for sample 1 and 7.

If the data are of good quality (i.e. high signal to noise), which is the case for six out of the nine X-ray binaries, it becomes possible to observe a preference in the fits for certain dust samples. This is especially evident in GX 5-1, GX 17+2 and GX 13+1. When the quality of the data declines, it allows almost every type of dust to be fitted equally well. This effect can be observed in the observations of 4U 1702-49, GRS 1758-258 and 4U 1728-34. Therefore, we will not use these sources in the discussion of the dust composition. The implications of Figure 3.4 will be discussed in Section 3.5.1.

### 3.4.3 Silicon abundances and depletion

The silicon K-edge allows the possibility of evaluating silicon in both gas and dust simultaneously. Consequently, this allows a study of the abundance and depletion of silicon on the nine different lines of sight towards the X-ray binaries. Table 3.3 gives the silicon column density ( $N^{\text{tot}}$ ), depletion, total silicon abundance ( $A_{\text{Si}}$ ), abundance of silicon in dust ( $A_{\text{Si}}^{\text{dust}}$ ). Finally,  $A_{\text{Si}}/A_{\odot}$  shows the deviation from the solar abundance of silicon. The allowed depletion ranges used in the fits are based upon values from Jenkins (2009). The ranges of are given in Table 3.4. Since we fit only one edge using dust models, we need to constrain the other elements within reasonable boundaries. For the edges, for which we do not have dust features, we use gas absorption-like profiles in the SPEX model.

Table 3.4: Depletion ranges used in the spectral fitting

Element	depletion range
Silicon	0.41 – 0.96
Iron	0.7 – 0.97
Magnesium	0.47 – 0.95
Oxygen	0.02 – 0.42

Depletion ranges in this table are based on depletion values from Jenkins (2009).

## 3.5 Discussion

### 3.5.1 Dust composition toward the Galactic Center

The results of the fits of the nine X-ray binaries are summarized in Figure 3.4. Since this figure contains information about the crystallinity, the mineralogy, and the ratio between iron and magnesium, we discuss each of the properties of the dust separately. We will also put emphasis on the results of the fits of GX 5-1, GX 13+1 and GX 17+2, since for these sources the quality of the data in terms of signal-to-noise around the Si K-edge is the best with respect to the other sources.

#### 3.5.1.1 Crystallinity

From the fits of all the X-ray binaries we observe that crystalline dust models can be fitted to the Si K-edge. We calculate the ratio of crystalline versus amorphous dust ( $\zeta_1$ ). The ratio here is defined as:  $\zeta_1 = \text{crystalline dust} / (\text{crystalline dust} + \text{amorphous dust})$ . Examining the best fitting dust mixture of GX 5-1, we find a value of:  $\zeta_1 = 0.12$  and when considering the errors we find an upper limit of on the crystallinity of  $\zeta_1 < 0.29$ . GX 13+1 can be analysed in the same way. The obtained ratio of  $\zeta_1$  is here:  $\zeta_1 = 0.07$  and an upper limit of  $\zeta_1 < 0.35$ . For GX 17+2 we find the lowest crystallinity:  $\zeta_1 = 0.04$  and an upper limit of  $\zeta_1 < 0.17$ . The other sources in the analysis - focussing on 4U 1630-47, GX 340+00 and 4U 1705-44 - show a similar result, although the errors on the dust measurements increase because of the data quality.

As seen above, despite the errors the X-ray binaries with the best signal to noise are best fitted by a mixture of mainly amorphous dust and a contribution of crystalline dust which varies between  $\zeta_1 = 0.04 - 0.12$ . These amounts of crystalline dust are large in comparison with results from the infrared (Section 3.1). An explanation may be found in that we are observing special lines of sight with freshly produced crystalline dust grains that have not fully been amorphized by the processes in the ISM. This result may be in line with the results from the Stardust mission (Westphal et al., 2014), where some of the interstellar silicate dust particles were detected with a crystalline core. However, it is unclear why the X-ray lines of sight towards the central Galactic environment would systematically sample a different environment than the infrared lines of sight.

An alternative explanation for this apparent discrepancy can be found in the different methods used to study the silicate dust. XAFS, especially the features close to the edge, are

sensitive to short range order, whereas, in the infrared, observation are focussed on long range disorder in the dust particles.

There are multiple processes to form crystalline and amorphous dust (e.g., Dorschner et al., 1995; Jäger et al., 2003; Speck et al., 2011). The different techniques used in the laboratory to synthesize amorphous dust show that some of these samples are glassy, others are porous and some samples are not homogeneously amorphous, but show the onsets of crystallisation. All of these samples produce amorphous infrared dust features, albeit with differences in the peak position of the 10 and 18  $\mu\text{m}$  features (Speck et al., 2011). Furthermore, a polycrystalline material can also smear the dust features (Marra et al., 2011) in the infrared and we may thus not perceive sharp crystalline features in the spectrum (Speck et al., 2011). However, the short range crystalline structure between the atoms in a polycrystal are still intact and XAFS may appear in the spectrum. Specifically, even if the material becomes slightly amorphous or glassy, XAFS may still appear in the X-ray spectrum, but are less pronounced and tend to shift with energy when the material becomes more and more disordered (Mastelaro and Zanotto, 2018). Therefore, what may be perceived as amorphous dust in the infrared, can still be observed as crystalline dust in the X-rays. More laboratory research is necessary to make a complete comparison between the crystalline and amorphous dust characteristics in the infrared and the X-rays. On the other hand, high quality astronomical spectra are necessary to put firmer limits on the amount of crystalline dust observed in the spectra of X-ray binaries.

### 3.5.1.2 Iron in silicates

Our sample set contains olivines and pyroxenes with different iron and magnesium content. Already from the laboratory data it can be observed that the influence of a changing iron content of the dust invokes only small differences in the XAFS (Figure 3.1). Small shifts in the peaks can be observed in the laboratory data, but in view of the resolution of the *Chandra* spectra, these subtle changes will not be detected in the spectra. We note that the samples 2, 3, 4, 5 and 6 almost never contribute to the best fit. What these samples have in common is that all of them are iron-poor pyroxenes. Therefore, the reason that these samples do not fit the edge is twofold and the structure of the dust is of greater influence here than the iron content, since the structural differences in the crystal-types can be distinguished in the models. Iron is highly depleted in the ISM and is expected to reside in dust particles. Silicates may provide a possibility to store some of the iron in dust. However, even if our fits prefer slightly more iron-rich silicates, not all the iron that should be present in the ISM is accounted for. The missing iron can be present in other forms of dust. A possibility could be that iron is included in metallic form in GEMS (Bradley, 1994) or in iron nanoparticles (Bilalbegović et al., 2017). Our sample set currently contains pyroxene samples with a ratio of  $\text{Mg}/(\text{Fe}+\text{Mg})=0.6$ . This is very similar to e.g. Kemper et al. (2004) ( $\text{Mg}/(\text{Fe}+\text{Mg})=0.5$ ). Previous studies do not show a strong evidence that this ratio should be much lower. Further constraints on the iron content would be provided by a multiple-edge fitting. The magnesium K-edge and the iron K-edge will give a direct impression of magnesium and iron in dust. Depending on the brightness of the source, the column density along the line of sight and the telescope and instruments that are used, it is possible to observe these edges. In the case of the Fe K-edge, the current instruments are not sensitive enough around the edge to detect the XAFS, but the future observatory, *Athena*, will be able to observe the Fe K-edge in detail (Rogantini et al., 2018).

### 3.5.1.3 Olivines, pyroxenes and oxides

Where the difference between iron rich and iron-poor dust models in the laboratory data is subtle, the difference between olivines, pyroxenes and quartz types in crystalline form is striking. This means that it is easier to identify differences in the mineralogy. In general, we observe that in almost all of the X-ray binaries, the best fitting dust mixture includes an olivine dust type (whether amorphous or crystalline), but not all the data have similar signal to noise. The three X-ray binaries with the best signal-to-noise, namely GX 5-1, GX 17+2 and GX 13+1, show both in the best fit as in the fits within 1 sigma a preference for amorphous olivine. The ratio of olivine to pyroxene can be expressed as  $\zeta_2 = \text{olivine}/(\text{pyroxene} + \text{olivine})$ . For GX 5-1, GX 17+2 and GX 13+1  $\zeta_2 = 1$  in case of the best fits. However, within 1 sigma from the best fitting dust mixtures, it is possible to obtain lower values of  $\zeta_2$  with a minimum of  $\zeta_2 = 0.8$ , meaning that we can obtain a good fit with a maximum of 20% pyroxene in the dust mix.

Thus, in the central Galactic environment we do not find much variation in the best fitting dust mixture. We compare this result with studies of silicates in the infrared. By analyzing the  $10\ \mu\text{m}$  silicate feature, Kemper et al. (2004) also find that olivine glasses account for most of the silicate mass in the diffuse ISM along the line of sight toward the GC. However, in the infrared, variations in the stoichiometry of the dust have been found along different lines of sight. Fitting both the  $10\ \mu\text{m}$  and  $18\ \mu\text{m}$  silicate features of Wolf-Rayet stars representing both the local ISM and the GC, Chiar and Tielens (2006) find that a mix of olivine and pyroxene silicates produce a good match to their data, and that a greater contribution by mass of pyroxene dust is required. Observing the same line of sight as Kemper et al. (2004), Min et al. (2007) find a stoichiometry of the silicate dust that lies in between that of olivine and pyroxene. In future X-ray studies, it is therefore interesting to investigate samples with a stoichiometry in between that of olivine and pyroxene.

The role of  $\text{SiO}_2$  dust in the ISM is not well known. This type of dust may form in the ISM and may be present in the form of  $\text{SiO}_2$  nanoparticles, although there is limited insight of how these dust particles may form and they have not been detected in the ISM (Li and Draine, 2002; Krasnokutski et al., 2014). The presence of  $\text{SiO}_2$  may be supportive of the formation of grains in the interstellar medium (Krasnokutski et al., 2014, and references therein). The three  $\text{SiO}_2$  samples in our sample set, can be fitted within one sigma of the best fit, most notably in 4U 1630-47. Considering the overall contribution of  $\text{SiO}_2$  in the fits of GX 13+1, GX 5-1 and GX 17+2, we do not find evidence for  $\text{SiO}_2$  to be dominant component in interstellar dust.

## 3.5.2 Silicon abundances and depletion

The results from Table 3.3 allow us to study the dense environment in the Galactic plane and in the vicinity of the GC. The abundance of silicon can be derived from infrared data, using observations of the  $10$  and  $18\ \mu\text{m}$  features (Aitken and Roche, 1984; Roche and Aitken, 1985; Tielens et al., 1996). In the local solar environment the silicon abundance in dust can be derived to be  $5.2 \pm 1.8 \times 10^{-5}$  per H-atom, using data from Roche and Aitken (1984); Tielens et al. (1996) who observed nearby Wolf-Rayet stars. On sight lines toward the GC the abundance of silicon in dust is often found to be lower, namely  $3.0 \pm 1.8 \times 10^{-5}$  per H-atom (Roche and Aitken, 1985). This discrepancy may be caused by the presence of large particles ( $> 3\ \mu\text{m}$ )

near the GC. The results of the dust abundance near the GC are also more uncertain, since these infrared silicon abundances depend on an estimate of the visual extinction ( $A_V$ ) derived from  $N_H/A_V$  ratio of the local solar neighborhood (Bohlin et al., 1978) and this method may be more uncertain toward the GC (Tielens et al., 1996). On average our results of the silicate dust abundance,  $4.2 \pm 0.4 \times 10^{-5}$  per H-atom, fall in between the abundances found by Roche and Aitken (1985) to the GC and Roche and Aitken (1984); Tielens et al. (1996) in the local solar environment, but individual lines of sight deviate significantly from the average. We did not find a relation between the silicon dust abundance and the distance of the source from the GC ( $R_{GC}$ ), also called Galactocentric radius. There appears also to be no obvious relations between the abundance of silicon and the distance from the plane of the Galaxy, but this can be attributed to the vicinity of all our sources to the plane.

Besides the abundance of silicon in dust, we can also investigate the total abundance of silicon along the nine lines of sight toward the X-ray binaries. For elements such as Fe, Mg, O and Si, an increase in the abundance toward the GC is observed (Pedicelli et al., 2009; Rolleston et al., 2000; Davies et al., 2009). The vicinity of the X-ray binaries to the GC gives us a unique opportunity to study the behaviour of this gradient in the inner region of the Galaxy, from around 0.9 kpc from the center of the Galaxy. Rolleston et al. (2000) found a Galactic abundance gradient of silicon of  $-0.06 \pm 0.01$  dex/kpc for Galactocentric radii  $R_{GC} > 6$  kpc. For Galactocentric radii  $R_{GC} < 6$  kpc there is no clear gradient was found, as was shown by Davies et al. (2009). They find a gradient for the azimuthal abundance of  $-0.8 \pm 0.1$  dex/kpc for silicon, but the observations have a large scatter. Of course the area of the Galactic bulge provides a different environment from the surrounding Galactic disk. Using Figure 3.5 we can investigate a possible gradient of abundances toward the Galactic plane. Here we show the total abundance of silicon versus  $R_{GC}$ . The abundances obtained from the X-ray binaries are shown in black. The other data points are abundances of silicon of a sample of B-type stars (in purple) from Rolleston et al. (2000) and abundances derived from observations of cepheids (in light blue) from Andrievsky et al. (2002) for comparison. The star symbol at 8.5 kpc indicates the position of the sun and the two yellow bands show the environments of the Galactic bulge and the Galactic molecular ring. The dashed-dotted line shows the solar abundance of silicon. We find a gradient of  $0.06 \pm 0.01$  dex/kpc for the abundances derived from the X-ray binary observations. The gradient is indicated by the dashed line. Instead of the increase of the silicon abundance observed at radii larger than 6 kpc from the center, we observe a slight decrease. We note that the error on this gradient is large and that it can be observed from Figure 3.5 that all the abundances are close to solar. If this decrease is real, it might be caused by an increase of the typical grain size of the silicate grains in the Galactic central area to which the X-rays are not sensitive. In that case the X-rays are a probe for the volume of large grains. This is supported by the observation of a scattering feature just before the edge indicating the possible presence of large grains as described in Chapter 2. However, we also note here, that the error on the distance should also be taken into account before a firm conclusion about the gradient can be made. Furthermore, the errors on the abundance measurements can be reduced by more and longer observations of the sources. In the case of GX 13+1 the errors are already small due to the number of observations we included in the fit and therefore serves as a good example to show the benefit of new observations. All these elements considered, we can conclude that the increase of abundance of silicon at Galactocentric radii  $> 6$  kpc is not observed in the inner part of the Galaxy.

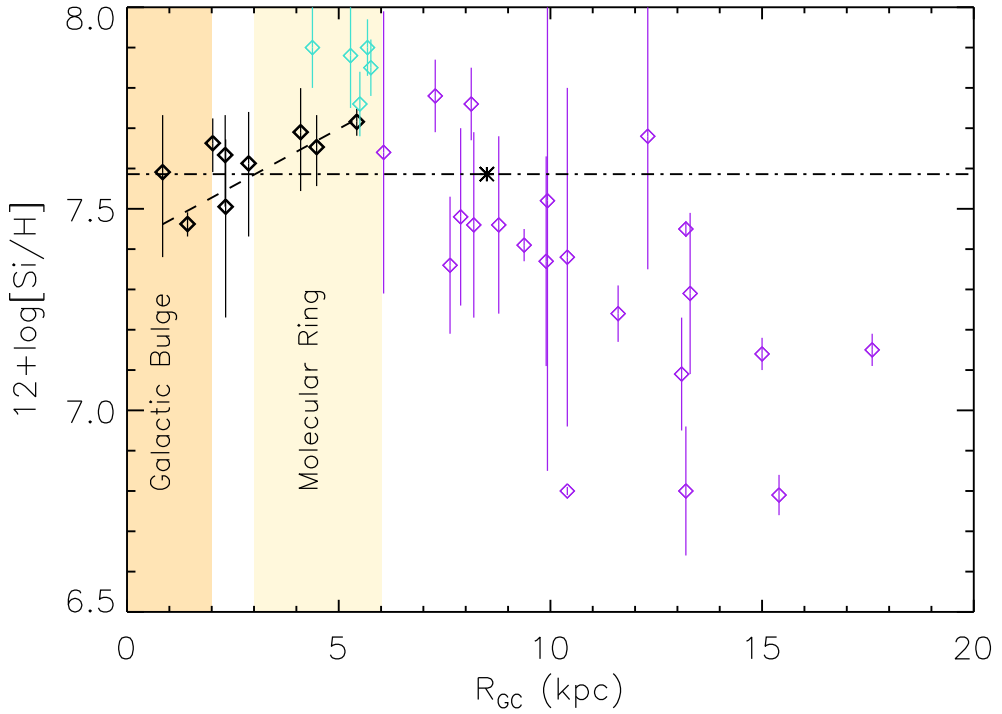


**Figure 3.5:** The total silicon abundance expressed in logarithmic units, with hydrogen by definition 12.0 versus the Galactocentric distance in kpc. The star symbol indicates the position of the Sun and the two yellow bands indicate the position of the Galactic bulge and the molecular ring. The dashed-dotted line indicates the solar abundance and the dashed line the gradient in the abundances obtained from the X-ray nine binaries.

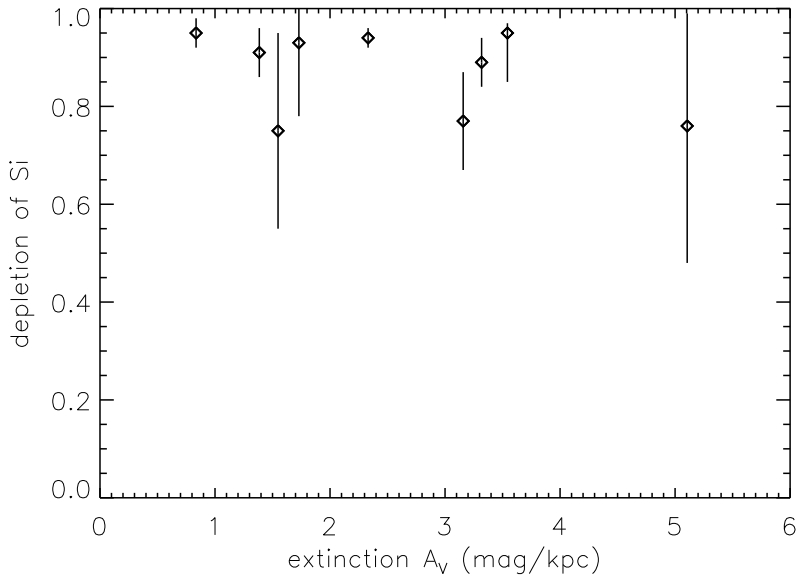


Figure 3.6: Depletion versus visual extinction ( $A_V$ ).

The depletion of elements such as Fe, Mg, O and Si in to dust shows a correlation with the extinction along the line of sight (Jenkins, 2009; Voshchinnikov and Henning, 2010). Where Voshchinnikov and Henning (2010) probe the depletion up to a distance of 7 kpc from the Sun, we are able to observe the depletion of silicon at larger distances and in the less well explored environment of the Galactic central region. Furthermore, we are able to observe both gas and dust simultaneously and in this way we obtain a direct measure of the depletion. Assuming the relation for visual extinction  $N_H/A_V = 1.9 \times 10^{21} \text{cm}^{-2} \text{mag}^{-1}$  (Bohlin et al., 1978), is still valid in the dense environment of the central part of the Galaxy, we obtain the result of the depletions versus the extinction,  $A_V$ , shown in Figure 3.6. Not all of the X-ray binaries follow the average extinction of 2 mag/kpc. Four lines of sight that have extinctions higher than 3 mag/kpc. We do not observe a clear trend in the data. This lack of correlation can be explained by the environment in which the X-ray binaries reside. The central part of the Galaxy has a complex structure as we already noted earlier in this section. All the X-ray binaries are located in this area, so we may be observing local variations in the ISM.

### 3.6 Summary and Conclusion

In this chapter, we fitted the Si edge of of the absorbed spectra along 9 different lines of sight. We used a total of 14 new dust extinction profiles, representing to a good degree the silicate content of the ID. We measured the absorption profiles of these 14 interstellar dust analogues at the Soleil synchrotron facility in Paris. The laboratory absorption measurements were converted into extinction cross-section in order to obtain models for suitable for interstellar dust

studies. We obtained the following results:

- We find that most lines of sight can be well fitted by amorphous olivine. The contribution of crystalline dust to the fits is larger than found in the infrared. For the sources with the best signal-to-noise (i.e. GX 5-1, GX 13+1 and GX 17+2), we find values of the crystallinity range between  $\zeta_1 = 0.04 - 0.12$ , with upper limits on these values of  $\zeta_1$  ranging between 0.17 and 0.35. A possible explanation may lie in the nature of X-rays, which is such that it facilitates to study the short-range order between the atoms, contrary to the long-range disorder in the infrared. In this way, we may observe crystallinity in polycrystalline and partly glassy material. More high quality observations will allow us to put further constraints on this parameter.
- Iron-poor pyroxenes are not preferred in the fits. It is however difficult to put a precise limit on the amount of iron in silicates, since the Si K-edge is not very sensitive to changes in the iron content. In order to investigate the contribution of iron in silicates we need to involve the Fe K-edge. Observations of the Fe K-edge in X-ray binaries will be possible with the future *Athena* observatory. Future studies may therefore benefit from additional iron rich pyroxene dust in the sample set.
- In almost all of the X-ray binaries, the dust mixture best fitting the Si K-edge includes an olivine dust type.
- For the first time, we study the GC environment in the X-rays using the Si K-edge in the spectra of X-ray binaries located in this environment. From the fits, we obtained the total abundance of silicon, the dust abundance and the depletion. We investigated trends for the total abundance versus the Galactocentric distance. Here we observe the local variations in the complex environment of the GC. In the case of the total abundance versus the Galactocentric distance we find a gradient of  $0.06 \pm 0.01$  dex/kpc. We observe a decrease of the silicon abundance toward the GC. This may be caused by silicon atoms locked up in large ( $> 3 \mu\text{m}$ ) dust particles in these dense environments.

## Acknowledgments

Dust studies at Leiden Observatory are supported through the Spinoza Premie of the Dutch science agency, NWO. E.C. and D.R. acknowledge support from NWO-Vidi grant 639.042.525. H.M. and P.M. are grateful for support of the Deutsche Forschungsgemeinschaft under Mu 1164/8-2 and Mu 1164/9-1. We acknowledge SOLEIL for provision of synchrotron radiation facilities and we would like to thank Delphine Vantelon for assistance in using beamline LUCIA. This research made use of the Chandra Transmission Grating Catalog and archive (<http://tgcatalog.mit.edu>). Furthermore, we made use of the FLUO self absorption correction code provided by Daniel Haskell.

### 3.A Data tables LMXBs

We give a detailed overview of the data obtained from the best fits of X-ray binaries GX 5-1, 4U 1630-47, GX 13+1, 4U 1702-429, 4U 1728-34, GX 340+00, GRS 1758-258, GX 17+2

and 4U 1705-44. In the tables of this section we give the parameters values corresponding to the best fits of each of the sources. The best fits of each of these sources are shown in the corresponding figures.

*GX 5-1*: The fitting of GX 5-1 is explained in Section 3.4.2 for illustration. We found a column density of  $5.8 \pm 0.2 \times 10^{22} \text{cm}^{-2}$ . This value can be compared to previous studies: the column density of GX 5-1 was measured by Predehl and Schmitt (1995) to range between 2.78 and  $3.48 \times 10^{22} \text{cm}^{-2}$  depending on the continuum model. More recent values of the column density are  $2.8 \times 10^{22} \text{cm}^{-2}$  with *Chandra* data by Ueda et al. (2005) and  $3.07 \pm 0.04 \times 10^{22} \text{cm}^{-2}$  by Asai et al. (2000, using ASCA archival data). In Chapter 2 we made use of the short, 0.24 ks, observation of obsid 716 in order to minimize the effect of pile up on the estimate of the column density. This resulted in a column density of  $3.4 \pm 0.1 \times 10^{22} \text{cm}^{-2}$ . These values are lower than the one we find for the spectra used in this study. However, there is a considerable time difference between the observation used in this analysis (July 2017) and the previous observation in TE mode by *Chandra* (July 2000). From the observation listed above, we already note that the observed column density of the source can vary. This variation may be associated to changes over time intrinsic to the source. Such differences in the column density can for instance be observed as well in EXO 0748-676 (van Peet et al., 2009). Furthermore, GX 5-1 deviates from the linear relation between the scattering optical depth and the column density (see Figure 7 of Predehl and Schmitt, 1995). In the case that the interstellar medium is solely responsible for the total amount of absorption, a lower column density is expected for GX 5-1 with respect to the observed scattering optical depth. Since  $N_{\text{H}}$  is observed to be larger, the increase can be associated with the source.

*4U 1630-47*: There are four data sets used in the fitting of the 4U 1630-47 (Table 3.6, Figure 3.7). The source continuum of the source is modelled using two black body models. All observations show outflowing gas, which is modelled by the XABS model. The ionization parameter  $\xi$  in the XABS model is defined as  $\xi = L/nr^2$ , where  $L$  is the ionizing luminosity,  $n$  the gas density and  $r$  the distance of the gas from the source. We find a column density of  $N_{\text{H}} = 9.7 \pm 0.1 \times 10^{22} \text{cm}^{-2}$ , making it the densest line of sight in our study. This value is in agreement with i.a., Neilsen et al. (2014), who find a best-fit column density of  $N_{\text{H}} = 9.4^{+0.5}_{-1.1} \times 10^{22} \text{cm}^{-2}$ .

*GX 13+1*: The continuum of GX 13+1 is fitted with a disk blackbody and Comptonisation model (Table 3.7, Figure 3.8). All the observations have a XABS component, in order to model outflowing gas from the source. In the case of the observation with obsid 11814, a second XABS model is introduced in order to fit the non outflowing ionized gas along the line of sight. The column density of GX 13+1 is in agreement with values found by Pintore et al. (2014) and D’Ai et al. (2014).

*4U 1702-429*: This X-ray binary was modelled using a disk blackbody and a Comptonisation model, resulting in a value of  $N_{\text{H}} 2.3 \pm 0.2 \times 10^{22} \text{cm}^{-2}$ , similar to results found by Iaria et al. (2016) (Table 3.8, Figure 3.9).

*4U 1728-34*: In the case of 4U 1728-34 the continuum was as well modelled by using a disk blackbody and a Comptonisation model (Table 3.8, Figure 3.10). This source is a bursting low mass X-ray binary, and two bursts occur in the spectrum of obsid 2748. These bursts do not affect the modeling of the Si K-edge. The  $N_{\text{H}}$  is in agreement with values found by Di Salvo et al. (2000a) of  $3.1 \pm 0.1 \times 10^{22} \text{cm}^{-2}$ , using a similar modeling and data from the *BeppoSAX* satellite, which covers a wide energy range of 0.12-100 keV, making it especially suitable for

Table 3.5: Best fit parameters for GX 5-1

Obsid	13714	13715
$N_{\text{H}}^{\text{cold}} (10^{22} \text{ cm}^{-2})$	5.8 ± 0.2	
$k_{\text{B}} T_{\text{bb}} (\text{keV})$	0.31 ± 0.01	0.33 ± 0.01
$k_{\text{B}} T_{0 \text{comt}} (\text{keV})$	0.30 ± 0.03	0.30 ± 0.03
$k_{\text{B}} T_{1 \text{comt}} (\text{keV})$	28 ± 9	23 <sup>+12</sup> <sub>-6</sub>
$\tau_{\text{comt}} (\text{keV})$	1.0 <sup>+0.2</sup> <sub>-0.7</sub>	1.2 ± 0.6
$F_{0.5-2 \text{keV}} (10^{-10} \text{ erg cm}^{-2} \text{ s}^{-1})$	3.8 ± 0.4	3.6 ± 0.4
$F_{2-10 \text{keV}} (10^{-8} \text{ erg cm}^{-2} \text{ s}^{-1})$	1.8 ± 0.2	1.7 ± 0.2
$C^2/\nu$	2026/1603	

This fit was produced using the following SPEX models: a blackbody model, a Comptonisation model, the AMOL model, cold gas model (HOT with  $k_{\text{B}} T = 5 \times 10^{-4}$ ) and XABS.

hydrogen column density measurements.

*GX 340+00*: is well fitted by a powerlaw model in combination with a blackbody model. We added a Gaussian model in order to fit the iron  $K_{\alpha}$  emission-line feature around 6.4 keV. The obtained column density of hydrogen is:  $6.6 \pm 0.2 \times 10^{22} \text{ cm}^{-2}$ . This value is similar to results from Seifina et al. (2013), who make use of data from *BeppoSAX* and *RXTE* and find values of  $\sim 5.5 - 6.5 \times 10^{22} \text{ cm}^{-2}$  for several models. It is below values found by (Cackett et al., 2010) of  $0.9 - 1.1 \times 10^{23} \text{ cm}^{-2}$  using *XMM-Newton* data.

*GRS 1758-258*: The continuum of GRS 1758-258 is best fitted by a blackbody and a steep power law function (Smith et al., 2001) (Table 3.9, Figure 3.12).

*GX 17+2*: The continuum of GX 17+2 modelled using a blackbody model in combination with powerlaw function (Table 3.9, Figure 3.13). The column density is estimated by Cackett et al. (2009) to lie between  $3.12 \pm 0.05$  and  $4.63 \pm 0.08 \times 10^{22} \text{ cm}^{-2}$ , using *Chandra* data. This column density is higher than the value found in our analysis of  $2.0 \pm 0.1 \times 10^{22} \text{ cm}^{-2}$ . However, our analysis is in agreement with the analysis of Di Salvo et al. (2000b), who use data from *BeppoSAX*.

*4U 1705-44*: The continuum of 4U 1705-44 is also modelled using a blackbody model in combination with powerlaw function (Table 3.9, Figure 3.14). The column density is in agreement with data from *BeppoSAX* (Piraino et al., 2016, model 2).

### 3.B Si K-edge models

Figure 3.15 shows the extinction profiles around the Si K-edge for the compounds 1 to 14, see Table 3.1. All the profiles are implemented in the AMOL model of the spectral fitting code SPEX. The absolute cross-sections of the models used in this analysis are available in tabular form on the following website: [www.sron.nl/~elisa/VIDI/](http://www.sron.nl/~elisa/VIDI/). Furthermore, we show the laboratory edges from Figure 3.1 in individual panels for comparison in Figure 3.16.

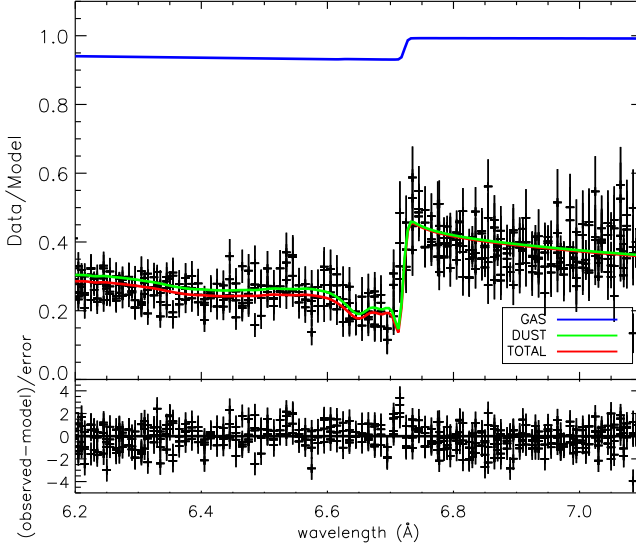


Figure 3.7: Si K-edge of 4U 1630-47.

Table 3.6: Best fit parameters for 4U 1630-47

Obsid	13714	13715	13716	13717
$N_{\text{H}}^{\text{cold}} (10^{22} \text{ cm}^{-2})$			$9.7 \pm 0.1$	
$k_{\text{B}} T_{\text{bb1}} (\text{keV})$	$0.62 \pm 0.01$	$0.62 \pm 0.01$	$0.60 \pm 0.01$	$0.63 \pm 0.01$
$k_{\text{B}} T_{\text{bb2}} (\text{keV})$	$1.2 \pm 0.3$	$1.2 \pm 0.4$	$1.2 \pm 0.4$	$1.2 \pm 0.5$
$N_{\text{H}}^{\text{xabs}} (10^{22} \text{ cm}^{-2})$			$9.2 \pm 0.2$	
$\log \xi^{\text{xabs}} (\text{erg cm s}^{-1})$			$4.1 \pm 0.2$	
$z v_{\text{out}}^{\text{xabs}} (10^2 \text{ kms}^{-1})$			$-1.0^{+1.3}_{-1.0}$	
$N_{\text{H}}^{\text{xabs2}} (10^{22} \text{ cm}^{-2})$			$9.0 \pm 0.2$	
$\log \xi^{\text{xabs2}} (\text{erg cm s}^{-1})$			$4.3 \pm 0.1$	
$z v_{\text{out}}^{\text{xabs2}} (10^2 \text{ kms}^{-1})$			$-7.8 \pm 0.3$	
$F_{0.5-2 \text{ keV}} (10^{-12} \text{ erg cm}^{-2} \text{ s}^{-1})$	$8.2 \pm 2$	$8.2 \pm 2.0$	$7.8 \pm 1.9$	$8.0 \pm 1.8$
$F_{2-10 \text{ keV}} (10^{-9} \text{ erg cm}^{-2} \text{ s}^{-1})$	$4.1 \pm 0.9$	$4.0 \pm 0.9$	$3.8 \pm 0.8$	$4.4 \pm 0.9$
$C^2/\nu$			$5258/4028$	

This fit was produced using the following SPEX models: two blackbody models, the AMOL model, cold gas model (HOT with  $k_{\text{B}} T = 5 \times 10^{-4}$ ) and two XABS models. Both XABS models are coupled to the four observations, since these observations were performed in succession.

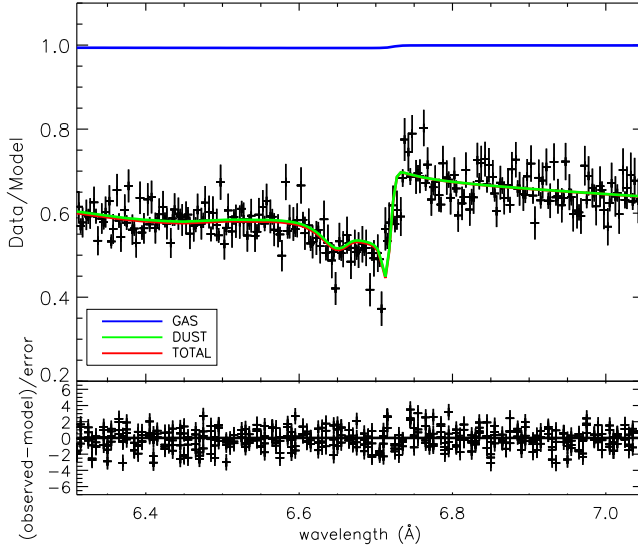


Figure 3.8: Si K-edge GX 13+1.

Table 3.7: Best fit parameters for GX 13+1

Obsid	11814	11815	11816	11817
$N_{\text{H}}^{\text{cold}} (10^{22} \text{ cm}^{-2})$		$3.1 \pm 0.1$		
$k_{\text{B}} T_{\text{dbb}} (\text{keV})$	$0.72 \pm 0.18$	$0.99 \pm 0.06$	$0.87 \pm 0.25$	$0.32 \pm 0.14$
$k_{\text{B}} T_{0 \text{comt}} (\text{keV})$	$0.70 \pm 0.03$	$0.79 \pm 0.03$	$0.80 \pm 0.06$	$0.70 \pm 0.02$
$k_{\text{B}} T_{1 \text{comt}} (\text{keV})$	$12 \pm 3$	$11 \pm 2$	$12_{-3}^{+8}$	$11 \pm 1$
$\tau_{\text{comt}} (\text{keV})$	$1.4 \pm 0.2$	$0.54 \pm 0.09$	$0.20_{-0.19}^{+0.30}$	$1.9_{-0.6}^{+0.4}$
$N_{\text{H}}^{\text{xabs1}} (10^{23} \text{ cm}^{-2})$	$1.1 \pm 0.1$	$1.8 \pm 0.1$	$4.1 \pm 0.1$	$3.2 \pm 0.1$
$\log \xi^{\text{xabs1}}$	$4.3 \pm 0.5$	$4.3 \pm 0.3$	$4.3 \pm 0.1$	$4.5 \pm 0.1$
$z v_{\text{out}}^{\text{xabs1}} (10^2 \text{ kms}^{-1})$	$-4.4_{-5.3}^{+3.0}$	$-5.5_{-1.5}^{+1.9}$	$-6.2_{-2.1}^{+3.7}$	$-3.5 \pm 1.4$
$N_{\text{H}}^{\text{xabs2}} (10^{21} \text{ cm}^{-2})$	$1.1 \pm 0.2$	-	-	-
$\log \xi^{\text{xabs2}} (\text{erg cm s}^{-1})$	$3.0 \pm 0.1$	-	-	-
$z v^{\text{xabs2}} (10^2 \text{ kms}^{-1})$	$> -0.1$	-	-	-
$F_{0.5-2 \text{ keV}} (10^{-10} \text{ erg cm}^{-2} \text{ s}^{-1})$	$1.4 \pm 0.1$	$1.8 \pm 0.2$	$1.8 \pm 0.2$	$1.6 \pm 0.2$
$F_{2-10 \text{ keV}} (10^{-9} \text{ erg cm}^{-2} \text{ s}^{-1})$	$5.6 \pm 0.6$	$6.6 \pm 0.7$	$6.5 \pm 0.7$	$6.8 \pm 0.7$
$C^2/\nu$	$5910/4738$			

This fit was produced using the following SPEX model components: a disk blackbody, a Comptonisation model, the AMOL model, cold gas model (i.e. HOT with  $k_{\text{B}} T = 5 \times 10^{-4}$ ) and two XABS models.

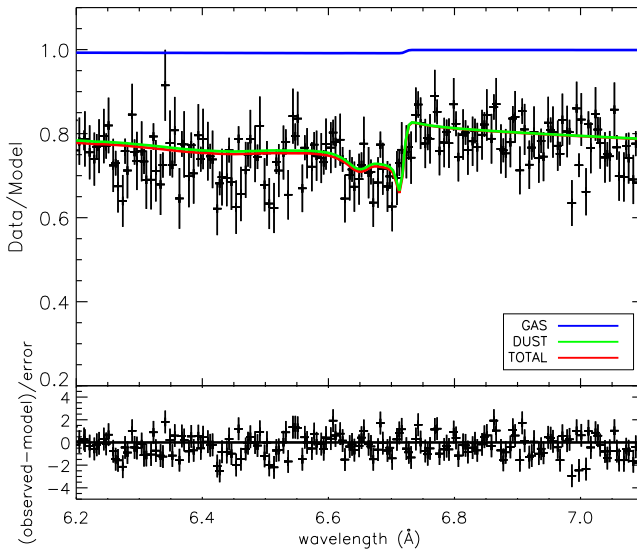


Figure 3.9: Si K-edge 4U 1702-429.

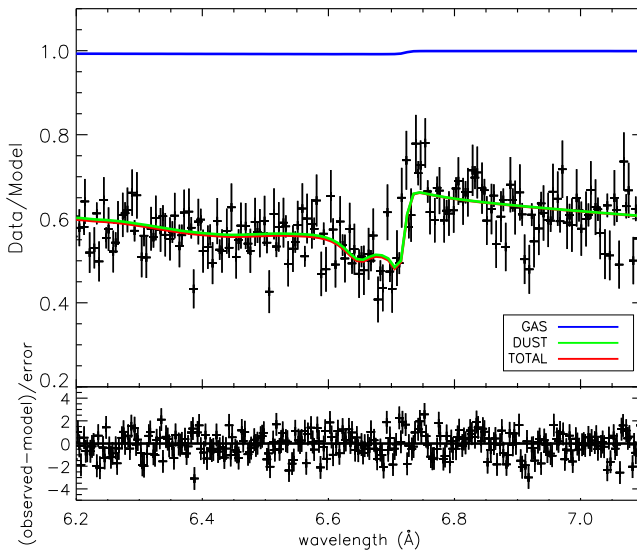


Figure 3.10: Si K-edge 4U 1728-34.

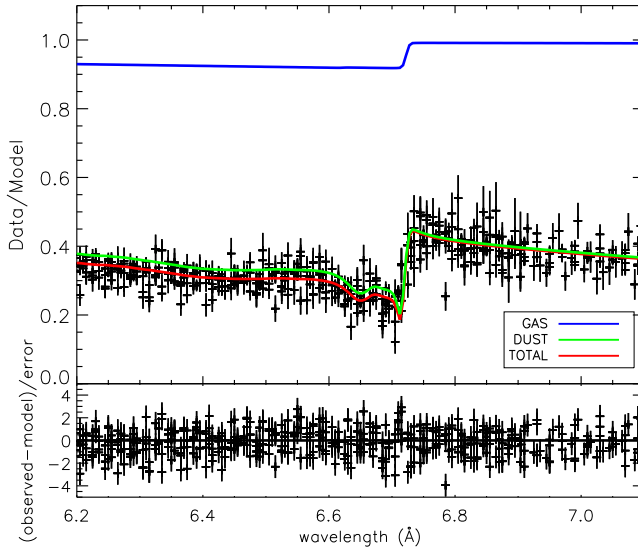


Figure 3.11: Si K-edge GX 340+00.

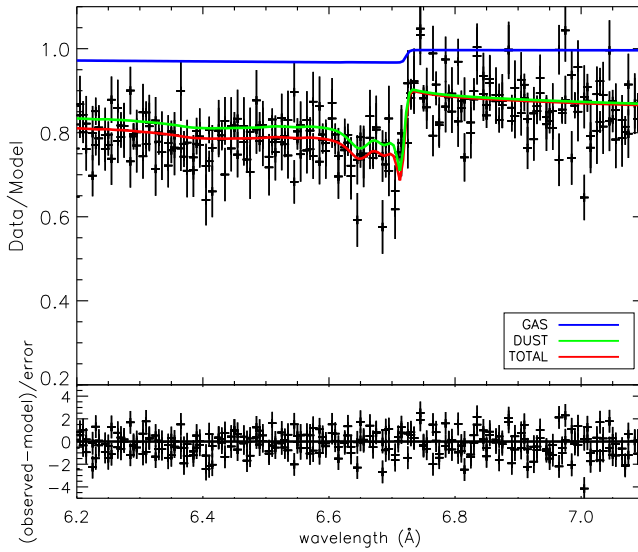


Figure 3.12: Si K-edge GRS 1758-258.

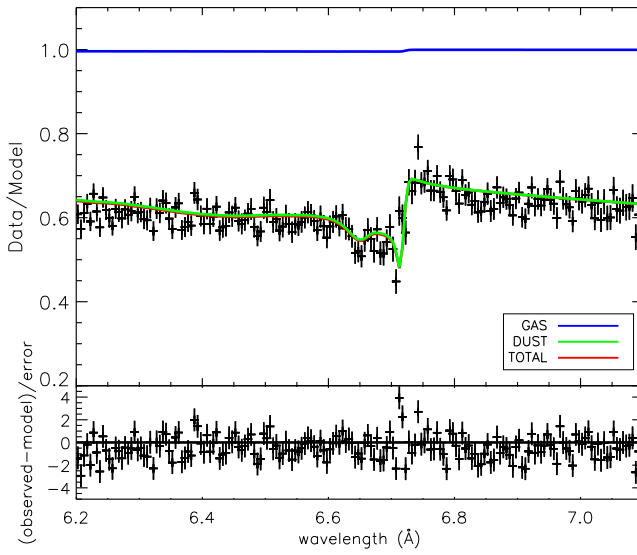


Figure 3.13: Si K-edge GX 17+2.

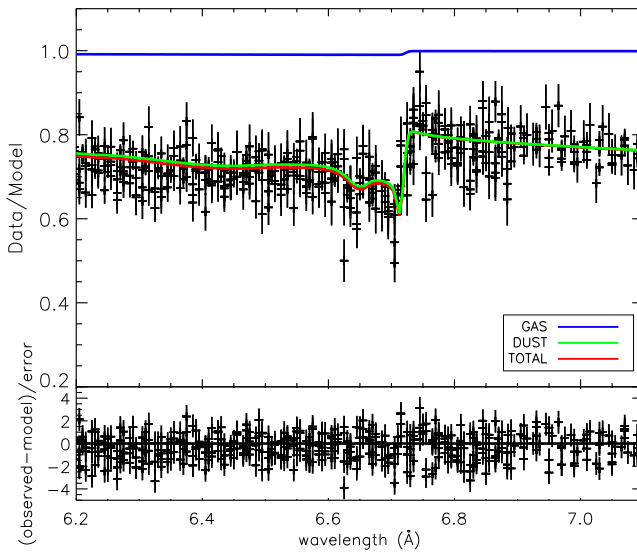


Figure 3.14: Si K-edge 4U 1705-44.

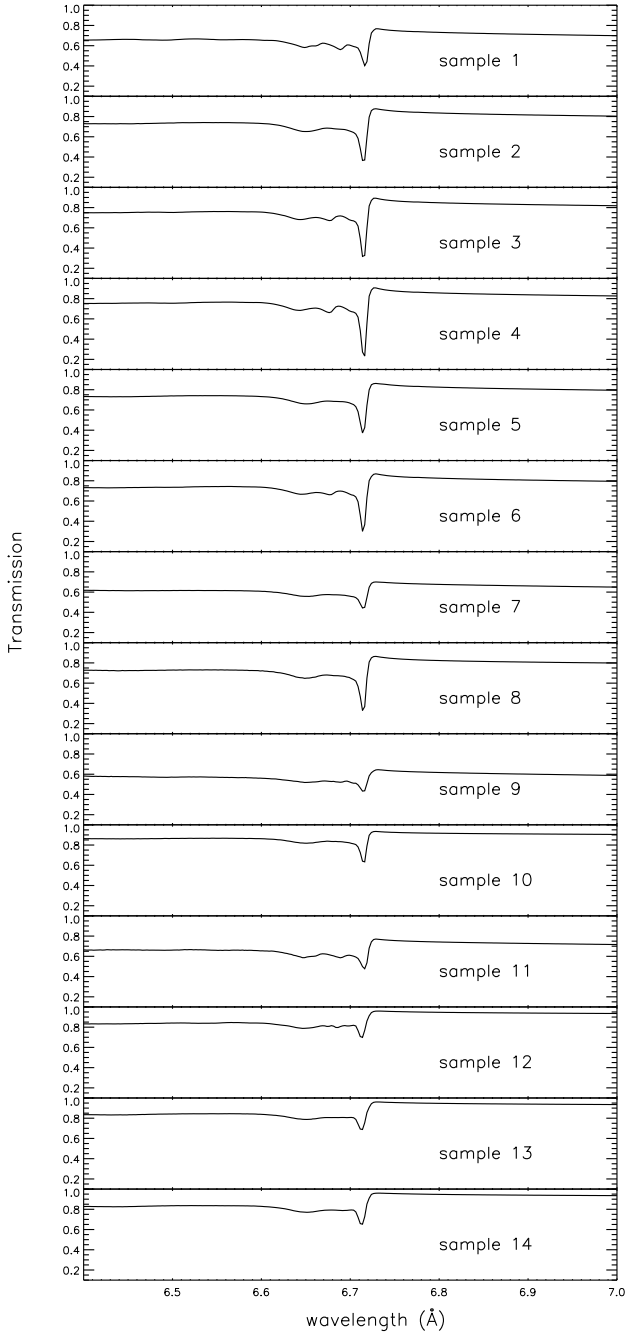


Figure 3.15: Transmission of the six dust extinction models (absorption and scattering) of the Si K-edge. The silicon column density has been set here to  $10^{18} \text{ cm}^{-2}$  for all the dust models. Each model is indicated by a number which corresponds to the numbers in Table 3.1.

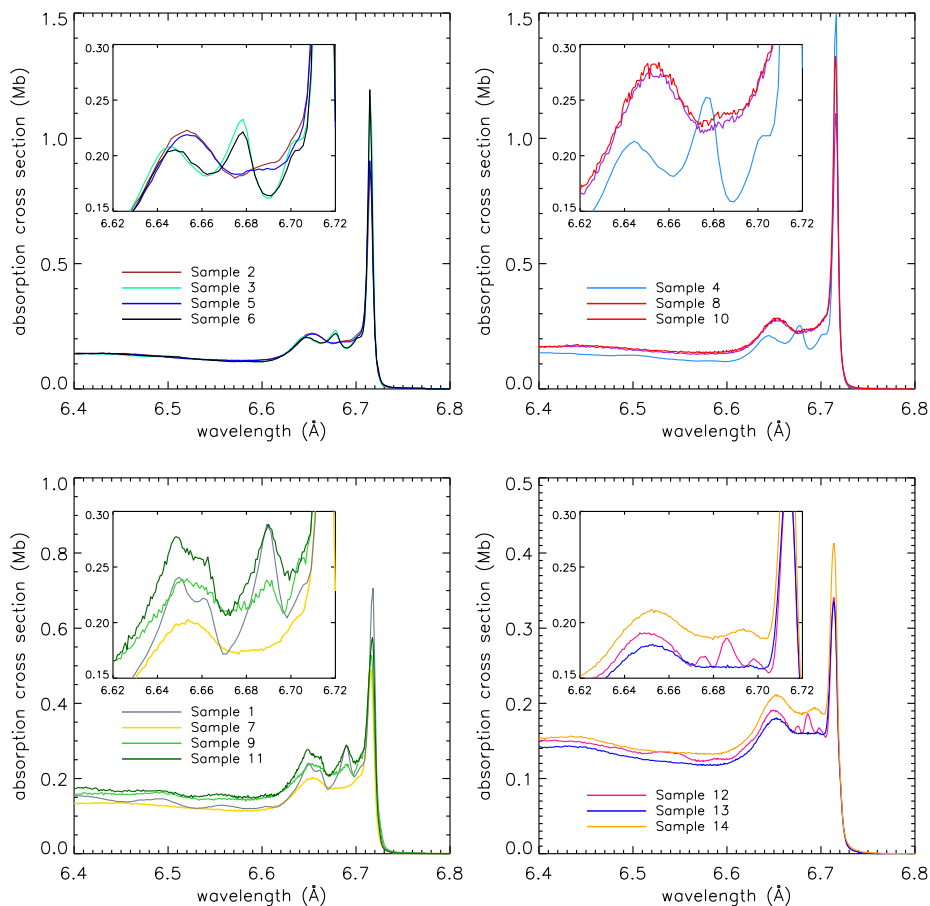


Figure 3.16: The Si K-edge of dust samples 1-14, see Table 3.1. The x-axis shows the energy in  $\text{\AA}$  and the y-axis shows the amount of absorption indicated by the cross-section (in Mb per Si atom). The samples are shown in different panels for easier comparison. The top left panel shows the difference between amorphous and crystalline pyroxenes (i.e. samples 2, 3, 5 and 6). The top right panel shows the difference between amorphous and crystalline enstatite (samples 4 and 10), including as well an amorphous pyroxene. The bottom left panel focusses on the olivine dust samples and the bottom right panel shows our three quartz samples.

Table 3.8: Best fit parameters for 4U 1702-429, 4U 1728-34 and GX 340+00

Source	4U 1702-429	4U 1728-34	GX 340+00			
Obsid	11045	2748	1921	18085	19450	20099
$N_{\text{cold}}$ ( $10^{22} \text{ cm}^{-2}$ )	$2.3 \pm 0.2$	$3.5^{+0.2}_{-0.5}$		$6.6 \pm 0.2$		
$k_B T_{\text{hb}}$ (keV)	-	-	$2.1^{+0.7}_{-0.1}$	$1.1 \pm 0.1$	$1.0 \pm 0.1$	$1.0 \pm 0.1$
$\Gamma_{\text{pow}}$	-	-	$1.6 \pm 0.1$	$1.5 \pm 0.1$	$2.0 \pm 0.1$	$1.8 \pm 0.1$
$k_B T_{\text{dhh}}$ (keV)	$0.74^{+0.22}_{-0.10}$	$0.27^{+0.01}_{-0.05}$	-	-	-	-
$E_{\text{gauss}}$ (keV)	-	-	$6.6 \pm 0.1$	-	$6.4 \pm 0.1$	$6.3 \pm 0.1$
$FWHM_{\text{gauss}}$ (keV)	-	-	$0.40 \pm 0.08$	-	$2.3^{+0.2}_{-0.1}$	$2.9 \pm 0.2$
$k_B T_{0 \text{ compt}}$	$0.47^{+0.21}_{-0.07}$	$0.44^{+0.05}_{-0.10}$	-	-	-	-
$k_B T_{1 \text{ compt}}$ (keV)	$2.5^{+0.3}_{-0.2}$	$2.1^{+0.5}_{-0.17}$	-	-	-	-
$\tau_{\text{compt}}$	$7.0^{+9.3}_{-0.6}$	$2.5^{+3.4}_{-2.1}$	-	-	-	-
$F_{0.5-2 \text{ keV}}$ ( $10^{-11} \text{ erg cm}^{-2} \text{ s}^{-1}$ )	$5.6 \pm 1.0$	$0.8 \pm 0.1$	$2.5 \pm 0.2$	$4.0 \pm 0.4$	$4.3 \pm 0.3$	$4.4 \pm 0.3$
$F_{2-10 \text{ keV}}$ ( $10^{-9} \text{ erg cm}^{-2} \text{ s}^{-1}$ )	$0.6 \pm 0.1$	$1.7 \pm 0.1$	$6.2 \pm 0.4$	$10 \pm 1$	$7.6 \pm 0.5$	$9.4 \pm 0.7$
$\chi^2/\nu$	2350/2144	1403/1326		4777/3954		

The fit of 4U 1702-429 was produced using the following SPEX model components: a disk blackbody, a Comptonisation model, AMOL model, cold gas model (i.e. HOT with  $k_B T = 5 \times 10^{-4}$ ) and XABS model.

The fit of 4U 1728-34 was produced using the following SPEX model components: a disk blackbody, a Comptonisation model, AMOL, cold gas model and XABS. The fit of GX 340+00 was produced using the following SPEX models: a blackbody, power-law, AMOL, cold gas model and XABS.

Table 3.9: Best fit parameters for GRS 1758-258, GX 17+2 and 4U 1705-44

Source	GRS 1758-258		GX 17+2		4U 1705-44		
Obsid	2429	2750	11088	5500	18086	19451	20082
$N_{\text{H}}^{\text{cold}}$ ( $10^{22} \text{ cm}^{-2}$ )		$2.5 \pm 0.1$				$2.0 \pm 0.1$	
$N_{\text{H}}^{\text{hot}}$ ( $10^{20} \text{ cm}^{-2}$ )		$2.4^{+3.4}_{-0.2}$				$0.29^{+0.18}_{-0.23}$	
$k_{\text{B}} T_{\text{hot}}$ (keV)		$1.3^{+0.5}_{-0.2}$		$0.12 \pm 0.02$		$0.28^{+0.87}_{-0.18}$	
$k_{\text{B}} T_{\text{bb}}$ (keV)	$0.38 \pm 0.01$	$0.42 \pm 0.01$	-	-	-	-	-
$\Gamma_{\text{pow}}$	$3.9^{+0.1}_{-0.3}$	$2.7 \pm 0.1$	-	-	-	-	-
$T_{\text{dbb}}$ (keV)	-	-	$1.7^{+0.2}_{-0.1}$	$0.42^{+0.07}_{-0.03}$	$0.99^{+0.16}_{-0.33}$	$0.53^{+0.18}_{-0.11}$	$0.43^{+0.08}_{-0.07}$
$k_{\text{B}} T_{0,\text{comt}}$ (keV)	-	-	$0.60 \pm 0.01$	$0.41 \pm 0.01$	$0.65^{+0.03}_{-0.09}$	$0.54 \pm 0.02$	$0.49 \pm 0.01$
$k_{\text{B}} T_{1,\text{comt}}$ (keV)	-	-	$30^{+6}_{-11}$	$21^{+20}_{-13}$	$47^{+39}_{-12}$	$40^{+53}_{-16}$	$18^{+22}_{-9}$
$\tau_{\text{comt}}$	-	-	$1.7^{+1.1}_{-0.6}$	$1.4^{+1.6}_{-1.3}$	$0.9^{+1.8}_{-0.6}$	$1.0^{+1.6}_{-0.7}$	$1.6^{+1.2}_{-0.9}$
$F_{0.5-2 \text{ keV}}$ ( $10^{-10} \text{ erg cm}^{-2} \text{ s}^{-1}$ )	$0.8 \pm 0.2$	$1.2 \pm 0.2$	$4.3 \pm 0.8$	$1.4 \pm 0.1$	$3.6 \pm 0.4$	$2.3 \pm 0.2$	$2.3 \pm 0.2$
$F_{2-10 \text{ keV}}$ ( $10^{-9} \text{ erg cm}^{-2} \text{ s}^{-1}$ )	$0.12 \pm 0.04$	$0.44 \pm 0.08$	$13 \pm 2$	$1.7 \pm 0.2$	$7.1 \pm 0.7$	$3.9 \pm 0.4$	$3.0 \pm 0.3$
$C^2/\nu$	4182/3770		1393/1109		5838/4459		

The fit of GRS 1758-258 was produced using the following SPEX model components: a blackbody, power-law, AMOL, cold gas model (i.e. HOT with  $k_{\text{B}} T = 5 \times 10^{-4}$ ) and hot gas (HOT).

The fit of GX 17+2 was produced using the following SPEX model components: a disk blackbody, a comptonisation, AMOL, cold gas model and hot gas (HOT).

The fit of 4U 1705-44 was produced using the following SPEX model components: a disk blackbody, a comptonisation, AMOL, cold gas model and hot gas (HOT).



## References

- Aitken, D. K. and Roche, P. F. (1984). A study of the unidentified dust emission features near 10 microns. *MNRAS*, 208:751–761.
- Andrievsky, S. M., Bersier, D., Kovtyukh, V. V., Luck, R. E., Maciel, W. J., Lépine, J. R. D., and Beletsky, Y. V. (2002). Using Cepheids to determine the galactic abundance gradient. II. Towards the galactic center. *A&A*, 384:140–144.
- Asai, K., Dotani, T., Nagase, F., and Mitsuda, K. (2000). Iron K Emission Lines in the Energy Spectra of Low-Mass X-Ray Binaries Observed with ASCA. *ApJS*, 131:571–591.
- Augusteijn, T., Kuulkers, E., and van Kerkwijk, M. H. (2001). The IR counterpart of the black-hole candidate 4U 1630-47. *A&A*, 375:447–454.
- Bandyopadhyay, R. M., Shahbaz, T., Charles, P. A., and Naylor, T. (1999). Infrared spectroscopy of low-mass X-ray binaries - II. *MNRAS*, 306:417–426.
- Bilalbegović, G., Maksimović, A., and Mohaček-Grošev, V. (2017). Missing Fe: hydrogenated iron nanoparticles. *MNRAS*, 466:L14–L18.
- Bohlin, R. C., Savage, B. D., and Drake, J. F. (1978). A survey of interstellar H I from L-alpha absorption measurements. II. *ApJ*, 224:132–142.
- Bohren, C. F. (2010). What did kramers and kronig do and how did they do it? *European Journal of Physics*, 31(3):573.
- Bradley, J. P. (1994). Chemically Anomalous, Preaccretionally Irradiated Grains in Interplanetary Dust From Comets. *Science*, 265:925–929.
- Bringa, E. M., Kucheyev, S. O., Loeffler, M. J., Baragiola, R. A., Tielens, A. G. G. M., Dai, Z. R., Graham, G., Bajt, S., Bradley, J. P., Dukes, C. A., Felter, T. E., Torres, D. F., and van Breugel, W. (2007). Energetic Processing of Interstellar Silicate Grains by Cosmic Rays. *ApJ*, 662:372–378.
- Bruzzone, P., Carranza, R., Lacoste, J. C., and Crespo, E. (2002). Kramers?kronig transforms calculation with a fast convolution algorithm. *Electrochimica Acta*, 48(4):341 – 347.
- Cackett, E. M., Miller, J. M., Ballantyne, D. R., Barret, D., Bhattacharyya, S., Boutelier, M., Miller, M. C., Strohmayer, T. E., and Wijnands, R. (2010). Relativistic Lines and Reflection from the Inner Accretion Disks Around Neutron Stars. *ApJ*, 720:205–225.

- Cackett, E. M., Miller, J. M., Homan, J., van der Klis, M., Lewin, W. H. G., Méndez, M., Raymond, J., Steeghs, D., and Wijnands, R. (2009). A Search for Iron Emission Lines in the Chandra X-Ray Spectra of Neutron Star Low-Mass X-Ray Binaries. *ApJ*, 690:1847–1855.
- Cash, W. (1979). Parameter estimation in astronomy through application of the likelihood ratio. *ApJ*, 228:939–947.
- Chen, L., Hou, J. L., and Wang, J. J. (2003). On the Galactic Disk Metallicity Distribution from Open Clusters. I. New Catalogs and Abundance Gradient. *AJ*, 125:1397–1406.
- Chiar, J. E. and Tielens, A. G. G. M. (2006). Pixie Dust: The Silicate Features in the Diffuse Interstellar Medium. *ApJ*, 637:774–785.
- Christian, D. J. and Swank, J. H. (1997). The Survey of Low-Mass X-Ray Binaries with the Einstein Observatory Solid-State Spectrometer and Monitor Proportional Counter. *ApJS*, 109:177–224.
- Costantini, E. and de Vries, C. P. (2013). Characterizing the chemistry of interstellar dust: the X-ray view. *Mem. Soc. Astron. Italiana*, 84:592.
- Costantini, E., Pinto, C., Kaastra, J. S., in't Zand, J. J. M., Freyberg, M. J., Kuiper, L., Méndez, M., de Vries, C. P., and Waters, L. B. F. M. (2012). XMM-Newton observation of 4U 1820-30. Broad band spectrum and the contribution of the cold interstellar medium. *A&A*, 539:A32.
- D'Ai, A., Iaria, R., Di Salvo, T., Riggio, A., Burderi, L., and Robba, N. R. (2014). Chandra X-ray spectroscopy of a clear dip in GX 13+1. *A&A*, 564:A62.
- Davies, B., Origlia, L., Kudritzki, R.-P., Figer, D. F., Rich, R. M., Najarro, F., Negueruela, I., and Clark, J. S. (2009). Chemical Abundance Patterns in the Inner Galaxy: The Scutum Red Supergiant Clusters. *ApJ*, 696:2014–2025.
- de Groot, F. M. F. (2012). Dips and peaks in fluorescence yield X-ray absorption are due to state-dependent decay. *Nature*, 4:766–767.
- de Vries, C. P. and Costantini, E. (2009). Physical properties of amorphous solid interstellar material from X-ray absorption spectroscopy of <ASTROBJ>Scorpius X-1</ASTROBJ>. *A&A*, 497:393–398.
- Di Salvo, T., Iaria, R., Burderi, L., and Robba, N. R. (2000a). The Broadband Spectrum of MXB 1728-34 Observed by BeppoSAX. *ApJ*, 542:1034–1040.
- Di Salvo, T., Stella, L., Robba, N. R., van der Klis, M., Burderi, L., Israel, G. L., Homan, J., Campana, S., Frontera, F., and Parmar, A. N. (2000b). The Discovery of a State-Dependent Hard Tail in the X-Ray Spectrum of the Luminous Z Source GX 17+2. *ApJ*, 544:L119–L122.

- Dorschner, J., Begemann, B., Henning, T., Jaeger, C., and Mutschke, H. (1995). Steps toward interstellar silicate mineralogy. II. Study of Mg-Fe-silicate glasses of variable composition. *A&A*, 300:503.
- Draine, B. T. (2003). Scattering by Interstellar Dust Grains. II. X-Rays. *ApJ*, 598:1026–1037.
- Draine, B. T. and Lee, H. M. (1984). Optical properties of interstellar graphite and silicate grains. *ApJ*, 285:89–108.
- Fabian, D., Henning, T., Jäger, C., Mutschke, H., Dorschner, J., and Wehrhan, O. (2001). Steps toward interstellar silicate mineralogy. VI. Dependence of crystalline olivine IR spectra on iron content and particle shape. *A&A*, 378:228–238.
- Flank, A.-M., Cauchon, G., Lagarde, P., Bac, S., Janousch, M., Wetter, R., Dubuisson, J.-M., Idir, M., Langlois, F., Moreno, T., and D. Vantelon, D. (2006). LUCIA, a microfocus soft XAS beamline. *Nuclear Instruments and Methods in Physics Research Section B: Beam Interactions with Materials and Atoms*, 246(1):269 – 274. Synchrotron Radiation and Materials Science.
- Galloway, D. K., Munro, M. P., Hartman, J. M., Psaltis, D., and Chakrabarty, D. (2008). Thermonuclear (Type I) X-Ray Bursts Observed by the Rossi X-Ray Timing Explorer. *ApJS*, 179:360–422.
- Henning, T. (2010). Cosmic Silicates. *ARA&A*, 48:21–46.
- Henning, T., Begemann, B., Mutschke, H., and Dorschner, J. (1995). Optical properties of oxide dust grains. *A&AS*, 112:143.
- Iaria, R., Di Salvo, T., Del Santo, M., Pintore, F., Sanna, A., Papitto, A., Burderi, L., Riggio, A., Gambino, A. F., and Matranga, M. (2016). Study of the reflection spectrum of the LMXB 4U 1702–429. *A&A*, 596:A21.
- Jäger, C., Fabian, D., Schrempel, F., Dorschner, J., Henning, T., and Wesch, W. (2003). Structural processing of enstatite by ion bombardment. *A&A*, 401:57–65.
- Jenkins, E. B. (2009). A Unified Representation of Gas-Phase Element Depletions in the Interstellar Medium. *ApJ*, 700:1299–1348.
- Kaastra, J. S. (2017). On the use of C-stat in testing models for X-ray spectra. *A&A*, 605:A51.
- Kaastra, J. S., de Vries, C. P., Costantini, E., and den Herder, J. W. A. (2009). Effective area calibration of the reflection grating spectrometers of XMM-Newton. I. X-ray spectroscopy of the Crab nebula. *A&A*, 497:291–310.
- Kaastra, J. S., Mewe, R., and Nieuwenhuijzen, H. (1996). SPEX: a new code for spectral analysis of X & UV spectra. In Yamashita, K. and Watanabe, T., editors, *UV and X-ray Spectroscopy of Astrophysical and Laboratory Plasmas*, pages 411–414.

- Keck, J. W., Craig, W. W., Hailey, C. J., Harrison, F., Hong, J. S., Kahn, S. M., Lubin, P. M., McLean, R., Pivovarov, M. J., Seiffert, M., Wurtz, R., and Ziocck, K. P. (2001). Long-Term Multiwavelength Observations of GRS 1758-258 and the Advection-dominated Accretion Flow Model. *ApJ*, 563:301–312.
- Kemper, F., Vriend, W. J., and Tielens, A. G. G. M. (2004). The Absence of Crystalline Silicates in the Diffuse Interstellar Medium. *ApJ*, 609:826–837.
- Krasnokutski, S. A., Rouillé, G., Jäger, C., Huisken, F., Zhukovska, S., and Henning, T. (2014). Formation of Silicon Oxide Grains at Low Temperature. *ApJ*, 782:15.
- Lee, J. C., Ogle, P. M., Canizares, C. R., Marshall, H. L., Schulz, N. S., Morales, R., Fabian, A. C., and Iwasawa, K. (2001). Revealing the Dusty Warm Absorber in MCG -6-30-15 with the Chandra High-Energy Transmission Grating. *ApJ*, 554:L13–L17.
- Lee, J. C., Xiang, J., Ravel, B., Kortricht, J., and Flanagan, K. (2009). Condensed Matter Astrophysics: A Prescription for Determining the Species-specific Composition and Quantity of Interstellar Dust Using X-rays. *ApJ*, 702:970–979.
- Li, A. and Draine, B. T. (2002). Are Silicon Nanoparticles an Interstellar Dust Component? *ApJ*, 564:803–812.
- Lin, D., Remillard, R. A., Homan, J., and Barret, D. (2012). The Spectral Evolution along the Z Track of the Bright Neutron Star X-Ray Binary GX 17+2. *ApJ*, 756:34.
- Lingenberg, D. (1986). PhD thesis, University of Frankfurt/M.
- Lodders, K. and Palme, H. (2009). Solar System Elemental Abundances in 2009. *Meteoritics and Planetary Science Supplement*, 72:5154.
- Marra, A. C., Lane, M. D., Orofino, V., Blanco, A., and Fonti, S. (2011). Midinfrared spectra and optical constants of bulk hematite: Comparison with particulate hematite spectra. *Icarus*, 211:839–848.
- Mastelaro, V. and Zanotto, E. (2018). X-ray Absorption Fine Structure (XAFS) Studies of Oxide Glasses - A 45-Year Overview. *Materials*, 11:204.
- Mie, G. (1908). Beiträge zur Optik trüber Medien, speziell kolloidaler Metallösungen. *Annalen der Physik*, 330:377–445.
- Min, M., Waters, L. B. F. M., de Koter, A., Hovenier, J. W., Keller, L. P., and Markwick-Kemper, F. (2007). The shape and composition of interstellar silicate grains. *A&A*, 462:667–676.
- Molster, F. J., Waters, L. B. F. M., Tielens, A. G. G. M., and Barlow, M. J. (2002). Crystalline silicate dust around evolved stars. I. The sample stars. *A&A*, 382:184–221.
- Neilsen, J., Coriat, M., Fender, R., Lee, J. C., Ponti, G., Tzioumis, A. K., Edwards, P. G., and Broderick, J. W. (2014). A Link between X-Ray Emission Lines and Radio Jets in 4U 1630-47? *ApJ*, 784:L5.

- Nittler, L. R. (2005). Constraints on Heterogeneous Galactic Chemical Evolution from Meteoritic Stardust. *ApJ*, 618:281–296.
- Oosterbroek, T., Penninx, W., van der Klis, M., van Paradijs, J., and Lewin, W. H. G. (1991). EXOSAT observations of the X-ray burst source 4U 1702 - 42. *A&A*, 250:389–394.
- Parmar, A. N., Stella, L., and White, N. E. (1986). The evolution of the 1984 outburst of the transient X-ray source 4U 1630 - 47. *ApJ*, 304:664–670.
- Pedicelli, S., Bono, G., Lemasle, B., François, P., Groenewegen, M., Lub, J., Pel, J. W., Laney, D., Piersimoni, A., Romaniello, M., Buonanno, R., Caputo, F., Cassisi, S., Castelli, F., Leurini, S., Pietrinferni, A., Primas, F., and Pritchard, J. (2009). On the metallicity gradient of the Galactic disk. *A&A*, 504:81–86.
- Pinto, C., Kaastra, J. S., Costantini, E., and de Vries, C. (2013). Interstellar medium composition through X-ray spectroscopy of low-mass X-ray binaries. *A&A*, 551:A25.
- Pinto, C., Kaastra, J. S., Costantini, E., and Verbunt, F. (2010). High-resolution X-ray spectroscopy of the interstellar medium. XMM-Newton observation of the LMXB GS 1826-238. *A&A*, 521:A79.
- Pintore, F., Sanna, A., Di Salvo, T., Guainazzi, M., D’Ai, A., Riggio, A., Burderi, L., Iaria, R., and Robba, N. R. (2014). Testing rate-dependent corrections on timing mode EPIC-pn spectra of the accreting neutron star GX 13+1. *MNRAS*, 445:3745–3754.
- Piraino, S., Santangelo, A., Mück, B., Kaaret, P., Di Salvo, T., D’Ai, A., Iaria, R., and Egron, E. (2016). Broadband observations of the X-ray burster 4U1705-44 with BeppoSAX. *A&A*, 591:A41.
- Posch, T., Kerschbaum, F., Mutschke, H., Dorschner, J., and Jäger, C. (2002). On the origin of the 19.5  $\mu$  m feature. Identifying circumstellar Mg-Fe-oxides. *A&A*, 393:L7–L10.
- Predehl, P. and Schmitt, J. H. M. M. (1995). X-raying the interstellar medium: ROSAT observations of dust scattering halos. *A&A*, 293:889–905.
- Ravel, B. and Newville, M. (2005). *ATHENA, artemis, hephaestus*: data analysis for x-ray absorption spectroscopy using *ifeffit*. *Journal of Synchrotron Radiation*, 12(4):537–541.
- Roche, P. F. and Aitken, D. K. (1984). An investigation of the interstellar extinction. I - Towards dusty WC Wolf-Rayet stars. *MNRAS*, 208:481–492.
- Roche, P. F. and Aitken, D. K. (1985). An investigation of the interstellar extinction. II - Towards the mid-infrared sources in the Galactic centre. *MNRAS*, 215:425–435.
- Rogantini, D., Costantini, E., Zeegers, S. T., de Vries, C. P., Bras, W., de Groot, F., Mutschke, H., and Waters, L. B. F. M. (2018). Investigating the interstellar dust through the Fe K-edge. *A&A*, 609:A22.
- Rolleston, W. R. J., Smartt, S. J., Dufton, P. L., and Ryans, R. S. I. (2000). The Galactic metallicity gradient. *A&A*, 363:537–554.

- Savage, B. D. and Sembach, K. R. (1996). Interstellar Abundances from Absorption-Line Observations with the Hubble Space Telescope. *ARA&A*, 34:279–330.
- Seifina, E., Titarchuk, L., and Frontera, F. (2013). Stability of the Photon Indices in Z-source GX 340+0 for Spectral States. *ApJ*, 766:63.
- Smith, D. M., Heindl, W. A., Swank, J. H., and Markwardt, C. B. (2001). Black-Hole Candidate GRS 1758-258 Enters an “Off” State. *The Astronomer’s Telegram*, 66.
- Speck, A. K., Pitman, K. M., and Hofmeister, A. M. (2015). Better Alternatives to “Astronomical Silicate”: Laboratory-based Optical Functions of Chondritic/Solar Abundance Glass with Application to HD 161796. *ApJ*, 809:65.
- Speck, A. K., Whittington, A. G., and Hofmeister, A. M. (2011). Disordered Silicates in Space: A Study of Laboratory Spectra of “Amorphous” Silicates. *ApJ*, 740:93.
- Stern, E., Newville, M., Ravel, B., Yacoby, Y., and Haskel, D. (1995). The {UWXAFS} analysis package: philosophy and details. *Physica B: Condensed Matter*, 208-209:117–120. Proceedings of the 8th International Conference on X-ray Absorption Fine Structure.
- Sylvester, R. J., Kemper, F., Barlow, M. J., de Jong, T., Waters, L. B. F. M., Tielens, A. G. G. M., and Omont, A. (1999). 2.4-197  $\mu$  m spectroscopy of OH/IR stars: the IR characteristics of circumstellar dust in O-rich environments. *A&A*, 352:587–599.
- Tielens, A. G. G. M. (2001). The Composition of Circumstellar and Interstellar Dust. In Woodward, C. E., Bica, M. D., and Shull, J. M., editors, *Tetons 4: Galactic Structure, Stars and the Interstellar Medium*, volume 231 of *Astronomical Society of the Pacific Conference Series*, page 92.
- Tielens, A. G. G. M., Wooden, D. H., Allamandola, L. J., Bregman, J., and Witteborn, F. C. (1996). The Infrared Spectrum of the Galactic Center and the Composition of Interstellar Dust. *ApJ*, 461:210.
- Ueda, Y., Mitsuda, K., Murakami, H., and Matsushita, K. (2005). Study of the Galactic Interstellar Medium from High-Resolution X-Ray Spectroscopy: X-Ray Absorption Fine Structure and Abundances of O, Mg, Si, S, and Fe. *ApJ*, 620:274–286.
- Valencic, L. A. and Smith, R. K. (2013). Interstellar Abundances toward X Per, Revisited. *ApJ*, 770:22.
- van Peet, J. C. A., Costantini, E., Méndez, M., Paerels, F. B. S., and Cottam, J. (2009). Properties of the ionised plasma in the vicinity of the neutron-star X-ray binary EXO 0748-676. *A&A*, 497:805–813.
- Voshchinnikov, N. V. and Henning, T. (2010). From interstellar abundances to grain composition: the major dust constituents Mg, Si, and Fe. *A&A*, 517:A45.
- Wang, Q. D. (2009). Global Hot Gas in and around the Galaxy. In Smith, R. K., Snowden, S. L., and Kuntz, K. D., editors, *American Institute of Physics Conference Series*, volume 1156 of *American Institute of Physics Conference Series*, pages 257–267.

- Wang, Q. D., Nowak, M. A., Markoff, S. B., Baganoff, F. K., Nayakshin, S., Yuan, F., Cuadra, J., Davis, J., Dexter, J., Fabian, A. C., Grosso, N., Haggard, D., Houck, J., Ji, L., Li, Z., Neilsen, J., Porquet, D., Ripple, F., and Shcherbakov, R. V. (2013). Dissecting X-ray-Emitting Gas Around the Center of Our Galaxy. *Science*, 341:981–983.
- Weingartner, J. C. and Draine, B. T. (2001). Dust Grain-Size Distributions and Extinction in the Milky Way, Large Magellanic Cloud, and Small Magellanic Cloud. *ApJ*, 548:296–309.
- Westphal, A. J., Stroud, R. M., Bechtel, H. A., Brenker, F. E., Butterworth, A. L., Flynn, G. J., Frank, D. R., Gainsforth, Z., Hillier, J. K., Postberg, F., Simionovici, A. S., Sterken, V. J., Nittler, L. R., Allen, C., Anderson, D., Ansari, A., Bajt, S., Bastien, R. K., Bassim, N., Bridges, J., Brownlee, D. E., Burchell, M., Burghammer, M., Changela, H., Cloetens, P., Davis, A. M., Doll, R., Floss, C., Grün, E., Heck, P. R., Hoppe, P., Hudson, B., Huth, J., Kearsley, A., King, A. J., Lai, B., Leitner, J., Lemelle, L., Leonard, A., Leroux, H., Lettieri, R., Marchant, W., Oglione, R., Ong, W. J., Price, M. C., Sandford, S. A., Tresseras, J.-A. S., Schmitz, S., Schoonjans, T., Schreiber, K., Silversmit, G., Solé, V. A., Srama, R., Stadermann, F., Stephan, T., Stodolna, J., Sutton, S., Trieloff, M., Tsou, P., Tyliczszak, T., Vekemans, B., Vincze, L., Von Korff, J., Wordsworth, N., Zevin, D., Zolensky, M. E., and aff14 (2014). Evidence for interstellar origin of seven dust particles collected by the Stardust spacecraft. *Science*, 345:786–791.
- Wiscombe, W. J. (1980). Improved mie scattering algorithms. *Appl. Opt.*, 19(9):1505–1509.
- Yao, Y., Schulz, N., Wang, Q. D., and Nowak, M. (2006). Chandra Detection of Fe XVII in Absorption: Iron Abundance in the Hot Gaseous Interstellar Medium. *ApJ*, 653:L121–L124.
- Yao, Y. and Wang, Q. D. (2005). X-Ray Absorption Line Spectroscopy of the Galactic Hot Interstellar Medium. *ApJ*, 624:751–764.
- Yao, Y. and Wang, Q. D. (2007). The Galactic Central Diffuse X-Ray Enhancement: A Differential Absorption/Emission Analysis. *ApJ*, 666:242–246.
- Zeegers, S. T., Costantini, E., de Vries, C. P., Tielens, A. G. G. M., Chihara, H., de Groot, F., Mutschke, H., Waters, L. B. F. M., and Zeidler, S. (2017). Absorption and scattering by interstellar dust in the silicon K-edge of GX 5-1. *A&A*, 599:A117.
- Zeidler, S., Posch, T., and Mutschke, H. (2013). Optical constants of refractory oxides at high temperatures. Mid-infrared properties of corundum, spinel, and  $\alpha$ -quartz, potential carriers of the 13  $\mu\text{m}$  feature. *A&A*, 553:A81.



## Abstract

*Aims* We present a study on the prospects of observing carbon, sulfur, and other lower abundance elements (namely Al, Ca, Ti and Ni) present in the interstellar medium using future X-ray instruments. We focus in particular on the detection and characterization of interstellar dust along the lines of sight.

*Methods* We compare the simulated data with different sets of dust aggregates, either obtained from past literature or measured by us using the SOLEIL-LUCIA synchrotron beamline. Extinction by interstellar grains induces modulations of a given photoelectric edge, which can be in principle traced back to the chemistry of the absorbing grains. We simulated data of instruments with characteristics of resolution and sensitivity of the current *Athena*, XARM and Arcus concepts.

*Results* In the relatively near future, the depletion and abundances of the elements under study will be determined with confidence. In the case of carbon and sulfur, the characterization of the chemistry of the absorbing dust will be also determined. For aluminum and calcium, despite the large depletion in the interstellar medium and the prominent dust absorption, in many cases the edge feature may not be changing significantly with the change of chemistry in the Al- or Ca- bearing compounds. The extinction signature of large grains may be detected and modeled, allowing a test on different grain size distributions for these elements. The low cosmic abundance of Ti and Ni will not allow us a detailed study of the edge features.

## 4.1 Introduction

Absorption and scattering in the X-ray band has proved a useful diagnostic of the interstellar dust (ID) properties. By virtue of the broad band coverage, the X-ray band displays many photoelectric absorption edges, caused by the mixture of gas and dust intervening along the line of sight towards bright background sources (Draine, 2003; Hoffman and Draine, 2016). Absorption by interstellar grains is detected as a result of the interaction between the incoming X-ray photon and the electrons inside the grain's atoms. The multiple-generated photoelectron-waves interfere with each other both constructively and destructively. This interference pattern depends on the complexity of the chemical compound and the distance of the electrons from the nucleus. Each pattern is a fingerprint of a given material (Rehr and Albers, 2000). The extinction cross section, the sum of the absorption and scattering cross section (e.g., Draine, 2003; Corrales et al., 2016) in the X-ray band, provides, in principle, not only direct estimate on the chemistry of the interstellar medium (ISM), but also information on the size distribution, crystallinity and porosity of the intervening grains (Hoffman and Draine, 2016; Zeegers et al., 2017; Rogantini et al., 2018). In recent years, the deep features of the Fe L and O K and Si K-edges have been studied using the grating spectrometers on board the X-ray Observatories *Chandra* and *XMM-Newton*. These studies made use of absorption profiles either taken from the literature (Costantini et al., 2012; Pinto et al., 2010, 2013; Valencic and Smith, 2013) or obtained with dedicated synchrotron measurements (Lee et al., 2009; Zeegers et al., 2017).

Outside the energy band where the sensitivity and resolution of the current instruments is maximized, it is at this moment challenging to study interstellar dust. An example is given by the tentative study of the C K-edge (Schneider and Schmitt, 2010), which was severely hampered by various instrumental effects, although the carbon edge would formally be included in the energy range of *Chandra*-LETGS.

In this chapter, we investigate the prospective of observing and modeling the elements of the ID which have not been yet studied, which happen to fall in the 1.5–8.3 keV band (Al, S, Ca, Ti, Ni) and at  $E < 0.5$  keV (carbon).

In Fig. 4.1 we show the abundance pattern of the photoelectric absorption edges of the elements (with atomic number  $A=6-30$ ) as a function of the X-ray energy. The empty diamonds mark the edges that have been already studied by current instruments unveiling the dust features: the O K and Fe L-edges at 0.534 and 0.7 keV respectively (Lee et al., 2009; Costantini et al., 2012; Pinto et al., 2010, 2013; Valencic and Smith, 2013); the Mg and Si K-edges at 1.3 and 1.84 keV respectively (Zeegers et al., 2017, Rogantini et al. in prep.). The black triangles mark the edges presented in this work. We present the Fe K-edge, marked with a light gray triangle in the figure, in a separate paper (Rogantini et al., 2018), but see also (Lee and Ravel, 2005). The middle panel shows the range of depletion, defined as the amount of dust over the total amount of matter in the ISM (dust and gas) that is expected for a given element. The wide range of depletions for some elements is due to the different density environments where those are observed (e.g., Jenkins, 2009).

In the lower panel of Fig. 4.1 we show the energy range of present and future missions. The solid line highlights the region where the instrument capabilities (resolution and effective

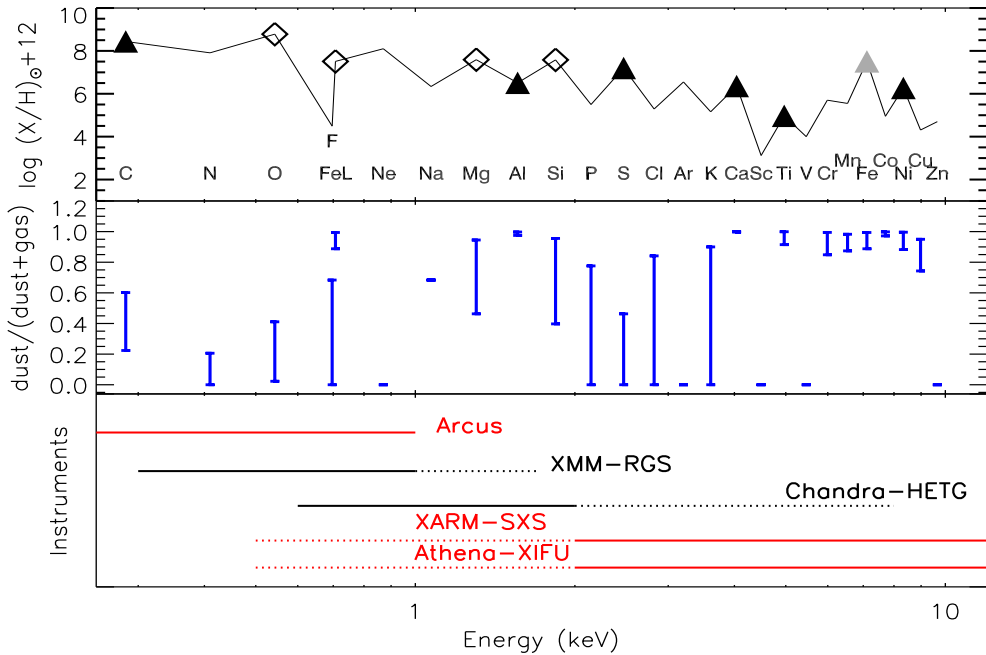


**Figure 4.1:** Upper panel: abundance pattern as a function of energy for the absorbing elements in the X-ray band. The K-edge energy is indicated, except from Fe, for which both the K- and the L-edges, at 7.1 and  $\sim 0.7$  keV, respectively, can be studied. Abundances follow Lodders (2010) and they are expressed in terms of  $\log(X/H)+12$ . In this frame, the abundance of hydrogen is 12. The open diamond mark the elements that are accessible by current instruments. The triangles are the relevant elements that will be accessible by future instruments to study dust. The black triangles are the subject of this work. Middle panel: range of depletions as reported by Jenkins (2009) for all elements, except: C (Jenkins, 2009; Whittet, 2003), F (Snow et al., 2007), Na (Turner, 1991), S (Gry and Jenkins, 2017), K (Snow, 1975), Ca (Crinklaw et al., 1994), Co (Federman et al., 1993), Al (Jenkins and Wallerstein, 1996), Ar (Sofia and Jenkins, 1998). Lower panel: energy range covered by present and future (red) missions. The solid line highlights the energy range where the capabilities of the instruments are optimal for observing absorption by dust.

area) are optimal to observe the dust absorption features. The *Chandra* and *XMM-Newton* observatory (both launched in 1999, Weisskopf, 1999; Jansen et al., 2001) are still in operation. The grating spectrometer *Arcus* will cover the soft X-ray range (Table 4.2). It is a NASA mission currently in the study phase, with a possible launch date of 2023 (Smith et al., 2016). The calorimeter on board of the X-ray Astronomy Recovery Mission (XARM, to be launched around 2020)<sup>1</sup> is planned to have the same characteristics of the one on board of the lost *Hitomi* satellite (Mitsuda et al., 2014). Finally, we display the energy coverage of the *Athena* calorimeter XIFU (Barret et al., 2016), to be launched in 2030. Both XARM and *Athena's* calorimeter will be optimal to observe the higher energy dust features (Table 4.2).

#### 4.1.1 The elements in this study

One of the major players in the ID, carbon, constitutes around 20% of the total depleted mass in the Galaxy (Whittet, 2003). Its depletion covers a relatively narrow range of values, (Figure 4.1) showing that it is not a strong function of environmental density. It has been hypothesized that the majority of carbon should be locked in graphite grains, as a likely explanation for the 2175 Å emission feature (Draine, 1989, 2003, and references therein). Graphite has been commonly adopted in ID models (e.g., Mathis et al., 1977). However, observational evidences pointed out that graphite could not explain the variability of the 2175 Å feature (Fitzpatrick and Massa, 2007). Furthermore, in analogy with the silicates, which are found to be amorphous, also graphite was deemed unlikely to survive in large quantities in the harsh environment of the ISM. Graphite should therefore face a natural process of amorphisation (Compiègne et al., 2011).

The idea of carbon as a single and separate phase from the silicate population does not agree with a scenario of a constantly evolving and mixing medium (Jones et al., 2017). Hydrogenated Amorphous Carbon (HAC) may indeed coat the silicate grains, forming a single population (e.g., Duley et al., 1989), with different characteristics with respect to the environment where they reside and depending on the particle size (e.g., Jones et al., 2017, and references therein). However, this scenario has so far not been confirmed by polarization studies. The carbon feature at 3.4 μm shows a negligible degree of polarization with respect to the silicate feature at 9.7 μm, pointing to two distinct grain populations (Whittet, 2011).

Finally, under special condition of high pressure, for instance in a shocked environment, graphite and amorphous carbon can turn into nano-diamonds, which can constitute as much as 5% of the amount of C in the ISM (Tielens et al., 1987), possibly with H and N inclusion (Van Kerckhoven et al., 2002; Bilalbegović et al., 2018). Diamonds of possible ISM origin have been found in meteorites (Lewis et al., 1987). An important carbon carrier are Polycyclic Aromatic Hydrocarbons (PAH), large (Å-sized) molecules formed by carbon and hydrogen in a honeycomb structure. They constitute up to about 10% of the carbon abundance (e.g., Tielens, 2013). PAHs are quite sensitive to ionizing radiation from far-ultraviolet to X-rays and they are easily destroyed near star formation sites at AU distance scale (e.g., Siebenmorgen and Krügel, 2010), up to kpc scale, for active galaxies (Voit, 1992).

A part from C, other constituents can be studied in detail by future generation telescopes.

Sulfur in dust phase seems to be absent from the diffuse ISM (Sembach and Savage, 1996). However, a relative fast transition to a depletion approaching -1 dex is reported in

<sup>1</sup>the XARM mission has been recently renamed XRISM (X-Ray Imaging Spectroscopy Mission)

dense media, such as molecular clouds (Joseph et al., 1986). In molecular clouds, sulfur can be included in aggregates such as  $\text{H}_2\text{S}$ ,  $\text{SO}_2$ ,  $\text{OCS}$ ,  $\text{SO}$ ,  $\text{H}_2\text{CS}$ ,  $\text{NS SiS}$ ,  $\text{CS}$ ,  $\text{HNCS}$ ,  $\text{CH}_3\text{SH}$  (Duley et al., 1980, and references therein) as well as other carbon-hydrogen bearing sulfates (e.g., Bilalbegović and Baranović, 2015). Molecular reactions may also lead to sulfur aggregation into polymeric forms, like  $\text{S}_8$  (e.g., Jiménez-Escobar and Muñoz Caro, 2011). However, even integrating the contribution of all S-bearing molecules, the absolute abundance of sulfur in molecular clouds compared to the diffuse ISM one, with a ratio of  $\sim 10^{-8}/10^{-5}$  is inexplicably low (Wakelam and Herbst, 2008). Inclusion into simple atomic sulfur or sulfur ices have been proposed to solve the missing-sulfur problem in molecular clouds (e.g., Vidal et al., 2017).

Sulfur in dust has been also detected near C-rich AGB stars, planetary nebulae (Hony et al., 2002) and protoplanetary disks (Keller et al., 2002), predominantly in form of troilite ( $\text{FeS}$ ). Finally, sulfur is abundant in solid form in planetary systems bodies, such as interplanetary dust particles, meteorites and comets (e.g., Wooden, 2008, and references therein).

The presence of sulfur in dust form in the ISM has been suggested in association with GEMS (Glasses with Embedded Metal and Sulfides, Bradley, 1994), where the  $\text{FeS}$  particles would be more concentrated on the surface of the glassy silicate. However, the majority of GEMS may well be of nebular origin, rather than the ISM (Keller and Messenger, 2008). Sulfur in  $\text{FeS}$ , consistent to be of ISM origin, has been recorded in the data from the Stardust mission (Westphal et al., 2014). This evidence revitalizes the idea of the presence of sulfur in dust-form also in less dense environments of the ISM. The presence of strong UV radiation and cosmic rays has been thought to be the cause for the extreme sputtering of the highly volatile S, for example from GEMS surfaces. Recent experiments however put to the test this hypothesis (Keller et al., 2010), showing that UV bombardment has in fact little influence on sulfur stuck on a grain surface.

Aluminum, calcium and titanium are extremely depleted in the ISM (Fig. 4.1). Ca and Ti show also a very similar depletion pattern as a function of gas density (Cranklaw et al., 1994). These two elements are found in gas only in tenuous environments, associated with warm inter cloud media in both the halo (Edgar and Savage, 1989) and the disk of the Galaxy (Cranklaw et al., 1994). The depletion of Ti is severe, regardless of the environment, ranging between -1 dex and -3.1 dex (Welty and Crowther, 2010). The ratio of column density between Ti II and Ca II, representative of the element neutral gas phase, is in general constant in the Galaxy ( $\sim 0.4$ , Hunter et al., 2006). Al, Ca and Ti have a similar condensation temperature (1400–1600 K, Field, 1974) and it has been hypothesized that, being the first to form in e.g., a stellar envelope or a supernova environment, they would form the core of complex dust grains with silicate and possibly ice mantles (e.g., Clayton, 1978). This would provide a natural shield for these Al, Ca, Ti-bearing compounds, preventing their destruction and ensuring a high depletion in the vast majority of the environments. Under the condition of thermodynamic equilibrium, aluminum first condenses in  $\text{Al}_2\text{O}_3$ . From there it may evolve into spinel ( $\text{MgAl}_2\text{O}_4$ ) and eventually into a Ca and Al-bearing silicate. The latter are stable compounds, thanks to very high binding energies (Trivedi and Larimer, 1981). Calcium is mostly locked in dust in silicates (e.g.,  $\text{CaMgSi}_2\text{O}_6$ , Field, 1974; Trivedi and Larimer, 1981). Calcium carbonates, possibly formed in AGB stars envelopes (e.g., Kemper et al., 2002), are believed to be unstable and therefore Ca inclusion in silicates, which form already at high temperatures, are favored (Ferrarotti and Gail, 2005). Titanium is produced by AGB stars mostly

**Table 4.1:** Samples of interstellar dust analogues used in this work

Specie	Name	atom	Ref	$E_{\text{SPEX}}$ (eV)	$E_{\text{Henke}}$ (eV)
C	graphite	C	Albella and Banks (1998)	2880	2842
AC	amorphous carbon	C	Albella and Banks (1998)		
HAC	hydrogenated amorphous carbon	C	Buijnsters et al. (2009)		
C	diamond	C	Albella and Banks (1998)		
$\text{MgAl}_2\text{O}_4$	spinel	Al	this work	1564	1559
$\text{Al}_2\text{O}_3$	aluminum oxide	Al	this work		
$\text{FeS}_2$	pyrite	S	Bonnin-Mosbah et al. (2002)		
$\text{FeS}$	troilite	S	<sup>1</sup>		
$\text{Fe}_{0.875}\text{S}$	pyrrhotite	S	<sup>1</sup>		
$\text{CaMgSi}_2\text{O}_6$	diopside crystal	Ca	Neuvill et al. (2007)	4041	4038
$\text{CaMgSi}_2\text{O}_6$	diopside glass	Ca	Neuvill et al. (2007)		
$\text{Ca}_3\text{Al}_2\text{O}_6$	tricalcium aluminate	Ca	Neuvill et al. (2007)		
$\text{CaAl}_2\text{O}_4$	calcium aluminate	Ca	Neuvill et al. (2007)		
$\text{TiO}_2$	titanium dioxide	Ti	Shin et al. (2013)	<sup>2</sup>	4966
Ni	metallic nickel	Ni	Van Loon et al. (2015)	8338	8331

<sup>1</sup> <http://www.esrf.eu/home/UsersAndScience/Experiments/XNP/ID21/php/Database-SCompounds.html>

<sup>2</sup> the Ti edge is not by default implemented in the SPEX model.

in the form of  $\text{TiO}_2$ , which constitute a seed nucleus later included in the larger/coated grains (e.g., Ferrarotti and Gail, 2006).

Nickel depletion is found to correlate with the one of Fe for a variety of environments, from planetary nebulae (Delgado-Inglada et al., 2016) to diffuse interstellar clouds (Jenkins, 2009). These two elements display a similar condensation temperature (1336 and 1354 K for Fe and Ni, respectively Wasson, 1985), which already point to a simultaneous inclusion into dust grains. However, it has been observed that in dense environments Ni is more depleted than Fe (e.g., Sembach and Savage, 1996; Delgado-Inglada et al., 2016).

## 4.2 Extinction profiles

In this chapter, we make use of literature values to infer the absorption absolute cross sections for all elements, except for Al (Sect. 4.2.1). Measurements of X-ray edges profiles are mostly carried out for industry and are rarely of interest for astronomical applications. For this reason, the sample selection is bound to be incomplete. The compounds used are listed in Table 4.1. We follow closely the method presented in Chapter 2 and Rogantini et al. (2018) to obtain the extinction profiles to be confronted to the astronomical data. The laboratory data are transformed to transmission spectra and matched (via  $\chi^2$  fitting) to tabulated transmission data of the same compound, where we assume an optically thin sample, as to mimic the conditions in the ISM. The transmission tables are provided by the Center for X-ray Optics at Lawrence Berkeley National laboratory based on tabulated data by Henke et al. (1993). From the trans-

mission spectra, the attenuation coefficient can be obtained and consequently we can obtain the imaginary part of the refractive index from this coefficient. The real part of the refractive index  $m$ , is calculated via the Kramers-Kronig relations (Bohren, 2010). The knowledge of  $m$  is needed in order to calculate the extinction cross section to involve both the effect of absorption and scattering. The extinction cross sections are calculated using Mie theory (Mie, 1908; Wiscombe, 1980) for C, Al and S. We used instead the anomalous diffraction theory (ADT, Van der Hulst 1957) for Ca, Ti and Ni. The ADT theory can be used when the ratio  $x = 2\pi a/\lambda \gg 1$  where  $a$  is the grain size and  $\lambda$  is the wavelength of the incident radiation. In order to obtain the extinction cross section for a range of dust grain radii, we assume the MRN size distribution (Mathis et al. 1977). The grain size is weighted by a power law of slope  $-3.5$  within a grain size range  $0.025\text{--}0.25 \mu\text{m}$ . Once the absolute cross section as a function of energy has been obtained, we implemented the extinction profiles in the already existing AMOL model in the fitting code SPEX (ver. 3.03, Kaastra et al., 1996). We note however that the edge energy as tabulated by Henke et al. (1993), may differ from the Verner cross sections implemented in SPEX (Verner et al., 1996). In this chapter, we apply a shift to the laboratory data in order to consistently compare them with the edge features as seen by SPEX. Those shifts are sometimes noticeable (Table 4.1).

#### 4.2.1 Laboratory data for aluminum

For Al, we made use of the laboratory data that we collected at the LUCIA beamline at the Soleil synchrotron facility. Both the samples,  $\text{Al}_2\text{O}_3$  and  $\text{MgAl}_2\text{O}_4$ , were commercially available from the Alfa-Aesar and Aldrich company, respectively. The samples, in powder form, were pressed on thin indium foil, placed on a copper support which was placed in a vacuum environment. The sample was then irradiated by an X-ray beam of which the energy is tuneable. The X-ray fine structures were measured through fluorescence. At these soft X-ray energies, this method is more practical than the more intuitive method of measuring the transmission through the sample, because for transmission measurements the samples have to be too thin to be easily handled. The fluorescent method to obtain the XAFS does require a correction for possible saturation. This correction was performed with the program FLUO, which is part of the UWXAFS software (Stern et al., 1995). A full description of the procedure for the analysis of the data can be found in Chapter 2.

### 4.3 Simulations

We present the prospects of detecting absorption K-edges relevant for dust studies using future missions (Fig. 4.1). The only instrument proposed for studying the soft X-ray energy band is, at this moment, the Arcus grating spectrometer<sup>2</sup> (Smith et al., 2016). For the energy above  $\sim 2$  keV, two microcalorimeters will provide an unprecedented resolution: *Resolve* and XIFU, on board of XARM<sup>3</sup> and *Athena*<sup>4</sup> (Nandra et al., 2013), respectively. The effective area and the resolving power of these three instruments at the energy of the features studied here are

---

<sup>2</sup><http://www.arcusxray.org/>

<sup>3</sup><https://heasarc.gsfc.nasa.gov/docs/xarm/>

<sup>4</sup><http://www.the-athena-x-ray-observatory.eu/>

reported in Table 4.2. With the chosen exposure time, we would obtain an associated error on the dust or gas column density of around 1% for C (Arcus) Al, S and Ca (XIFU).

The simulations were carried out having in mind realistic scenarios in our Galaxy, in order to prove the effective prospect of future instruments to measure physical parameters. We first simulated the data, considering the different instruments responses and including noise, assuming first that the photoelectric edge is only due to gas absorption. These simulations are confronted with models, folded with the appropriate response, which include an amount of gas set by the typical depletion found in the literature for a given element plus the contribution of a dust compound. We adopted the MRN dust size distribution in all cases (Mathis et al., 1977). However, the exceptional depletion of Al and Ca, joint to favorable observing conditions allowed us to test also the detectability of a distribution where the mass distribution is skewed towards larger grains (Draine and Fraisse, 2009). This distribution has a size range of  $a = 0.02 - 1 \mu\text{m}$ , with an average grain size of  $0.6 \mu\text{m}$ . The observing conditions are favorable for these two elements first because the brightness of the sources with a favorable  $N_{\text{H}}$  is often high (e.g., low mass X-ray binaries, LMXB, near the galactic center) and, second, the edges fall in a large effective-area region of the instrument.

The depletion of carbon has been optimistically assumed to be 0.6, but still implies a substantial role in gas absorption in the carbon edge. For this reason, although the edge feature itself can also be detected at relatively small column density (e.g.,  $N_{\text{H}} \sim 10^{20} \text{cm}^{-2}$ ), a much larger amount of matter is necessary to make the dust features evident. Here we simulated a column density of  $N_{\text{H}} = 1.6 \times 10^{21} \text{cm}^{-2}$  for a flux in the soft energy band of  $\sim 3 \times 10^{-9} \text{erg cm}^{-2} \text{s}^{-1}$  (Fig. 4.2). Note that for this column density, the CI absorption lines from gas are already saturated (Fig. 4.2), therefore they cannot be used straightforwardly to measure depletion. Although this value for a column density is not uncommon for LMXB, the source needs to be in an hypothetical high state to be well detected by an Arcus-like instrument as the effective area of such an instrument would fall rapidly at the carbon edge.

The cosmic abundance of Al is significantly less than the main ID components (Fig. 4.1). However, Al in the ISM is almost completely depleted into dust. We simulate here the contribution of  $\text{Al}_2\text{O}_3$  and  $\text{MgAl}_2\text{O}_4$  and compare them with a theoretical pure gas absorption (Fig. 4.3). At ISM temperature, Al, if it was totally in gas form, would be distributed between Al I and Al II. For this simulation, we selected the bright LMXB ( $F_{2-10 \text{keV}} \sim 3 \times 10^{-9} \text{erg cm}^{-2} \text{s}^{-1}$ ) GX 3+1 whose spectral parameters were obtained from *Chandra*-HETGS data (obsid 16492).

For the sulfur simulation (see Figure 4.4), we selected GX 5-1, which is among the brightest LMXB in the Galaxy, with a  $F_{2-10 \text{keV}} \sim 2.5 \times 10^{-8} \text{erg cm}^{-2} \text{s}^{-1}$ . The hydrogen column density is about  $3.4 \times 10^{22} \text{cm}^{-2}$  (Zeegers et al., 2017). The depletion of sulfur is unknown in the diffuse ISM, but it has been estimated that could be up to  $\sim 46\%$  (Fig. 4.1 and Gry and Jenkins, 2017). Here we simulate a more conservative 30% depletion. Given the relatively low depletion of S, the XAFS features (Fig. 4.8) would be less evident in the data.

The X-ray spectrum will be sensitive to calcium extinction only if the intervening column density is sufficiently high. This is due to the relatively high energy position of the photoelectric edge. Here we simulated GX 340+00 ( $F_{2-10 \text{keV}} \sim 2.5 \times 10^{-8} \text{erg cm}^{-2} \text{s}^{-1}$ ), with a column density of about  $N_{\text{H}} \sim 6.9 \times 10^{22} \text{cm}^{-2}$ , obtained from HETG-*Chandra* data fitting (obsid 6632).

For both titanium and nickel, we simulated a hypothetical source, for example near the

Table 4.2: Parameters of the instruments used in the simulations at the energy of the elements studied here.

Element	R E/ $\Delta E$	$A_E^{Eff}$ cm <sup>2</sup>	Inst.
C	2540	390	Arcus
Al	596	13898	XIFU
S	911(455)	7335(209)	XIFU(Resolve)
Ca	1545(772)	5471(271)	XIFU(Resolve)
Ti	1940	4211	XIFU
Ni	3290	1100	XIFU

GC, where also the occurrence of high column density molecular clouds is more frequent, that in outburst reaches a flux as high as GX 340+00. The column density must be sufficient to produce an edge-like modulation in the spectrum ( $N_H \sim 1.3 \times 10^{23} \text{ cm}^{-2}$ ).

## 4.4 Discussion

### 4.4.1 Carbon

In the simulation (see Figure 4.2), we included gas and the carbon forms that are believed to be most abundant (namely graphite, amorphous carbon and HAC). While the difference between graphite and amorphous carbon is subtle, HAC does have more distinctive features that may be more easily detected. The hydrogenation of carbon may point to either an environment protected from strong radiation or the presence of large grains, which are more resilient to radiation (Sect. 4.1.1).

For illustrative purposes, we also include diamonds (orange dashed line) in order to show the departure of this form of carbon from the shape of e.g., graphite. However, in practice, diamonds are believed to constitute no more than 5% of the carbon (Tielens, 2001). Its realistic inclusion would be non-detectable (dashed-dotted blue line in Figure 4.2). The same negligible effect may be produced by PAH, which we did not include in our simulation. The total amount along a line of sight is relatively low (Sect. 4.1.1) and the spectral features of PAH would be mixed with a more dominant amorphous carbon (or graphite) contribution. The sparse historical studies of PAH absorption profiles for the X-ray region have been recently revived (Reitsma et al., 2014, 2015). This will help in defining a shape for the summed contribution of the numerous different PAH in the ISM.

Furthermore, the carbon edge is not very sensitive to the size distribution of the grains (Draine, 2003).

### 4.4.2 Aluminum and calcium

The XIFU simulation shows that dust will be easily detectable, even if the edge itself produced a jump in the spectrum of only few %. However, from the Al edge alone, it would be difficult

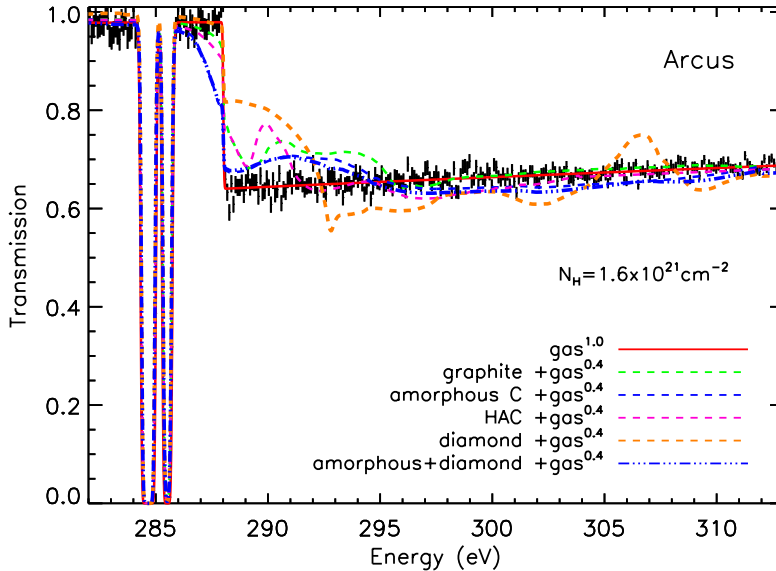


**Figure 4.2:** A 500 ks simulation of the carbon K-edge, using the Arcus grating, of an XRB in high state ( $F_{0.5-2 \text{ keV}} \sim 3 \times 10^{-9} \text{ erg cm}^{-2} \text{ s}^{-1}$ ). The simulation considers different carbon species, with a dust depletion of 60%. The two absorption lines belong to the atomic phase of C, namely C I.

to distinguish among different compounds.

We also note that contrary to other extinction profiles, the scattering peak, which appears as an emission-like feature before the edge-jump, is noticeable in Al. This peak is sensitive to the dust size distribution (Zeegers et al., 2017) and can be used, in principle, to estimate e.g., the mean grain size along the line of sight. As described above, we also tested the effect of the dust size distribution of Draine and Fraisse (2009) for  $\text{Al}_2\text{O}_3$ . The edge energy of Al lies in a zone sensitive to scattering (Draine, 2003), therefore in Fig. 4.3 the large particles contribution is evident. As shown in Rogantini et al. (2018), the role of a substantial scattering contribution to the extinction not only forces the edge energy to shift, but may also modify the appearance of the edge absorption features. Grains containing seeds of Al and Ca, which are shielded from erosion in the ISM, are believed to be of large size, due to the several layers of coatings surrounding those seeds elements (e.g., Clayton, 1978, and Sect. 4.1.1). With future instruments, we will therefore be able to test also the presence of larger particles for less abundant, but important, constituents of the ISM. The study of the Al edge will be however challenging, as Al is always a major component of X-ray space instruments (often in the form of foils). The extinction feature from Al in the ISM will be always blended with a relatively deep instrumental Al feature. This would need a careful calibration, adding uncertainty to the modeling.

Calcium is totally depleted in the ISM, therefore the main dust features will be detected (Fig. 4.5). However, calcium is mostly contained in silicates and aluminates, where oxygen is the main constituent. XAFS models shows that the first and main absorption feature is due to the nearest neighboring atom that the photoelectron wave will encounter (Lee and

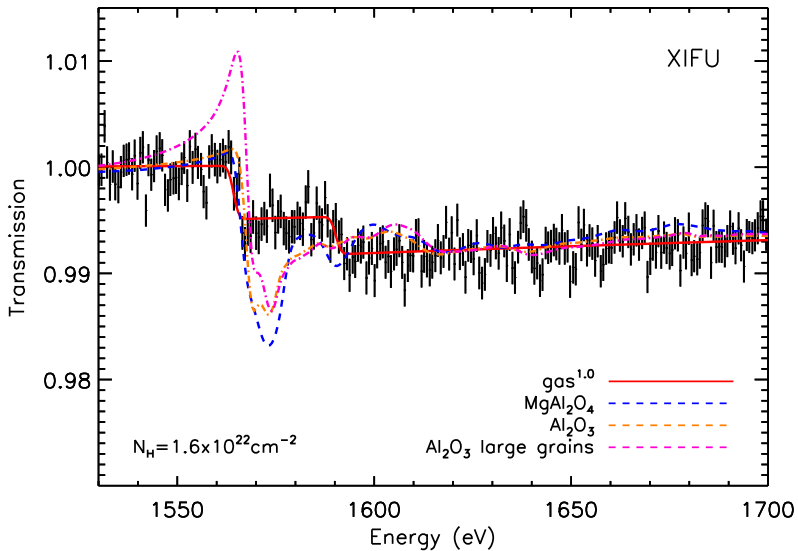


**Figure 4.3:** A 300 ks simulation of the aluminum K-edge, using the XIFU calorimeter, of the bright XRB GX 3+1 ( $F_{2-10\text{keV}} \sim 3 \times 10^{-9} \text{ erg cm}^{-2} \text{ s}^{-1}$ ). The dust depletion is 100%. The data have been binned for clarity.

Ravel, 2005). In the case simulated here, the absorption profile is dominated by oxygen (as is the case, to a lesser extent, in the Al edge), and only at higher energies are the secondary absorption features to be seen. For this reason, the Ca inclusion in a specific silicate may be hard to disentangle through the observed spectrum. However, calcite ( $\text{CaCO}_3$ , dashed orange line), due to its different internal structure, will show a distinctive pattern, which may be in principle disentangled. This will help in determining whether this elusive compound (Kemper et al., 2002) may be present in the ISM. We tested the contribution of possible large grains on anorthite (blue dashed-dotted line in Fig. 4.5). The contribution of larger grains does not produce a well detectable feature.

#### 4.4.3 Sulfur

In the diffuse ISM, sulfur is expected to have a modest depletion (Sect. 4.1.1). We use sulfur in conjunction with iron in the form of troilite, pyrothite and pyrite. FeS is a likely candidate for a diffuse interstellar environment, due to its inclusion in GEMS (Bradley, 1994; Bradley et al., 1999). The line of sight towards GX 5-1, at distance of  $\sim 9$  kpc is likely to cross also molecular clouds and this would apply for any source located near the galactic center. The dust inclusion of sulfur in molecular clouds is still an open issue (Sect. 4.1.1). Some of the S must be associated to ices and carbon-hydrogen aggregates, while the rest may be in the form of FeS or atomic gas. Even the sum of all known S-bearing molecules would be unlikely to exceed few % of the total S abundance. Therefore any significant depletion detected by XARM or XIFU would naturally point to the role of S in GEMS. This amount of S depletion would still not procure visible deviations from the observed total dust spectral energy distribution

(Köhler et al., 2014).

#### 4.4.4 Titanium and nickel

Due to its extremely low abundance in the Universe, titanium will be challenging to detect (Fig. 4.6). Nickel is about twenty times more abundant than Ti, however Ni will be also difficult to study (Fig. 4.7). The large column densities required to produce a Ni edge, will cause also strong absorption by iron, whose K absorption edge lies at 7100 eV, only 1.2 keV away from the one of nickel. Under the conditions of this simulation, the optical depth of iron will be around 18 times larger than the one of nickel. The net effect is that the Ni edge “sees” a continuum which is much lower than the one of the source, reducing the signal to noise ratio in that feature. Both titanium and nickel are however completely depleted in most ISM environments, therefore even a column density estimate will be useful to constrain the abundance of these two elements, which are a product of explosions of both massive stars and white dwarfs.

## 4.5 Conclusion

In this chapter, we have shown how improved instrumental sensitivity and resolution will help in understanding new aspects of the composition of ID. Our results can be summarized as follows:

Future instruments, with characteristics similar to the Arcus mission, will be able to disentangle between the major components of carbon, namely amorphous carbon (or graphite) and hydrogenated carbon. The effect of minor constituents of C in the ISM (e.g., nano-diamonds and PAH) will be challenging to detect.

Instruments with improved capabilities at energies  $>2$  keV as *Athena-XIFU* or *XARM-Resolve* will be able to determine the main chemical characteristics of elements like Al and Ca. It will be possible in particular to distinguish between calcium in carbonates and silicates, and investigate the dust size distribution of these heavily depleted elements.

*Athena-XIFU* or *XARM-Resolve* will be able to determine the depletion of sulfur in the ISM. This in turn will help clarify the S inclusion in GEMS, which are sometimes considered as one of the main forms of silicates in the ISM.

## Acknowledgements

Dust studies at Leiden Observatory are supported also through the Spinoza Premie of the Dutch science agency, NWO. The Netherlands Institute for Space Research is supported financially by NWO. E.C. and D.R. acknowledge the support of the NWO-VIDI grant 639.042.525. We acknowledge SOLEIL for provision of synchrotron radiation facilities and we would like to thank Delphine Vantelon for assistance in using the LUCIA beamline and Harald Mutschke for procuring the Al-bearing samples. We also thank Alessandra Candian for useful comments on the manuscript. This research made use of the Chandra Transmission Grating Catalog and archive (<http://tgcatalog.mit.edu>).

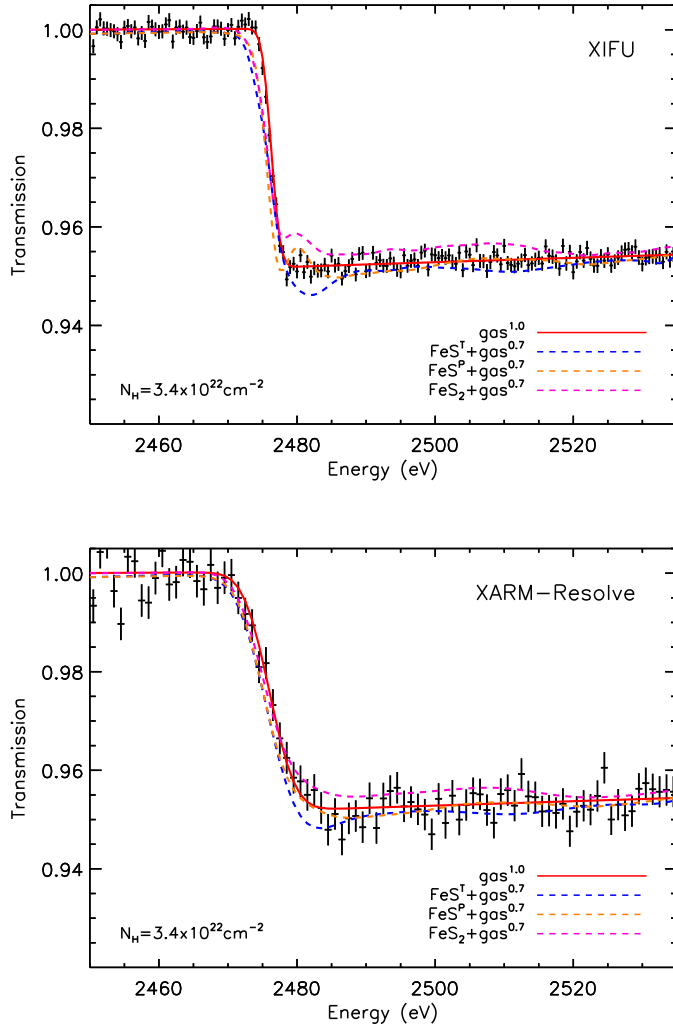


**Figure 4.4:** Simulation of the sulfur K-edge, using the XIFU calorimeter with an exposure time of 150 ks (top) and XARM-Resolve with a 400 ks exposure time (bottom), of a the bright XRB GX 5–1 ( $F_{2-10\text{keV}} \sim 2.5 \times 10^{-8} \text{ erg cm}^{-2} \text{ s}^{-1}$ ). The simulation considers different sulfur species, with a dust depletion of 30%.

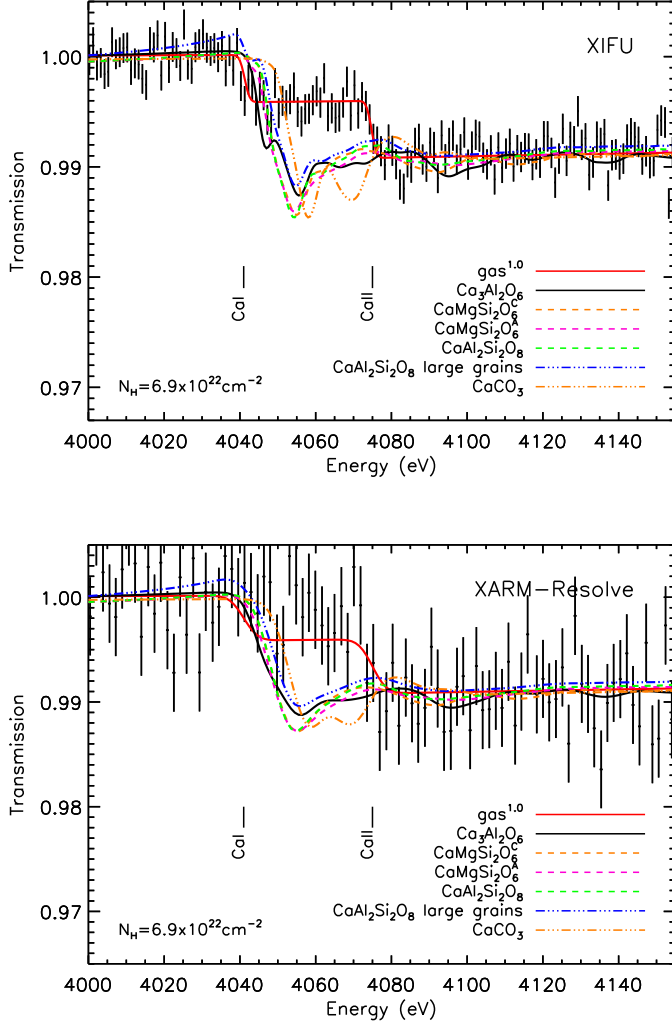


**Figure 4.5:** Simulation of the calcium K-edge, using the XIFU calorimeter with exposure time 300 ks, (top) and the XARM-Resolve with a 500 ks exposure time (bottom). We used the bright XRB GX 340+00 ( $F_{2-10\text{keV}} \sim 1.3 \times 10^{-8} \text{ erg cm}^{-2} \text{ s}^{-1}$ ). The simulation considers different calcium species, with a dust depletion of 100%. The data have been binned for clarity.

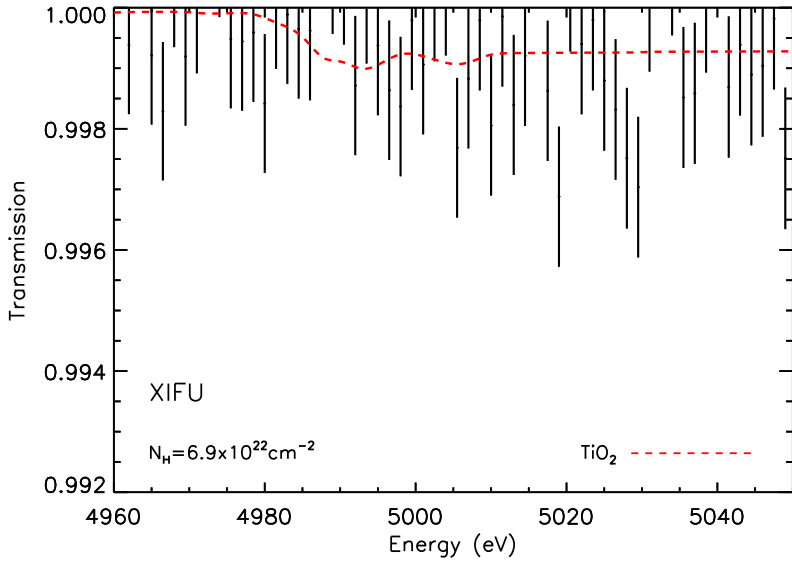


**Figure 4.6:** A 500 ks simulation of the titanium K-edge, using the XIFU calorimeter, using the bright XRB GX340+00 ( $F_{2-10\text{keV}} \sim 1.3 \times 10^{-8} \text{ erg cm}^{-2} \text{ s}^{-1}$ ) as template. The dust depletion is 100%. The data have been binned for clarity.

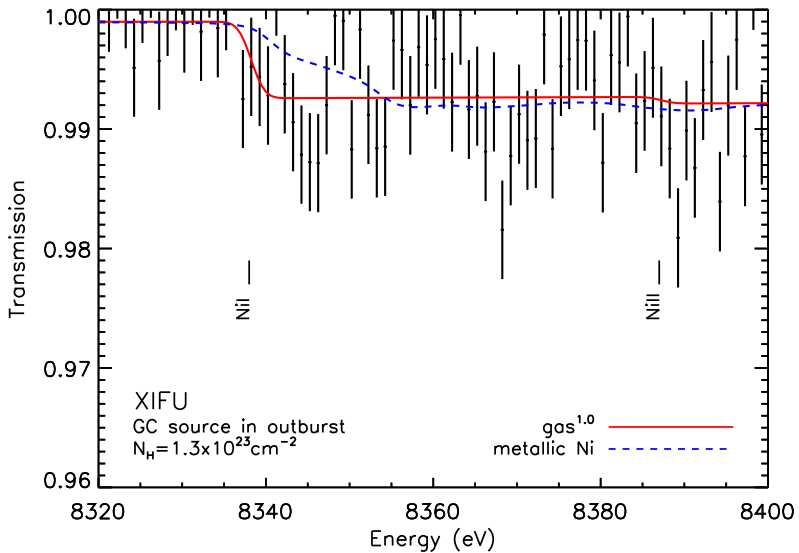


**Figure 4.7:** A 300 ks simulation of the nickel K-edge, using the XIFU calorimeter, assuming that a highly absorbed source near the GC reaches in outburst the same flux level as GX340+00 ( $F_{2-10\text{keV}} \sim 1.3 \times 10^{-8} \text{ erg cm}^{-2} \text{ s}^{-1}$ ). The dust depletion is 100%. The data have been binned for clarity.

## 4.A Extinction profiles

We show here the extinction profiles in transmission, normalized for the continuum, of the compounds presented in this chapter. Their formula and literature reference is reported in Table 4.1.

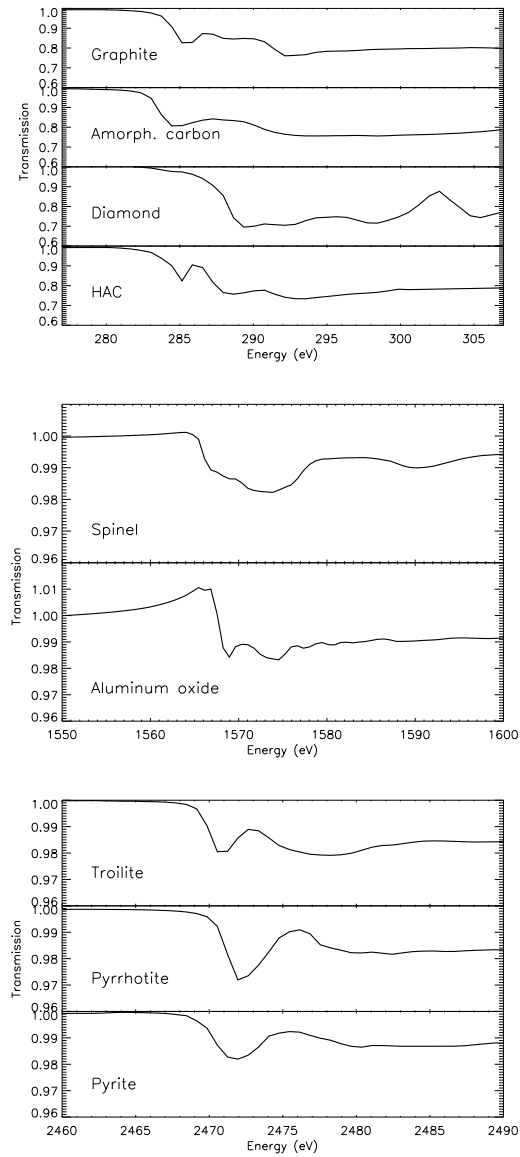


**Figure 4.8:** The extinction profiles of the C, Al and S compounds presented in this chapter. The dust column densities of the elements are the same used for the simulations. The edge energy is as reported in the literature as well as the original energy resolution.

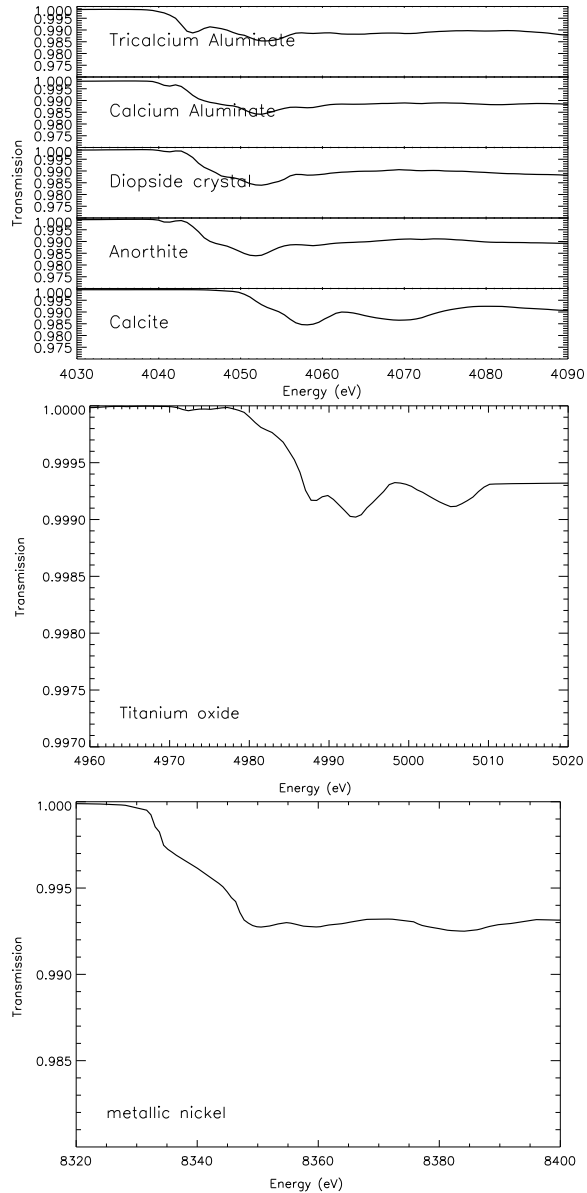


**Figure 4.9:** The extinction profiles of the Ca, Ti and Ni compounds presented in this chapter. The dust column densities of the elements are the same used for the simulations. The edge energy is as reported in the literature as well as the original energy resolution.

## References

- Albella, J. M. and Banks, D. K. a. (1998). Composition and Bonding in Amorphous Carbon Films Grown by Ion Beam Assisted Deposition: Influence of the Assistance Voltage. *Diamond and related materials, DRM elsevier*, 215:425–435.
- Barret, D., Lam Trong, T., den Herder, J.-W., and et al. (2016). The Athena X-ray Integral Field Unit (X-IFU). In *Space Telescopes and Instrumentation 2016: Ultraviolet to Gamma Ray*, volume 9905, page 99052F.
- Bilalbegović, G. and Baranović, G. (2015). Sulphur-bearing species in molecular clouds. *MNRAS*, 446:3118–3129.
- Bilalbegović, G., Maksimović, A., and Valencic, L. A. (2018). Tetrahedral hydrocarbon nanoparticles in space: X-ray spectra. *MNRAS*, 476:5358–5364.
- Bohren, C. F. (2010). What did kramers and kronig do and how did they do it? *European Journal of Physics*, 31(3):573.
- Bonnin-Mosbah, M., Métrich, N., Susini, J., Salomé, M., Massare, D., and Menez, B. (2002). Micro X-ray absorption near edge structure at the sulfur and iron K-edges in natural silicate glasses. *Spectrochimica Acta*, 57:711–725.
- Bradley, J. P. (1994). Chemically Anomalous, Preaccretionally Irradiated Grains in Interplanetary Dust From Comets. *Science*, 265:925–929.
- Bradley, J. P., Keller, L. P., Snow, T. P., Hanner, M. S., Flynn, G. J., Gezo, J. C., Clemett, S. J., Brownlee, D. E., and Bowey, J. E. (1999). An infrared spectral match between GEMS and interstellar grains. *Science*, 285.
- Buijnsters, J. G., Gago, R., Jiménez, I., Camero, M., Agulló-Rueda, F., and Gómez-Aleixandre, C. (2009). Hydrogen quantification in hydrogenated amorphous carbon films by infrared, Raman, and x-ray absorption near edge spectroscopies. *Journal of Applied Physics*, 105(9):093510–093510–7.
- Clayton, D. D. (1978). Precondensed matter - Key to the early solar system. *Moon and Planets*, 19:109–137.
- Compiègne, M., Verstraete, L., Jones, A., Bernard, J.-P., Boulanger, F., Flagey, N., Le Bourlot, J., Paradis, D., and Ysard, N. (2011). The global dust SED: tracing the nature and evolution of dust with DustEM. *A&A*, 525:A103.

- Corrales, L. R., García, J., Wilms, J., and Baganoff, F. (2016). The dust-scattering component of X-ray extinction: effects on continuum fitting and high-resolution absorption edge structure. *MNRAS*, 458:1345–1351.
- Costantini, E., Pinto, C., Kaastra, J. S., in't Zand, J. J. M., Freyberg, M. J., Kuiper, L., Méndez, M., de Vries, C. P., and Waters, L. B. F. M. (2012). XMM-Newton observation of 4U 1820-30. Broad band spectrum and the contribution of the cold interstellar medium. *A&A*, 539:A32.
- Crinklaw, G., Federman, S. R., and Joseph, C. L. (1994). The depletion of calcium in the interstellar medium. *ApJ*, 424:748–753.
- Delgado-Inglada, G., Mesa-Delgado, A., García-Rojas, J., Rodríguez, M., and Esteban, C. (2016). The Fe/Ni ratio in ionized nebulae: clues on dust depletion patterns. *MNRAS*, 456:3855–3865.
- Draine, B. (1989). On the Interpretation of the  $\lambda$  2175 Å Feature. In Allamandola, L. J. and Tielens, A. G. G. M., editors, *Interstellar Dust*, volume 135 of *IAU Symposium*, page 313.
- Draine, B. T. (2003). Interstellar Dust Grains. *ARA&A*, 41:241–289.
- Draine, B. T. and Fraisse, A. A. (2009). Polarized Far-Infrared and Submillimeter Emission from Interstellar Dust. *ApJ*, 696:1–11.
- Duley, W. W., Jones, A. P., and Williams, D. A. (1989). Hydrogenated amorphous carbon-coated silicate particles as a source of interstellar extinction. *MNRAS*, 236:709–725.
- Duley, W. W., Millar, T. J., and Williams, D. A. (1980). Interstellar chemistry of sulphur. *MNRAS*, 192:945–957.
- Edgar, R. J. and Savage, B. D. (1989). The density distribution of refractory elements away from the Galactic plane. *ApJ*, 340:762–774.
- Federman, S. R., Sheffer, Y., Lambert, D. L., and Gilliland, R. L. (1993). Detection of boron, cobalt, and other weak interstellar lines toward Zeta Ophiuchi. *ApJ*, 413:L51–L54.
- Ferrarotti, A. S. and Gail, H.-P. (2005). Mineral formation in stellar winds. V. Formation of calcium carbonate. *A&A*, 430:959–965.
- Ferrarotti, A. S. and Gail, H.-P. (2006). Composition and quantities of dust produced by AGB-stars and returned to the interstellar medium. *A&A*, 447:553–576.
- Field, G. B. (1974). Interstellar abundances: gas and dust. *ApJ*, 187:453–459.
- Fitzpatrick, E. L. and Massa, D. (2007). An Analysis of the Shapes of Interstellar Extinction Curves. V. The IR-through-UV Curve Morphology. *ApJ*, 663:320–341.
- Gry, C. and Jenkins, E. B. (2017). The nearby interstellar medium toward  $\alpha$  Leo. UV observations and modeling of a warm cloud within hot gas. *A&A*, 598:A31.

- Henke, B. L., Gullikson, E. M., and Davis, J. C. (1993). X-Ray Interactions: Photoabsorption, Scattering, Transmission, and Reflection at  $E = 50\text{--}30,000$  eV,  $Z = 1\text{--}92$ . *Atomic Data and Nuclear Data Tables*, 54:181–342.
- Hoffman, J. and Draine, B. T. (2016). Accurate Modeling of X-ray Extinction by Interstellar Grains. *ApJ*, 817:139.
- Hony, S., Waters, L. B. F. M., and Tielens, A. G. G. M. (2002). The carrier of the “30”  $\mu\text{m}$  emission feature in evolved stars. A simple model using magnesium sulfide. *A&A*, 390:533–553.
- Hunter, I., Smoker, J. V., Keenan, F. P., Ledoux, C., Jehin, E., Cabanac, R., Melo, C., and Bagnulo, S. (2006). Early-type stars observed in the ESO UVES Paranal Observatory Project - I. Interstellar NaI UV, TiII and CaII K observations\*. *MNRAS*, 367:1478–1514.
- Jansen, F., Lumb, D., Altieri, B., Clavel, J., Ehle, M., Erd, C., Gabriel, C., Guainazzi, M., Gondoin, P., Much, R., Munoz, R., Santos, M., Schartel, N., Texier, D., and Vacanti, G. (2001). XMM-Newton observatory. I. The spacecraft and operations. *A&A*, 365:L1–L6.
- Jenkins, E. B. (2009). A Unified Representation of Gas-Phase Element Depletions in the Interstellar Medium. *ApJ*, 700:1299–1348.
- Jenkins, E. B. and Wallerstein, G. (1996). Hubble Space Telescope Observations of Interstellar Lines in Three High-Latitude Stars. *ApJ*, 462:758.
- Jiménez-Escobar, A. and Muñoz Caro, G. M. (2011). Sulfur depletion in dense clouds and circumstellar regions. I.  $\text{H}_2\text{S}$  ice abundance and UV-photochemical reactions in the  $\text{H}_2\text{O}$ -matrix. *A&A*, 536:A91.
- Jones, A. P., Köhler, M., Ysard, N., Bocchio, M., and Verstraete, L. (2017). The global dust modelling framework THEMIS. *A&A*, 602:A46.
- Joseph, C. L., Snow, Jr., T. P., Seab, C. G., and Crutcher, R. M. (1986). Interstellar abundances in dense, moderately reddened lines of sight. I - Observational evidence for density-dependent depletion. *ApJ*, 309:771–782.
- Kaastra, J. S., Mewe, R., and Nieuwenhuijzen, H. (1996). SPEX: a new code for spectral analysis of X & UV spectra. In Yamashita, K. and Watanabe, T., editors, *UV and X-ray Spectroscopy of Astrophysical and Laboratory Plasmas*, pages 411–414.
- Keller, L. P., Hony, S., Bradley, J. P., Molster, F. J., Waters, L. B. F. M., Bouwman, J., de Koter, A., Brownlee, D. E., Flynn, G. J., Henning, T., and Mutschke, H. (2002). Identification of iron sulphide grains in protoplanetary disks. *Nature*, 417:148–150.
- Keller, L. P., Loeffler, M. J., Christoffersen, R., Dukes, C., Rahman, Z., and Baragiola, R. (2010). Irradiation of FeS: Implications for the Lifecycle of Sulfur in the Interstellar Medium and Presolar FeS Grains. In *Lunar and Planetary Science Conference*, volume 41 of *Lunar and Planetary Inst. Technical Report*, page 1172.

- Keller, L. P. and Messenger, S. (2008). Relict Amorphous Silicates in Stardust Samples. *Meteoritics and Planetary Science Supplement*, 43:5227.
- Kemper, F., Jäger, C., Waters, L. B. F. M., Henning, T., Molster, F. J., Barlow, M. J., Lim, T., and de Koter, A. (2002). Detection of carbonates in dust shells around evolved stars. *Nature*, 415:295–297.
- Köhler, M., Jones, A., and Ysard, N. (2014). A hidden reservoir of Fe/FeS in interstellar silicates? *A&A*, 565:L9.
- Lee, J. C. and Ravel, B. (2005). Determining the Grain Composition of the Interstellar Medium with High-Resolution X-Ray Spectroscopy. *ApJ*, 622:970–976.
- Lee, J. C., Xiang, J., Ravel, B., Kortright, J., and Flanagan, K. (2009). Condensed Matter Astrophysics: A Prescription for Determining the Species-specific Composition and Quantity of Interstellar Dust Using X-rays. *ApJ*, 702:970–979.
- Lewis, R. S., Ming, T., Wacker, J. F., Anders, E., and Steel, E. (1987). Interstellar diamonds in meteorites. *Nature*, 326:160–162.
- Lodders, K. (2010). Solar System Abundances of the Elements. *Astrophysics and Space Science Proceedings*, 16:379.
- Mathis, J. S., Rumpl, W., and Nordsieck, K. H. (1977). The size distribution of interstellar grains. *ApJ*, 217:425–433.
- Mie, G. (1908). Beiträge zur Optik trüber Medien, speziell kolloidaler Metallösungen. *Annalen der Physik*, 330:377–445.
- Mitsuda, K., Kelley, R. L., Akamatsu, H., Bialas, T., and et al. (2014). Soft x-ray spectrometer (SXS): the high-resolution cryogenic spectrometer onboard ASTRO-H. In *Space Telescopes and Instrumentation 2014: Ultraviolet to Gamma Ray*, volume 9144 of *Proc. SPIE*, page 91442A.
- Nandra, K., Barret, D., Barcons, X., Fabian, A., den Herder, J.-W., Piro, L., Watson, M., Adami, C., Aird, J., Afonso, J. M., and et al. (2013). The Hot and Energetic Universe: A White Paper presenting the science theme motivating the Athena+ mission. *ArXiv e-prints*.
- Neuville, D. R., Cormier, L., Roux, J., de Ligny, D., Flank, A.-M., Henderson, G. S., and Lagarde, P. (2007). An In Situ High Temperature Investigation of Cation Environments in Aluminate and Silicate Glasses and Liquids at the LUCIA Beamline. In Hedman, B. and Pianetta, P., editors, *X-ray Absorption Fine Structure - XAFS13*, volume 882 of *American Institute of Physics Conference Series*, pages 413–415.
- Pinto, C., Kaastra, J. S., Costantini, E., and de Vries, C. (2013). Interstellar medium composition through X-ray spectroscopy of low-mass X-ray binaries. *A&A*, 551:A25.
- Pinto, C., Kaastra, J. S., Costantini, E., and Verbunt, F. (2010). High-resolution X-ray spectroscopy of the interstellar medium. XMM-Newton observation of the LMXB GS 1826-238. *A&A*, 521:A79.

- Rehr, J. J. and Albers, R. C. (2000). Theoretical approaches to x-ray absorption fine structure. *Reviews of Modern Physics*, 72:621–654.
- Reitsma, G., Boschman, L., Deuzeman, M. J., González-Magaña, O., Hoekstra, S., Cazaux, S., Hoekstra, R., and Schlathölter, T. (2014). Deexcitation Dynamics of Superhydrogenated Polycyclic Aromatic Hydrocarbon Cations after Soft-x-Ray Absorption. *Physical Review Letters*, 113(5):053002.
- Reitsma, G., Boschman, L., Deuzeman, M. J., Hoekstra, S., Hoekstra, R., and Schlathölter, T. (2015). Near edge X-ray absorption mass spectrometry on coronene. *J. Chem. Phys.*, 142(2):024308.
- Rogantini, D., Costantini, E., Zeegers, S. T., de Vries, C. P., Bras, W., de Groot, F., Mutschke, H., and Waters, L. B. F. M. (2018). Investigating the interstellar dust through the Fe K-edge. *A&A*, 609:A22.
- Schneider, P. C. and Schmitt, J. H. M. M. (2010). X-raying the AU Microscopii debris disk. *A&A*, 516:A8.
- Sembach, K. R. and Savage, B. D. (1996). The Gas and Dust Abundances of Diffuse Halo Clouds in the Milky Way. *ApJ*, 457:211.
- Shin, S. I., Go, A., Kim, I. Y., and et al. (2013). A beneficial role of exfoliated layered metal oxide nanosheets in optimizing the electrocatalytic activity and pore structure of pt-reduced graphene oxide nanocomposites. *Energy Environ. Sci.*, 6:608.
- Siebenmorgen, R. and Krügel, E. (2010). The destruction and survival of polycyclic aromatic hydrocarbons in the disks of T Tauri stars. *A&A*, 511:A6.
- Smith, R. K., Abraham, M. H., Allured, R., Bautz, M., Bookbinder, J., and et al. (2016). Arcus: the x-ray grating spectrometer explorer. In *Space Telescopes and Instrumentation 2016: Ultraviolet to Gamma Ray*, volume 9905 of *Proc. SPIE*, page 99054M.
- Snow, T. P., Destree, J. D., and Jensen, A. G. (2007). The Abundance of Interstellar Fluorine and Its Implications. *ApJ*, 655:285–298.
- Snow, Jr., T. P. (1975). The depletion of interstellar elements and the interaction between gas and dust in space. *ApJ*, 202:L87–L90.
- Sofia, U. J. and Jenkins, E. B. (1998). Interstellar Medium Absorption Profile Spectrograph Observations of Interstellar Neutral Argon and the Implications for Partially Ionized Gas. *ApJ*, 499:951–965.
- Stern, E. A., Newville, M., Ravel, B., Yacoby, Y., and Haskel, D. (1995). The UWXAFS analysis package: philosophy and details. *Physica B Condensed Matter*, 208:117–120.
- Tielens, A. G. G. M. (2001). The Composition of Circumstellar and Interstellar Dust. In Woodward, C. E., Bica, M. D., and Shull, J. M., editors, *Tetons 4: Galactic Structure, Stars and the Interstellar Medium*, volume 231 of *Astronomical Society of the Pacific Conference Series*, page 92.

- Tielens, A. G. G. M. (2013). The molecular universe. *Reviews of Modern Physics*, 85:1021–1081.
- Tielens, A. G. G. M., Seab, C. G., Hollenbach, D. J., and McKee, C. F. (1987). Shock processing of interstellar dust - Diamonds in the sky. *ApJ*, 319:L109–L113.
- Trivedi, B. M. P. and Larimer, J. W. (1981). A semiempirical model for heavy element depletion in the interstellar medium. *ApJ*, 248:563–568.
- Turner, B. E. (1991). Observations and chemistry of interstellar refractory elements. *ApJ*, 376:573–598.
- Valencic, L. A. and Smith, R. K. (2013). Interstellar Abundances toward X Per, Revisited. *ApJ*, 770:22.
- Van Kerckhoven, C., Tielens, A. G. G. M., and Waelkens, C. (2002). Nanodiamonds around HD 97048 and Elias 1. *A&A*, 384:568–584.
- Van Loon, L. L., Throssell, C., and Dutton, M. D. (2015). Comparison of nickel speciation in workplace aerosol samples using sequential extraction analysis and x-ray absorption near-edge structure spectroscopy. *Environ. Sci.: Processes Impacts*, 17:922–931.
- Verner, D. A., Ferland, G. J., Korista, K. T., and Yakovlev, D. G. (1996). Atomic Data for Astrophysics. II. New Analytic FITS for Photoionization Cross Sections of Atoms and Ions. *ApJ*, 465:487.
- Vidal, T. H. G., Loison, J.-C., Jaziri, A. Y., Ruaud, M., Gratier, P., and Wakelam, V. (2017). On the reservoir of sulphur in dark clouds: chemistry and elemental abundance reconciled. *MNRAS*, 469:435–447.
- Voit, G. M. (1992). Destruction and survival of polycyclic aromatic hydrocarbons in active galaxies. *MNRAS*, 258:841–848.
- Wakelam, V. and Herbst, E. (2008). Polycyclic Aromatic Hydrocarbons in Dense Cloud Chemistry. *ApJ*, 680:371–383.
- Wasson, J. T. (1985). *Meteorites: Their record of early solar-system history*.
- Weisskopf, M. C. (1999). The Chandra X-Ray Observatory (CXO): An Overview. *ArXiv Astrophysics e-prints*.
- Welty, D. E. and Crowther, P. A. (2010). Interstellar TiII in the Milky Way and Magellanic Clouds. *MNRAS*, 404:1321–1348.
- Westphal, A. J., Stroud, R. M., Bechtel, H. A., and et al. (2014). Evidence for interstellar origin of seven dust particles collected by the Stardust spacecraft. *Science*, 345:786–791.
- Whittet, D. C. B., editor (2003). *Dust in the galactic environment*.

- Whittet, D. C. B. (2011). Spectropolarimetry of Interstellar Dust and Ice Features. In Bastien, P., Manset, N., Clemens, D. P., and St-Louis, N., editors, *Astronomical Polarimetry 2008: Science from Small to Large Telescopes*, volume 449 of *Astronomical Society of the Pacific Conference Series*, page 93.
- Wiscombe, W. J. (1980). Improved mie scattering algorithms. *Appl. Opt.*, 19(9):1505–1509.
- Wooden, D. H. (2008). Cometary Refractory Grains: Interstellar and Nebular Sources. *Space Sci. Rev.*, 138:75–108.
- Zeegers, S. T., Costantini, E., de Vries, C. P., Tielens, A. G. G. M., Chihara, H., de Groot, F., Mutschke, H., Waters, L. B. F. M., and Zeidler, S. (2017). Absorption and scattering by interstellar dust in the silicon K-edge of GX 5-1. *A&A*, 599:A117.



# 5

## Interstellar dust scattering of X-rays: the case of AU Microscopii

### Abstract

*Context* The scattering of X-rays by interstellar dust produces halos of diffuse emission around a background source. These halos are used to study the properties of the dust encountered along the line of sight toward the source.

*Aims* We explore the theory of X-ray scattering for a new parameter space where the small angle approach is no longer valid and where the size distribution of the dust includes large ( $> 1 \mu\text{m}$ ) particles. We apply this theory, for the first time, to the environment of stellar debris disks where such conditions apply. We use as a best test case the debris disk of AU Microscopii (AU Mic).

*Methods* We make use of the anomalous diffraction theory to calculate the scattering efficiency and the differential scattering cross-section. To model the dust size distribution and dust composition we make use of state of art dust models of the AU Mic debris disk. We construct 40 dust halo models where we vary the stellar wind strength, size distribution and dust composition. These models are compared to a *Chandra* HRC-I observation of AU Mic.

*Results* A model with a moderate stellar wind strength, a dust size distribution with a steep slope and a dust composition of graphite and astro-silicate would most effectively enhance a dust halo. We find that the size distribution and the stellar wind strength are dominant parameters, whereas the dust composition is of less importance to the halo intensity. From the observational point of view, the theoretical models do not succeed in producing a significant scattering halo, using the current spatial resolution of *Chandra*.

## 5.1 Introduction

X-ray scattering halos are commonly observed around bright X-ray binaries. These halos arise when the X-rays are scattered by the dust grains along the line of sight. They provide a powerful tool to study the intervening interstellar dust. The possibility of observing such a halo was first proposed by Overbeck (1965). In the last two decades, many X-ray halos have been observed around bright X-ray sources. The earliest observations of X-ray halos were carried out with the *Einstein* (e.g., Mauche and Gorenstein, 1986; Gallagher et al., 1995) and ROSAT satellites (Predehl and Schmitt, 1995). Later studies were carried out using the X-ray telescopes XMM-*Newton* and *Chandra* (e.g. Tan and Draine, 2004; Costantini et al., 2005; Smith et al., 2006; Valencic and Smith, 2015). The size and brightness of the X-ray halo depend on the source flux from which the scattered X-rays originate, but also on the particle size distribution, the location of the dust grains along the line of sight, as well as the chemical composition of the dust. In comparison to the source, the halo is faint, containing at most 20% of the soft X-ray emission of the source (Predehl and Schmitt, 1995). Furthermore, the scattering angle is small and forward directed (Overbeck, 1965; Martin, 1970; Hayakawa, 1973), which implies that the dust halo has an arcminute-scale maximum angular size. To observe the halo, it is necessary to use sensitive instruments with a sub arcminute angular resolution, a compact point spread function (PSF) and a low detector background in order to separate the source and the faint halo (Smith and Dwek, 1998). XMM-*Newton* and (especially) *Chandra* provide such an angular resolution. However, determining the dust properties from scattering halos is difficult. The shape of the dust halo depends on both the dust size distribution and the position of the dust along the line of sight, creating a degeneracy between the two effects. When the dust halo is measured at multiple energies it becomes easier to separate the effect of the dust positions from the intrinsic dust properties (Valencic and Smith, 2015). However, the exact position of these clouds, remains difficult to determine. The degeneracy can only be removed in cases of special observing conditions, such as the observation of scattering rings (Vaughan et al., 2004; Tiengo et al., 2010; Heinz et al., 2015; Beardmore et al., 2016; Vasilopoulos and Petropoulou, 2016) or the use of supporting data, e.g., CO-maps (e.g., Smith et al., 2006; Beardmore et al., 2016).

In this study, we apply the theory of scattering halos to an environment which has never been explored before, namely dusty debris disks. As a case study we consider the young, flaring M dwarf star AU Microscopii (Robinson et al., 2001; Hawley et al., 1996). Around this star, a debris disk can be observed (Kalas et al., 2004). This is a circumstellar belt of dust and debris. The sizes of the particles in the disk range from small dust particles up to large unobservable planetesimals (e.g., Lagrange et al., 2000; Wyatt and Dent, 2002). In the youngest stars the dust may be a remnant of the protoplanetary disk, where most of the gas has been expelled from the disk (Wyatt, 2008). This may be the case for AU Mic. However, since the age of the star is estimated to be  $23 \pm 3$  Myr (Mamajek and Bell, 2014), the dust in the debris disk may be the result of constant collisions originating from a so-called birth ring consisting of larger planetesimals (Strubbe and Chiang, 2006). The stellar wind constantly removes the smallest dust particles, which are replenished with dust newly produced by collisions between the planetesimals (Su et al., 2005; Song et al., 2005). Debris disks are interesting objects to study in order to obtain a complete understanding of the dynamics in extrasolar planetary systems. For instance, by studying the properties of the dust in the disk, the composition and

structure of the unseen populations of planetesimals can be investigated (Wyatt, 2008; Krivov, 2010).

The debris disk of AU Mic has been extensively studied at multiple wavelengths from the X-rays (Magee et al., 2003; Mitra-Kraev et al., 2005) and UV (Robinson et al., 2001) to infrared and submillimetre wavelengths (MacGregor et al., 2013). The debris disk can be detected by an infrared excess in the spectral energy distribution (SED) of the star due to the presence of the dust (Tsikoudi, 1988; Song et al., 2002). Since AU Mic is a nearby star, its debris disk can be imaged directly. This has been done at wavelengths from the optical to the near-infrared using the *Hubble Space Telescope* with instruments STIS and ACS (Kalas et al., 2004; Krist et al., 2005) and the Keck II telescope (Metchev et al., 2005), probing dust scattering by submicron sized dust grains. The images revealed a large debris disk, viewed almost perfectly edge-on, which is slightly clumpy in nature and asymmetric. The disk has also been resolved by ALMA (MacGregor et al., 2013). These observations at longer wavelengths show the thermal radiation of larger grains and give an indication of the spatial distribution of these particles. The star itself has been observed in the X-rays several times by different observatories: both *XMM-Newton* and *Chandra* collected images and spectral data of the star. AU Mic is one of the brightest nearby X-ray sources. The X-rays in young M stars, like AU Mic, originate from the corona of the star. This is different from X-ray binaries, where the X-rays originate from the area around a neutron star or black hole, where material from the companion star is falling towards it and is heated to very high temperatures. AU Mic is observed to flare in the UV (Robinson et al., 2001) and X-rays (Mitra-Kraev et al., 2005). These flares may cause short periodical increases in the radiation pressure of the star, which, in that way, causes more and larger particles to be blown out of the disk.

In this chapter, we investigate the possibility of observing the scattered X-ray radiation from the debris disk. In doing so we explore a parameter space which is different from what is common in X-ray halo analysis. This provides us with the possibility to further explore the applications of the halo theory. There are a number of clear differences when we apply the theory to a debris disk compared to X-ray binaries. In contrast to studies of X-ray binaries, we know where the dust is located along the line of sight. In this case, distances towards the star and the disk are well determined. AU Microscopii is part of the  $\beta$  Pictoris moving group and the distance towards the star is  $9.94 \pm 0.13$  pc (Perryman et al., 1997; van Leeuwen, 2007). The debris disk of AU Mic extends at least over 210 AU, based on images at optical wavelength (Kalas et al., 2004; Krist et al., 2005). We are observing dust close to the source in comparison with the total distance to the star, which implies that the scattering halo will be narrow. The dust size distribution deviates from the general ISM, since the smallest particles are blown out of the disk due to the radiation pressure of the star. We base our modeling of the disk on a recent study by Schüppler et al. (2015) and Augereau and Beust (2006) (hereafter S15 and AB06, respectively), taking into account the composition and structure of the dust grains, the size distribution of the grains and stellar activity. In our analysis of the debris disk we make use of observations from *Chandra*.

The chapter is structured as follows: in Section 5.2 we describe the halo theory under the geometrical conditions of a debris disk. In Section 5.3 we show the observation of the debris disk with *Chandra*. In Section 5.5 we discuss the results of the fits to the dust halo of AU Mic and in Section 5.6 we give our conclusions.

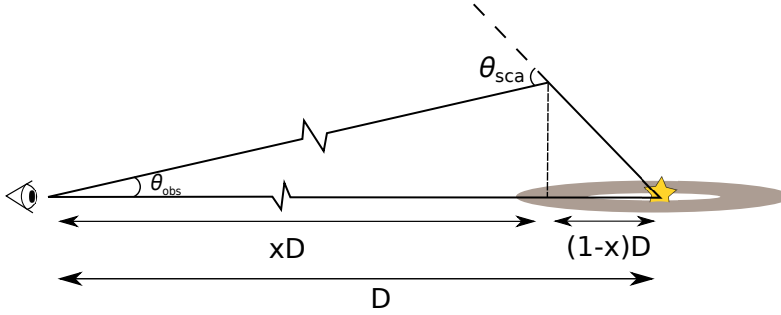


Figure 5.1: Geometry of X-ray scattering in the debris disk of AU Mic. The total distance to the source, given by  $D$ , is 9.93 pc. The dust is situated in the debris disk which extends over 210 AU. The distance from the dust to the source is indicated by  $(1-x)D$  and the distance from the observer to the dust is given by  $xD$ . The scattering angle is indicated by  $\theta_{\text{sca}}$  and  $\theta_{\text{obs}}$  indicated the angle at which the scattered X-rays are observed.

## 5.2 X-ray dust models for debris disk: the halo model

The scattering intensity of the scattering halo can be obtained using the general equation (Mathis and Lee, 1991):

$$I(\theta_{\text{obs}}) = N_{\text{H}} \int_{E_{\text{min}}}^{E_{\text{max}}} S(E) dE \times \int_{a_{\text{min}}}^{a_{\text{max}}} n(a) da \times \int_0^1 \frac{f(x) \cos(\theta_{\text{sca}} - \theta_{\text{obs}})}{(1-x)^2} \frac{d\sigma(a, E, \theta_{\text{sca}}, x)}{d\Omega} dx, \quad (5.1)$$

where  $I(\theta_{\text{obs}})$  is the intensity of the halo at a certain observed angle from the source. The integration is computed over the energy given by  $E$ , particle size given by  $a$  and the fractional distance to the source given by  $x$ , where  $x = 0$  at the observer and  $x = 1$  at the source.  $N_{\text{H}}$  is the hydrogen column density towards the source.  $S(E)$  is the spectral energy distribution of the source. The function  $f(x)$  is the density of hydrogen at a distance  $xD$ , relative to the average density on the line of sight toward the X-ray source (Mathis and Lee, 1991).  $D$  is the total distance to the source.  $n(a)$  is the particle size distribution. The differential scattering cross-section  $\frac{d\sigma}{d\Omega}$  is a function of  $a$ ,  $E$ , and  $\theta_{\text{sca}}$ .

Since the particle size distributions used in this analysis contain large particles ( $> 1 \mu\text{m}$ ), we make use of the Anomalous Diffraction Theory (ADT) to calculate  $\frac{d\sigma}{d\Omega}$ . The Rayleigh-Gans approximation only holds for smaller grains (Hoffman and Draine, 2016). Furthermore, Mie theory cannot be used due to round-off errors that arise for values of the size parameter ( $X = \frac{2\pi a}{\lambda}$ ) larger than  $10^4$  (Hoffman and Draine, 2016). We use the ADT code `adt.f`<sup>1</sup> to calculate  $\frac{d\sigma}{d\Omega}$ .

In the case of AU Mic, the vertical optical depth does not exceed  $\tau = 5 \times 10^{-3}$ , which indicates that the disk is optically thin (AB06). In Figure 5.1 we describe the geometry of the

<sup>1</sup>available at: [www.astro.princeton.edu/~draine/scattering.html](http://www.astro.princeton.edu/~draine/scattering.html)

system. Here, it can be seen that the dust is situated relatively close to the source in comparison with the total distance towards AU Mic. Therefore, we cannot use the commonly applied small angle approximation between the observed angle,  $\theta_{\text{obs}}$ , and the scattering angle,  $\theta_{\text{sca}}$ , but we use the formal relation (e.g., Smith et al., 2016):

$$\theta_{\text{sca}} = \arctan\left(\frac{x \tan(\theta_{\text{obs}})}{1 - x}\right) \quad (5.2)$$

$f(x)$  can be expressed as:

$$f(x) = \frac{n_{\text{H}}(x)D}{N_{\text{H}}}, \quad (5.3)$$

where  $n_{\text{H}}(x)$  is the number density of hydrogen particles (Smith and Dwek, 1998). If the dust were smoothly distributed along the line of sight  $f(x) = 1$ . The total column density of hydrogen measured in the X-rays consist of both atomic and molecular hydrogen. The atomic hydrogen traces mostly the contribution of the ISM, whereas molecular hydrogen traces the circumstellar stellar matter. A value of  $N_{\text{H}} = 1 \times 10^{18} \text{ cm}^{-2}$  for the contribution of the ISM has been found by Monsignori Fossi et al. (1996) using a calculation based on other stars and by Wood et al. (2005) using H I Ly $\alpha$  emission lines. The ISM absorption can also be calculated directly using the EUV line flux ratio of the Fe XVI doublet at 335 and 360 Å lines, following Sanz-Forcada et al. (2003, and references therein), resulting in a value of  $N_{\text{H}} = 1 \times 10^{18} \text{ cm}^{-2}$ . The disk around AU Mic contains molecular hydrogen. This is accounts for the majority of the hydrogen along the line of sight. The value, however, has a large uncertainty. Following the discussion in Schneider and Schmitt (2010) we assume a value of  $N_{\text{H}} < 1 \times 10^{19} \text{ cm}^{-2}$  as an upper limit for the total hydrogen column density. In this analysis of the AU Mic debris disk we assume, as a first approach, that the contribution of the ISM to the column density is negligible and that the density within the disk is constant. The integration over  $x$  in Equation 5.1 can then be performed solely over the disk. With these assumptions Equation 5.3 is now simplified to:

$$f = \frac{D}{R_{\text{disk}}}, \quad (5.4)$$

where  $D$  is the total distance (i.e. from the observer to the star) and  $R_{\text{disk}}$  is the radius the debris disk.

### 5.2.1 Particle size distribution

The size distribution of particles within a debris disk of the type of AU Mic is determined by the collisions in the disk. The dust is thought to originate from a so-called birth ring of larger colliding bodies that act as a dust particle reservoir. After a certain dynamical time the disk will reach a collisional equilibrium state (Backman and Paresce, 1993; Augereau and Beust, 2006).

The size distribution can be expressed as:

$$n(a)da = K_i a^{-q} da \quad (5.5)$$

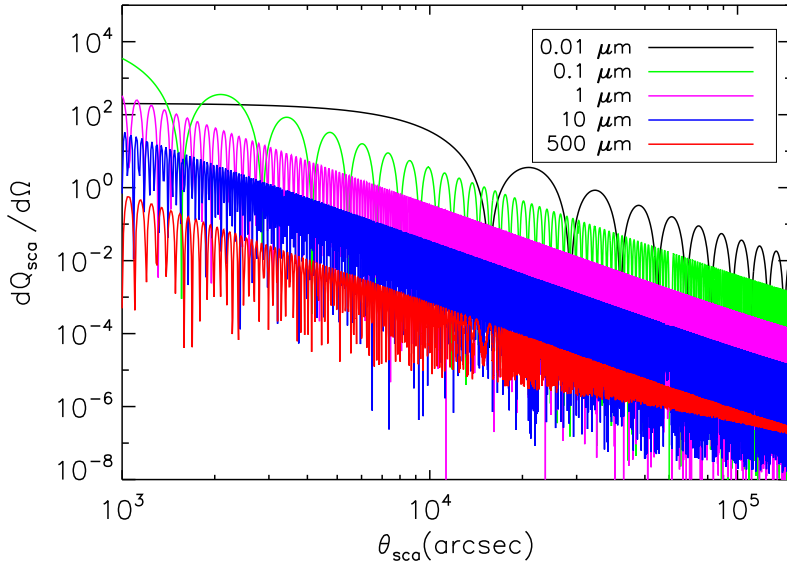


Figure 5.2: The differential scattering efficiency versus the scattering angle for several particle sizes, up to 500 micron. The calculations were done using the `adt.f` code.

The value of  $q$  determines the slope of the size distribution. The larger the absolute value, the steeper the distribution becomes. A value of  $q = 3.5$  would hold for systems in collisional equilibrium (Dohnanyi, 1969).

However, the slope of the dust size distribution of debris disks can deviate from the classical value valid for a collisional equilibrium (Durda and Dermott, 1997; Wyatt and Dent, 2002). The disk can often be modeled using values of  $q$  larger than 3.5. In the case of AU Mic, there are different possible values of the slope. In our modeling, we include both a flatter and steeper distribution than the typical one. We use 3.3, 3.5, 3.8 and 4.1 (S15; AB06).

The parameter  $K_i$  takes care of the normalisation of the size distribution for a certain dust composition  $i$ . The value of the normalisation is different depending on the chemical composition of the dust and the dust size distribution. For the derivation of  $K_i$  we follow the method of Mauche and Gorenstein (1986):

$$\int \sigma_{\text{sca}}(a) a^{-q} n(a) da = n_g \sigma_{\text{sca}}, \quad (5.6)$$

with  $n_g \sigma_{\text{sca}} = 0.18 \text{ kpc}^{-1}$  at 1 keV for standard grain parameters (Mauche and Gorenstein, 1986) of interstellar dust. We use ADT to calculate  $Q_{\text{sca}}$ , from which we obtain  $\sigma_{\text{sca}} = Q_{\text{sca}} \pi a^2$  and apply a numerical integration over the dust distribution models relevant for AU Mic.

The size of the smallest particles in the disk depends on the stellar wind strength and the stellar radiation pressure of the star. The radiation pressure can remove the smallest particles from the disk. The opposite effect is the Poynting-Robertson drag, which can be ignored,

Table 5.1: Models of the AU Mic debris disk

Model	Composition	B.S. ( $\mu\text{m}$ )		optical constants ( $n, k \times 10^{-5}$ )
		SW50	SW300	
M1	sil33+car33+vac33	0.07	0.48	(0.81, 4.19)
M2	sil50+car50	0.04	0.35	(0.99, 5.16)
M3	sil25+car25+ice25+vac25	0.07	0.51	(0.87, 4.05)
M4	sil10+car10+ice40+vac40	0.11	0.71	(0.77, 3.25)
M5	sil15+car15+vac70	0.16	0.93	(0.55, 2.82)

Models used to describe the composition of the dust in the debris disk AU Mic following the modeling of S15. The first column indicates the names of the five different dust mixture models. The second column describes the content of the dust mixtures, where for example sil25+car25+ice25+vac25 stands for volume fractions of 25% astro-silicate, 25% graphite, 25% water ice and 25% vacuum to indicate the level of porosity. The third and the fourth column show the minimum size a dust grain in the disk can have, smaller particles are blown out of the disk due to the stellar wind. The third column indicates the minimum grain sizes (i.e., the blowout size, B.S.) for moderate stellar wind strength (SW50) and the fourth column indicates the minimum grain sizes for strong stellar wind strength. The fifth column shows the optical constants  $n$  and  $k$  for each dust mixture at 1 keV.

since the time scale, on which P-R drag would become important is very long, which means that the debris disk would become so low in density that it is no longer detectable with current instrumentation (Wyatt, 2005, AB06).

The total stellar wind force acts upon the particles in a similar way as the radiation pressure: the particles can either be blown from the disk, due to the stellar wind pressure, or dragged towards the star, due to a loss of angular momentum created by the stellar wind, which acts as headwind on the particles (Burns et al., 1979). The latter effect is referred to as stellar wind drag. If the stellar wind is strong, which it is in the case of young flaring M stars such as AU Mic, the effect of the stellar wind drag on the dust particles in the disk is small. The stellar wind pressure does in fact effectively remove the smallest particles from the disk. The particles are either expelled from the disk or end up in the outer parts of the disk. The stronger the stellar wind, the larger the particles that are blown out of the disk.

The minimum size that a particle in the disk can have is referred to as the blowout size. The stellar wind strength is expressed in multiples of the solar mass loss rate ( $\dot{M}_\odot = 2 \times 10^{-14} M_\odot \text{yr}^{-1}$ ). Following the modeling of S15 and AB06, we use two different stellar wind strengths (SW): SW50 representing a moderately strong stellar wind i.e.  $\dot{M}_\star = 50\dot{M}_\odot$  and SW300, representing 300 times the solar wind strength ( $\dot{M}_\star = 300\dot{M}_\odot$ ). In the case of the SW50 model, flares are ignored (S15;AB06), while the SW300 model averages over the flare and quiescent phases (S15). The high wind strength causes the stellar wind pressure to be greater than the radiation pressure (S15). Here, we will not consider a model where there is no stellar wind activity, since modeling of AU Mic system shows a strong preference for a model including stellar wind activity, which is supported by the frequently observed flares in AU Mic (Cully et al., 1993). The largest particles in the size distribution have a modest influence on the total scattering, since they are less represented due to the slope of the size distribution. In this analysis, we will include particle sizes up to 1 mm (see Figure 5.3) and assume spherical particles.

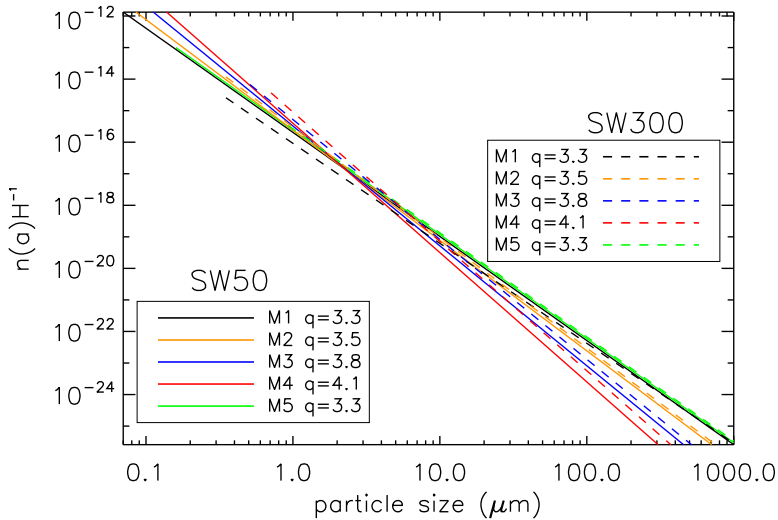


Figure 5.3: The particle size distribution for a subset of dust models used in this analysis. The models differ in slopes and size range and for each of these we selected the dust compositions as indicated in Table 5.1. The dashed set of models show the size distribution of the strong stellar wind model (SW300) and the colors indicate the different slopes for which we chose one dust mixture as an example. The slope  $q=3.3$  is repeated to also show the M5 dust mixture. In the same way, we show the models for the moderately strong stellar wind model (SW50).

## 5.2.2 Scattering efficiency versus energy and particle size

The scattering efficiency of a particle changes for different particle sizes and at different energy (Figure 5.4). We use the optical constants of an astro-silicate (Draine and Lee, 1984; Laor and Draine, 1993). The strength of the scattering efficiency,  $Q_{\text{sca}}$ , is indicated by the color bar. At certain values of the energy and particle size, scattering is more efficient. At 1 keV, for example, the most efficient scatterers have sizes between 0.4 and 1  $\mu\text{m}$ . As the energy increases the particle size of the efficient scatterers also increases. However, at certain energy values the efficiency drops abruptly. This is due to the absorption edges of respectively oxygen, iron (L-edge), magnesium and silicon, as indicated in Figure 5.4. At the edge an X-ray photon is more likely to be absorbed, because it has an energy just above the binding energy of the electron. At slightly higher energies close to the edge  $Q_{\text{sca}}$  increases and decreases, these features are the X-ray Absorption Fine Structures (XAFS). The XAFS arises when a X-ray photon excites a core electron, which in turn causes an outwardly propagating photo-electron wave. The wave is scattered by the neighboring atoms from which new waves will emanate. These waves are superimposed on the wave function of the photo-electron, causing constructive and destructive interference near the edge. This effect propagates in the optical constants, which in turn influences the absorption and scattering efficiencies. At energies near the edge  $Q_{\text{sca}}$  can change rapidly. As the particle size increases beyond 1  $\mu\text{m}$ ,  $Q_{\text{sca}}$  stabilizes to a value

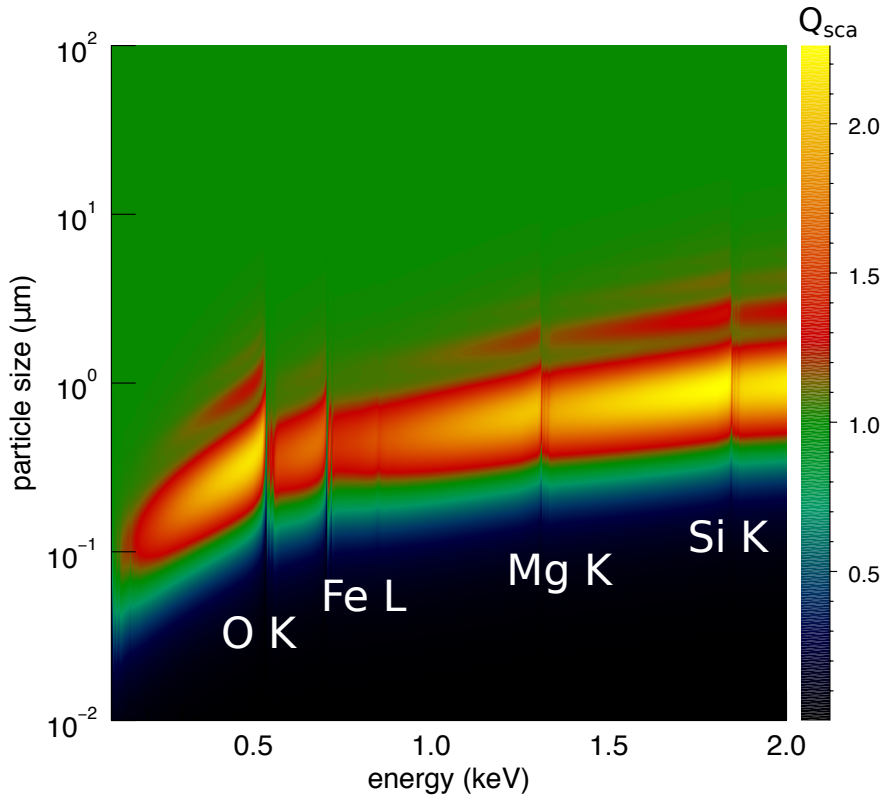


Figure 5.4: Scattering efficiency, indicated by the colorbar, as a function of the Energy in keV versus the particles size in  $\mu\text{m}$  for an astro-silicate. The positions of the oxygen K-edge, iron L-edge, magnesium K-edge and silicon K-edge are indicated in the figure.

of 1, which is expected in the geometrical regime where the wavelength is small compared to the particle size.

### 5.2.3 Dust mixtures in debris disks

Although the planetesimals, from which the dust in the debris disk originate, cannot be directly detected, the dust in the debris disk can help in revealing the composition of these planetesimals. They are often compared to Kuiper belt objects and the dust in debris disks may thus resemble the chemical composition and porous structure of comets in the Solar system (Wyatt, 2008; A'Hearn et al., 2005).

The chemical composition of dust in debris disks can be probed by studying distinctive features in the mid- and far-infrared spectra of the disks. Several disks were well matched with a mixture of amorphous and crystalline silicates and carbonaceous material (i.e. HD

69830, Beichman et al. (2005); Lisse et al. (2007), HD 172555, Lisse et al. (2009),  $\beta$  Pic-toris, de Vries et al. (2012), Fomalhaut, Lebreton et al. (2013)). In some cases also water ice was detected (i.e. HD 181327, Chen et al. (2008); Lebreton et al. (2012)). The debris disk of AU Mic in particular is best modeled using porous grains containing a heterogeneous mixture of silicate, graphite and ice (Graham et al., 2007; Fitzgerald et al., 2007). Therefore, we use the optical constants of graphite, astro-silicate (Draine, 2003) and water ice in our analysis to calculate the optical constants of the dust mixtures. In the case of water ice, we took the optical constants of water from the CXRO X-ray database (Henke et al., 1993) with a density of  $0.9167 \text{ g/cm}^3$ . In Table 5.1 we indicate the different mixtures that we used in the analysis, here we follow the analysis and nomenclature in Schuppler et al. 2015. Five different dust mixtures are used with different contributions of silicates (sil), graphite (car) and water ice (ice). We test several levels of porosity, indicated by the percentages of vacuum (vac) in the grains. The first column in Table 5.1 indicated the number of the model. The second column gives the composition, where the corresponding number indicated the volume fraction of the material in percentages. In the fourth column, the blowout sizes are given per dust mixture and stellar wind model (S15). We also give the optical constants ( $n$  and  $k$ ) for the dust mixtures at 1 keV in the fifth column. The optical constants of the composite dust particles are generally obtained using a mixing rule (also referred to as the effective optical constants). S15 use the Bruggeman mixing rules (Bruggeman, 1935), which cannot be applied in our case, since the particles are large compared to the wavelength. Different mixing rules predict different values of the optical constants, but they are bound by a maximum value, so called Wiener bounds (Wiener, 1910). We approach the value of the effective optical constants by the maximum value ( $\epsilon_{\text{eff,max}}$ ) they would have in the following way:

$$\epsilon_{\text{eff,max}} = \sum f_i \epsilon_i, f_i = \frac{V_i}{V_{\text{total}}}. \quad (5.7)$$

Here  $f_i$  is the volume fraction of the  $i$ th component of the mixture and  $\epsilon_i$  is the permittivity. The optical constants  $n$  and  $k$  can be derived from  $\epsilon_{\text{eff,max}}$ .

### 5.3 X-ray scattering by dust in the AU Mic debris disk

AU Microscopii was observed three times by *Chandra* and both spectral and imaging data are available. In the first two observations, with obsid 17 and 8894, gratings were used in order to obtain stellar spectra. The images from these observations cannot be used in this analysis, since the presence of a grating affects the radial profile, which we want to extract. Therefore, we use image data taken by the High Resolution Camera (HRC) (Murray et al., 2000). One of the two detectors, the HRC-I detector, of this instrument is optimized for imaging. The HRC has an energy range from 0.06-10 keV albeit without energy resolution of the source. AU Mic was observed on the 17th of August 2010 (obsid 12236) for a duration of 23.9 ks. The HRC detector is most efficient at  $1.5 \text{ keV}^2$ . The source is expected to be bright around 0.5-1 keV (Magee et al., 2003). Our models will therefore be tested at 1 keV.

The data needed some processing in addition to the standard pipeline. In particular, the event image showed a jet-like ghost. This is a well-known artefact which originates in the

<sup>2</sup><http://cxc.harvard.edu/csc/columns/ebands.html>

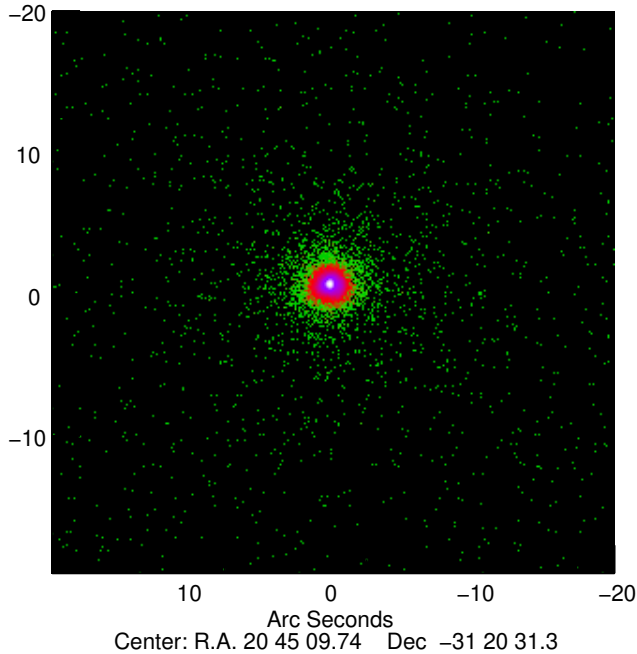
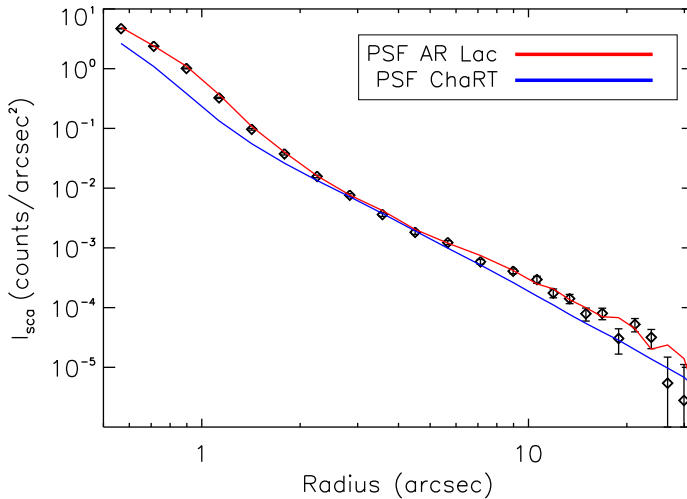


Figure 5.5: *Chandra* HRC-I observation of AU Mic (obsid 12236) after the application of additional processing in order to remove a jet-like ghost feature.

HRC-I detector (Murray et al., 2000). The ghost is usually reduced to  $< 0.1\%$  of the total flux by standard processing. In the case of the observation of AU Mic, the jet was still present in the reduced images. A solution to this problem is to filter out these events by ignoring the third amplifier. This decreases the flux slightly, but since we are interested in the morphology of the halo, the slight reduction in the overall brightness of the source does not affect our analysis. The final image can be seen in Figure 5.5.

We extracted the surface brightness profile using 23 logarithmically spaced annuli for the spatial analysis of the halo. This was done using the standard CIAO software<sup>3</sup>. We evaluate the halo up to 30 arcsec away from the source. We conservatively assume a circular geometry around the source, since we do not have any imaging information on the geometry of the disk in the X-rays. Observations at different wavelength have indeed revealed different disk geometries (e.g., HST (Kalas et al., 2004), ALMA (MacGregor et al., 2013)), tracing different dust particle sizes. The X-rays may reveal a geometry which is slightly different from what is observed at longer wavelengths, since the X-rays are sensitive to the very small submicron dust particles, as can be seen in Figure 4. These small dust particles can be pushed into eccentric or unbound trajectories due to the stellar wind interacting with the disk and may, in this way, end up slightly out of the plane of the disk (Boccaletti et al., 2015).

<sup>3</sup>[http://cxc.harvard.edu/ciao/threads/radial\\_profile/](http://cxc.harvard.edu/ciao/threads/radial_profile/)



**Figure 5.6:** This figure shows the radial profile, halo intensity versus radius in arcsec, of the observation of AU Mic, indicated by the diamond symbols. The blue line shows the PSF obtained using ChaRT and the red line shows the radial profile of the star AR-Lac which is used as a PSF in this chapter.

The PSF of the image was first obtained using the *Chandra* ray tracing software: ChaRT (Carter et al., 2003) and using CALDB and CIAO with version 4.7.3 and 4.9 respectively. The PSF obtained by ChaRT and the in-flight PSF are known to deviate. At small angles this is caused by an asymmetry in the PSF of *Chandra*, which becomes apparent when the image is deconvolved with the PSF. The asymmetry has a hook-like structure and occurs in the images at  $\sim 0.6 - 0.8$  arcsec and changes over the long time scales. This feature appeared between October 1999 and December 2000 and was first observed in the calibration data of the star AR Lacertae (AR Lac). Over time this star has been regularly observed in order to monitor the asymmetry. Therefore, we used AR Lac as a point like source. This is an unresolved spectroscopic binary star. This system has no known disk and can therefore be used as a PSF calibrator. In this way, we can compare the PSF obtained by ChaRT. We use an observation of 20 ks from the 16th of December 2010 (obsid 13182), close in time to the observation of AU Mic. In Figure 5.6 we show the radial brightness profile of both AR Lac and AU Mic compared to the ChaRT-PSF. As can be seen, the radial profile of AR Lac closely follows that of AU Mic at both small angles ( $< 1$  arcsec) and angles  $> 10$  arcsec.

## 5.4 The halo modeling

We constructed the halo models using the five different dust compositions listed in Table 5.1, four different values of the size distribution, as well as two different values of the stellar wind strength. This resulted in 40 halo models. The dust halo intensity was derived using equation 5.1, where we used ADT to calculate the  $d\sigma/d\Omega$  and the energy is fixed to 1 keV (see

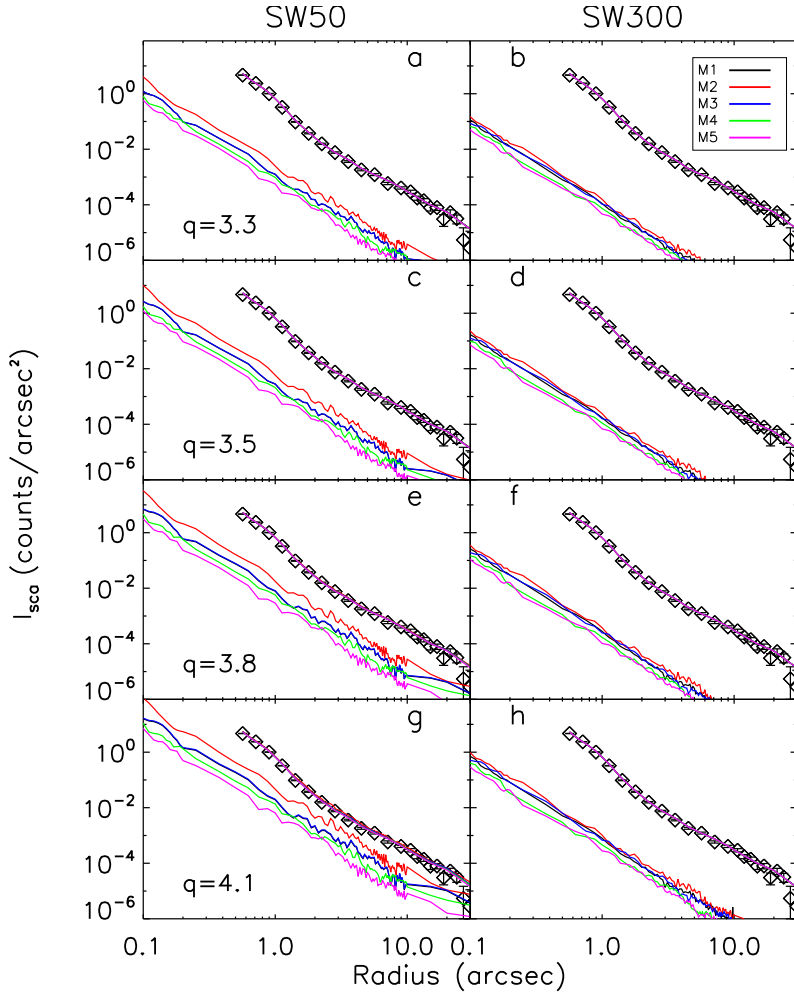


Figure 5.7: This figure contains all the models considered in this analysis, forty models in total. The two columns show the different stellar wind activity. Each row indicates a different value of the slope of the size distribution  $q$ . The colors in each panel indicated the different dust mixture models (M1, M2, M3, M4 and M5) used in this analysis. The contribution of the scattering dust to the radial profile, where the PSF is subtracted, is shown by the lines below the observed profile. In this way, the differences between dust mixtures can be observed more easily. The models are also shown in the case where the PSF is included. In almost all the models, the contribution of the scattered dust is so small, that the models fall on top of each other. The diamond symbols indicate the data points of the radial profile of AU Mic.

Section 5.2.3). These models are compared with the observation of AU Mic in Figure 5.7. The halo models are evaluated from 0.1 arcsec up to 30 arcsec. The small angles (0.1-0.5 arcsec) are included to show the behaviour of the models for angles that are inaccessible for *Chandra*. The plots on the left-hand side show the results for the low stellar wind strength (SW50) and the column on the right-hand side the high stellar wind strength (SW300). The rows indicate the different values of the slope of the dust size distribution. The diamond symbols indicate the data points of the radial profile of AU Mic. The halo has been modeled out to a radial distance of 30 arcsec. Beyond 30 arcsec the intensity of the source drops and our models do not show any significant contribution of the halo. Beyond 10 arcsec we used a coarser spacing of the data points, since the calculations for angles larger than this value become time consuming. When the slope of the size distribution becomes steeper, the amount of small particles increases. These particles are the effective scatterers (Figure 5.4). This effect is particularly visible in the left column, because if the stellar wind is strong (SW300), most of the small ( $<1 \mu\text{m}$ ) particles are blown out of the disk. This means that the most effective scatterers are now removed from the model, whereas they are still present in the moderately strong stellar wind model (SW50). The five dust mixtures (M1, M2, M3, M4 and M5) are represented in Figure 5.7 by different colors. The contribution of the scattering dust to the radial profile, where the PSF is subtracted, is shown by the lines below the observed profile. In this way, the differences between dust mixtures can be observed more easily. The models are also shown in the case where the PSF is included. For most of the models the halo contribution is very low and therefore the dust mixture models in almost all of the frames fall on top of each other. The models in panel *g* have the highest impact on the scattering halo. These models have the steepest size distribution ( $q=4.1$ ) and a moderate stellar wind strength (SW50). The dust mixture that contributes the most to the scattering halo is the M2 dust mixture, which contains volume fractions of 50% astro-silicate and 50% graphite.

## 5.5 Discussion

In this chapter, we explore a new parameter space, which is different from the parameter space addressed in studies of X-ray halos of X-ray binaries. In this new parameter space the small angle approximation is no longer valid (see Section 5.2.1). Moreover, we address a broader size distribution, where we include large particles with sizes up to 1 mm as prescribed by studies on debris disks. The smallest particles in the size distributions of our models are still considered large when compared to the Mathis-Rumpl-Nordsieck (MRN, Mathis et al. (1977)) size distribution which is commonly used when studying dust in the ISM. The smallest particles in the MRN distribution have a size of  $0.005 \mu\text{m}$  in comparison to the smallest particles in our models of  $0.04 \mu\text{m}$ .

We applied the scattering theory to the nearest edge-on debris disk, AU Mic. Here we make use of the state of the art dust models based on the modeling of this disk in scattered light (S15;AB06). The parameters of the dust models that affect the dust halo are the slope of the size distribution, the composition of the dust, the stellar wind activity and the value of  $N_{\text{H}}$ .

The halo is of course also affected by the brightness of the source itself. AU Mic is a unique source in this type of study, since it is a very bright nearby X-ray source, but also because it

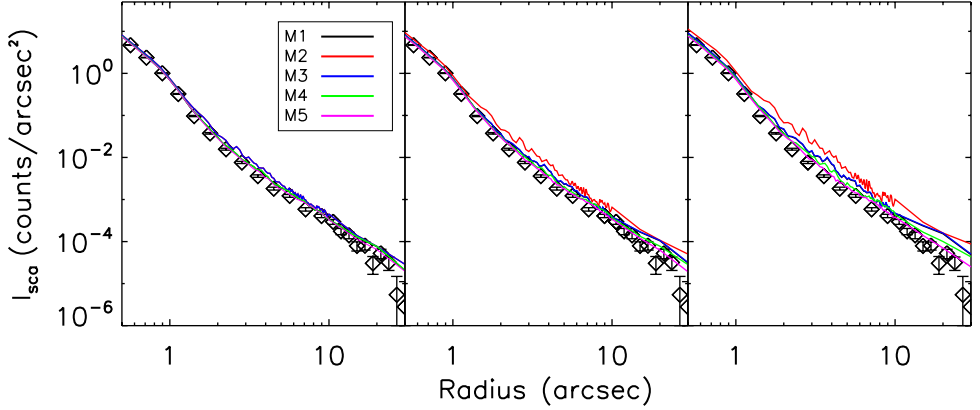


Figure 5.8: In this figure the panel shows the observation of AU Mic and five dust models with  $q=4.1$  and SW50,  $N_H = 1 \times 10^{19} \text{ cm}^{-2}$  and different dust mixtures. This panel corresponds with the lower left panel of Figure 5.7. The middle panel shows the same models, but now with  $N_H = 5 \times 10^{19} \text{ cm}^{-2}$  and the right panel shows the models with  $N_H = 1 \times 10^{20} \text{ cm}^{-2}$ .

has an edge-on configuration, which makes it in principle possible to observe the X-ray dust scattering. There exist more nearby debris disks, such as those of  $\epsilon$  Eridani or Fomalhaut but these do not have an edge-on configuration. If the disk was slightly more face-on, the scattering angles involved become very large and the intensity of the scattered light drops precipitously. Other edge-on debris disks, such as the one of  $\beta$  Pictoris at a distance of 19.4 parsec or HD 139664 at a distance of 17.5 pc (Kalas et al., 2006), are situated too far away for current spatial resolution and are not as bright in the X-rays as AU Mic.

A moderately strong stellar wind model is favored in both the analysis of S15 and AB06. In our analysis, such a model provides the best conditions to observe the dust halo, since this model includes the smaller dust particles, that are the efficient scatterers.

The slope of the size distribution is an important parameter as well. For a flat distribution, the halo will not be prominent, since the small dust particles will be less prominently represented, which are the effective scatterers. Previous studies show that the value of the slope of the size distribution is still uncertain (AB06). S15 show a preference for a relatively shallow slope of 3.3, whereas Kalas et al. (2004) predict a steeper slope. The stellar wind may indeed also affect the size distribution of the grains since the smallest particles are more affected by transport than by collisions (S15). We also investigated the effect of the dust composition on the dust halo. As can be seen in Figure 5.7 the differences between the five different dust mixtures are at most one order of magnitude in the case of SW50. We also note that none of the dust models produce an observable dust signature in the halo.

Nevertheless, we can explore the parameter space slightly further. In Section 5.2 we determined the column density along the line of sight:  $1 \times 10^{19} \text{ cm}^{-2}$ . This value is an upper limit, since the value of the vertical optical depth is at most  $\tau = 5 \times 10^{-3}$  in the visible

(AB06). A direct measurement of the  $N_{\text{H}}$  was performed by Schneider and Schmitt (2010) using *Chandra* LETGS data obtaining a  $N_{\text{H}} < 1 \times 10^{19} \text{ cm}^{-2}$ . The LETGS spectrum used in the analysis suffers from a high background contamination and the carbon edge used in the analysis contains a contribution from the carbon in the UV/Ion shield of the HRC-S detector. This introduces an uncertainty in the  $N_{\text{H}}$ . From UV measurements a different upper limit of  $N_{\text{H}} < 5 \times 10^{19} \text{ cm}^{-2}$  was obtained (France et al., 2007; Schneider and Schmitt, 2010). We increase the column density and explore at which value we may be able to observe the dust halo. In Figure 5.8 we show the results for the best case result from Figure 5.7 with the steepest slope ( $q=4.1$ ) and moderate stellar wind strength (SW50), thus favoring the small particles. The first panel in Figure 5.8 shows the situation as in Figure 5.7. The second panel show the same models, but now with a  $N_{\text{H}}$  of  $5 \times 10^{19} \text{ cm}^{-2}$  and the third panel show the models with a  $N_{\text{H}}$  of  $1 \times 10^{20} \text{ cm}^{-2}$ . As can be seen in the second panel, most of the halo models, except for M5, begin to be visible. The effect is clearer in the third panel where all the models produce a visible dust halo above the PSF.

## 5.6 Conclusion

In this chapter, we explored a new parameter space in X-ray halo theory. We applied it to a realistic environment, where we use the system of AU Mic as a model. We find that models with a steeper slope, moderately strong stellar wind model and a composition of silicates and graphite are the ones that would enhance a theoretical halo. The models do not produce a significant scattering halo, using the current spatial resolution. Future X-ray missions may enable us to observe the X-ray halo of debris disks. Such a X-ray telescope would require a PSF which has a FWHM  $< 0.5$  arcsec, i.e. smaller than the FWHM of *Chandra*. A possible future X-ray telescope called Lynx (also known as the X-ray Surveyor) may provide a more favorable angular resolution<sup>4</sup>. Such a PSF combined with an adequate effective area will make it possible to further explore the parameter space and in that way better constrain the dust size distribution and composition of the dust of the AU Mic debris disk system.

## Acknowledgements

Dust studies at SRON and Leiden Observatory are supported through the Spinoza Premie of the Dutch science agency, NWO. We would like to thank Vinay Kashyap and Diab Jerius for their helpful suggestions concerning the data reduction. E.C. acknowledges support from NWO-Vidi grant 639.042.525.

---

<sup>4</sup><https://wwwastro.msfc.nasa.gov/lynx/>

## References

- A'Hearn, M. F., Belton, M. J. S., Delamere, W. A., Kissel, J., Klaasen, K. P., McFadden, L. A., Meech, K. J., Melosh, H. J., Schultz, P. H., Sunshine, J. M., Thomas, P. C., Veverka, J., Yeomans, D. K., Baca, M. W., Busko, I., Crockett, C. J., Collins, S. M., Desnoyer, M., Eberhardy, C. A., Ernst, C. M., Farnham, T. L., Feaga, L., Groussin, O., Hampton, D., Ipatov, S. I., Li, J.-Y., Lindler, D., Lisse, C. M., Mastrodemos, N., Owen, W. M., Richardson, J. E., Wellnitz, D. D., and White, R. L. (2005). Deep Impact: Excavating Comet Tempel 1. *Science*, 310:258–264.
- Augereau, J.-C. and Beust, H. (2006). On the AU Microscopii debris disk. Density profiles, grain properties, and dust dynamics. *A&A*, 455:987–999.
- Backman, D. E. and Paresce, F. (1993). Main-sequence stars with circumstellar solid material - The VEGA phenomenon. In Levy, E. H. and Lunine, J. I., editors, *Protostars and Planets III*, pages 1253–1304.
- Beardmore, A. P., Willingale, R., Kuulkers, E., Altamirano, D., Motta, S. E., Osborne, J. P., Page, K. L., and Sivakoff, G. R. (2016). Lord of the Rings - Return of the King: Swift-XRT observations of dust scattering rings around V404 Cygni. *MNRAS*, 462:1847–1863.
- Beichman, C. A., Bryden, G., Gautier, T. N., Stapelfeldt, K. R., Werner, M. W., Misselt, K., Rieke, G., Stansberry, J., and Trilling, D. (2005). An Excess Due to Small Grains around the Nearby K0 V Star HD 69830: Asteroid or Cometary Debris? *ApJ*, 626:1061–1069.
- Boccaletti, A., Thalmann, C., Lagrange, A.-M., Janson, M., Augereau, J.-C., Schneider, G., Milli, J., Grady, C., Debes, J., Langlois, M., Mouillet, D., Henning, T., Dominik, C., Maire, A.-L., Beuzit, J.-L., Carson, J., Dohlen, K., Engler, N., Feldt, M., Fusco, T., Ginski, C., Girard, J. H., Hines, D., Kasper, M., Mawet, D., Ménard, F., Meyer, M. R., Moutou, C., Olofsson, J., Rodigas, T., Sauvage, J.-F., Schlieder, J., Schmid, H. M., Turatto, M., Udry, S., Vakili, F., Vigan, A., Wahhaj, Z., and Wisniewski, J. (2015). Fast-moving features in the debris disk around AU Microscopii. *Nature*, 526:230–232.
- Bruggeman, D. A. G. (1935). Berechnung verschiedener physikalischer Konstanten von heterogenen Substanzen. I. Dielektrizitätskonstanten und Leitfähigkeiten der Mischkörper aus isotropen Substanzen. *Annalen der Physik*, 416:636–664.
- Burns, J. A., Lamy, P. L., and Soter, S. (1979). Radiation forces on small particles in the solar system. *Icarus*, 40:1–48.

- Carter, C., Karovska, M., Jerius, D., Glotfelty, K., and Beikman, S. (2003). ChaRT: The Chandra Ray Tracer. In Payne, H. E., Jedrzejewski, R. I., and Hook, R. N., editors, *Astronomical Data Analysis Software and Systems XII*, volume 295 of *Astronomical Society of the Pacific Conference Series*, page 477.
- Chen, C. H., Fitzgerald, M. P., and Smith, P. S. (2008). A Possible Icy Kuiper Belt around HD 181327. *ApJ*, 689:539–544.
- Costantini, E., Freyberg, M. J., and Predehl, P. (2005). Absorption and scattering by interstellar dust: an XMM-Newton observation of <ASTROBJ>Cyg X-2</ASTROBJ>. *A&A*, 444:187–200.
- Cully, S. L., Siegmund, O. H. W., Vedder, P. W., and Vallerga, J. V. (1993). Extreme Ultraviolet Explorer deep survey observations of a large flare on AU Microscopii. *ApJ*, 414:L49–L52.
- de Vries, B. L., Acke, B., Blommaert, J. A. D. L., Waelkens, C., Waters, L. B. F. M., Vandembussche, B., Min, M., Olofsson, G., Dominik, C., Decin, L., Barlow, M. J., Brandeker, A., di Francesco, J., Glauser, A. M., Greaves, J., Harvey, P. M., Holland, W. S., Ivison, R. J., Liseau, R., Pantin, E. E., Pilbratt, G. L., Royer, P., and Sibthorpe, B. (2012). Comet-like mineralogy of olivine crystals in an extrasolar proto-Kuiper belt. *Nature*, 490:74–76.
- Dohnanyi, J. S. (1969). Collisional Model of Asteroids and Their Debris. *J. Geophys. Res.*, 74:2531–2554.
- Draine, B. T. (2003). Scattering by Interstellar Dust Grains. II. X-Rays. *ApJ*, 598:1026–1037.
- Draine, B. T. and Lee, H. M. (1984). Optical properties of interstellar graphite and silicate grains. *ApJ*, 285:89–108.
- Durda, D. D. and Dermott, S. F. (1997). The Collisional Evolution of the Asteroid Belt and Its Contribution to the Zodiacal Cloud. *Icarus*, 130:140–164.
- Fitzgerald, M. P., Kalas, P. G., Duchêne, G., Pinte, C., and Graham, J. R. (2007). The AU Microscopii Debris Disk: Multiwavelength Imaging and Modeling. *ApJ*, 670:536–556.
- France, K., Roberge, A., Lupu, R. E., Redfield, S., and Feldman, P. D. (2007). A Low-Mass H<sub>2</sub> Component to the AU Microscopii Circumstellar Disk. *ApJ*, 668:1174–1181.
- Gallagher, D., Cash, W., and Green, J. (1995). A search for an X-ray scattering halo around Scorpius X-1. *ApJ*, 439:976–982.
- Graham, J. R., Kalas, P. G., and Matthews, B. C. (2007). The Signature of Primordial Grain Growth in the Polarized Light of the AU Microscopii Debris Disk. *ApJ*, 654:595–605.
- Hawley, S. L., Gizis, J. E., and Reid, I. N. (1996). The Palomar/MSU Nearby Star Spectroscopic Survey. II. The Southern M Dwarfs and Investigation of Magnetic Activity. *AJ*, 112:2799.

- Hayakawa, S. (1973). Cosmic X-Rays and Interstellar Dust. In Greenberg, J. M. and van de Hulst, H. C., editors, *Interstellar Dust and Related Topics*, volume 52 of *IAU Symposium*, page 283.
- Heinz, S., Burton, M., Braiding, C., Brandt, W. N., Jonker, P. G., Sell, P., Fender, R. P., Nowak, M. A., and Schulz, N. S. (2015). Lord of the Rings: A Kinematic Distance to Circinus X-1 from a Giant X-Ray Light Echo. *ApJ*, 806:265.
- Henke, B. L., Gullikson, E. M., and Davis, J. C. (1993). X-Ray Interactions: Photoabsorption, Scattering, Transmission, and Reflection at  $E = 50\text{--}30,000$  eV,  $Z = 1\text{--}92$ . *Atomic Data and Nuclear Data Tables*, 54:181–342.
- Hoffman, J. and Draine, B. T. (2016). Accurate Modeling of X-ray Extinction by Interstellar Grains. *ApJ*, 817:139.
- Kalas, P., Graham, J. R., Clampin, M. C., and Fitzgerald, M. P. (2006). First Scattered Light Images of Debris Disks around HD 53143 and HD 139664. *ApJ*, 637:L57–L60.
- Kalas, P., Liu, M. C., and Matthews, B. C. (2004). Discovery of a Large Dust Disk Around the Nearby Star AU Microscopii. *Science*, 303:1990–1992.
- Krist, J. E., Stapelfeldt, K. R., Golimowski, D. A., Ardila, D. R., Clampin, M., Martel, A. R., Ford, H. C., Illingworth, G. D., and Hartig, G. F. (2005). Hubble Space Telescope ACS Images of the GG Tauri Circumbinary Disk. *AJ*, 130:2778–2787.
- Krivov, A. V. (2010). Debris disks: seeing dust, thinking of planetesimals and planets. *Research in Astronomy and Astrophysics*, 10:383–414.
- Lagrange, A.-M., Backman, D. E., and Artymowicz, P. (2000). Planetary Material around Main-Sequence Stars. *Protostars and Planets IV*, page 639.
- Laor, A. and Draine, B. T. (1993). Spectroscopic constraints on the properties of dust in active galactic nuclei. *ApJ*, 402:441–468.
- Lebreton, J., Augereau, J.-C., Thi, W.-F., Roberge, A., Donaldson, J., Schneider, G., Maddison, S. T., Ménard, F., Riviere-Marichalar, P., Mathews, G. S., Kamp, I., Pinte, C., Dent, W. R. F., Barrado, D., Duchêne, G., Gonzalez, J.-F., Grady, C. A., Meeus, G., Pantin, E., Williams, J. P., and Woitke, P. (2012). An icy Kuiper belt around the young solar-type star HD 181327. *A&A*, 539:A17.
- Lebreton, J., van Lieshout, R., Augereau, J.-C., Absil, O., Mennesson, B., Kama, M., Dominik, C., Bonsor, A., Vandeportel, J., Beust, H., Defrère, D., Ertel, S., Faramaz, V., Hinz, P., Kral, Q., Lagrange, A.-M., Liu, W., and Thébault, P. (2013). An interferometric study of the Fomalhaut inner debris disk. III. Detailed models of the exozodiacal disk and its origin. *A&A*, 555:A146.
- Lisse, C. M., Beichman, C. A., Bryden, G., and Wyatt, M. C. (2007). On the Nature of the Dust in the Debris Disk around HD 69830. *ApJ*, 658:584–592.

- Lisse, C. M., Chen, C. H., Wyatt, M. C., Morlok, A., Song, I., Bryden, G., and Sheehan, P. (2009). Abundant Circumstellar Silica Dust and SiO Gas Created by a Giant Hyper-velocity Collision in the  $\sim 12$  Myr HD172555 System. *ApJ*, 701:2019–2032.
- MacGregor, M. A., Wilner, D. J., Rosenfeld, K. A., Andrews, S. M., Matthews, B., Hughes, A. M., Booth, M., Chiang, E., Graham, J. R., Kalas, P., Kennedy, G., and Sibthorpe, B. (2013). Millimeter Emission Structure in the First ALMA Image of the AU Mic Debris Disk. *ApJ*, 762:L21.
- Magee, H. R. M., Güdel, M., Audard, M., and Mewe, R. (2003). An XMM-Newton observation of the flare star AU MIC. *Advances in Space Research*, 32:1149–1154.
- Mamajek, E. E. and Bell, C. P. M. (2014). On the age of the  $\beta$  Pictoris moving group. *MNRAS*, 445:2169–2180.
- Martin, P. G. (1970). On the interaction of cosmic X-rays with interstellar grains. *MNRAS*, 149:221.
- Mathis, J. S. and Lee, C.-W. (1991). X-ray halos as diagnostics of interstellar grains. *ApJ*, 376:490–499.
- Mathis, J. S., Rumpl, W., and Nordsieck, K. H. (1977). The size distribution of interstellar grains. *ApJ*, 217:425–433.
- Mauche, C. W. and Gorenstein, P. (1986). Measurements of X-ray scattering from interstellar grains. *ApJ*, 302:371–387.
- Metchev, S. A., Eisner, J. A., Hillenbrand, L. A., and Wolf, S. (2005). Adaptive Optics Imaging of the AU Microscopii Circumstellar Disk: Evidence for Dynamical Evolution. *ApJ*, 622:451–462.
- Mitra-Kraev, U., Harra, L. K., Güdel, M., Audard, M., Branduardi-Raymont, G., Kay, H. R. M., Mewe, R., Raassen, A. J. J., and van Driel-Gesztelyi, L. (2005). Relationship between X-ray and ultraviolet emission of flares from dMe stars observed by XMM-Newton. *A&A*, 431:679–686.
- Monsignori Fossi, B. C., Landini, M., Del Zanna, G., and Bowyer, S. (1996). A Time-resolved Extreme-Ultraviolet Spectroscopic Study of the Quiescent and Flaring Corona of the Flare Star AU Microscopii. *ApJ*, 466:427.
- Murray, S. S., Chappell, J. H., Kenter, A. T., Juda, M., Kraft, R. P., Zombeck, M. V., Meehan, G. R., Austin, G. K., and Gomes, J. J. (2000). Event screening for the Chandra X-Ray Observatory High-Resolution Camera (HRC). In Flanagan, K. A. and Siegmund, O. H., editors, *X-Ray and Gamma-Ray Instrumentation for Astronomy XI*, volume 4140 of *Proc. SPIE*, pages 144–154.
- Overbeck, J. W. (1965). Small-Angle Scattering of Celestial X-Rays by Interstellar Grains. *ApJ*, 141:864.

- Perryman, M. A. C., Lindegren, L., Kovalevsky, J., Hoeg, E., Bastian, U., Bernacca, P. L., Cr ez e, M., Donati, F., Grenon, M., Grewing, M., van Leeuwen, F., van der Marel, H., Mignard, F., Murray, C. A., Le Poole, R. S., Schrijver, H., Turon, C., Arenou, F., Froeschl e, M., and Petersen, C. S. (1997). The HIPPARCOS Catalogue. *A&A*, 323:L49–L52.
- Predehl, P. and Schmitt, J. H. M. M. (1995). X-raying the interstellar medium: ROSAT observations of dust scattering halos. *A&A*, 293:889–905.
- Robinson, R. D., Linsky, J. L., Woodgate, B. E., and Timothy, J. G. (2001). Far-Ultraviolet Observations of Flares on the dM0e Star AU Microscopii. *ApJ*, 554:368–382.
- Sanz-Forcada, J., Brickhouse, N. S., and Dupree, A. K. (2003). The Structure of Stellar Coronae in Active Binary Systems. *ApJS*, 145:147–179.
- Schneider, P. C. and Schmitt, J. H. M. M. (2010). X-raying the AU Microscopii debris disk. *A&A*, 516:A8.
- Sch uppeler, C., L ohne, T., Krivov, A. V., Ertel, S., Marshall, J. P., Wolf, S., Wyatt, M. C., Augereau, J.-C., and Metchev, S. A. (2015). Collisional modelling of the AU Microscopii debris disc. *A&A*, 581:A97.
- Smith, R. K., Dame, T. M., Costantini, E., and Predehl, P. (2006). The X-Ray Halo of GX 5-1. *ApJ*, 648:452–460.
- Smith, R. K. and Dwek, E. (1998). Soft X-Ray Scattering and Halos from Dust. *ApJ*, 503:831–842.
- Smith, R. K., Valencic, L. A., and Corrales, L. (2016). The Impact of Accurate Extinction Measurements for X-Ray Spectral Models. *ApJ*, 818:143.
- Song, I., Weinberger, A. J., Becklin, E. E., Zuckerman, B., and Chen, C. (2002). M-Type Vega-like Stars. *AJ*, 124:514–518.
- Song, I., Zuckerman, B., Weinberger, A. J., and Becklin, E. E. (2005). Extreme collisions between planetesimals as the origin of warm dust around a Sun-like star. *Nature*, 436:363–365.
- Strubbe, L. E. and Chiang, E. I. (2006). Dust Dynamics, Surface Brightness Profiles, and Thermal Spectra of Debris Disks: The Case of AU Microscopii. *ApJ*, 648:652–665.
- Su, K. Y. L., Rieke, G. H., Misselt, K. A., Stansberry, J. A., Moro-Mart ın, A., Stapelfeldt, K. R., Werner, M. W., Trilling, D. E., Bendo, G. J., Gordon, K. D., Hines, D. C., Wyatt, M. C., Holland, W. S., Marengo, M., Megeath, S. T., and Fazio, G. G. (2005). The Vega Debris Disk: A Surprise from Spitzer. *ApJ*, 628:487–500.
- Tan, J. C. and Draine, B. T. (2004). X-Ray Scattering Halos from the Galactic Center: Implications for Diffuse Emission around Sagittarius A\*. *ApJ*, 606:296–305.

- Tiengo, A., Vianello, G., Esposito, P., Mereghetti, S., Giuliani, A., Costantini, E., Israel, G. L., Stella, L., Turolla, R., Zane, S., Rea, N., Götz, D., Bernardini, F., Moretti, A., Romano, P., Ehle, M., and Gehrels, N. (2010). The Dust-scattering X-ray Rings of the Anomalous X-ray Pulsar 1E 1547.0-5408. *ApJ*, 710:227–235.
- Tsikoudi, V. (1988). Flare stars detected by the Infrared Astronomical Satellite. *AJ*, 95:1797–1800.
- Valencic, L. A. and Smith, R. K. (2015). Interstellar Dust Properties from a Survey of X-Ray Halos. *ApJ*, 809:66.
- van Leeuwen, F. (2007). Validation of the new Hipparcos reduction. *A&A*, 474:653–664.
- Vasilopoulos, G. and Petropoulou, M. (2016). The X-ray dust-scattered rings of the black hole low-mass binary V404 Cyg. *MNRAS*, 455:4426–4441.
- Vaughan, S., Willingale, R., O’Brien, P. T., Osborne, J. P., Reeves, J. N., Levan, A. J., Watson, M. G., Tedds, J. A., Watson, D., Santos-Lleó, M., Rodríguez-Pascual, P. M., and Schartel, N. (2004). The Discovery of an Evolving Dust-scattered X-Ray Halo around GRB 031203. *ApJ*, 603:L5–L8.
- Wiener, O. (1910). Zur Theorie der Refraktionskonstanten. *Berichte über die Verhandlungen der Königlich-Sächsischen Gesellschaft der Wissenschaften zu Leipzig, Math.-phys. Klasse*, 62:256–277.
- Wood, B. E., Redfield, S., Linsky, J. L., Müller, H.-R., and Zank, G. P. (2005). Stellar Ly $\alpha$  Emission Lines in the Hubble Space Telescope Archive: Intrinsic Line Fluxes and Absorption from the Heliosphere and Astrospheres. *ApJS*, 159:118–140.
- Wyatt, M. C. (2005). The insignificance of P-R drag in detectable extrasolar planetesimal belts. *A&A*, 433:1007–1012.
- Wyatt, M. C. (2008). Evolution of Debris Disks. *ARA&A*, 46:339–383.
- Wyatt, M. C. and Dent, W. R. F. (2002). Collisional processes in extrasolar planetesimal discs - dust clumps in Fomalhaut’s debris disc. *MNRAS*, 334:589–607.

# Nederlandstalige samenvatting

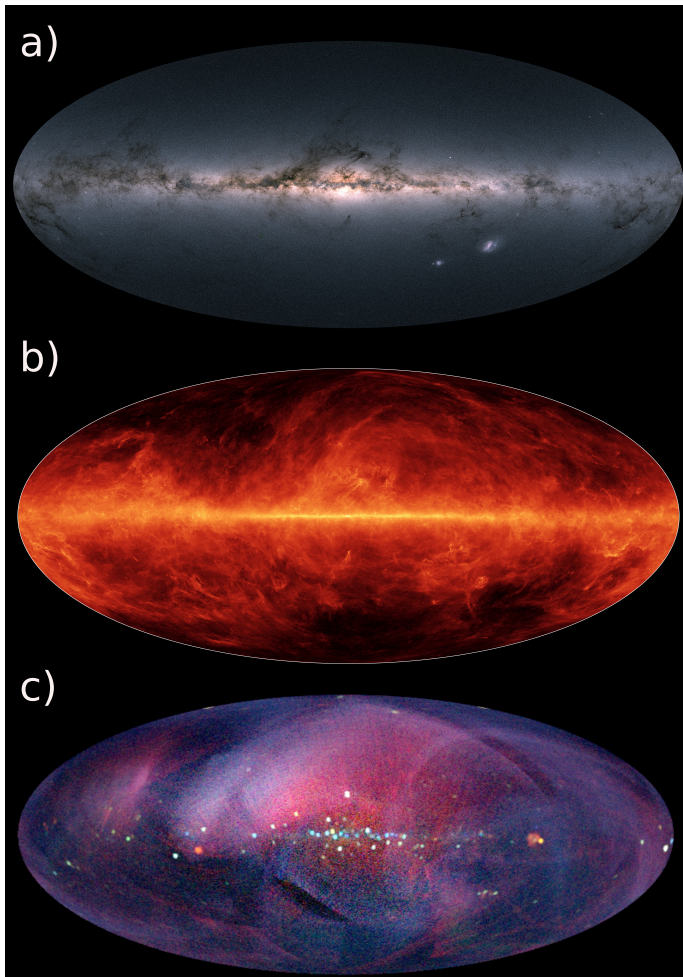
## X-ray spectroscopy of interstellar dust from the laboratory to the Galaxy

### Interstellair stof vanuit een historisch perspectief

De ruimte tussen de sterren, die het interstellair medium (ISM) wordt genoemd, is niet leeg. Tussen de sterren zien we wolken bestaande uit fijne stofdeeltjes en gassen, die variëren van vorm en in grootte en dichtheid. Deze wolken kunnen bijvoorbeeld worden waargenomen als donkere plekken in ons eigen sterrenstelsel, de Melkweg. Ze vormen een contrast met het licht van de sterren, zie bovenaan Figuur A.1. De ontwikkeling in de kwaliteit van telescopen in de 18e eeuw maakte het mogelijk om deze donkere plekken in de Melkweg beter te kunnen bestuderen. Dit leidde tot een toename in de interesse in dit soort objecten. In het begin dacht men dat deze donkere plekken gaten in de hemel waren. De astronoom William Herschel heeft bijvoorbeeld gezegd: "Hier ist wahrhaftig ein Loch im Himmel!". Echter, aan het begin van de 20ste eeuw werd ontdekt dat deze zogenaamde gaten in de lucht in werkelijkheid voorgrond objecten zijn, namelijk wolken die het licht van de sterren erachter (gedeeltelijk) tegenhouden. Aan het einde van de 19e eeuw begon Barnard de wolken te fotograferen en publiceerde deze foto's in een catalogus in 1919. De foto's lieten details zien die met het blote oog niet kunnen worden waargenomen. Agnes Clerke omschreef de wolken in haar boek 'Problems in Astrophysics' als verduisterende objecten. In 1847 ontdekte Friedrich von Struve dat zelfs in het geval dat er geen wolken worden waargenomen die het sterlicht belemmeren, er nog steeds een deel van het sterlicht wordt uitgedoofd. De sterren lijken roder van kleur dan dat ze in werkelijkheid zijn. Het duurde tot 1930 voordat bewezen werd dat de oorzaak van het deels uitdoven en roder worden van het sterlicht (in de sterrenkunde noemt men dit extinctie, namelijk de verstrooiing en absorptie van licht) wordt veroorzaakt door interstellair stofdeeltjes. Schalén en Trumpler ontdekten dit effect onafhankelijk van elkaar in respectievelijk 1929 en 1930.

### Waarom bestuderen we interstellair stof?

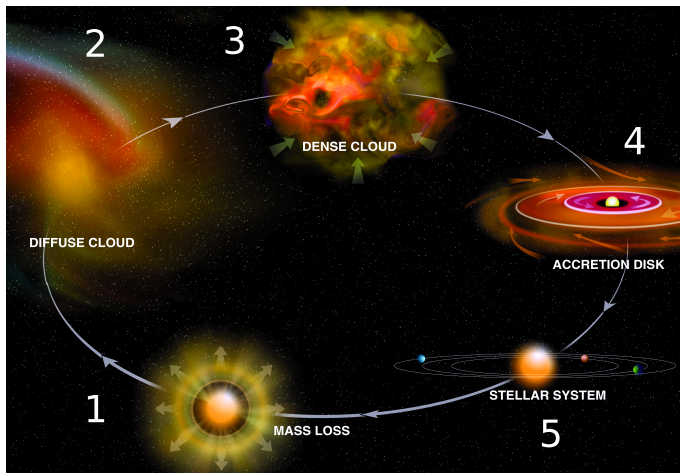
Sinds de ontdekking van interstellair stof zijn wetenschappers de aanwezigheid van dit stof steeds meer gaan waarderen. In het begin werd het compleet genegeerd, daarna werd het gezien als een belemmering wanneer men sterren en sterrenstelsels wilde observeren, maar sinds de jaren 60 van de vorige eeuw wordt het stof meer en meer gezien als een belangrijke en



**Figuur A.1:** De Melkweg in drie verschillende golflengtes: a) zichtbaar licht, waarbij donkere plekken gas en stofwolken zijn: GAIA 330-1050 nm, bron: ESA/Gaia/DPAC - b) infrarood: koude stofdeeltjes die oplichten in infrarood, bron: ESA/NASA/JPL-Caltech - c) Röntgenstraling: De stipjes zijn röntgendubbelsterren, bron: JAXA/RIKEN/MAXI team.

drijvende factor in de vele processen die in het universum plaatsvinden. De belangrijke rol van stof in het universum laat zich het beste uitleggen door te kijken naar de levenscyclus van sterren, waar stof in elke fase van de cyclus een belangrijke rol vervuld, zie Figuur A.2. Sterren verrijken het universum met elementen, die worden geproduceerd in het nucleosynthese proces en door sterwinden of (super) novae de ruimte in worden geslingerd. Op deze manier verzorgen sterren het bouw materiaal voor interstellair stof. Het stof wordt waarschijnlijk gevormd als een condensaat in de atmosferen van sterren die zich in een laat stadium van hun evolutie bevinden, in de nasleep van een geweldadige supernova explosie en wellicht in het

ISM zelf. Wanneer gas en stof in de ruimte samenpakken tot een zeer dichte wolk, kan er een nieuwe ster worden gevormd in de kern van zo'n wolk. Stof speelt een cruciale rol tijdens het formatieproces van de ster: van het instorten van de wolk onder de invloed van zwaartekracht tot het vormen van planeten. Kosmisch stof kan overal worden waargenomen: in ons zonnestelsel, rond jonge sterren, in gigantische wolken, in de Melkweg, maar ook in ver weg gelegen sterrenstelsels en het is al heel vroeg in de geschiedenis van ons universum aanwezig. Om deze reden kan stof ons helpen om te begrijpen hoe het vroege universum zich heeft ontwikkeld. Naast de argumenten die hier al zijn gegeven, is er natuurlijk nog een andere reden die pleit voor het bestuderen van kosmisch stof. Wij en alles om ons heen bestaan uit dit stof. Als we de oorsprong van het leven op aarde willen begrijpen, is het dus noodzakelijk om te weten te komen wat de oorsprong van het stof is, waar het uit bestaat en hoe het wordt gevormd.



**Figuur A.2:** De levenscyclus van sterren en interstellair stof in vijf stadia: 1) geëvolueerde ster, 2) diffuse wolk, 3) dichte wolk, 4) protostellaire schijf en 5) evolved planetary system. stelsel met planeten. In iedere fase van stervorming speelt stof een cruciale rol. Bron: Bill Saxton, NRAO/AUI/NSF.

## De eigenschappen van interstellair stof

Aangezien stof een belangrijke rol speelt in vele processen in het universum is het een essentieel onderdeel in vele astronomische modellen. Om nauwkeurige interstellaire stofmodellen te ontwikkelen is het belangrijk om onder andere te begrijpen wat de eigenschappen van het stof zijn, waar het stof uit bestaat, op welke manier het een wisselwerking aangaat met straling, wat de grootteverdeling is van de stofdeeltjes, wat hun vorm en interne structuur is, en of deze eigenschappen veranderen in verschillende omgevingen. Aangezien we weten welke elementen door sterren geproduceerd worden en in welke hoeveelheden, kunnen we de abundantie van een element (de aanwezige hoeveelheid vergeleken met waterstof) in de gas fase vergelijken

met astronomische waarnemingen<sup>5</sup>. Deze waarnemingen laten ons zien dat de abundantie van enkele elementen lager is dan verwacht, wat tot de conclusie leidt dat deze missende elementen opgesloten zitten in stofdeeltjes. Stof bestaat hoofdzakelijk uit koolstof (C), silicium (Si), ijzer (Fe), magnesium (Mg) en zuurstof (O). Als we deze informatie combineren met theorie, sterrenkundige waarnemingen (bv. infrarood spectroscopie) en studies van meteorieten, dan kan het stof in het interstellair medium in grote lijnen in twee hoofdgroepen worden opgedeeld; namelijk silicaten (bv., pyroxeen- en olivijntypes, vergelijkbaar met fijne zandkorrels op aarde) en koolstofhoudend stof (vergelijkbaar met roet), met daaraan toegevoegd oxiden (eg., MgO, SiO, SiO<sub>2</sub>), carbiden (grotendeels SiC) en metallisch ijzer.

Desondanks zijn er nog veel onzekerheden wat betreft interstellair stof. We weten niet precies hoe en waar stof wordt geproduceerd en hoe de eigenschappen van stof veranderen in verschillende omgevingen. We willen weten wat er met stof gebeurt in de meest geweldadige omgeving van het interstellair medium, waar stof wordt gebombardeerd met straling en kosmische deeltjes, en tevens wordt vernietigd door schokgolven. Deze invloeden veranderen mogelijk de interne structuur van het stof. Als de stofdeeltjes een kristallijne structuur hadden voor hun introductie in het interstellair medium, dan kunnen ze mogelijk deze structuur kwijtraken waarbij ze meer en meer amorf wordt, zie Figuur A.3. Bovendien weten we niet precies wat de chemische samenstelling van de stofdeeltjes is.

## Dit proefschrift

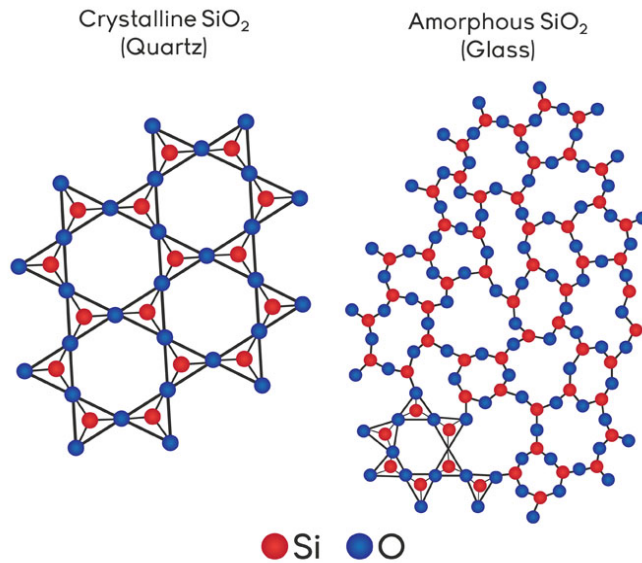
Hoge resolutie röntgenspectroscopie vormt een belangrijke techniek in de studie naar interstellair stof. Door spectrale kenmerken in röntgenspectra en verstrooiingshalos rond röntgenbronnen te bestuderen kunnen we -zoals eerder vermeld- wellicht enkele fundamentele vragen over interstellair stof beantwoorden. In dit proefschrift concentreren we ons op stof van het silicaattype, een van de hoofdbestanddelen van interstellair stof.

Röntgenstralen zijn buitengewoon geschikt om silicaten te bestuderen door de aanwezigheid van spectrale absorptiekenmerken van zuurstof, magnesium, silicium en ijzer in het röntgengebied van het spectrum. Deze elementen vormen de belangrijkste onderdelen van silicaten. We gebruiken met name het spectrale absorptiekenmerk van Silicium, ook wel de Si K-rand genoemd<sup>6</sup>, om de eigenschappen van silicaatstof te onderzoeken. Voor elk type silicaatstof zijn de spectrale kenmerken in de rand, ook wel Röntgenabsorptiefijnstructuren (XAFS) een klein beetje verschillend. Dit betekent dat ze een unieke vingerafdruk voor het stof vormen.

Heldere lage massa Röntgen dubbelsterren in de melkweg zijn ideale bronnen om het tussenliggende stof en gas langs de zichtlijn te bestuderen, door ze simpelweg te gebruiken als lantaarns die door het interstellair medium schijnen, waarbij stof en gas de straling deels absorbeert en verstrooid. Deze bronnen bestaan uit twee onderdelen, een neutronenster of zwart gat dat materiaal verzameld van een buurster, gewoonlijk een normale hoofdreeksster (en dus geen reuzenster). Deze systemen zijn erg helder qua röntgenstraling, omdat het verzamelde

<sup>5</sup>Waterstof en helium, geproduceerd in de Oerknal, zijn de meest veelvoorkomende elementen in het universum. Alle zwaardere en minder veelvoorkomende elementen worden in de levenscyclus van sterren geproduceerd.

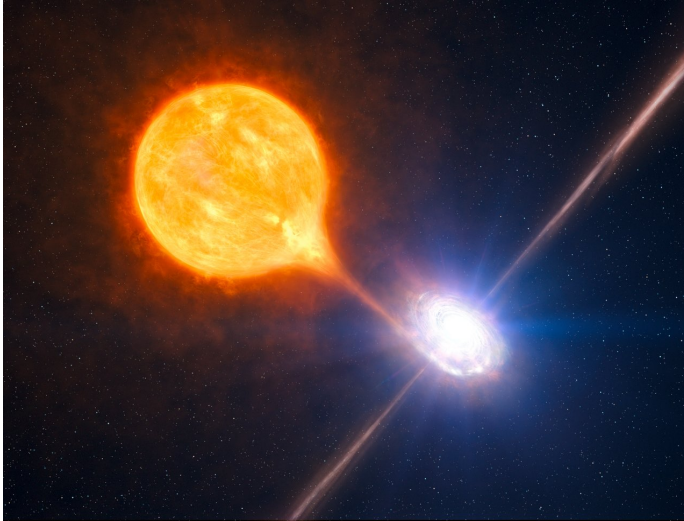
<sup>6</sup>Dit absorptiekenmerk komt voor op de ionisatie-energie van een kernatoom in de K-electronenschil van een siliciumatoom en ziet eruit als een rand of drempel.



**Figuur A.3:** Links het silicaat kwarts, dat een kristallijne structuur heeft. Rechts glas met dezelfde atomaire compositie, maar nu zonder de kristallijne geordendheid van de atomen (amorf). In quartz is ieder silicium atoom verbonden met vier andere silicium atomen via “zuurstof bruggen” en vormt daarmee een symmetrische tetraëder. Voor de duidelijkheid is het vierde silicium atoom en de daarbij behorende zuurstof brug weggelaten. Bron: NDT Resource Center, Center for NDE, Iowa State University.

materiaal van de buurster een schijf vormt rond de neutronenster of het zwarte gat. Door de vrijkomende gravitationele energie van de invallende materie in de schijf zal deze in röntgenstraling oplichten, zie Figuur A.4. De aardatmosfeer absorbeert röntgenstraling, waardoor we de straling afkomstig van de röntgendubbelsterren niet rechtstreeks vanaf de grond kunnen meten. Dit betekent dat we gebruik moeten maken van röntgentelescopen in die zich in de ruimte bevinden. In dit proefschrift maken we gebruik van data van het Chandra röntgenobservatorium, een röntgensatelliet gelanceerd in 1999. De spectra van dit observatorium zijn zeer bruikbaar voor stofstudies dankzij hun hoge spectrale resolutie. Bovendien kunnen we profiteren van het rijkgevulde Chandra data archief waarin vele spectra van röntgendubbelsterren zijn opgenomen.

In Hoofdstuk 2 gebruikten wij het spectrum van de röntgendubbelster GX 5-1 als een test om interstellair stof langs de zichtlijn naar deze bron te bestuderen. We gebruikten een set van zes verschillende silicaatmonsters, afkomstig uit de natuur of kunstmatig ontwikkeld in een laboratorium, en hebben hun röntgenspectra bij de Soleil synchrotronfaciliteit in Parijs gemeten. Deze metingen werden geschikt gemaakt voor toepassing in voor astronomische modellen om zodoende het spectrum van de Röntgendubbelster te verklaren. We concluderen dat de kristallijne olivijnsilicaten het beste het spectrum verklaren. Bovendien geeft een verstrooiingskenmerk net onder de absorptie-energie van de K-rand een aanwijzing voor de grootteverdeling van stofdeeltjes. De invloed van de aanwezigheid van grote deeltjes langs de

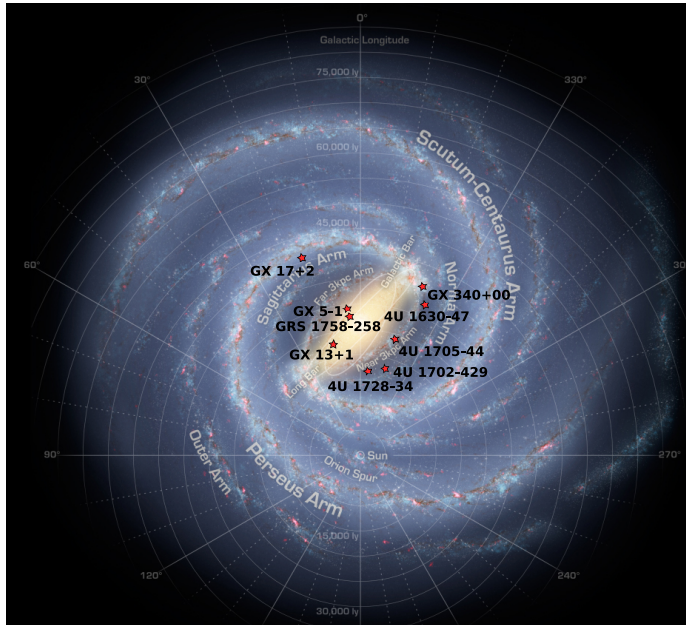


Figuur A.4: Artistieke weergave van een röntgendubbelster, bron: ESO/L. Calzada/M.Kornmesser.

zichtlijn is bestudeerd door de K-rand te modelleren met twee verschillende verdelingen van deeltjesgroottes. Hier vinden we indicaties voor de aanwezigheid van grote stofdeeltjes langs de zichtlijn naar GX 5-1.

In Hoofdstuk 3 hebben wij onze set van silicaatmonsters uitgebreid naar 14 en hun Silicium K-rand kenmerken in een tweede meetreeks bij de Soleil synchrotronfaciliteit in 2017 vastgelegd. We hebben ook het aantal waargenomen röntgendubbelsterren uitgebreid tot 9 bronnen waarvan de locatie te zien is in Figuur A.5. Deze bronnen bevinden zich in de dichtste gebieden van ons Sterrenstelsel en dit maakt het mogelijk om stof te verkennen in gebieden van ons Sterrenstelsel die anders moeilijk te bestuderen zijn. We vinden dat amorf olivijn dominant is in de meeste waarnemingen, maar dat er nog steeds een belangrijke bijdrage van kristallijne silicaten is. Dit is in tegenstelling tot eerdere resultaten in het infrarood, waar minder dan 2% van het stof als amorf wordt gedetecteerd. Dit verschil kan misschien worden toegewezen aan de gevoeligheid van XAFS voor korte afstandinteracties, terwijl in het infrarood metingen meer toegespitst zijn op lange afstandinteracties binnen de stofdeeltjes. Variaties in de abundantie van elementen tussen verschillende gebieden van ons Sterrenstelsel zijn een belangrijke factor in het begrijpen van de vorming en chemische evolutie van het Sterrenstelsel. De chemische samenstelling van de Galactische schijf varieert met tijd, aangezien sterren almaar het interstellair medium blijven verrijken. Normaal wordt in grote lijnen een toename in abundantie gemeten richting het Galactisch centrum. Wij vinden daarentegen dat in de binnenste gebieden van het Sterrenstelsel de abundanties van Silicium afvlakt en dichtbij het Galactische centrum zelfs afneemt. Dit kan wellicht worden veroorzaakt door een toename in grootte van de typische silicaatkorrels of door verschillen in de chemische evolutie van de Galactische kern vergeleken met de schijf van het Sterrenstelsel.

In Hoofdstuk 4 onderzoeken we de mogelijkheden van absorptierandstudies met toekomstige



**Figuur A.5:** Artistieke weergave van een bovenaanzicht van de Melkweg, gebaseerd op infraroodbeelden van de Spitzer Space Telescope van de NASA. De rode sterren geven de positie van de LMXB's aan. Bron: NASA/JPL-Caltech/R. Hurt

stige ruimtetelescopen: XARM (2021), Arcus (2023) en Athena (2028). We concentreren ons op de K-rand van koolstof, zwavel, aluminium, nikkel, titanium en calcium. In de relatief nabije toekomst zal de depletie en abundantie van deze elementen met zekerheid worden bepaald. In het geval van koolstof en zwavel zal ook de chemische samenstelling van het absorberende stof kunnen worden bepaald. Voor aluminium en calcium zullen - ondanks de grote depletie in het interstellair medium en de prominente absorptie door stof- in vele gevallen de spectrale rand kenmerken niet significant veranderen, zelfs wanneer er een verandering in de chemische samenstelling van de aluminium en calcium-houdende stoffen plaatsvindt. Het extinctiesignaal van grote stofkorrels kan worden gedetecteerd en gemodelleerd, waardoor het mogelijk wordt verschillende verdelingen van stofdeeltjesgroottes te testen. De lage kosmische abundantie van titanium en nikkel zullen helaas een gedetailleerde studie van spectrale rand kenmerken belemmeren.

In het laatste hoofdstuk, Hoofdstuk 5, verkennen we de mogelijkheid om het verstrooien van röntgenstralen door stofdeeltjes in een puinschijf rond een ster te meten. We zien dat modellen met een relatief sterke sterrenwind en een samenstelling van silicaten en grafiet een verstrooiingshalo in theorie kunnen versterken. Na het vergelijken van modellen met waarnemingen van een stelsel met een ster en een schijf vinden we dat deze modellen geen significant verstrooiende halo genereren, wanneer we dit meten met de huidige scherpte van röntgentelescopen. Met behulp van toekomstige röntgenmissies kan deze röntgenhalo rond sterren met puinschijven wellicht wel gemeten worden.

Tot slot, dit proefschrift laat zien dat röntgenspectroscopie een krachtige methode is om fundamentele vragen over interstellair stof te beantwoorden. In de nabije toekomst, als nieuwe breedband extinctiemodellen worden gecombineerd met de spectra van toekomstige röntgentelescopen zal deze methode lang lopende onzekerheden in modellen weghalen. Momenteel -zoals gepresenteerd in dit proefschrift- biedt de Silicium K-rand in spectra van röntgendubbelsterren al belangrijke inzichten in de chemie van interstellair silicaatstof.

*"We are stardust, we are golden  
We are billion year old carbon"*

Woodstock - Crosby, Stills and Nash, written by Joni Mitchell



# Westfriese samenvatting

## *omzet deur: Ina Slot*

### X-ray spectroscopy of interstellar dust

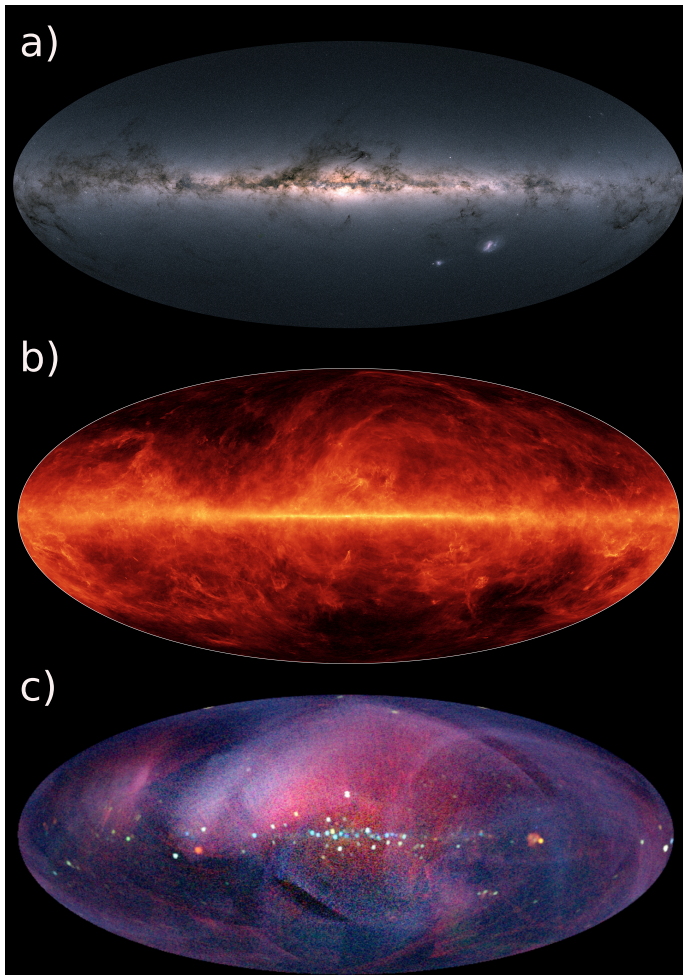
from the laboratory to the Galaxy

#### Stof tussen sterre, wat dochte ze deer voorheen van?

De ruimte tussen de sterre hiet 't interstellair medium (ISM). Die ruimte is vezelf niet leeg. Tussen de sterre ziene we wolke van iele stofdeêltjes en gasse, die allegaar aars benne. Ze he- wwe are vurme, ze benne niet even groôt en ok niet allegaar even dicht. Deuze wolke kè-je bebobbeêld zien as donkere plekke in oôze oigen Melkweg. De sterre geve licht en die wolke niet. Zuks kè-je goed bekoike bovenan Feguur A.6. De telescope in de 18e eêuw werde al beterder, dat de mense konne deuze donkere plekke ok al beterder bestudere. Vezelf wouwe ze meer wete van die plekke. Eerst bedochte ze dat 't gate in de hemel ware. De astronoom William Herschel zee bebobbeêld: 'Hier is eerlijk waar een gat in de hemel!'. Maar twei eêuwe later hadde ze in de smieze dat 't gien gate ware, maar een soortement 'inde weg zitters': wolke die 't licht van de sterre deerachter voor een deêl teughouwe. An 't end van de 19e eêuw begon Barnard kiekies te maken van de wolke en hai zette die beêlde in 1919 in een mooi boek. Op die kiekies kon je alderhand kloine dinge zien die je met je oigen oge nooit zien kenne zou. Agnes Clerke skreef over de wolke in heur boek 'Problems in Astrophysics' en zai noemde ze verduisterde objecte. In 1847 deed Friedrich von Struve een nuwe ontdekking. Ok al zien je gien wolke die 't sterrelicht teughouwe, den nag douft 'r een deêl van dat licht uit. De sterre loike puur rooierder van kleur asdat ze in 't echt benne. Pas in 1930 konne ze bewoi- ze dat 't deêls uitdove en 't rooier worre van 't sterlicht (in de sterrekunde hiet dat extinctie: 't verstrooien en opslorpe van licht) komt deur interstellaire stofdeêltjes. Schalén en Trumpler ontdekte dut baiegaar, de eerst in 1929 en de tweidst in 1930, maar ze wiste 't niet van mekaar.

#### Weerom bestudere we die stof tussen sterre?

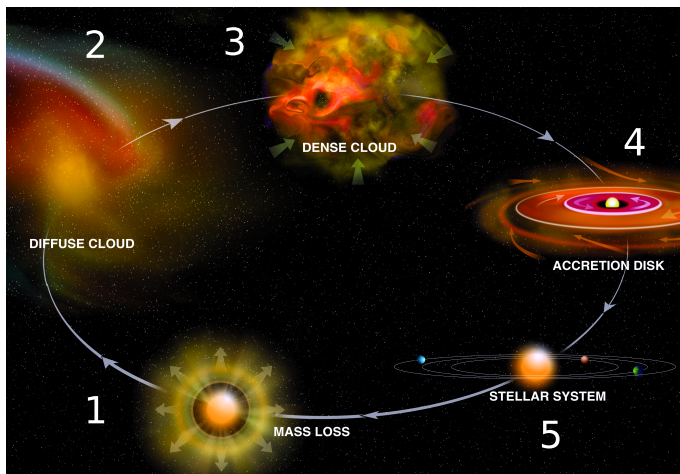
Nei de ontdekking van 't interstellair stof raakte de wetenskappers deer al meer mee in 't zin. In 't begin niet, toe hadde ze d'r hêlegaar niks mee op. Later vonde ze 't stof enkeld maar verveulend, want 't zat in de weg as ze sterre en sterrestelsels bekoike wouwe. Maar sinds de jare zestig van de vorige eêuw ziene ze 't al meer as een ansasser bai alles wat 'r beurt in 't grôte heelal. De belangroike rol van stof in 't heelal kè-je 't beste begroipe al koik je nei de levensloop van sterre. In alle paiemente van die levensloop heb stof pittig wat in de melk te



Figuur A.6: De Melkweg in drie verschillende golflengtes: a) licht wat we zien kenne, de donkere plekke benne gas en stofwolke: GAIA 330-1050 nm, © ESA/Gaia/DPAC - b) infrarood: kouwe stofdeeltjes die oplichte in infrarood, © ESA/NASA/JPL-Caltech - c) Röntgenstraling: de stippies benne röntgendubbelsterre, © JAXA/RIKEN/MAXI team.

brokkelen, koik maar nei Feguur A.7. Sterre make 't heelal roiker met elemente, die maakt worre in 't nucleosynthese proces. Die elemente worre deur sterwinde of een (super) novae de ruimte in bonjourd. Zo zurge sterre voor de bouwstiene van interstellair stof. 't Stof wordt denkelyk maakt as een condensaat in de atmosfere van sterre die puur latig in hullie evolutie zitte, in 't achterend van een onwoize supernova-ontploffing en meskien wel in 't ISM zelf. Al klontere gas en stof in de ruimte samen tot een barre dichte wolk den ken d'r een nuwe ster maakt worre in de middend van zō'n wolk. Stof is merakel belangroik bai 't maken van de ster: van 't in mekaar lazeren van de wolk deur de zwaartekracht tot 't maken van planete.

Kosmisch stof kè-je overal teugenkomme: in oôs zonnestelsel, rond jonge sterre, in skoftig grôte wolke, in de Melkweg, maar ok in sterrestelsels die een heël end weg legge. En die stof is 'r al heël vroeg in de geskiedenis van oôs heelal. Deerom ken 't oôs helpe om d'r achter te kommen hoe of 't vroege heelal grôter worren is. Dut benne al pittig wat redenaties die zegge: gaan kosmisch stof bestudere. Maar d'r is nag een are reden. Wai, en alles wat rondom oôs is, bestane uit deuze stof. Al wulle we 't begin van 't leven op deuze wirreld begroipe den moete we te weten komme wat de oorsprong is van 't stof, weer of 't van maakt is en hoe of 't maakt wordt.



Figuur A.7: De levensloop van sterre en interstellair stof in 5 stadia: 1) geëvolueerde ster, 2) diffuse wolk, 3) dichte wolk, 4) protostellare skoif en 5) stelsel met planete. In alle dêle van stervorming speelt stof een cruciale rol. © Bill Saxton, NRAO/AUI/NSF.

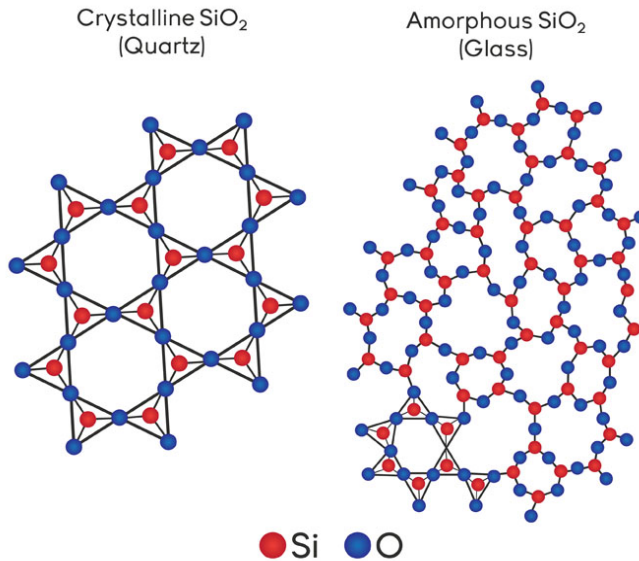
## De eigenskappe van interstellair stof

Omdat stof een grôte rol speelt in veul processe in 't heelal is 't een belangroik onderdeel in heël wat astronomische medelle. Om percieze interstellaire stofmedelle te ontwikkelen is 't van belang om onder meer te snappen wat de eigenskappe van 't stof benne, weer 't stof van maakt is, op wat voor manier 't een wisselwerking angaat met straling, wat de verdêling in grôotte is van de stofdeêltjes, wat hullies medêl en hullies makelai van binnen is, en of deuze eigenskappe verandere in verskillende omgevings. We wete wat voor êlemente deur sterre maakt worre en ok in wat voor hoeveulhede. Dat we kenne de abundatie van een êlement (de hoeveulheid die d'r is in vergeloeiking met waterstof) in de gasfase vergeloeike met astronomische waarnemings.<sup>7</sup> Die waarnemings woize uit dat de abundantie van een paar êlemente

<sup>7</sup>Waterstof en helium, maakt in de Oerknal, benne êlemente die 't meist voorkomme in 't heelal. Alle êlemente die sweerder benne en die weer d'r minder van benne, worre in de levensloop van de sterre maakt.

leiger is asdat je verwachte zou. Dat je kenne vaststelle dat de êlemente die misse, in stofdeêltjes opslôten zitte. Stof bestaat voor 't groôte deêl uit koôlstof (C), silicium (Si), oizer (F), magnesium (Mg) en zuurstof (O). Al legge we deuze kennis én boekewoishoid, sterrekundige waarnemings (bevobbeêld infraroôdspectroscopie) en studies van meteoriete bai mekaar den kenne we 't stof in 't interstellair medium in grôte loine opdêle in twei hoofdgroep: silicate (bevobbeêld pyroxeen- en olivointypes, die je vergeloike kenne met foine zandkorrels op aarde) en koôlstofhouwende stof (te vergeloiken met roet) met deerbai den ok nag oxiden (eg., MgO, SiO, SiO<sub>2</sub>), carbide (meistens SiC) en metallisch oizer.

Dat we wete gerust wel een zoôt, maar d'r benne ok nag zat dinge onzeker met dat interstellair stof. We wete niet percies hoe en weerzo stof maakt wordt en hoe de oigensappe van stof aars worre in verskillende omgevings. We wulle ok graag wete wat of 'r met stof beurt in de buurt van 't instellair medium weer 't puur grof te keer gaat. Deer wordt stof beskôten met straling en kosmische deêltjes en stikmaakt met lillijke skokgolve. Deur al deuze onwoizigheid verandert meskien de makelai van 't stof. Al hadde de stofdeêltjes een kristalloine makelai voordat ze in 't instellair medium kwamme den zouwe ze deuze makelai kwoit rake kenne en al meer zonder vurm rake, koik maar nei Feguur A.8. Deerbai wete we ok niet percies wat of de chemische samenstelling van de stofdeêltjes is.

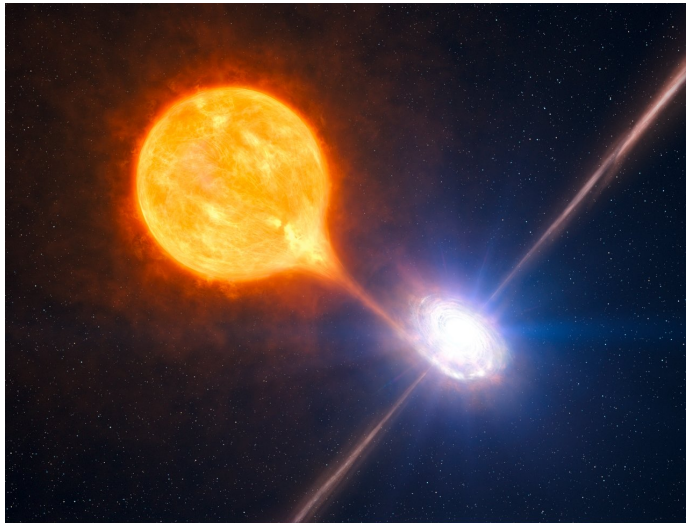


**Feguur A.8:** Links 't silicaat kwarts, dat een kristallijne structuur heb. Rechts glas met dezelfde atomaire compositie, maar nou zonder de kristalloine geordendheid van de atome (amorf). In quartz heb elk silicium atoom een band met vier are silicium atome deur "zuurstof bregge". Samen make ze een symmetrische tetraëder. Om niet in de tist te raken, liete we 't vierde silicium atoom en z'n zuurstof breg weg. Bron: NDT Resource Center, Center for NDE, Ioawa State University.

## Dut proefskrift

Hoge resolutie röntgenspectroscopie is een belangroike techniek in de studie nei interstellair stof. As we spectrale kenmerke in röntgenspectra en verstrooiingshalos rond röntgenbronne bestudere, kenne we -zoas al zoid is- meskien een paar wezelijke vrage over interstellair stof beantwoorde. In dut proefskrift benne we vooral in de weer met stof van 't silicaatype, ien van de hoofbestanddele van interstellair stof.

Röntgenstrale benne verlegen best om silicate te bestuderen. Dat komt omdat 'r spectrale absorptiekenmerke van zuurstof, magnesium, silicium en oizer in 't röntgengebied van 't spectrum zitte. Deuze êlemente benne de belangroikste onderdele van silicate. We gebruike met name 't spectrale absorptiekenmerk van Silicium, dat we ok wel de Si K-rand noeme<sup>8</sup>, om de oigenskappe van silicaatstof te onderzoeken. Voor elk type silicaatstof benne de spectrale kenmerke in de rand, ok wel Röntgenabsorptiefoinstructure (XAFS) kloin effies aars. Dut betekent dat ze een unieke vingerofdruk voor 't stof vorme.



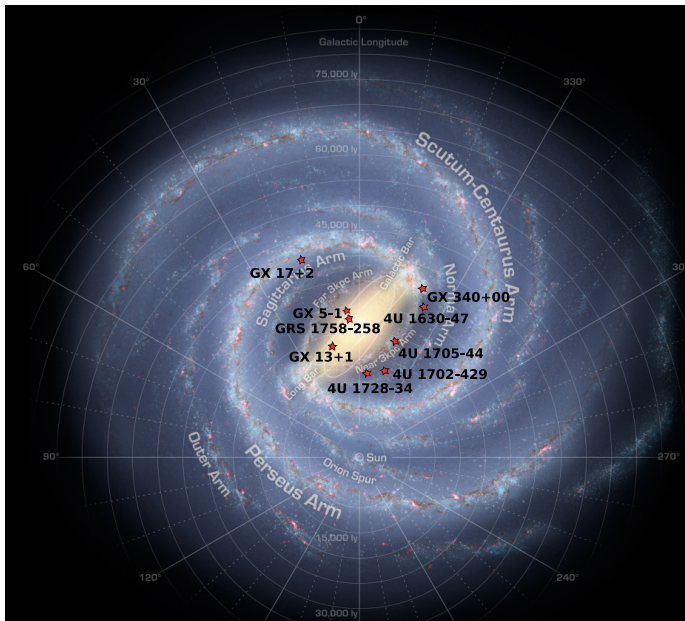
Figuur A.9: Kunstig beeld van een röntgendubbelster, bron: ESO/L. Calçada/M.Kornmesser

In de Melkweg benne heldere lage massa Röntgen dubbelsterre. Dat benne verlegen beste bronne om goed te koiken nei 't stof wat 'r tussen loit en 't gas langs de zichtloin. Dat doene we deur ze heël gewoôn te gebruiken as een lanteerns die deur 't interstellair medium skoine, deerbai wordt de straling deur stof en gas voor een deël opslurpt en verstrooid. Deuze bronne bestane uit twee onderdele, een neutrônester of swart gat dat spul bai mekaar sweëlt van een ster in de buurt, deurgaans een gewône hoofdreeksster (dat gien reuzester). Deuze systeme benne pittig helder wat röntgenstraling angaat, omdat 't spul van de buurster wat bai mekaar sweëld is een skoif maakt rond de neutrônester of 't swarte gat. Deur de gravitationële energie

<sup>8</sup>Dut absorptiekenmerk komt voor op de ionisatie-energie van een kernatoom in de K-electronenschil van een siliciumatoom en ziet 'r uit as een rand of drumpel.

die vraikomt van 't invallende spul in de skoif zal deuze röntgenstraling oplichte, koik maar nei Feguur A.9. De aardatmosfeer slurpt röntgenstraling op. Deorum kenne we de straling van de röntgendubbelsterre niet drekt in ien keer vanof de grond mete. Nei, röntgentelescope die in de ruimte zwurve, zalle oôs helpe. In dut proefskrift make we gebruik van data van 't Chandra röntgenobservatorium, een röntgensatelliet die in 1999 de ruimte inzwuupt is. De spectra van dut observatorium benne heël best voor stofstudies omdat ze een barre hoge spectrale resolutie hewwe. En deer komt ok nag bai dat we profoit hewwe van 't roike Chandra data archief, deer zitte een zoôt spectra van röntgendubbelsterre in.

In Hoofdstuk 2 gebrukte we 't spectrum van de röntgendubbelster GX 5-1 as een test om interstellair stof langs de zichtloin nei de bron te bekoiken. We dede dat met een stel van zes verskillende silicaatmonsters, die kwamme uit de netuur of ware met een kunsie maakt in een laboratorium, en we hewwe hullies röntgenspectra bai de Soleil synchrotronfacilitoit in Perois meten. Deuze metings werde klaarmaakt om ze toe te passen in astronomische medelle om zodoend 't spectrum van de Röntgendubbelster uit te tisten. We bedochte dat de kristalloine olivoin silicate 't spectrum 't beste verklare kenne. En deerbai komt ok nag dat een verstrooiingskenmerk net onder de opslurp-kraft van de K-rand een anwoizing geeft voor de grôteverdeling van de stofdeeltjes. Wat die grôte deeltjes langs de zichtloin allegaar doene, bekeke we deur de K-rand in medel te brengen met twei verskillende verdélings van deeltjesgrôte. Hier vonde we anwozings dat 'r grôte stofdeeltjes langs de zichtloin nei GX5-1 benne.



Feguur A.10: Kunstig beëld van een anbliek van boven van de Melkweg, maakt nei infraroôdbeëldje van de Spitzer Space Telescope van de NASA. De roike sterre woize de plaas an van de LMXB's. © NASA/JPL-Caltech/R. Hurt

In Hoofdstuk 3 hewwe we oôze set van silicaatmonsters grôter maakt nei 14 en hullies Silicum K-rand in 2017 in een tweede meetreeks vastloid bai de Soleil synchrotronfacilitoet. We hewwe ok de röntgendubbelsterre die we zage, vergroôt tot negen bronne. Hullies plaas kenne we zien in Feguur A.10. Deuze bronne zitte in de alderdichste plaase van oôs Sterrestelsel. Deerom kenne we stof bekoike in barre lastige gebiede van dat Sterrestelsel. We vinde dat amorf olivoin de baas is in de meiste waarnemings, maar dat 'r nag altoid een grôte baidrage is van kristalloine silicate. Dut is aars as de resultate die we eerder zagge in 't infraroôd, deer werd minder as 2% van 't stof as amorf vonden. Dut verskil ken meskien komme deur de gevoelighoid van XAFS voor interacties die kortbai benne. In 't infraroôd benne metings meer doende met interacties binnen de stofdeêltjes van puur vedder weg. Verskille in de abundantie van êlemente tussen alderhand gebiede van oôs Sterrestelsel benne belangroik voor 't snappen van de makerai en de chemische evolutie van 't Sterrestelsel. De chemische samenstelling van de Galactische skoif is altemet aars met toid, omdat sterre 't interstellair medium alsmar roikerder make. 't Is gewoôn dat de abundantie meer wordt al mete we richting 't Galactisch centrum. Maar we vinde dat in de binnenste plaase van 't Sterrestelsel de abundantie van Silicum vlakker wordt en dicht in de buurt van 't Galactisch centrum zellefs mindert. Meskien komt dat deur de typische silicaatkorrels die al grôterder worre of deur verskille in de chemische evolutie van de Galactische kern in vergeloiking met de skoif van 't Sterrestelsel.

In Hoofdstuk 4 koike we nei wat 'r ken met absorptierandstudies met ruimtetelesope van de kommende toid: XARM (2021), Arcus (2023) en Athena (2028). We koike heêl sekuur nei de K-rand van koôlstof, zwavel, aluminium, nikkel, titanium en calcium. Over niet als te lange toid zal de depletie en abundantie van deuze êlemente met zekerhoid vaststeld worre. In 't geval van koôlstof en zwavel zal ok de chemische samenstelling van 't opslurpende stof bepaald worre kenne. Voor aluminium en calcium zalle - ondanks de grôte depletie in 't interstellair medium en de prominente opslurping deur stof - de spectrale rand kenmerke een zoôt kere niet aars worre, zellefs al verandert de chemische samenstelling van de stoffe waar aluminium en calcium inzit. 't Extinctiesignaal van grôte stofkorrels ken zocht en in medel douwd worre, den kenne verskillende verdêlings van stofdeêltjes test worre. 't Is nôselijk maar de lage kosmische abundantie van titanium en nikkel zalle een sekure studie van spectrale rand kenmerke teughouwe.

In 't leste hoofdstuk, Hoofdstuk 5, koike we of we 't verstrooien van röntgenstrale deur stofdeêltjes in een puinskoif rondom een ster mete kenne. We ziene dat medelle met een nagal sterke sterrewind en een samenstelling van silicate en grafiet een verstrooiingshalo versterke kenne. Maar dut ziene we enkeld in theorie, niet in 't echie. Neidat we medelle vergeleke met waarnemings van een stelsel met een ster en een skoif vinde we dat deuze medelle gien duidelijk verstrooiende halo voor mekaar kroige, al mete we zuks met de teughwoordige skerpte van röntgentelesope. Meskien ken deuze röntgenhalo rond sterre met puinskoive in de kommende toid wel meten worre met de röntgenmissies die d'r den benne.

We benne an 't end van de akker. In dut proefskrift kè-je zien dat röntgenspectroscopie een goeie manier is om antwoorde te vinden op grondige vrage over interstellair stof. In de toid die komme gaat - al worre nuwe breedband extinctiemedelle mongen met de spectra van toekomstige röntgentelesope - zal deuze manier van doen lang lopende onzekere zake in medelle weghale. Opheden - zoas in dut proefskrift opskreven staat- geeft de Silicum K-rand in spectra van röntgendubbelsterre al een hêle beste koik op de chemie van interstellair silicaatstof.

*“Zelfs als ik ooit de adde ben  
Dan weet je dat ik ergens ben  
Dan ben ik alsnog, in de lucht als sterrenstof”*

Sterrenstof - De Jeugd van Tegenwoordig

# English summary

## X-ray spectroscopy of interstellar dust from the laboratory to the Galaxy

### Interstellar Dust from an Historical perspective

The space between stars, also called the interstellar medium (ISM), is not a perfect vacuum. Between the stars, we can observe clouds of dust and gas of varying shapes, densities and sizes. These clouds can be observed, for instance, as dark patches in our own Galaxy contrasting with the light from the stars, as can be seen in panel a of Figure A.11. The development in the quality of telescopes in the 18th century made it possible to observe these dark parts of the Galaxy in more detail, which led to an increase in interest in these objects. At first, some of the dark patches were thought to be holes in the sky (William Herschel: “Hier ist wahrhaftig ein Loch im Himmel”). However, in the early 20th century, these ‘holes’ were eventually discovered to be foreground clouds obscuring the stars behind them. In the 1890s Barnard started to photograph these clouds (eventually published in a catalogue, Barnard (1919)), which revealed many details, invisible to the naked eye. Agnes Clerke described them in her book ‘Problems in Astrophysics’ as obscuring bodies. Even in the case where no clouds are observed towards a star, it was found, already as early as 1847, that extinction of light still takes place. It took until 1930 to prove that the extinction, shown by the reddening of stars, is indeed caused by interstellar dust particles (independently described by Schalén (1929) and Trumpler (1930)).

### Motivation

Since its discovery, the way dust has been perceived slowly changed. At first it was completely ignored, then it was considered to be a hindrance when trying to observe the stars and galaxies, but since the 1960s, dust has been more and more seen as an important component that drives many processes in the universe. The important role of dust in the universe is best shown by its role in every stage of the life cycle of stars, Figure A.12. Stars enrich the universe with elements, produced during the nucleosynthesis process and in this way, provide the building blocks for the interstellar dust particles, which are thrown into space by e.g., stellar winds or (super) novae. Dust is thought to form as condensates in the atmospheres of evolved stars, or in the aftermath of a violent supernova explosion, and perhaps as well in the ISM itself. When clouds of gas and dust clump together, a new star can be formed in the core of such a dense

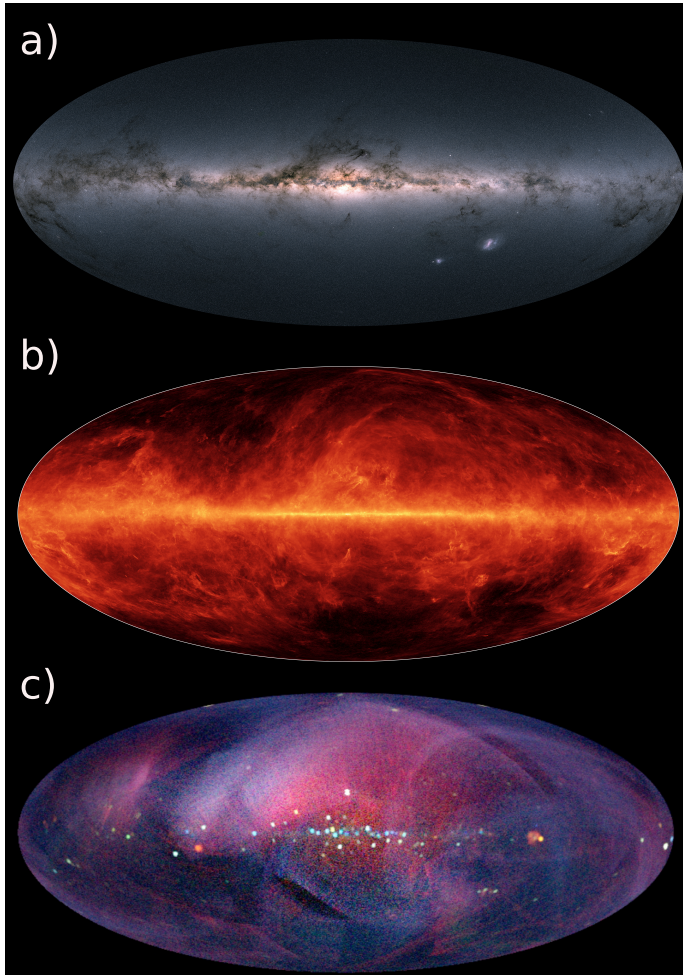


**Figure A.11:** The Galaxy in three different wavelengths: a) The visible-near infrared: GAIA 330-1050 nm, image credit: ESA/Gaia/DPAC - b) infrared: Planck cold dust (20 K) map, image credits: ESA/NASA/JPL-Caltech - c) The X-rays: 0.5-16 keV MAXI all-sky survey, image credits: JAXA/RIKEN/MAXI team.

cloud. During the formation process of a star, dust plays a crucial role: from the collapse of the cloud to the formation of planets. Cosmic dust can be observed virtually everywhere: in our solar system, around young stars, in giant clouds, the Galaxy, but also in distant galaxies and it is already present in the earliest eras of the universe. Hence, studying dust can help us to understand how the universe evolved. Besides the already given arguments in favor of dust studies, there is of course another important reason to study dust; we and everything around us all consists of cosmic dust. Therefore, if we want to understand the origin of life, it is necessary to understand the origin, formation and composition of cosmic dust.

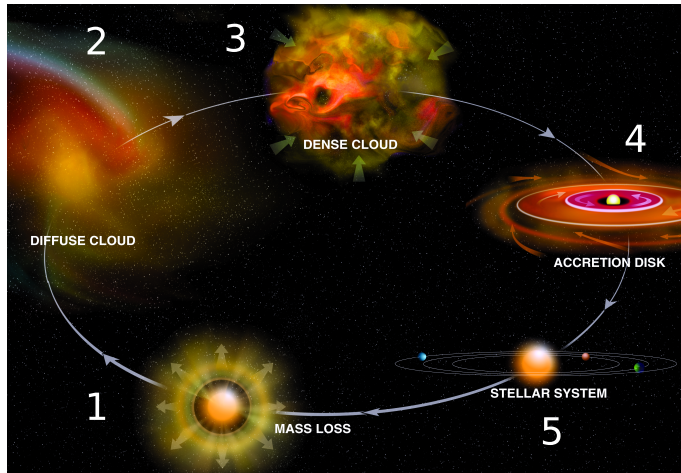


**Figure A.12:** The life cycle of stars and interstellar dust in five stages: 1) evolved star, 2) diffuse cloud, 3) dense cloud, 4) protostellar disk phase and 5) evolved planetary system. At each stage in this cycle dust plays a crucial role. Image credit: Bill Saxton, NRAO/AUI/NSF.

## The properties of interstellar dust

Since dust plays a role in many processes in the universe, it has become an essential component in many astronomical models. In order to develop accurate interstellar dust models, it is important to understand the properties of dust, what interstellar dust exactly consists of, how it interacts with radiation, what the grain size distribution is, what the shape and internal structure of the grains is, and whether these properties change in different environments. Since we know what elements stars produce and in which quantities, we can compare the abundance of an element (meaning the expected occurrence of an element with respect to hydrogen) in the gas phase with observations<sup>9</sup>. These observations show us that the abundance of some elements is lower than expected, which leads to the conclusion that these missing elements are locked up in dust particles. Dust thus exists mainly of carbon (C), silicon (Si), iron (Fe), magnesium (Mg) and oxygen (O). Combining this information with theory, astronomical observations (e.g., infrared spectroscopy) and studies of meteorites, dust in the ISM can be roughly divided into two main groups, namely silicates (e.g., pyroxene and olivine types, comparable to fine sand grains on earth) and carbonaceous dust (comparable to soot), with the addition of oxides (e.g., MgO, SiO, SiO<sub>2</sub>), carbides (mainly SiC) and metallic iron. However, there are still many uncertainties about interstellar dust. We do not exactly know how and where dust is produced, and how the properties of dust change in different environments. We would like to know what happens to dust in the violent environment of the ISM, where dust is bombarded by radiation and cosmic ray particles, and destroyed by shock waves. This may change the internal structure of the dust. If the dust grains had a crystalline structure

<sup>9</sup>Hydrogen and helium, produced in the Big Bang, are the most abundant elements in the universe. All the heavier and less abundant elements are produced in the life cycle of stars.

before their encounter with the ISM, they may lose this structure and become more and more amorphous, see Figure A.13. Furthermore, we do not exactly know the chemical composition of the dust particles.

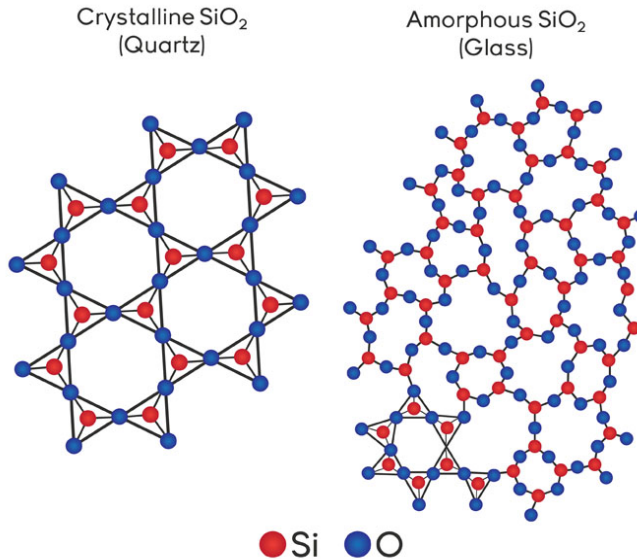


**Figure A.13:** On the left, the crystalline silicate quartz. On the right, glass with the same composition as quartz, but without the crystalline structure (amorphous). In quartz, every silicon atom is connected with four other silicon atoms via a so-called oxygen bridge and, in this way, forms a symmetrical tetrahedra. For clarity, the fourth silicon atom and the corresponding oxygen bridge are omitted. Image credit: NDT Resource Center, Center for NDE, Iowa State University.

## This thesis

High resolution X-ray spectroscopy is an important tool in interstellar dust studies. By studying dust features in X-ray spectra and scattering haloes around X-ray sources, we may be able to answer some of the fundamental questions about interstellar dust, as mentioned above. In this thesis, we focus on silicate dust types, one of the main constituents of ID. The X-rays are particularly suitable to study silicates due to the presence of absorption features of O, Mg, Si and Fe in the X-ray band. These elements form the most important components of silicates. We mainly use the silicon absorption feature, called the Si K-edge<sup>10</sup>, to study the properties of silicate dust. For each type of silicate dust, the features in the edge, called X-ray absorption fine structures (XAFS), are slightly different. This means that they are a unique fingerprint of the dust.

<sup>10</sup>This absorption feature occurs at the ionisation energy of a core atom in the K-shell of a silicon atom.

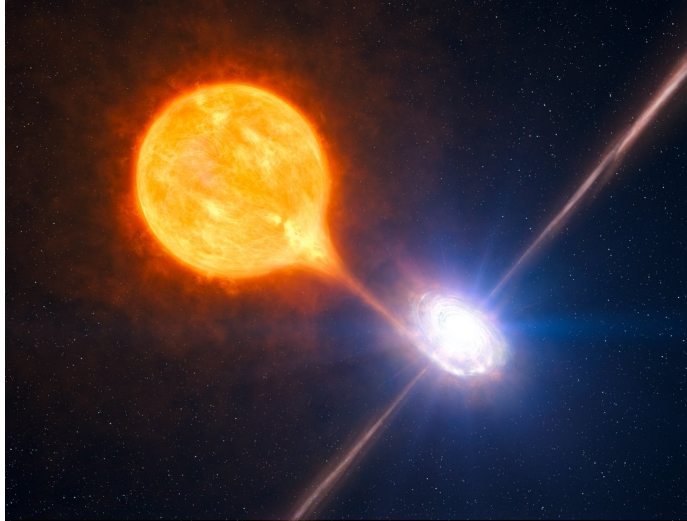
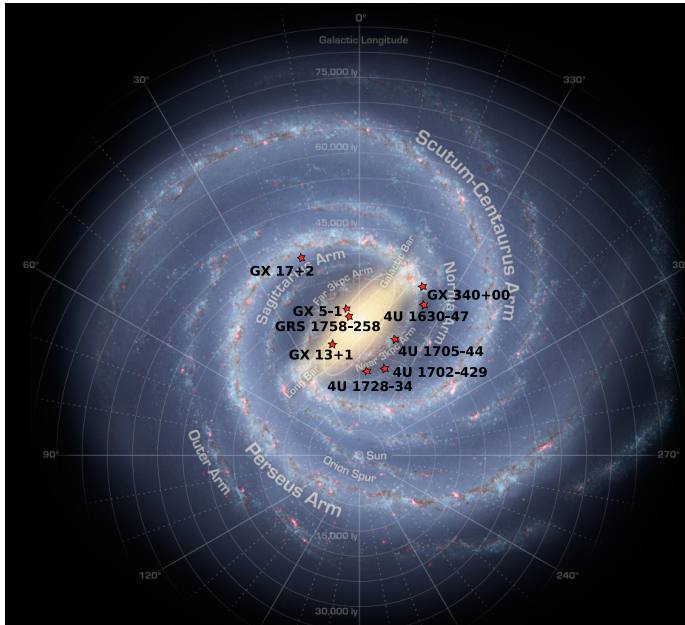


Figure A.14: Artist's impression of an X-ray binary, image credit: ESO/L. Calzada/M.Kornmesser.

Bright low mass X-ray binaries in the Milky Way are ideal sources to study the intervening gas and dust along their lines of sight, simply using them as a lantern shining through the ISM. These sources consist of two components, a neutron star or a black hole which accretes material from a companion star, usually a normal star (viz., not a giant star). These systems are very bright in X-rays, because the accreted material from the companion star forms a disk around the accretor, which emits in the X-rays due to the gravitational potential energy of the infalling matter. We cannot directly observe the X-ray radiation from Earth due to the Earth's atmosphere, therefore we need X-ray telescopes in space to observe the X-ray binaries. In this thesis, we make use of data from the Chandra X-ray observatory, an X-ray satellite launched in 1999. The spectra from this observatory are highly suitable for dust studies thanks to their high spectral resolution. Furthermore, we profit from the rich Chandra data archive which contains spectra of many X-ray binaries.

In Chapter 2 we used the spectrum of the X-ray binary GX 5-1 as a test case to study interstellar dust along the line of sight of this source. We used a set of six different silicates and measured their X-ray spectra at the Soleil synchrotron facility. These measurements were adapted to astronomical models and fitted to the spectrum of the X-ray binary. We find that the crystalline olivine silicate best fitted the spectrum. Furthermore, the scattering feature which occurs just below the K-shell absorption energy provides direct link to the grain particle size distribution. The impact of the presence of large particles along the line of sight is studied by modeling the edge with two different particle size distributions. Here we find indications for the presence of large particles along the line of sight towards GX 5-1.

In Chapter 3 we expanded our set of silicate samples to 14 and measured their Si K-edge features in a second measurement run at the Soleil synchrotron facility in 2017. We also expanded the number of observed X-ray binaries to nine different sources of which the location



**Figure A.15:** Artist's conception of a top-down view of the Milky Way, based on infrared images from NASA's Spitzer Space Telescope. The red stars indicate the position of the LMXBs studied in this thesis. Image credit: NASA/JPL-Caltech/R. Hurt

can be seen in Figure A.15. These sources are located in the densest regions of our Galaxy and this makes it possible to explore the dust in these regions of our Galaxy, which are otherwise hard to study. We find that amorphous olivine is dominant in most of the fits, but that there is still a significant contribution of crystalline silicates. This contrasts with results from the infrared, where less than 2% of amorphous dust is detected. The difference may be attributed to the sensitivity of XAFS to short range order, whereas, in the infrared, observations are focused on long range disorder in the dust particles. Variations in the abundance of elements between different regions of the Galaxy are a key factor in understanding the formation and chemical evolution of the Galaxy. The chemical composition of the Galactic disk varies with time as stars continually enrich the ISM. Generally, an increase in abundance is measured toward the Galactic Center (GC). We find that the in the inner regions of the Galaxy abundances of silicon flattens and even decrease toward the GC. This may be caused by an increase in the typical silicate grains size or differences in the chemical evolution of the GC environment in comparison to the Galactic disk.

In Chapter 4 we present an outlook for edge studies with future telescopes: XARM (2021), Arcus (2023) and Athena (2028). We focus on the K-edges of carbon (C), sulfur (S), aluminium (Al), nickel (Ni), titanium (Ti) and calcium (Ca). In the relatively near future, the depletion and abundances of these elements will be determined with confidence. In the case of C and S, the characterization of the chemistry of the absorbing dust will be also determined. For Al and Ca, despite the large depletion in the interstellar medium and the prominent dust

absorption, in many cases the edge feature may not be changing significantly with the change of chemistry in the Al- or Ca- bearing compounds. The extinction signature of large grains may be detected and modeled, allowing a test on different grain size distributions for these elements. The low cosmic abundance of Ti and Ni will not allow us a detailed study of the edge features.

Lastly, in Chapter 5, we explore the possibility of detecting X-ray scattering by dust particles in a debris disk. We use as a best test case the debris disk around the star AU Microscopii. We find that models with a moderately strong stellar wind model and a composition of silicates and graphite are the ones that would enhance a theoretical halo. After comparing the models with observations of AU Microscopii, we find that the models do not produce a significant scattering halo, using the current spatial resolution. However, future X-ray missions may enable us to observe the X-ray halo of debris disks.

In conclusion, we showed that X-ray spectroscopy provides a powerful method to answer fundamental questions about interstellar dust. In the near future, when combining new broadband extinction models with the spectra of upcoming X-ray missions, this method will settle long standing uncertainties in the modeling of interstellar dust. Presently, as presented in this thesis, the silicon K-edge in the spectra of X-ray binaries already offers important insights into the chemistry of interstellar silicate dust.

*“Is there going to be anything left? - Only stardust”*

Doolin Dalton/Desperado (reprise) - Eagles

# Curriculum Vitae

I was born on December 15th 1985 in the city of Alkmaar. I lived in Broek op Langedijk, where I attended the local primary school de Phoenix. My interest in astronomy started when my father took me to Dwingeloo when I was 8 years old, where we visited the local planetarium and the radio telescope. I was totally fascinated and it inspired me to give a talk in class about the solar system, for which I made models of the planets and the Sun from Styrofoam. From that moment on, I wanted to know as much as possible about this mysterious universe we live in. I attended het Han Fortmann college and chose the specialisation science and technology, which would give me access to study astronomy in Leiden. Although astronomy was not yet officially part of the physics curriculum, we did occasionally spend some time on it at school. I will never forget racing back to school in 2004 when the summer holiday already started to see the Venus transit. After obtaining my gymnasium diploma, I started the astronomy bachelor in 2004 in Leiden. In my bachelor research project, I studied the gas content variation in the mass-metallicity relation of galaxies under the supervision of Jarle Brinchmann. In 2009, I obtained my bachelor diploma and consequently started the scientific astronomy master. For my minor master research project, I worked on the modelling of weak gravitational lensing in galaxy clusters. My major master research project was about the feasibility of transit photometry in debris disks, under supervision of Matt Kenworthy. This resulted in a paper published in 2014. It was this project that made me very enthusiastic about doing research. During my studies and between obtaining my master's degree and starting a PhD, I worked as a tour guide at the historical Old Leiden Observatory. I was also involved in the organisation of the many outreach events which were held in this building. For these efforts, I was awarded the Kaiser outreach prize in 2013.

In the same year, I was selected to join the application round for a PhD position in Leiden. I accepted the offer to start a PhD with Elisa Costantini and Xander Tielens about interstellar dust. I worked both in Leiden at the observatory and in Utrecht at SRON. This combination, although it involved quite some travelling between the two cities, proved to be very nice and refreshing experience. As part of my teaching duties in Leiden I assisted Ignas Snellen and Michiel Hogerheijde with the course Praktische Sterrenkunde (2013-2015). This involved assisting with the observing practicum with the telescopes at the Old Observatory. In 2015 I was chair in the board of the Kaiser Lente Lezingen, a series of lectures for the general public. During my PhD, I attended two schools: the SUCCESS 2014 school about X-ray spectroscopy in Les Houches, France and the ASTRO-H school on spectroscopy in Tokyo, Japan. In 2017, I went to the Soleil Synchrotron facility in Paris to perform XAFS measurements on interstellar dust samples. I had the opportunity to present my work at various conferences and workshops in Amsterdam, Boston, Prague (EWASS 2017), Taipei, Tokyo, Heidelberg, Garching, Dublin and in Copenhagen, where I gave an invited talk at the Cosmic Dust conference which is organised every 5 years. I will continue my scientific career at the ASIAA in Taipei, Taiwan.



# Acknowledgments

Although writing a dissertation and doing research can sometimes feel like a lonely process, this thesis would not be in existence without the help and support of the people mentioned here. First, I would like to thank my supervisors Elisa and Xander. Thank you for putting your trust in me; I am very happy that in 2013 you were already convinced I would be writing this last page of my thesis someday. Elisa, thank you for all the advice you gave me throughout the PhD on how to sail through this world. You are a great travelling companion as well and I have wonderful memories of all the conferences and workshops we visited! Xander, thank you for all your support, the fun skype calls from all over the world and wise lessons about life.

I am very grateful for the support from the laboratory group of Jena observatory and in particular Harald Mutschke, who provided and produced the samples, without which this project would not have been possible. I greatly appreciate the help of Frank de Groot, pointing us to the right beamlines and making the world of XAFS less mysterious. I also want to thank Cor de Vries for all his help and advice, particularly on the laboratory part of this PhD. Furthermore, a PhD project at two different institutes would not be possible without the help of the support staff of both Leiden and SRON. My thanks also to Frank Uittenbosch and Jelle de Plaa for their assistance with all sorts of computer and software related problems.

Dear SRON friends: François, Daniele, Cátia, Igone, Junjie, Liyi, Kristhell, Francesca, Giacomo, Ioanna, Marianne, Zuzanna, Margherita, Missagh, Davide, Manuel, Hiroki, Laura, Ton, Jeroen, Theo, Remco and Lucien. Thank you for all the great coffee and lunch breaks, borrels and colloquium dinners. SRON would not have been so much fun without you. Ton, thank you for pulling me out of my work and the great conversations we subsequently had about what kind of exciting objects the sky would have to offer to observe in the coming week, even when we knew it would be pouring rain. Cátia, my PhD sister! Like you already remarked, it was a good thing Elisa hired us both and more or less at the same time. How nice to have such a good friend in the office next door! I will never forget how we ran through the textile city Nipori in Tokyo, Japan, searching for the perfect fabrics in the shops. Thank you for your support, all the nice conversations and for making such a great photograph of the artwork on the cover of this thesis! Igone, I will never forget the n times we went from Leiden to Utrecht and back in your car and all our interesting conversations along the way. After I took a nasty fall with my bike in the last year of the PhD, you (and your car) were a life saver. Thank you for your friendship, your support and for being my paranymph! I would like to thank my office mates at SRON: Manuel, Laura, Jeroen and Daniele. You certainly made every day in the office a lot more fun. Daniele, it was great to have a “dusty accomplice” during this PhD. I am very happy that we could work together and solve some interesting problems. Besides that, you manage to always cheer everyone up!

And of course, there are my friends from Leiden throughout the years! Arthur, Jesse,

Stephanie, Emanuele, Alex, Dominique, Josha, Xiaohu and Dennis. I would like to thank my office mates from office 529: Heather, Alessandra, Mher, Maria, Isabel, Irene, Cameron, Corentin, Martijn and Dario and of course the other current and former ISM group members who were not also inhabitants of 529: Francisco, Liz, Pedro, Marcelo, Pablo, Kim, Kirstin, Claudia, Daniel Harsono and Cornelia. Heather, Isabel and Alessandra, thanks for all the uplifting and supportive conversations we had and for your good advice! Alex, we share a great interest in the history of Leiden Observatory which led to the organisation of many interesting events (such as the Kaiser Lente Lezingen) and lovely distractions throughout my PhD. You are a great friend and I wish you all the best with your PhD project in Sweden.

Tessa, Suzan, Mandy, Maaïke, Liset en Marleen, wat fantastisch dat onze vriendschap sinds de middelbare school heeft standgehouden. Bedankt voor alle keren dat jullie mij uit mijn werk hebben getrokken en voor al jullie gezelligheid! Ik wil hier ook graag Kees Kerstens bedanken: Kees, zonder jouw advies was ik met veel minder zelfvertrouwen naar de middelbare school gegaan. My thanks to H el ene and Jos for all the great weekends I could spend in Limburg, it always felt like a very welcome holiday during stressful times. My brothers, Guido (how great that we both did a PhD at the same time, although in different countries!), Esben (my other paranimph!), Math e (good luck with your PhD at CWI) and Benth en (good luck with your PhD at the mathematical institute in Leiden), I want to thank you for all your support and understanding. Having diplomas from all the different studies of the Leiden beta faculty is quite a unique thing. We should combine our knowledge in a paper one day! A big thank you to my parents, Marianne and Siem, who put up with all my frustrations, but luckily you were also there to share the great moments with me. It was a lot of fun to be able to let you take part in my PhD journey, sometimes literally when you joined me for a short vacation after a conference. You taught me never to give up and that is why this thesis is dedicated to you both. Many thanks also to my mother, Marianne, for designing the beautiful thesis cover! Gilles, thank you for always being there for me. In the moments that I have doubts about a thousand things at the same time, you master the art of calming me down. I still feel so lucky to have met you during the second year of my studies and that from then on, we were able to share this experience from the bachelors to the PhD and now further into the future, wherever it may bring us.

Thank you all,  
Sascha

# List of acronyms

ACIS: Advanced CCD Imaging Spectrometer  
ACS: Advanced Camera for Surveys  
ADT: Anomalous Diffraction Theory  
AGB: Asymptotic Giant Branch  
ALMA: Atacama Large Millimeter/submillimeter Array  
AU: Astronomical Unit  
CC: Continuous Clocking  
CCD: Charge-Coupled Device DDA: Discrete dipole approximation  
FFT: Fast Fourier Transform  
FWHM: Full Width Half Maximum  
GC: Galactic Center  
GEMS: Glass with Embedded Metal and Sulphides  
HAC: Hydrogenated Amorphous Carbon  
HEG: High Energy Grating  
HETG: High-Energy Transmission Grating  
HETGS: High-Energy Transmission Grating Spectrometer  
HRC: High Resolution Camera HST: Hubble Space Telescope  
ID: Interstellar Dust  
ISM: Interstellar Medium  
LETGS: Low Energy Transmission Grating Spectrometer  
LMXB: Low Mass X-ray Binary  
LOS: Line Of Sight  
LUCIA: Line for Ultimate Characterisation by Imaging and Absorption  
LURE: Laboratory for the Use of Electromagnetic Radiation  
MEG: Medium Energy Grating  
MRN: Mathis-Rumpl-Nordsieck  
NWO: Nederlandse Organisatie voor Wetenschappelijk Onderzoek  
PAH: Polycyclic aromatic hydrocarbons  
PSF: Point spread function  
ROSAT: Röntgensatellit  
TE: Time Exposure  
TGCat: Chandra Transmission Grating Catalog  
SED: Spectral Energy Distribution  
SOLEIL: Optimized Light Source of Intermediate Energy to LURE  
STIS: Space Telescope Imaging Spectrograph  
SW: Stellar Wind  
UV: Ultraviolet

IR: Infrared

XAFS: X-ray Absorption Fine Structure

XARM: X-ray Astronomy Recovery Mission

XIFU: X-ray Integral Field Unit





*Inveniam viam aut faciam*

